Field Measurement and Finite Element Simulation of Pavement Responses to Standard and Reduced Tire Pressure

By

Qingfan Liu

A Thesis Submitted to the Faculty of Graduate Studies of

The University of Manitoba

in Partial Fulfillment of the Requirements of the degree of

MASTER OF SCIENCE

Department of Civil Engineering

University of Manitoba

Winnipeg, Manitoba

THE UNIVERSITY OF MANITOBA

FACULTY OF GRADUATE STUDIES

*****

COPYRIGHT PERMISSION

Field Measurement and Finite Element Simulation of Pavement Responses to Standard and Reduced Tire Pressure

By

Qingfan Liu

A Thesis Submitted to the Faculty of Graduate Studies of

The University of Manitoba in Partial Fulfillment of the Requirements of the degree

Of

MASTER OF SCIENCE

ABSTRACT

The spring thaw period significantly reduces the bearing capacity of low volume asphalt roads. To compensate for the reduced bearing capacity, highway agencies apply spring load restriction (SLR) to limit the damage caused by heavy loads during the thaw-weakened period. While the imposition of SLR may reduce road damage, it has a major impact on truck productivity. An alternative to reducing truck loads is the reduction of truck tire pressure. The reduced tire pressure lowers the tire-pavement contact pressure and the associated damage during the spring period.

Research was conducted on two pavement sections, a thin asphalt pavement and a thin asphalt-treated surface. These two structures are representative of the majority of provincial pavement types subject to spring load restriction in Manitoba, Canada. The test sections were instrumented with weather and environmental sensors, strain and deflection gauges. Pavement moisture and temperature were collected continuously, while pavement strain and reflection were monitored during field test period. Tire pressure control systems (TPCS) tests were carried out at the instrumented sections in spring and fall 2009.

The purposes of this research were:

- To evaluate the impact of reduced truck tire pressure on the strain response of low volume spring-restricted roads;

- To provide a reasonable prediction of the bearing capacity of thaw-weakened roads in Manitoba

Based on the measured moisture and temperature of various layers, the test sections of pavement can be divided into four periods: deep frost, rapid strength loss, rapid strength recovery, and slow strength recovery. Different thawing indices were examined to implement spring load restriction in Manitoba.

Measured maximum tensile strain at the bottom of asphalt layer decreased by an average of 15-20% when tire pressure was reduced by 50%. Measured strain at the bottom of asphalt layer in fall is about 60% less than in spring. The effects of gauge orientation, truck speed, and tire offset from the strain gauge were also analyzed. A finite element (FE) model with static load was developed and verified.

Primary conclusions of this research are:

- The bearing capacity is lower in spring than in normal condition for flexible pavements subject to deep frost action.
- A tire pressure control system is effective to reduce bottom up failure of the pavement, and is less effective to prevent rutting.
- Pavement bearing capacity could be predicted using the finite element method with reasonable accuracy.

ACKNOWLEDGEMENTS

I would like to take this opportunity to thank many people who made the completion of this research possible. Without their encouragement, help, and consideration, the research would likely not have been finished.

My sincere thanks go to Dr. Ahmed Shalaby for his precise advice. His invaluable guidance and inputs for this research are highly appreciated. Without his timely mentorship throughout this research, it is impossible to have my thesis finished.

I want to express my gratitude to Professor Alan Clayton for his encouragement and suggestions.

I would like to acknowledge my colleagues, Ms. Leonnie kavanagh, Mr. Scott Sparrow, to name but a few, in the Pavement Research Group at the University of Manitoba for their cooperation, comments, and help.

Thanks to the staff from Manitoba Infrastructure and Transportation, Fpinnovations-FERIC division for their continued support for carrying out the instrumentation and field tests. The contributions of Dr. Gani Ganapathy, Dr. Mohammad Alauddin Ahammed, Mr. Steve Mercier, and Mr. Allan H. Bradley are greatly appreciated. Special thanks to Mr. Said Kass and Ms. Nicole Fleur for their coordinating of this research.

The financial support provided by Manitoba Conservation and Manitoba Infrastructure and Transportation is gratefully acknowledged.

I would like also to sincerely acknowledge the the TAC foundation EBA Engineering Consultants Ltd. Scholarship awarded to me in 2010 as a financial aid to complete my degree and researches.

I would like to sincerely thank my parents and my wife for their understanding, inspiration and encouragement throughout my study.

TABLE OF CONTENTS

LIST OF TABLES

LIST OF FIGURES

NOMENCLATURE

A1L1 - A1 (class) Level 1 (load)

A1N - A1 (class) Normal (load)

AC - Asphalt Concrete

ASG - Asphalt Strain (horizontal) Gauge

ASG-VS - Asphalt Strain Gauge - Vertical Strain

AST - Asphalt Surface Treatment

BC - British Columbia

CRREL - Cold Regions Research and Engineering Laboratory

CTI - Central Tire Inflation

CTL - Construction Technology Laboratories

DAS - Data Acquisition System

FD - Frost Depth

FE - Finite Element

FERIC - Forest Engineering Research Institute of Canada

FI - Freezing Index

FWD - Falling Weight Deflectometer

GB - Granular Base

GCTS - Geotechnical Consulting and Testing Systems

LTPP - Long Term Pavement Performance

MB - Manitoba

MDD - Multi-Depth Deflectometer

MIT - Manitoba Infrastructure and Transportation

Mn/DOT - Minnesota Department of Transportation

PR304 - Provincial Road 304

PTH11 - Provincial Truck Highway 11

RTAC - Roads and Transportation Association of Canada (normal load)

TAC - Transportation Association of Canada

SCG - Soil Compression Gauge

SHRP - Strategic Highway Research Program

SLR - Spring Load Restrictions

SWCC - Soil Water Characteristic Curve

TD - Thaw Depth

TDR - Time Domain Reflectometer

TI - Thawing Index

TPCS - Tire Pressure Control System

VMC - Volumetric Moisture Content

VTI - Variable Tire Inflation

WCR - Water Content Reflectometer

CHAPTER 1 INTRODUCTION

1.1 THE RESEARCH

Spring load restrictions (SLR) are used by Canadian transportation agencies to protect weak pavement structures from damage caused by heavy trucks during the spring thaw period. Commercial truck payloads must be reduced considerably to meet axle weight restrictions. This reduction results in increased truck payload cost and imposes significant pressure on truck-based industries and their related work force.

An alternative to reducing payloads is reducing tire pressures or reducing tire pressures in combination with smaller payload reduction. While both methods reduce vehicle-induced rutting of thaw-weakened pavement structures, the reduction of tire pressures can theoretically reduce asphalt pavement fatigue cracking more effectively than reducing loads alone (Bradley, 2006). The reduction of tire pressures appears to be a viable way to allow trucks to haul greater payloads, especially for the final three or more weeks of the spring load restriction period.

In 2004, the British Columbia (BC) Ministry of Transportation initiated a program to exempt trucks with tire pressure control systems (TPCS) from seasonal load restrictions on approved routes. The technical foundation for the BC program was research

conducted from 2000 to 2004 by the Forest Engineering Research Institute of Canada (FERIC), in conjunction with a variety of BC forest companies and provincial ministries.

Forest companies participating in the new BC program have been able to resume hauling with full payloads two to four weeks before the end of SLR period. This has resulted in significant competitive advantages—especially through improved harvesting efficiencies, reduced inventories and extended operating seasons. The BC program has generated considerable attention across Canada.

The SLR duration is 59 days in Manitoba. This has impacts on the competitiveness of the Manitoba transportation industry as well as on the quality of living of those who are reliant on this industry.

Manitoba Conservation and Manitoba Infrastructure and Transportation (MIT) commissioned a study to be conducted by FPInnovations and the University of Manitoba. The purpose of the study is to support the development of seasonal load restriction policies that consider the benefits of reduced tire pressure. Two test sections on provincial truck highway 11 (PTH11) and provincial road 304 (PR304) have been selected for instrumentation since the project required the instrumentation of road sections in Manitoba.

1.2 OBJECTIVES AND SCOPE

The objectives of this study are:

- To understand the pavement profiles of moisture and temperature, the strain distribution under various tire loads, and the relationship among strain and moisture, temperature, truck speed, and tire load.

- To evaluate the impacts of reduced truck tire pressure on the strain response of low volume spring restricted roads using data from the Manitoba instrumented test sites.

- To support the development of spring load restriction policies that considers the benefits of reduced tire pressure.

1.3 RESEARCH APPROACH AND EXPERIMENT DESIGN

The following research approaches were undertaken to achieve the objectives:

A literature review was performed to investigate the performance of pavement subject to frost action, spring load restriction, highway pavement instrumentation, falling weight deflectometer (FWD) test, tire pressure control system (TPCS) or the central tire

inflation (CTI) technique, and finite element modeling stress and strain with ABAQUS in pavements especially during spring thaw.

Based on the modified Berggren equation, a model was established to predict the frost depths of the test pavements. The model was calibrated against the results of the best-fit statistical analysis according to the temperature conditions. Air temperature was collected on test sites and also obtained from weather station of Environment Canada at Winnipeg Richardson Automated Weather Observing System. Pavement temperature was gathered by thermistor string installed on sites.

FWD tests were performed in April and May 2009 to back calculate the layer moduli.

Hauling tests were carried out in both the spring and the fall.

A FE model would be developed to predict the performance of pavement under various conditions. Model inputs include tire contact pressure, layer moduli from FWD test. Model outputs were calibrated against strains measured at test sites under various thaw and traffic scenarios. The calibrated model was adjusted for the structure at the asphalt concrete (AC) pavement site, input parameters adjusted as necessary, and the model outputs validated against strains measured at test sites.

These approaches offer not only the possibility to improve trucking competitiveness but

also provide improved pavement protection. The implementation on these measures is anticipated to have a positive impact on provincial highways in Manitoba.

The specific steps of the project are as follows:

- Procure, calibrate, and install pavement instrumentation and data acquisition to monitor changes in moisture content, temperature, strain, deformations at different depths within the pavement structure.
- Prepare sensor installation report including the operation instruction of data acquisition system and sensors.
- Carry out TPCS tests in spring and fall.
- Collect data and prepare monitoring reports which focus on the quality and quantity of the data.
- A finite element (FE) model is developed to simulate the pavement responses which were calibrated and validated by the collected data.

The design of experiment is shown in Figure 1-1.

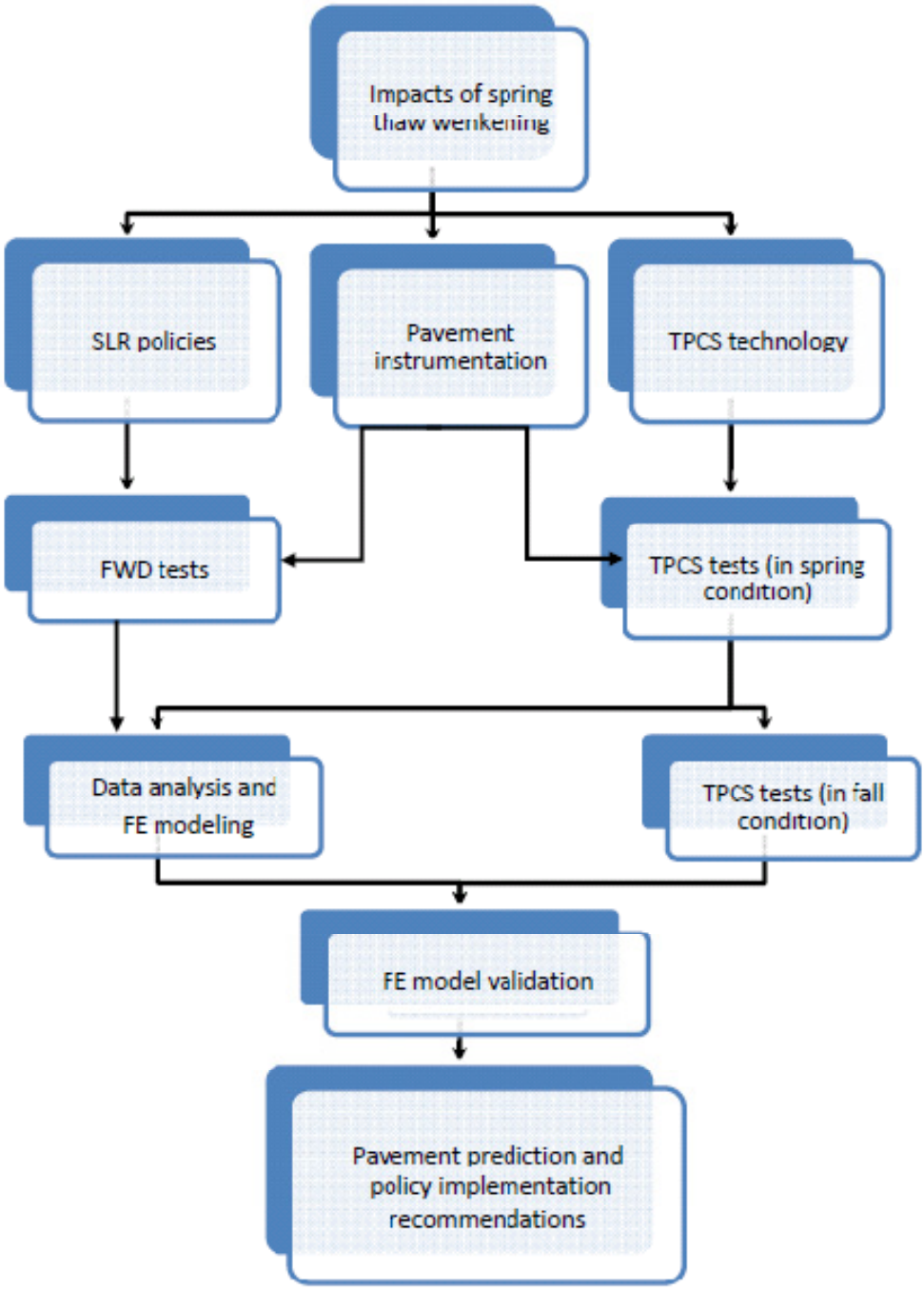

Figure 1- 1 Design of experiment.

1.4 THESIS ORGANIZATION

The thesis is divided into an abstract, seven chapters, and an appendix. As well, it contains a glossary of Acronyms and Terms.

The first chapter, Introduction, summarizes the research background involved and the basic framework for pavement design and management. Chapter 2 presents related literature, research, and some fundamental theories. Chapter 3 and Chapter 4 present the data and models of pavement temperature and volumetric moisture content, respectively. Tire Pressure Control System (TPCS) tests and field data are presented in Chapter 5. Finite element model with ABAQUS is described in Chapter 6. Chapter 7 addresses findings, issues, opportunities, and future prospects. The appendix summarizes the instrumentation of the research.

CHAPTER 2 LITERATURE REVIEW

2.1 INTRODUCTION

This chapter presents the literature review on performance of pavements subject to frost action, spring load restriction, highway pavement instrumentation, and finite element modeling stress and strain in pavements especially during spring thaw period.

2.2 PERFORMANCE OF HIGHWAYS SUBJECT TO FROST ACTION

Pavement structure is sometimes damaged during spring thaw season (Khan and Shalaby, 2002). During spring, the air temperature rises, thawing the pavement, which in turn increases the moisture content of the pavement structures. At the same time, as the heave subsides and the base and soil begin to consolidate, a significant decrease in pavement strength occurs. Soils and aggregate base materials are in a weakened state during and immediately following the thaw period (Goodings et al, 2009).

During the spring thaw period, spring-weakening occurs because the pavement foundation can become saturated with water from the thawing of ice lenses, thus reducing the structural adequacy of the base and subgrade. A large number of heavy vehicles cause partial ruts and alligator cracking to form in asphalt pavements, while drainage is obstructed by the frozen layers. As a result, the pavement does not have the designed load carrying capacity until the end of thawing (Kubo and Sugaware, 1982).

The length of time for pavement weakening depends on the frost depth, soil type, degree of saturation and drainage condition (Janoo and Berg, 1990). Figure 2-1 shows the annual strength history of flexible pavements subjected to deep frost action can be divided into four periods as follows (Scrivner et al, 1969):

Period	Description
A	deep frost
B	rapid strength loss
C	of rapid strength recovery
D	slow strength recovery

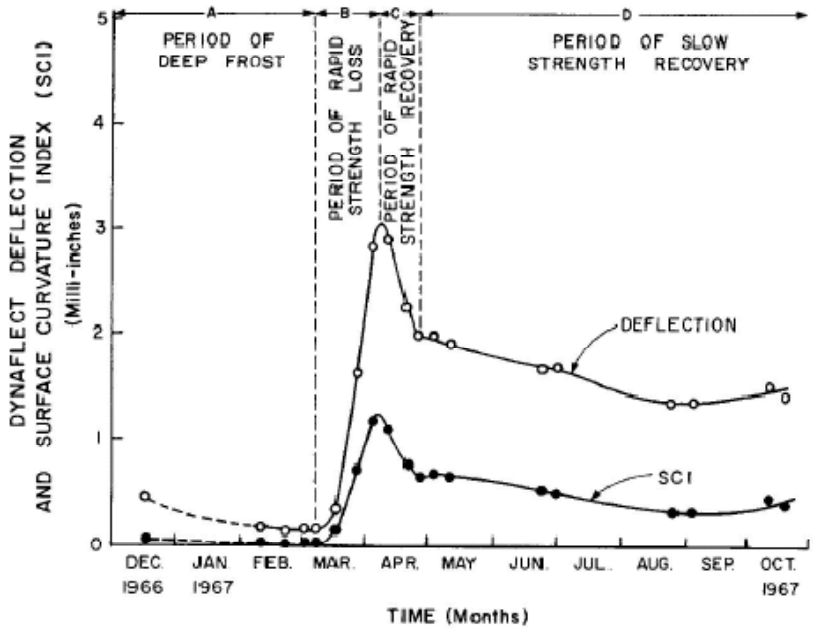

Figure 2-1 Four periods of strength history (Scrivner et al, 1969)

Period A begins with the first appearance of deep frost in the late fall or early winter. Period B begins with the abrupt increase of the deflection coinciding with the disappearance of frost from the ground in spring. Period C begins at the peak of the deflection curve. Period D begins at the point where the deflection curve levels off

following the spring peak. The second and third periods together constitute the critical period for flexible pavement.

Spring-weakening is not uniform through the spring period. Recent research conducted at the University of Manitoba has shown that the recovery of roadbed resilient modulus is much slower than originally anticipated and may not be completed by the end of the spring restrictions period, which in Manitoba is legislated not to exceed May 31.

2.3 SPRING LOAD RESTRICTION

SLR is a common countermeasure to the spring thaw weakening. SLR is implemented in the United States, Canada, France, Norway, Finland and Sweden. The SLR policy restricts the axle loading of heavy trucks during the spring thaw period. As a general practice, highway authorities usually apply SLR on secondary roads to prevent serious damage during spring thaw when bearing capacity of the foundation is reduced. Table 2-1(adopted from C-SHRP Technical Brief #21, 2000) summarizes the practices around the world. Table 2-2 shows some SLR related information in different provinces of Canada (C-SHRP Technical Brief #21, 2000).

Table 2-1 Summary of SLR practices in various countries

Country	SLR Implementation	Measuring Technique	Weight Restriction Type	Exemptions
USA	More than 20 states	No uniform method; Freezing and Thawing Indices recommended	Axle weight limit	Vehicle with permit, School bus
Canada	All provinces	No uniform method; Frost probes; Benkelman beam; Dynaflect testing	Axle weight limit	Emergency vehicles, Milk, water, mail and buses
France	North France	N/A*	Total weight limit	N/A*
Finland	Whole country	Benkelman beam measurements; Falling weight deflectometer	Total weight limit	Emergency vehicles, buses, Dairy transport, Trucks supplying retail shops, Fuel and animal fodder Permit
Norway	Whole country, repealed in 1994	Falling Weight Deflectometer, etc	Axle weight limit	Dairy and food delivery
Sweden	Whole country	Falling Weight Deflectometer	Axle weight limit	Dairy and food delivery

*not available

Table 2-2 Comparison of Basic and Seasonally Restricted Loads in Canada

Province	Allowable Weights Under Basic Regulations				Spring Load Restrictions			
	Tractor		Trailer		Tractor		Trailer	
	Steering	Drive	Tandem	Tridem	Steering	Drive	Tandem	Tridem
British Columbia[1]	**5500 kg**	**9100 kg**	**17000 kg** (1.2 to 1.85m)	**24000 kg** (2.4 to 3.7m)	• Restrictions imposed only when and where needed through engineering judgement • Overload permits suspended for numbered highways • Other highways restricted at 70% or 50% of basic axle weight (steering axle exempted)			
Alberta[2]	**5500 kg**	**9100 kg**	**17000 kg**	**23000 kg** (3.05 to 3.6m)	• 90%, 75% or 50% of basic axle weights			
					Not Restricted	**8190 kg** (90%) **6825 kg** (75%)	**15300 kg** (90%) **12750 kg** (75%)	**21500 kg** (90%) **18000 kg** (75%)
Saskatchewan[2]	**5500 kg**	**8200 kg**	**14500 kg**	**20000 kg**	• Reduction of load per tire from 10 kg/mm width to 6.25 kg/mm width to a maximum load of 1650 kg per tire • Some primary highways are downgraded to secondary highways during May and June			
					Not Restricted	**6600 kg**	**13200 kg**	**19800 kg**
Manitoba	**5500 kg** (A1 Hwys) **5500 kg** (B1 Hwys)	**9100 kg** (A1 Hwys) **8200 kg** (B1 Hwys)	**16000 kg** (A1 Hwys) (1.0 to 1.85m) **14500 kg** (B1 Hwys) (1.0 to 1.85m)	**23000 kg** (A1 Hwys) (3.05m) **20000 kg** (B1 Hwys) (3.05m)	• No restrictions to primary system or gravel roads • Steering axle not restricted • For other axles: • **Level 1** (beginning of thaw for 14 days): • A1 highways 90% of basic load • B1 highways 95% of basic load • **Level 2** (imposed 14 days after Level 1 and removed 1 week before removal of Level 1): • 65% of basic load			
Ontario[3]	**5000 kg**	**10000 kg**	**17200 kg**	**23000 kg**	• Primary network not restricted • Restrictions on some secondary provincial highways up to 50% of basic load • Commercial vehicles not to exceed 5000 kg • 2-axle tanker truck not to exceed 7500 kg/axle • Maximum of 5 kg/mm tire width			
Quebec	**5500 kg**	**10000 kg**	**18000 kg**	**21000 kg to 26000 kg**	**5500 kg**	**8000 kg**	**15500 kg**	**18000 kg to 22000 kg**
New Brunswick	**5500 kg**	**9100 kg**	**18000 kg**	**21000 kg** (2.4 to 3.0m) **23000 kg** (3.0 to 3.6m) **26000 kg** (3.6 to 4.8m)	• Three restriction levels: • All weather highways, arterials and most collectors allow 100% of basic load • Specific collectors and locals allow 90% of basic load • All other highways allow 80% of basic load • Tolerance removed for all levels			
	Tolerance 500 kg/axle							
Prince Edward Island	**5500 kg**	**6800 kg**	**13500 kg**	**18000 kg** (<3.6m) **19500 kg** (>3.6m)	• All weather highways, Trans-Canada arterials and some collectors allow 100% of basic load • Other highways allow 75% of basic load • Tolerance removed during thaw			
	Tolerance 500 kg/axle							
Nova Scotia	• **Combination 50000 kg + 500 kg/axle tolerance** • **5-axle Semi-trailer 41000 kg + 2500 kg tolerance** (Schedule C highways and some arterials and collectors) • **Other highways 38500 kg gross vehicle + 500 kg/axle tolerance**				• Tolerance removed during thaw • Max. gross weight 12000 kg for buses			
					Not Restricted	**6500 kg**	**12000 kg**	
Newfoundland	**No formal policy** **9100 kg Single, 12000 kg Tandem**				• Arterial and collector roads are all weather • Local roads monitored and restricted as needed			

1. Trailer weights are based on 10 kg/mm of tire width.
2. Values reported for Secondary highway system.
3. Weights based on tire width. Example given is for width of 279.4mm (11 in.).

Different jurisdictions use different methods to determine the time to place and lift SLR. The methods range from calendar date, to visual observation, to subsurface temperature measurement, to deflecting tests.

Some agencies base their decisions to impose SLR on visual observation of conditions that indicate the potential for spring load-related damage (such as pumping near cracks and shoulders). The down side of this approach is that by the time the thawing process manifests itself at the surface, significant damage may already have taken place.

The Canadian Good Roads Association developed a procedure using the Benkleman beam during the 1950s. This procedure was based on the relationship among deflection, actual pavement rebound, and pavement life.

The Dynaflect and Road Rater replaced the Benkleman beam in the 1970s. These devices proved faster and less expensive method to implement SLR. Further, by providing information about the curvature of the deflection bowl, these devices enabled engineers to assess the strength of the pavement structure during thaw weakening. The main shortcoming of these devices was the low vibratory loading. Low loads did not allow engineers to evaluate the materials at depth. Further, the vibratory loading often resulted in liquefaction of the soils near saturation and unrealistically high damage predictions (Goodings et al, 2009).

The falling weight deflectometer (FWD) is available after 1980s. The impacts of thaw weakening can be analyzed more accurately by using FWD. According to FWD data, the maximum damage may occur shortly after thawing begins, well before the maximum deflection according to Benkleman beam readings, meaning that to predict the thawing weakening on timely manner is the key of applying SLR.

In addition to the direct methods above, some indirect methods are also used by some agencies, historical data and weather forecast, for instance.

Thawing index is a useful indicator for SLR. Pavement surface thawing index is the accumulation of degree-days above a reference thawing temperature. The index is related to the penetration of thaw in the pavement structure. This concept has been adopted by Minnesota Department of Transportation (Mn/DOT). The thawing index (TI) is defined as the accumulative value of the difference between average daily air temperature and reference temperature. The reference temperature varies linearly from -1.7^0C on February 1st to -4.4^0C on March 15th. Observations of pavement deflection, the thawing index, frost depth and air temperature at MnROAD research in Mn/DOT showed that thawing reaches a critical state at a cumulative thawing index of 13^0C-days. SLR is posted when the 3-day forecast predicts a cumulative thawing Index in excess of 13^0C-days and continued increases well in excess of 13^0C-days. (C-SHRP Technical Brief #21, 2000). The SLR implementation method in Canada is summarized in Table 2-3(C-SHRP Technical Brief #21, 2000).

Table 2-3 Seasonally Load Restriction Implementation, Testing and Enforcement in Canada

Province	Start/End Dates	Testing	Exemptions	Enforcement
British Columbia	**Mid-February to Mid-June**	• Frost probes, weather synopsis, Benkelman Beam data for 20+ years, other historical data		• Permanent and portable scales
Alberta	**Start Date:** 30cm thaw and a heat flow model **End Date:** Determined with FWD testing	• FWD	• Milk, farm machinery, bread, water, heating fuel, fertilizer, mail and buses	• 20 staffed weigh scales, 20 self-weighing scales and portable scales
Saskatchewan	**Start Date:** Second or third week in March (weather dependent) **End Date:** Maximum six weeks after start date	• Benkelman Beam		• Permanent and portable scales
Manitoba	**Start Date:** (Level 1) • Southern Zone: March 23 • Northern Zone: April 15 **End Date:** May 31	• Benkelman Beam	• Essential commodities exempted	• Permanent and portable scales
Ontario	• Variable start and end dates. Typically first Monday in March to Mid May (Southern Region)		• Municipal, milk, emergency and public utility vehicles	• Permanent and portable scales
Québec	**North:** March 24 to May 25 **Central:** March 6 to May 12 **South:** March 21 to May 19 • Timing can be advanced or delayed based on frost probe data. Start of restrictions at 300 mm thaw and ending at 5 weeks after 900mm thaw below road surface	• 81 frost probes (1.5m to 3.5m depth) • Measured weekly during freeze, daily during thaw, and then weekly at end of thaw.	• Raw forest products exempted while hauling to primary processing plant. • Single unit trucks with non-detachable dumping mechanism • Road maintenance single unit vehicles	• Permanent and portable scales
New Brunswick	**Southern Zone:** Second week in March to mid-May **Northern Zone:** Third week in March to end of May • Timing varied according to severity of winter and spring conditions	• Dynaflect testing on 40 affected control sections on weekly basis during restriction period.	• Passenger buses and service vehicles.	• Permanent and portable scales
Prince Edward Island	**March 1 to April 30** • Timing varied according to severity of winter and spring conditions	• Dynaflect testing on random sections throughout restriction period.	• Commodities (potatoes, livestock, milk, fish, and live stock feed) .	• Portable scales
Nova Scotia	**Southern Region:** March 2 to April 24 **Central/Northern Regions:** March 2 to April 27	• Dynaflect testing on random control sections (all classes) from mid-February to end of April.	• Public utility and emergency vehicles.	• Portable scales
Newfoundland	**February to April** (Trans-Labrador Highway)			• Permanent and portable scales

It is still unclear whether SLR is economical or not from the total social cost perspective though it has been widely used in cold regions for many years. The implementation of SLR reduces the damage to the roads and thus saves money for road agencies; SLR also

imposes cost to the road users (Levinson, 2004). For example, it is estimated that SLR costs the paper industry USD 80 million per year in Sweden. The SLR cost in Finland is USD 0.2 million each day.

Some jurisdictions are considering lifting SLR or permitting higher loads. For instance, on January 1st, 1995 all axle load restrictions (affecting 35,000 out of 53,000 kilometers) during the spring thaw period within national and county networks of Norway were lifted. The local load restriction on most 10 ton roads were allowed for 8 tons, some sections even load 6 tons during spring thaw before 1995 in Norway. Practically, 6 tons limitation means the road is closed for heavy vehicles. According to Refsdat's study (Refsdal et al, 2004), up to 2003 there were no indications that the lifting of load restrictions in 1995 had resulted in reduced pavement serviceability although many experts still held the opinion that the ordinary serviceability measurements are not enough for complete understanding the deterioration of the roads.

2.4 VOLUMETRIC MOISTURE CONTENT IN PAVEMENT

Excessive moisture in base layers of a pavement can cause considerable damage and may lead to early deterioration. Moisture in pavements may enter through various points in the pavement structure, such as surface infiltration and through cracks, joints, and shoulders. Interrupted aquifers, springs, and drainage in cut areas may also have an

effect on pavement moisture. Excessive moisture in pavements can cause one or more of the following forms of deterioration: (Diefenderfer et al, 2001)

- Reduction of the shear strength of unbound subgrade and base/subbase material;
- Differential swelling in expansive subgrade soils;
- Movement of unbound fines into flexible pavement base/subbase courses;
- Frost heave and reduction of strength during frost melt;
- Pumping of fines and durability cracking in rigid pavements; and
- Stripping of asphalt in flexible pavements.

(a) TIME-DOMAIN REFLECTOMETER (TDR)

TDR is a nondestructive method for continually monitoring the moisture content of base layers. The TDR system records an electromagnetic waveform that can be analyzed as it is transmitted and reflected to characterize the nature of objects that reflect the waves. The waveform pulse is transmitted along a coaxial metallic cable shielded by a waveguide at a velocity that is influenced by the dielectric constant of material surrounding the conductors. This dielectric constant is a dimensionless ratio of a material's dielectric permittivity to the permittivity of free space. Changes in the dielectric constant of the surrounding material occur as its moisture content or conductivity changes.(LTPP, 2008)

Based on empirical approaches, three alternative methods are used to determine soil volumetric moisture content from dielectric constants:

- Topp's equation
- Klemunes' model
- Third-order polynomial *Ka* – soil gradation model

(b) WATER CONTENT REFLECTOMETER (WCR)

The fundamental principle for WCR operation is that an electromagnetic pulse will propagate along the probe rods at a velocity that is dependent on the dielectric permittivity of the material surrounding the line. As water content increases, the propagation velocity decreases because polarization of water molecules takes time. The travel time of the applied signal along two times the rod length is measured.

The applied signal travels the length of the probe rods and is reflected from the rod ends traveling back to the probe head. A part of the circuit detects the reflection and triggers the next pulse.

The frequency of pulsing with the probe rods in free air is about 70 MHz. This frequency is scaled down in the WCR circuit output stages to a frequency easily measured by a datalogger. The probe output frequency or period is empirically related to water content using a calibration equation.

Table 2-4 shows the calibration coefficients derived in the Campbell Scientific soils laboratory. Both linear and quadratic forms are presented. The choice of linear or quadratic forms depends on the expected range of water content and accuracy requirements. These coefficients should provide accurate volumetric water content in mineral soils with bulk electrical conductivity less than 0.5 S/m (Siemens per meter), bulk density less than 1.55 g cm^{-3}, and clay content less than 30%.

Table 2-4 Standard calibration coefficients for linear and quadratic forms

Linear		Quadratic		
C0	C1	C0	C1	C2
-0.4677	0.0283	-0.0663	-0.0063	0.0007

The linear equation is shown in equation 2-1:

$$VWC = -0.4677+0.0283*period \quad (2\text{-}1)$$

The quadratic equation is shown in equation 2-2:

$$VWC = -0.0663 - 0.0063*period + 0.0007*period \quad (2\text{-}2)$$

Period is in microseconds. The result of both calibration equations is volumetric water content on a fractional basis. Multiply by 100 to express in percent volumetric water content.

Figure 2-2 shows the difference between the linear and quadratic calibration forms over the typical range. A WCR CS616 output period of 16 microseconds is about 2% VWC and 32 microseconds is 47.25%. The linear calibration is within ±1.25% VWC of the

quadratic with underestimation of water content at wet and dry ends of the range and overestimates by up to about 1.2 % VWC at about 20% VWC.

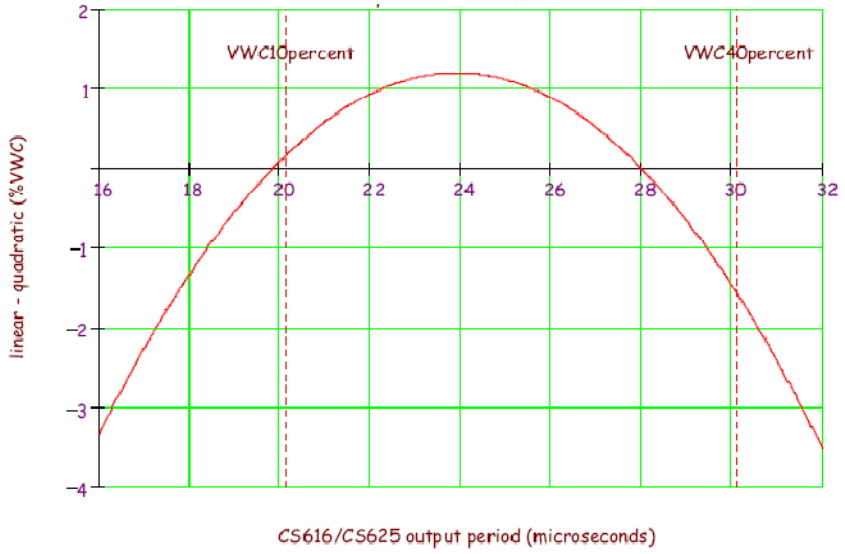

Figure 2-2 VMC difference between linear and quadratic calibrations (Source: CS616 instruction manual)

Another two groups of calibration coefficients are also recommended by Campbell Scientific Inc. depending on the soil properties as shown in Table 2-5 and 2-6, respectively.

Table 2-5 Calibration coefficients for sandy clay loam with bulk density 1.6 g cm^{-3} and electrical conductivity at saturation 0.4 dS m^{-1} for both linear and quadratic forms

Linear		Quadratic		
C0	C1	C0	C1	C2
-0.6200	0.0329	0.0950	-0.0211	0.0010

Table 2-6 Calibration coefficients for sandy clay loam with bulk density 1.6 g cm^{-3} and electrical conductivity at saturation 0.75 dS m^{-1} for both linear and quadratic forms

Linear		Quadratic		
C0	C1	C0	C1	C2
-0.4470	0.0254	-0.0180	-0.0070	0.0006

The amount of organic matter and clay in soil can alter the response of dielectric-dependent methods to changes in water content. This is apparent when mechanistic models are used to describe this measurement methodology. The electromagnetic energy introduced by the probe acts to re-orientate or polarize the water molecules. If other forces are acting on the polar water molecules, the force exerted by the applied signal will be less likely to polarize the molecules. This has the net effect of 'hiding' some of the water from the probe. Additionally, some clay sorbs water interstitially and thus inhibits polarization by the applied field.

Organic matter and some clay are highly polarized. These solid constituents can affect CS616 response to water content change and require specific calibration. This effect is opposite to that of the 'hiding' effect. It would be convenient if the calibration of water content to CS616 output period could be adjusted according to some parameter of the soil which reflects the character of the signal attenuation. However, such a parameter has not been identified. (Campbell Scientific, Inc., 2006)

The error in measured volumetric water content caused by the temperature dependence of the CS616 is shown in Figure 2-3. The magnitude of the temperature sensitivity changes with water content. Laboratory measurements were performed at various water contents and over the temperature range from 10^0C to 40^0C to derive a temperature correction for probe output period. Equation 2-4 can be used to correct the CS616 output period, $t_{uncorrected}$, to 20 ^{0}C knowing the soil temperature, T_{soil}. Figure

2-3 is showing the VMC error corrected by temperature correction as shown in equation 2-3(Campbell Scientific, Inc., 2006)

$$t_{corrected}(T_{soil}) = t_{uncorrected} + (20 - T_{soil}) * (0.526 - 0.052 * t_{uncorrected} + 0.00136 * t_{uncorrected}^2) \quad (2\text{-}3)$$

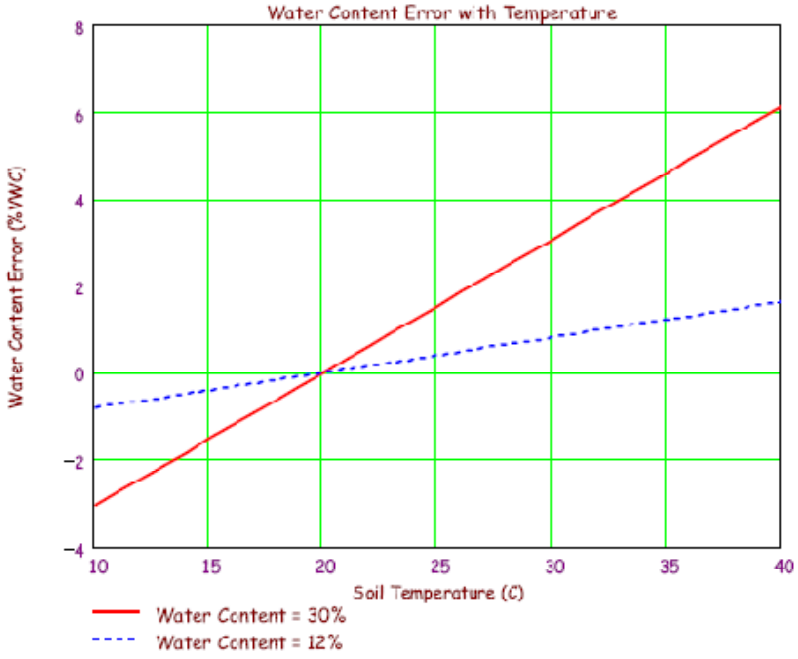

Figure 2-3 VMC error (%) corrected by temperature correction equation (Source: CS616 instruction manual)

2.5 SOIL SUCTION PROBES

Soil suction, according to Edlefsen and Anderson (1943), is commonly referred to the free energy state of soil-water, which can be measured in terms of its partial vapour pressure. (The University of Toledo (Mechanics of Unsaturated Soils), 2009)

(a) Matric Suction

A meniscus forms at the soil-air interface, due to the surface tension, which results in reduced vapour pressure in the water. The vapor pressure decreases, becomes more negative, and the matric suction pressure increases as the radius of curvature of the meniscus decreases.

The size of the soil pore decreases with a decrease in soil particle size which then affects the size of the radius of curvature and consequently the matric suction pressure. The vapor pressure decreases as the degree of saturation decreases.

(b) Osmotic Suction

The presence of dissolved ions in water decreases the soil vapor pressures, relative humidity, which then increases the total soil suction. Osmotic suction can be a significant portion of the total soil suction. (The University of Toledo (Mechanics of Unsaturated Soils), 2009).

(c) The Methods of Total Soil Suction Measurements

Different methods of soil suction measurement have been developed over the past years. Psychrometers and Filter Papers are the most popular methods.(The University of Toledo (Mechanics of Unsaturated Soils), 2009)

(d) Direct Measurement of Matric Suction

A ceramic material (typically) with uniform openings will act as a capillary medium when in contact with moisture according to Kelvin's equation. By using high air entry materials it is possible to directly measure the water pressure (less than atmospheric) using a pressure gage or transducer, Tensiometers and Pressure Plate Extractor, for instance.

(e) Indirect Measurement of Matric Suction

Moisture Blocks are usually chosen to measure matric suction indirectly.

(f) Measurement of Osmotic Suction

Osmotic suction can be measured by obtaining a sample of pore water, squeezing technique, and measuring the electrical conductivity. (Lungal and Si, 2008)

(g) FTC-100 Thermal conductivity soil suction sensors

The FTC sensor holds promise as a sensor for the in situ measurement of matric suction. The sensor is insensitive to salinity and soil type. The FTC sensor was developed by Geotechnical Consulting and Testing Systems (GCTS) based on previous models developed by Fredlund and other researchers at the University of Saskatchewan, Canada.

The measurement of matric suction using a thermal conductivity sensor is an indirect method. There are three relationships that indirectly relate the output of the sensor to the matric suction of the soil (Feng et al, 2002):

1. The output from the soil suction sensor is a voltage that is inversely proportional to the rate of dissipation of the thermal energy within the porous block;
2. The rate of dissipation of the thermal energy is dependent upon the water content of the porous block; and
3. The water content of the porous block is a function of the matric suction applied to the porous block by the surrounding soil.

Thermal conductivity soil suction sensors appear to be one of the promising devices for long-term in situ monitoring of soil suction. The accuracy of suction measurements using thermal conductivity sensors is dependent upon their calibration. (Feng and Frelund, 2003)

The calibration curve for a sensor represents the response of a sensor under several applied matric suctions. These responses are measured as a temperature rise in the sensor when a specific quantity of heat in applied to the ceramic. The calibration curve is fitted using a four- parameter sigmoidal curve with parameters, a, b, c, d as shown in equation 2-4.

$$\Psi = \left[\frac{b.(\Delta v - a)}{c - \Delta v}\right]^{d} \qquad (2\text{-}4)$$

Where:

Ψ =soil matric suction;

a=parameter designating the output voltage under saturated condition;

b=parameter designating the output voltage under dry conditions;

c=parameter designating the slope of the calibration curve;

d=parameter related to the inflection point on the calibration curve.

Due to hysteresis between the water content of a porous block and matric suction which is usually referred to as capillary hysteresis, the drying and wetting history of the porous block of the conductivity sensor need to be considered. If a single drying or wetting curve is used for calibration, an error will occur in the measurement if the senor undergoes drying and wetting cycles (Feng, 2002). Typical calibration curves are shown in Figure 2-4

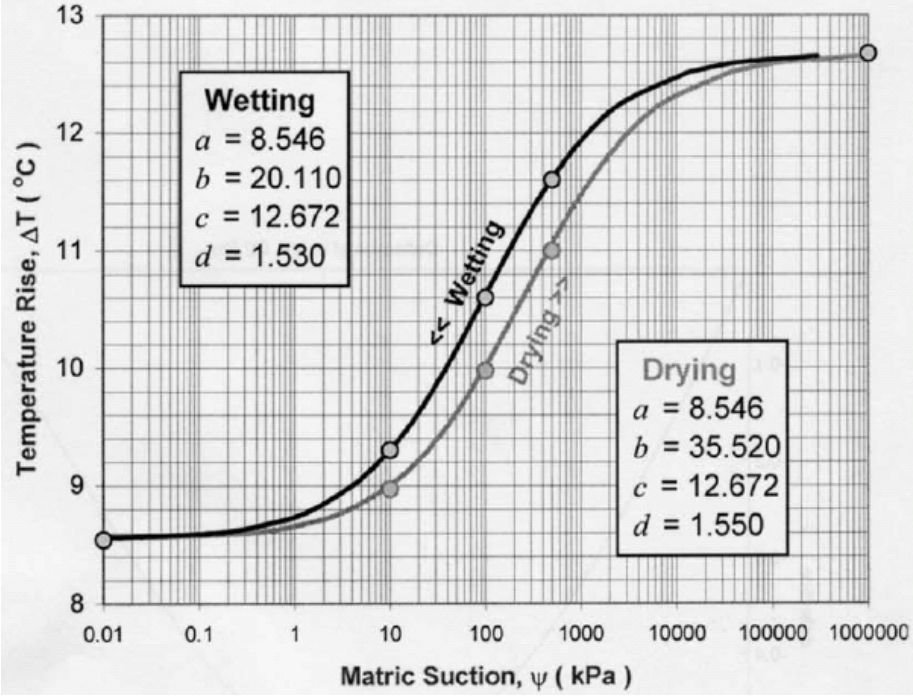

Figure 2-4 Typical calibration curve for FTC-100 (source: Man Feng, 2002)

The temperature rise used for the calibration curve corresponds to a standard temperature of 23^0C. This is the temperature maintained in the laboratory during the calibration process. Temperature rise in the field at ambient temperature can slightly deviate from the laboratory value. In order to eliminate the effect of thermal influences, a temperature correction technique was developed as shown in equation 2-5 (Shuai et al, 2002):

$$\Delta v_{23^0C} = \frac{0.0014t+0.5743}{0.6065} \quad \Delta v_t \qquad (2\text{-}5)$$

Where

t= the soil temperature,

Δv_{23^0C} =The output voltage at 23^0C,

Dv_t= the output voltage at temperature t.

The soil water characteristic curve (SWCC) is central to understanding variably saturated soil behavior. The SWCC describes the relationship between the volume of water in the soil and the energy state of that water (Gupta and Wang, 2006). The SWCC is also referred to as the moisture characteristic or moisture release curve.

SWCC can be viewed as a continuous sigmoidal function describing the water storage capacity of a soil as it is subjected to various soil suctions. SWCC contains important information regarding the amount of water contained in the pores at a given soil suction and the pore size distribution corresponding to the stress state in the soil. (Fredlund et al, 2002)

Figure 2-5 shows a typical plot of a soil-water characteristic curve for a silty soil, along with some its key characteristics. The air-entry value of the soil (i.e. bubbling pressure) is the matric suction where air starts to enter the largest pores in the soil. The residual water content is the water content where a large suction change is required to remove additional water from the soil. A tangent line is drawn from the inflection point. The curve in the high-suction range can be approximated by another line. The residual water content Θ_r can be approximated as the ordinate of the point at which the two lines intersect. The curve in Figure 2-5 is a desorption curve. The adsorption curve differs from the desorption curve as a result of hysteresis. The end point of the adsorption curve may differ from the starting point of the desorption curve because of air entrapment in the soil. Both curves have a similar form (Fredlund and Xing, 1994).

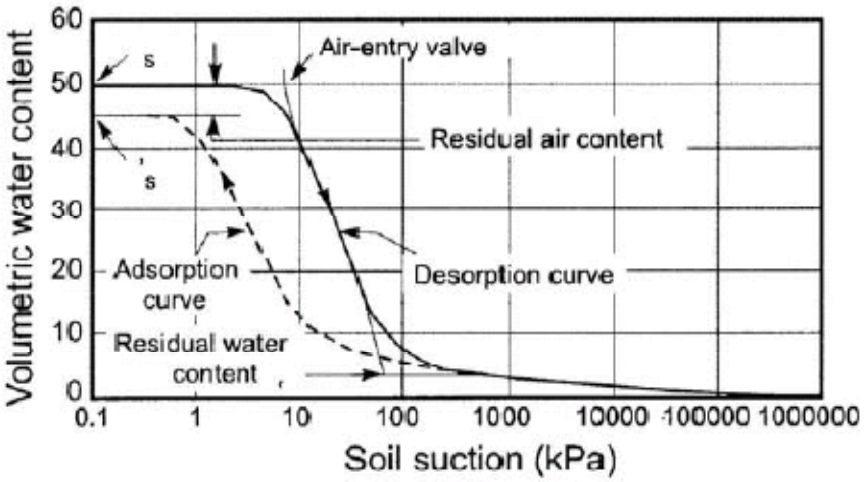

Figure 2-5 Typical soil-water characteristic curve for a silty soil (Source: Fredlund and Xing, 1994)

Typical soil-water characteristics curves (i.e. desorption curves) for different soils are shown in Figure2-6

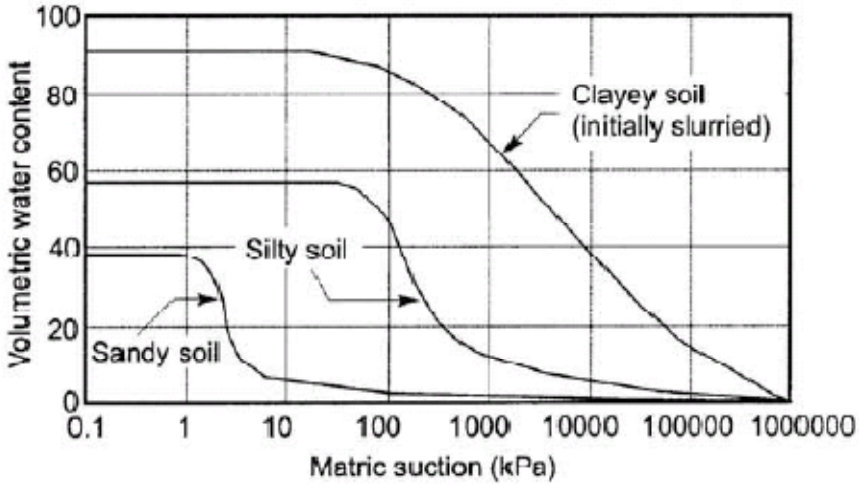

Figure 2-6 Typical soil-water characteristics curves for different soils (Source: Fredlund and Xing, 1994)

2.6 FINITE ELEMENT MODELING OF PAVEMENT RESPONSES

(a) Multi-layer model

Asphalt pavement is layered system; Burmister's layered theory is usually used to compute the pavement responses due to traffic loading. The advantage of the linear elastic multi-layer model is the quick computation speeds, which is based on certain simplifications.

Burmister (Burmister, 1943) addressed the two-layer linear elastic system problem for stress and strain distribution under a surface load. Acum and Fox (1951.) extended Burmister's solution and developed exact solutions for strength and deflection at the central line of three-layer systems. Layered elastic analytical solutions provided a basis for pavement structural design. However, they simplified the material behavior by

assuming linear elasticity. Huang (1967) and other researchers (Barksdale, 1967) introduced visco-elastic models for the asphalt layers of the system. This improves the analytical procedure considerably (Huang et al, 2001).

(b) Finite element model

Finite element models were developed to deal with more complicated loading conditions and pavement structures.

For traditional multi-layer model, it is always assumed that a uniform pressure, which is equal to the tire inflation pressure, is applied on the pavement surface over a circular area. However, recent studies have shown that the tire-pavement contact stress is not uniformly distributed. By comparison of computed pavement responses from finite element program using measured tire-pavement contact stress data with the results from multi-layer model in their study, Wang and Machemehl (2006) pointed out that the traditional tire model and the corresponding multi-layer model tended to overestimate the horizontal tensile strains at the bottom of AC layer and underestimate the vertical compressive strain at the top of the subgrade.

Several researchers have shown that non-uniform contact pressure causes higher pavement strains than uniform contact pressure (Yoo et al, 2006). Siddharthan et al. (2002) reported the difference in pavement responses between non-uniform and

uniform contact pressure is up to 30%. This suggests that the conventional assumption of a uniform pressure distribution is conservative, except in the case of tensile strain at the bottom of hot-mix asphalt. Similarly Tielking and Roberts (1987) reported that non-uniform contact stresses caused higher pavement strain at the bottom of asphalt than uniform contact stresses.

(c) Dynamic loading

While most analytical methods assume two dimensional axisymmetric conditions, Zaghloul (1993) and White (1998) applied three dimensional finite element with dynamic analyses to simulate the real traffic loads. Zaghloul employed a visco-elastic model for the asphalt concrete, an extended Drucker-Prager model for the granular base course and the Cam Clay model for the clay subgrade soils (Zaghloul, 1993).

In order to simulate the moving load in 3-D dynamic finite element analysis, a trapezoid shaped load amplitude function was applied to the structure. As presented in Figure 2-7, the segment AB represents the approaching of the truck, the segment BC represents the full truck load, and the segment CD represents the departure of the truck. In the 3-D finite element analysis, the segment AB or CD occupies ¼ of the total duration of the truck loading time. The element length along the traffic direction is divided in such a way that AB or CD equals the ¼ of the footprint of the wheel (Huang, 2001).

Three dimensional dynamic finite element analyses can be achieved through the application of load functions using commercial finite element software, ABAQUS, to simulate the traffic loads.

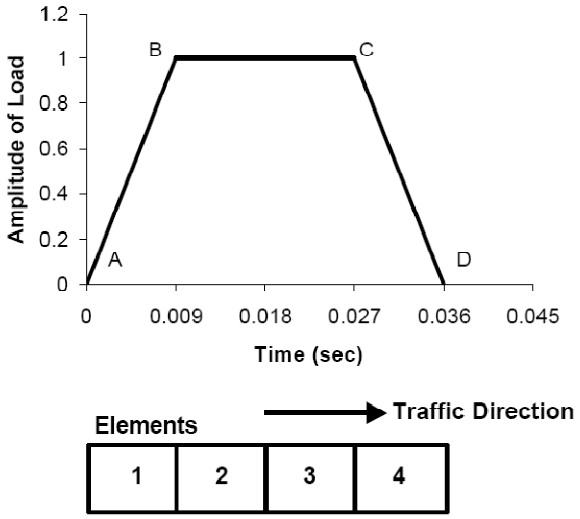

Figure 2-7 Load amplitude function (source: Huang, 2001)

2.7 TIRE PRESSURE CONTROL SYSTEM (TPCS)

TPCS is a system that maintains, monitors, and allows the driver/operator to adjust tire pressure while travelling from within the vehicle (CTI, 2009). Figure 2-8 shows the components of a typical TPCS assembly.

Another related concept is variable tire inflation (VTI) which means matching truck tire pressures with specific hauling conditions, defined by speed, terrain, load, and road

surface strength. The idea of varying tire inflations on vehicles has been around since at least World War II when the US military developed systems that allowed the driver to control tire pressure for the purpose of improving vehicle mobility. (CTI, 2009).

The failures of AC pavement in high tire pressure were more pronounced than those in lower tire pressure according to full-scale tests with reduced tire pressure (Grau, 1993).

According to the observations on a trial on Highland, Scotland, the test vehicle equipped with TPCS had the same fuel consumption, or slightly more, than the test vehicle before the trial. The cost of the TPCS system fitted to the test vehicle was 15,000 €. This is estimated to offer a payback period of 4.8 years. It was concluded that short term benefits have been identified over the course of the 13 month trial in respect of tire life, tire management, vehicle traction, and vehicle mobility and extended hauling seasons (Munro and MacCulloch, 2008).

A footprint is the contact area and the pressure of a tire on a road surface. At lower inflation pressures, the footprint of a bias ply tire will increase in both length and width, while a radial tire's (more popular than bias ply) belt plies limit the contact width of the tire to its design width(Della-Morette and Hodges, 1986) and forces the footprint to increase only in length(Brown and Sessions, 1999). Figure 2-9 shows the typical tire pressure and footprint size.

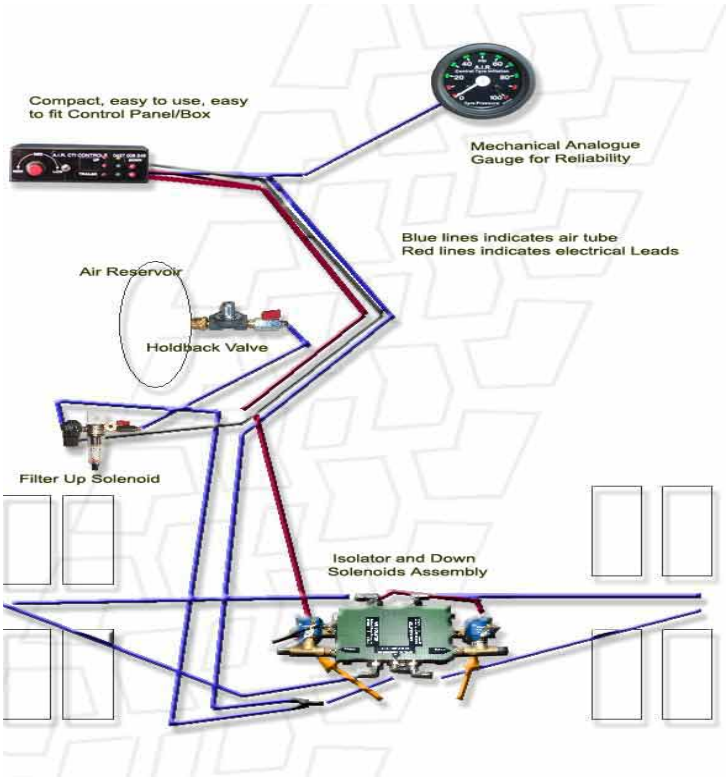

Figure 2-8 A typical assembly of central tire inflation (source: CTI, Homepage, 2009))

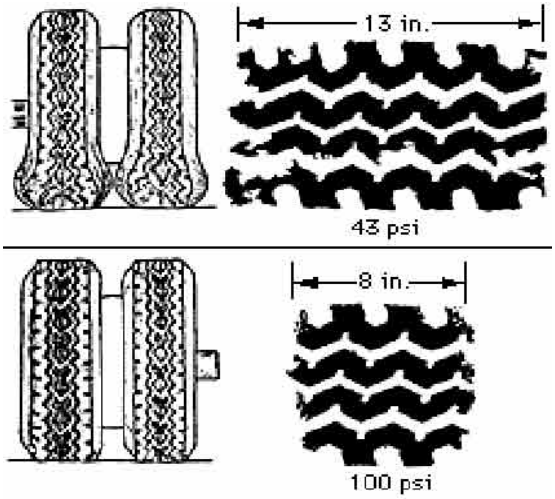

Figure 2-9 A radial tire's footprint will change size with different inflation pressures (Source: Brown and Sessions, 1999)

CHAPTER 3 PAVEMENT AND AIR TEMPERATURE AT TEST SITES

3.1 INTRODUCTION

The climate or environment in which a road structure is to establish has an important influence on the behavior and performance of the various materials in the road. Pavement temperature at the test sites is analyzed in this chapter.

3.2 PAVEMENT TEMPERATURE

3.2.1 PAVEMENT TEMPERATURE AT TWO SITES

The temperature of pavement structures is available from the mid November 2008 for both sites. Daily temperature is the average of the 12 readings for each day. Figure 3-1 and Figure 3-2 show daily pavement temperature at PTH11 and PR304, respectively.

3.2.2 PAVEMENT TEMPERATURE PROFILE DURING THAW PERIOD

Figure 3-3 show pavement temperature profiles during thaw period from March 1st to June 4, 2009 at PTH11. 'DailY' refers to daily pavement; while 'Day' refers to the average temperature during day time from 8:00 to 16:00.

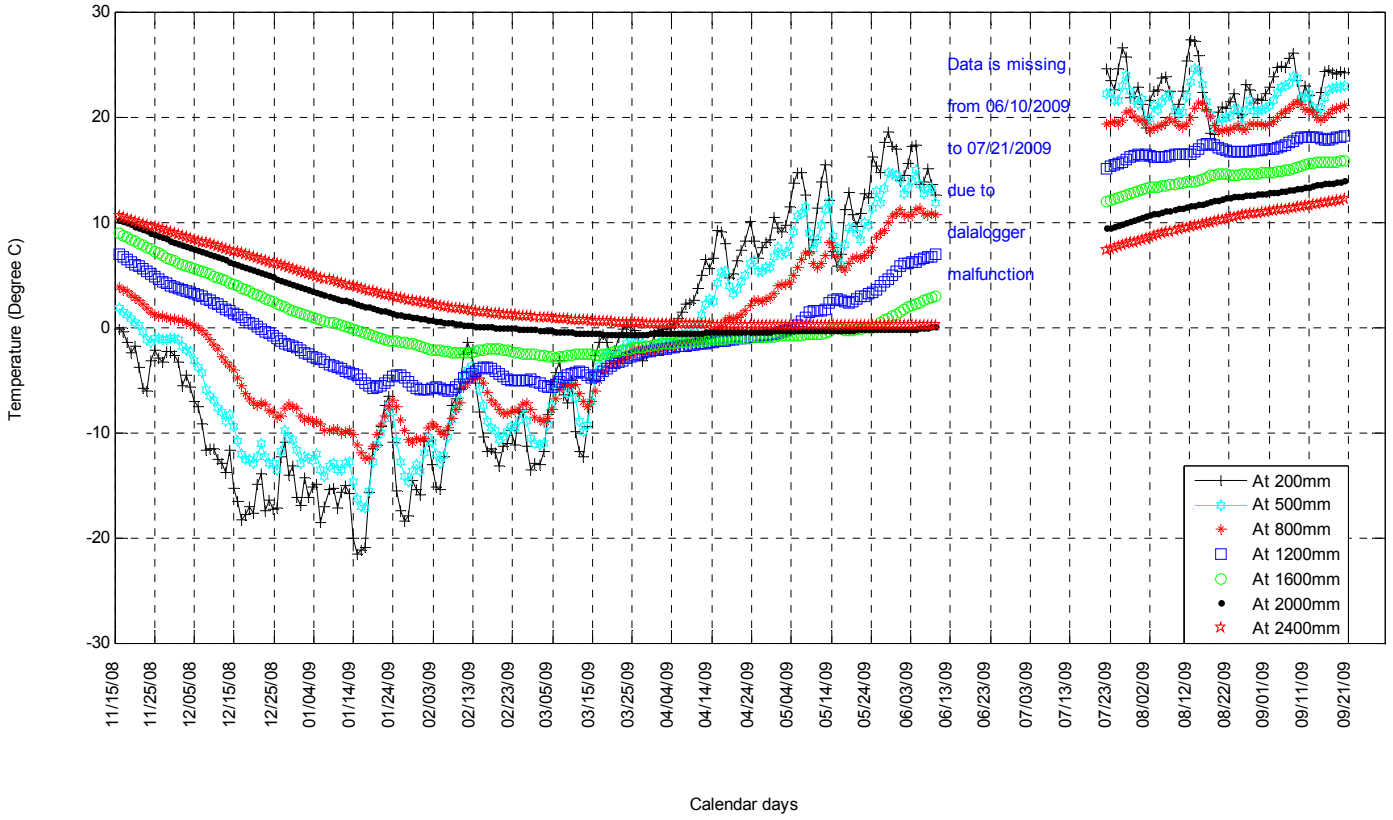

Figure 3-1 Pavement temperature at different depth of PTH11

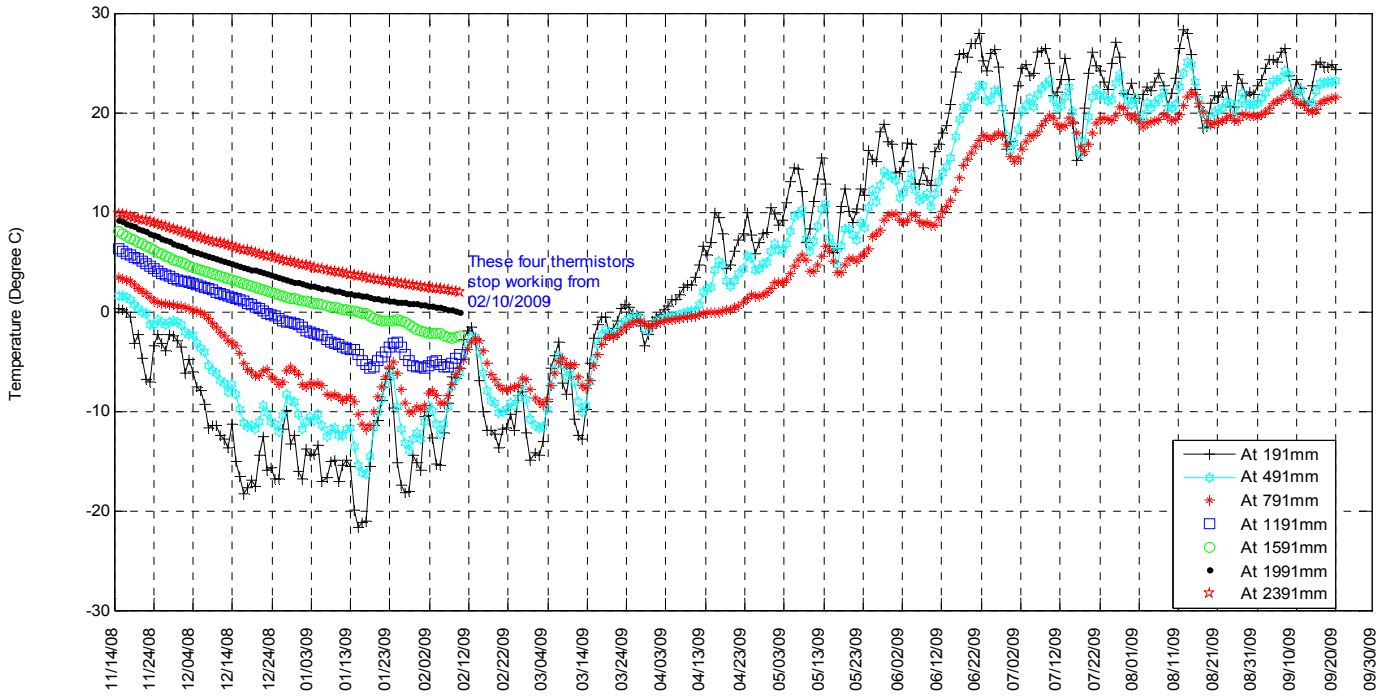

Figure 3-2 Pavement temperature at different depth of PR304

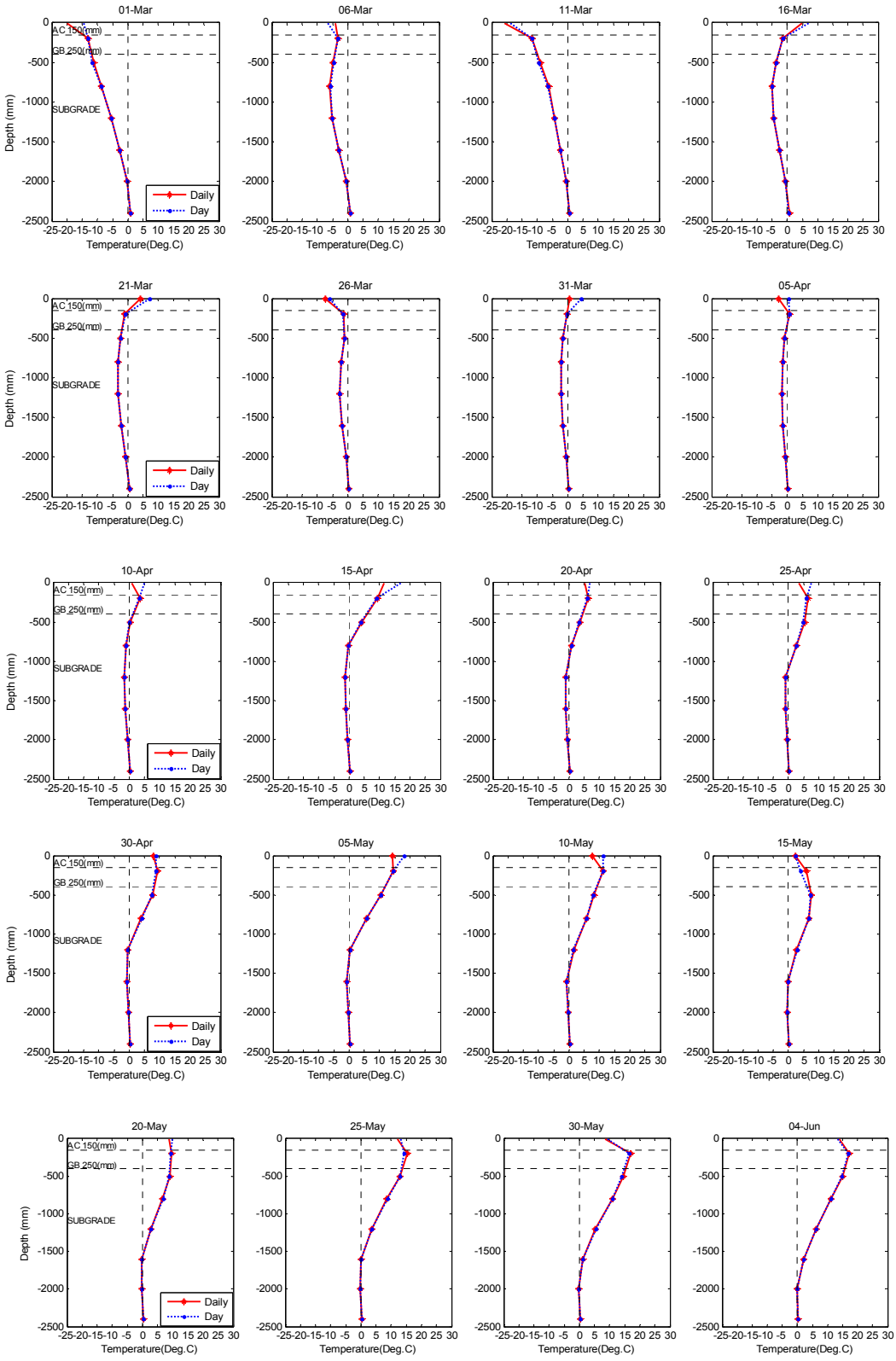

Figure 3-3 Pavement temperature profile during thaw period at PTH11

Due to the malfunction of four thermistors at the depths of 1191 mm, 1591 mm, 1991 mm, and 2391 mm, the temperature profile is available only to the depth of 791 mm during thaw period at PR304 as can be seen in Figure 3-4 and Figure 3-5.

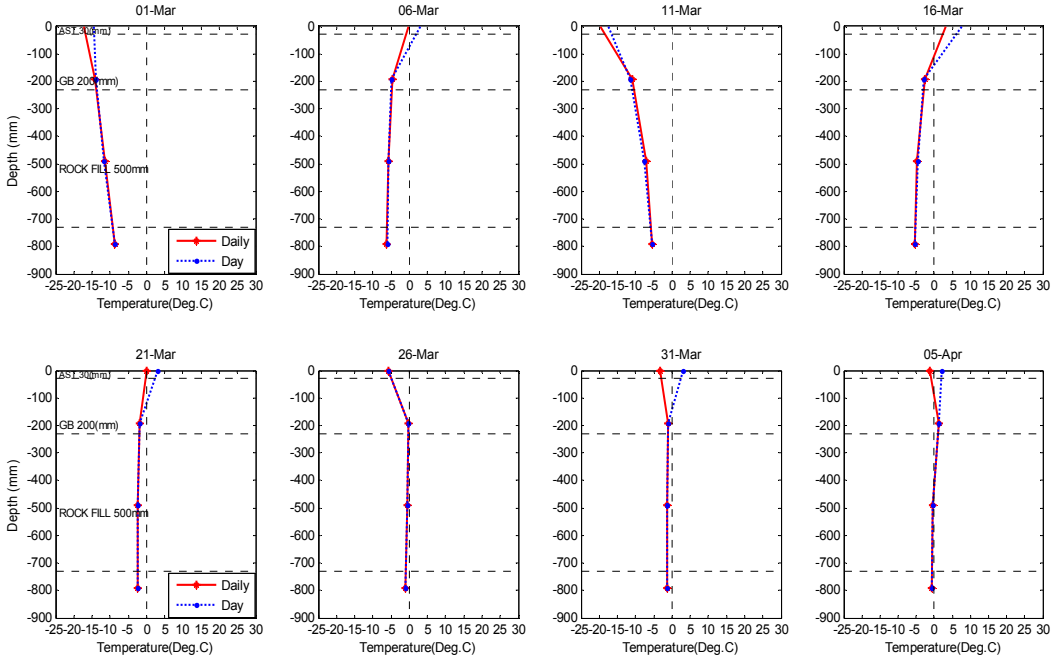

Figure 3-4 Pavement temperature profile during thaw period at PR304

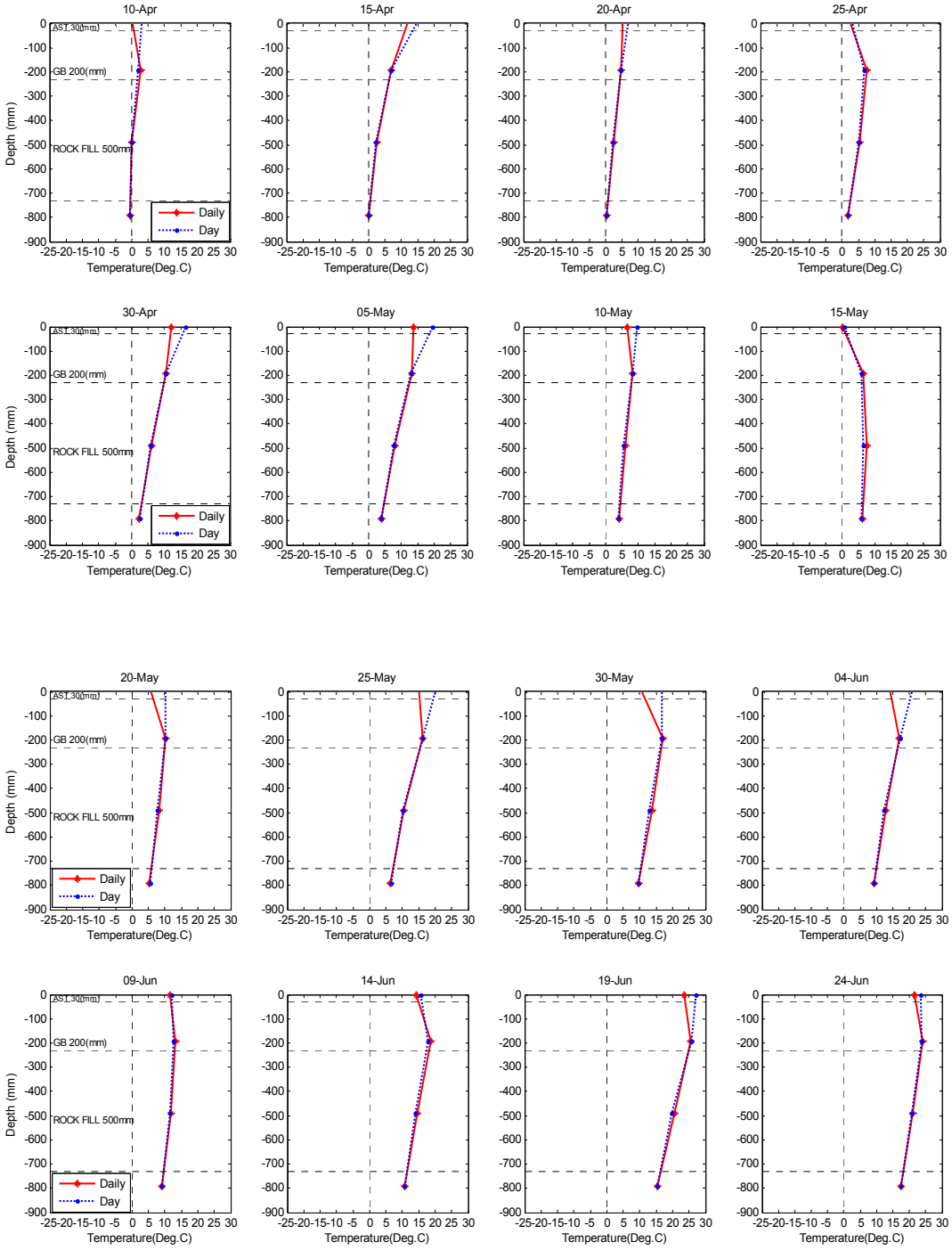

Figure 3-5 Pavement temperature profile during thaw period at PR304 (cont'd)

Alternatively, Figure 3-6 and Figure 3-7 shows the temperature profile at PR304 by the readings from soil suction probes. The temperature from soil suction probe is a little higher than that from thermistor at the same depth with on constant difference between them. The tiny heater within the soil suction probe makes this difference. According to the data from PR304 the difference is less than half degree Celsius.

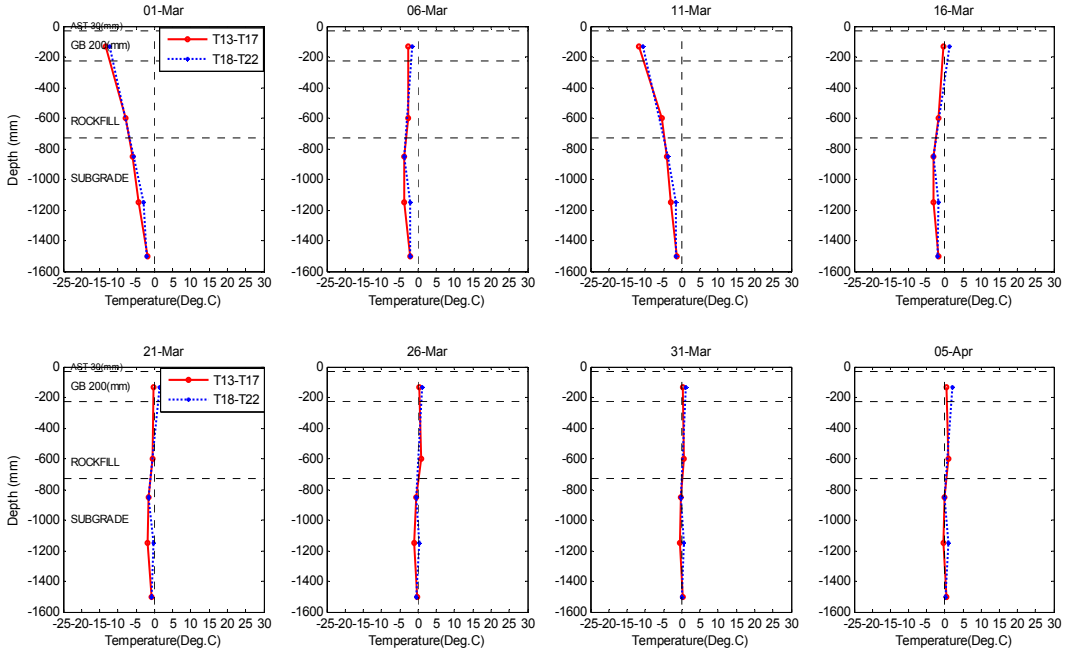

Figure 3-6 Pavement temperature profile by soil suction probes during thaw period at PR304

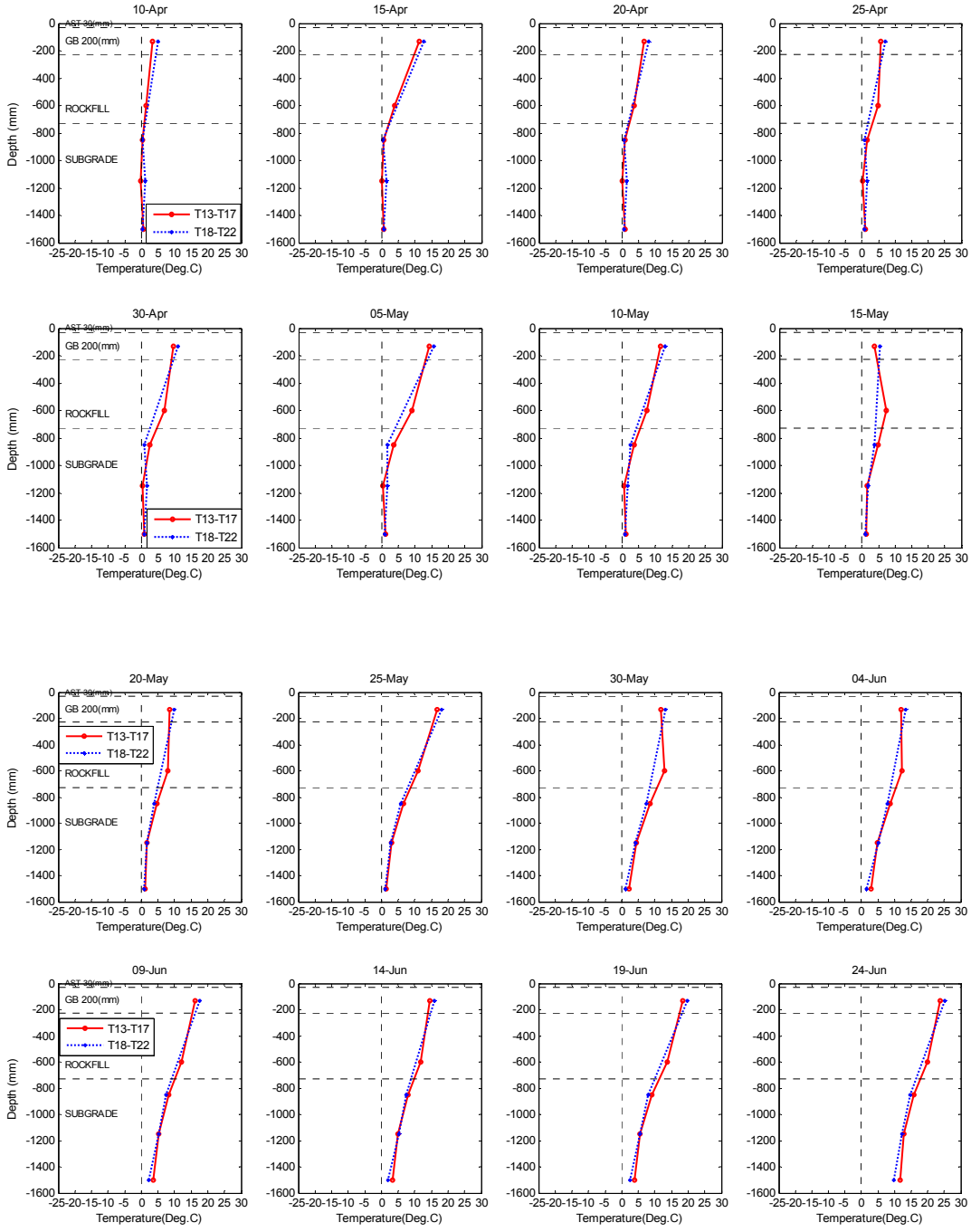

Figure 3-7 Pavement temperature profile by soil suction probes during thaw period at PR304 (cont'd)

3.3 AIR TEMPERATURE AT TEST SITES AND AT WEATHER STATION

Measured air temperature on test sites was compared with the air temperature from Environment Canada. Figure 3-8 and Figure 3-9 compare the temperatures at weather station and on sites. From these two figures, it can be seen that a linear relationship exists between the air temperature on test sites and the air temperature from weather station of Environment Canada at Winnipeg Richardson AWOS. The location of weather station of Environment Canada is as follows: Latitude: $49^0 55.200'$ N; Longitude: $97^0 13.800'$ W; elevation: 238.70 M. The weather station of Winnipeg Richardson AWOS is about 125 kilometers away from the test sites at PTH11 and PR304.

Linear regression was chosen to find the relation between temperatures at test sites and AWOS. The best fitted results are shown in equation 3-1:

$$\begin{cases} T_{304} = -0.2617 + 0.9687 \times T_{AWOS} & (R^2=0.9850\ F=16912\ P=0) \\ T_{11} = -0.2678 + 0.9693 \times T_{AWOS} & (R^2=0.9793\ F=9721\ P=0) \end{cases} \quad (3\text{-}1)$$

Where

T_{304} = air temperature at PR304,

T_{11} = air temperature at PTH11,

T_{AWOS} = air temperature at the weather station of Winnipeg Richardson AWOS

Figure 3-8 and Figure 3-9 show the relation between the air temperatures at test sites and the weather station of AWOS.

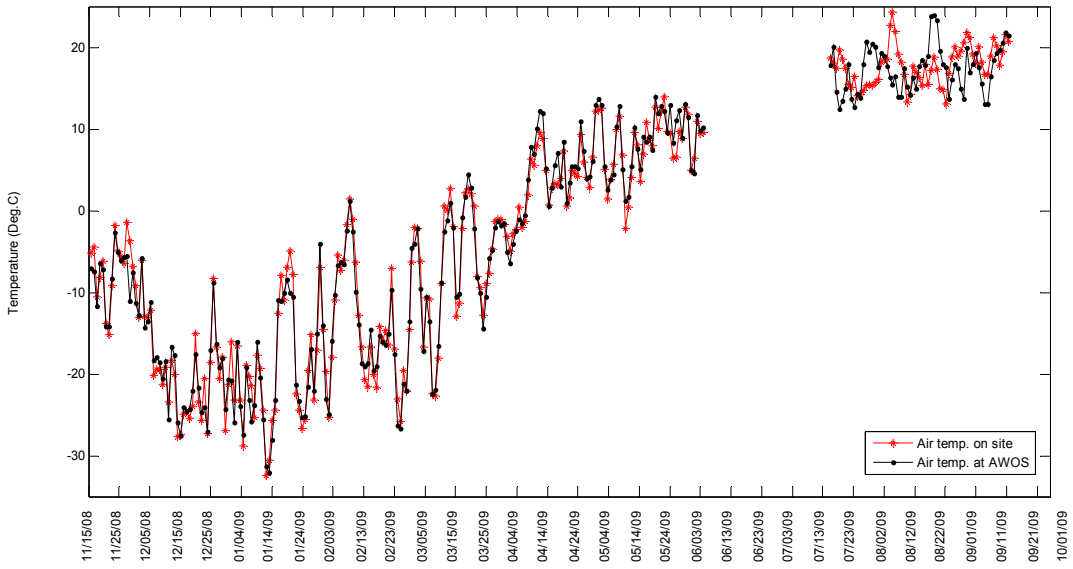

Figure 3-8 Air temperature at weather station and at PTH11

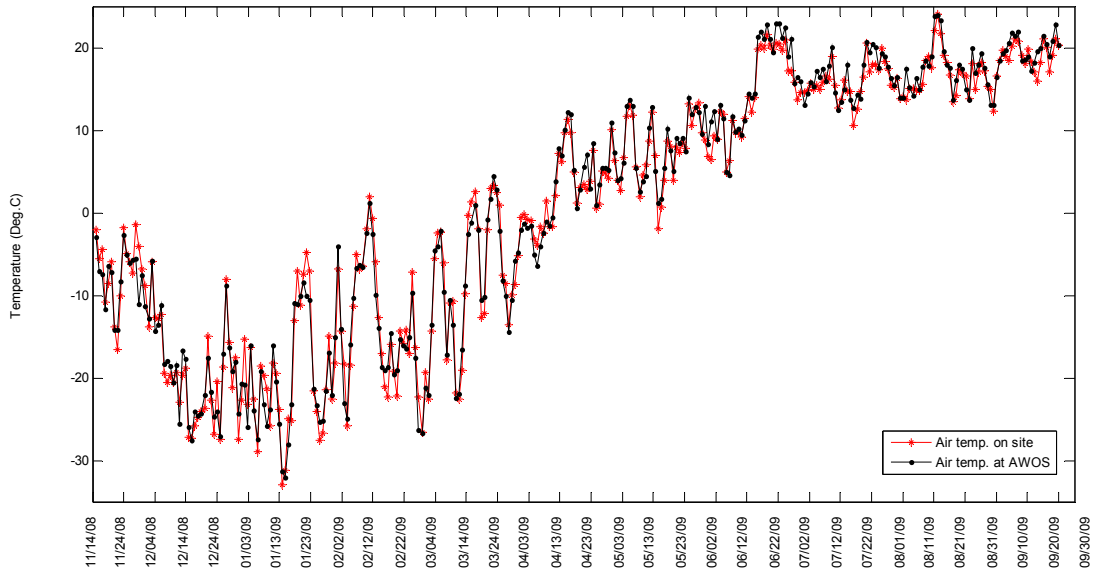

Figure 3-9 Air temperature at weather station and at PR304

3.4 FROST AND THAW DEPTH AT TWO SITES

3.4.1 AIR FREEZING AND AIR THAWING INDICES

Cumulative air freezing index (Fi_a) and air thawing index (Ti_a) were calculated from the readings of mini weather station on both sites.

The algorithm to calculate Fi_a is described by equation 3-2:

$$\begin{cases} Fi_{a(1)} = T_{air(1)} \\ Fi_{a(i+1)} = Fi_{a(i)} + T_{air(i+1)} \\ Fi_{a(i)} > 0 \xrightarrow{yields} Fi_{a(i)} = 0 \end{cases} \quad (3\text{-}2)$$

Where

i = number of days after November 1st (began to calculate Fi_a on November 1st, 2008),

$T_{air(i)}$= air temperature on day i (^{0}C),

$Fi_{a(i)}$= cumulative air freezing index on day i (^{0}C-days).

The freezing index is the minimum value of Fi_a at both sites. The freezing index at PTH11 is -2013.1 (^{0}C-days). The corresponding value at PR304 is -2011.9 (^{0}C-days).

The algorithm to calculate Ti_a is described by equation 3-3:

$$\begin{cases} Ti_{a(1)} = T_{air(1)} \\ Ti_{a(i+1)} = Ti_{a(i)} + T_{air(i+1)} \\ Ti_{a(i)} < 0 \xrightarrow{yields} Ti_{a(i)} = 0 \end{cases} \quad (3\text{-}3)$$

Where

$Ti_{a(i)}$= cumulative air thawing index on day i (^{0}C-days).

The meanings of other variables are as defined previously.

Figure 3-10 and Figure 3-11 show the cumulative air freezing and air thawing indices on both sites. Due to malfunction of datalogger, the indices are not available at PTH11 after June 10, 2009.

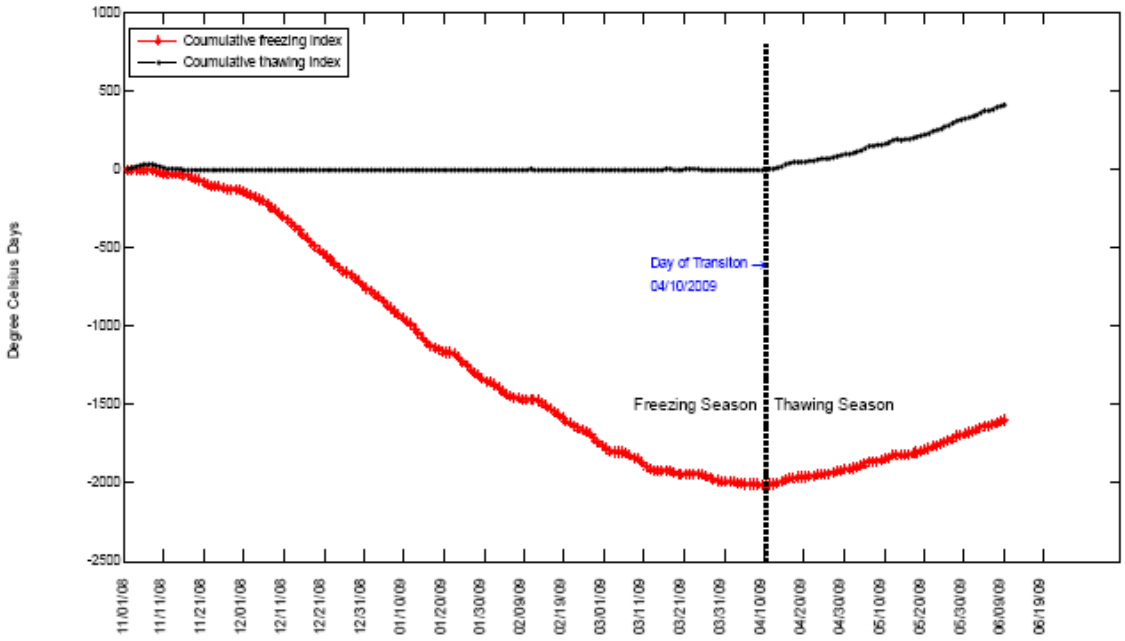

Figure 3-10 Cumulative freezing and thawing indices at PTH11

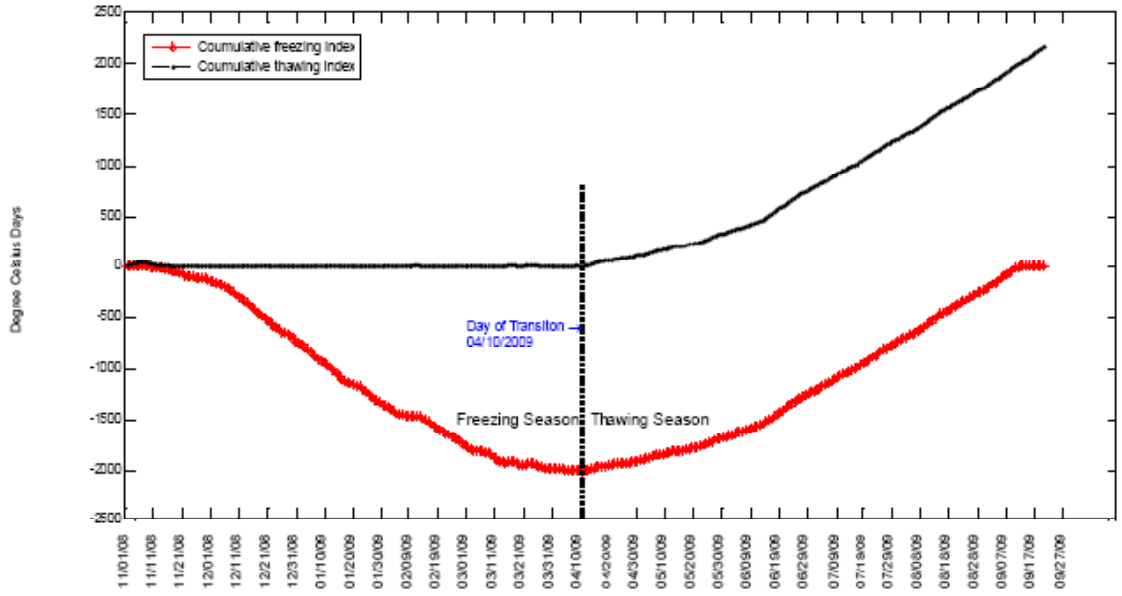

Figure 3-11 Cumulative freezing and thawing indices at PR304

3.4.2 PAVEMENT SURFACE THAWING INDICES

There is always a temperature lag between air and pavement surface. Mean annual ground surface temperatures (10 mm depth) differ from mean annual air temperature with no constant difference between them (Brown, 1963). The pavement surface thawing index can be calculated by using reference temperature or N-factor.

(a) Thawing index by Minnesota Department of Transportation

Pavement surface thawing index is the accumulation of degree-days above a reference thawing temperature. The index is related to the penetration of thaw in pavement structure. This concept has been adopted by Minnesota Department of Transportation (Mn/DOT) and is based on a refined thawing index (TI) as shown in equation 3-4 (Mn/DOT, 2009):

TI=Average Daily Air Temperature-Reference Temperature (3-4)

Based on research at Mn/DOT, Manitoba Infrastructure and Transportation (MIT) uses a reference temperature of 1.7 ^{o}C on March 1st that increases by 0.06 ^{o}C per day to calculate pavement surface thawing index (MIT, 2002).

The calculation of reference temperature is presented in equation 3-5 as follows:

$$\begin{cases} T_{R(1)} = 1.7 \\ T_{R(i+1)} = T_{R(i)} + 0.06 \times i \end{cases} \quad (3\text{-}5)$$

Where

i = number of days after March 1st,

$T_{R(i)}$= reference temperature on day i (^{o}C).

The calculation of pavement surface thawing index (TI_R) is shown in equation 3-6:

$$\begin{cases} TI_{R(1)} = T_{R(1)} + T_{air(1)} \\ TI_{R(i+1)} = TI_{R(i)} + T_{R(i+1)} + T_{air(i+1)} \\ TI_{R(i)} < 0 \xrightarrow{yields} TI_{R(i)} = 0 \end{cases} \quad (3\text{-}6)$$

Where

$T_{air(i)}$= air temperature on day i (^{o}C),

$TI_{R(i)}$= cumulative surface thawing index on day i based on reference temperature (^{o}C-days),

The meanings of other variables are as defined previously.

(b) Modified thawing index by MIT

In Manitoba, a modified pavement surface thawing index by reference temperature (TI_{RM}) is used to predict the date of SLR implementation. The calendar date at which the forecast values of the TI_{RM} exceed 15 degree Celsius-days and the forecast trend of the daily mean temperatures indicate continued increases in the TI_{RM} trigger the start of the enforcement of the spring weight restriction period. In cases where TI_{RM} is 0 ^{o}C or above and the average daily temperature is negative, only half of that negative value is added to the previous TI_{RM}. This adjustment is made to account for the fact that the pavement base layer does not re-freeze due to short-term small negative mean daily temperatures (MIT, 2002). The algorithm to calculate TI_{RM} is described by equation 3-7:

$$\begin{cases} TI_{RM(1)} = T_{R(1)} + T_{air(1)} \\ TI_{RM(i+1)} = TI_{RM(i)} + T_{R(i+1)} + T_{air(i+1)} \\ TI_{RM(i)} > 0 \text{ and } T_{air(i+1)} < 0 \xrightarrow{yields} TI_{RM(i+1)} = TI_{RM(i+1)} \text{-} 0.5 \text{ X } T_{air(i+1)} \\ TI_{RM(i)} \leq 0 \xrightarrow{yields} TI_{RM(i)} = 0 \end{cases} \quad (3\text{-}7)$$

Where

$TI_{RM(i)}$=Modified pavement surface thawing index by reference temperature in Manitoba.

The meanings of other variables are as defined previously.

Figure 3-12 compares the modified pavement surface thawing index by reference temperature in Manitoba and the pavement surface thawing index by reference temperature according to the research at Mn/DOT from March 1 through July 31, 2009. Figure 3-13 shows the difference at PTH11 from March 1 through May 5, 2009 for a closer look.

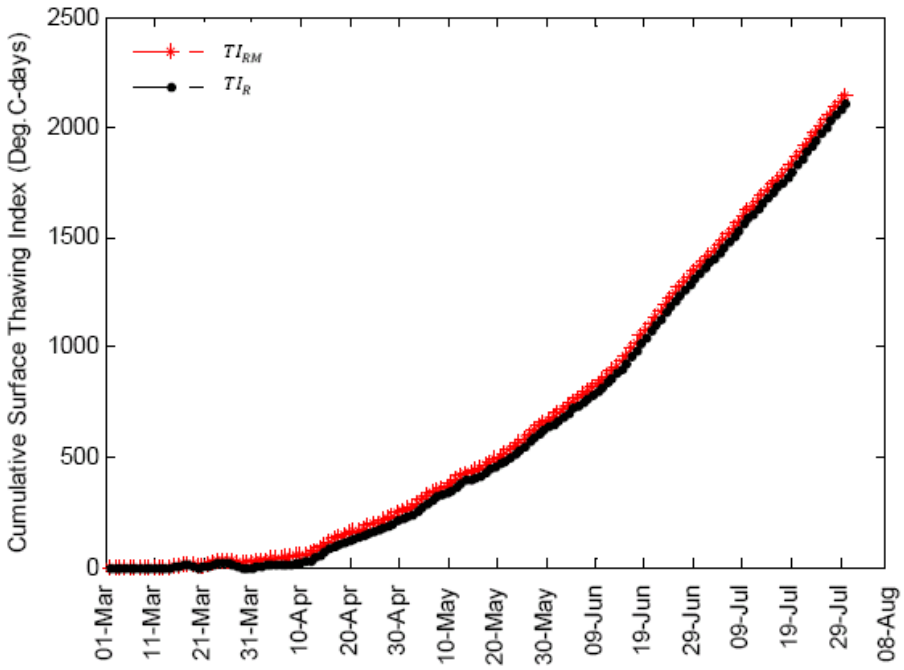

Figure 3-12 Thawing index and modified thawing index at PR304

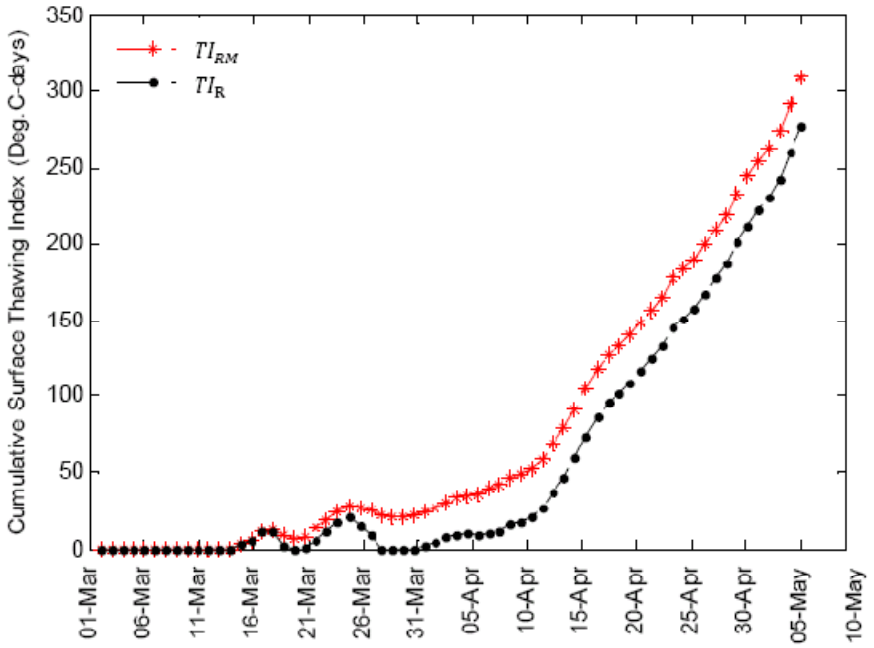

Figure 3-13 Thawing index and modified thawing index at PTH11

(c)N-factor and surface thawing index

The surface thawing index can also be estimated using an empirically determined surface N-factor which is defined as the ratio of the ground surface thawing index (TI_N) to the air thawing index (TI_a) as shown in equation 3-8 (Andersland and Ladanyi, 2004):

$$N_t = \frac{TI_N}{TI_a} \tag{3-8}$$

Where

N_t= thawing factor (N-factor),

TI_N= pavement surface thawing index by N-factor, and

TI_a= air thawing index.

Normal thawing factor N_t for asphalt pavement is in the range of 1.4--2.3 (Lunardini, 1978). For the pavement free of snow and ice, the N_t can be found in Figure 3-14.

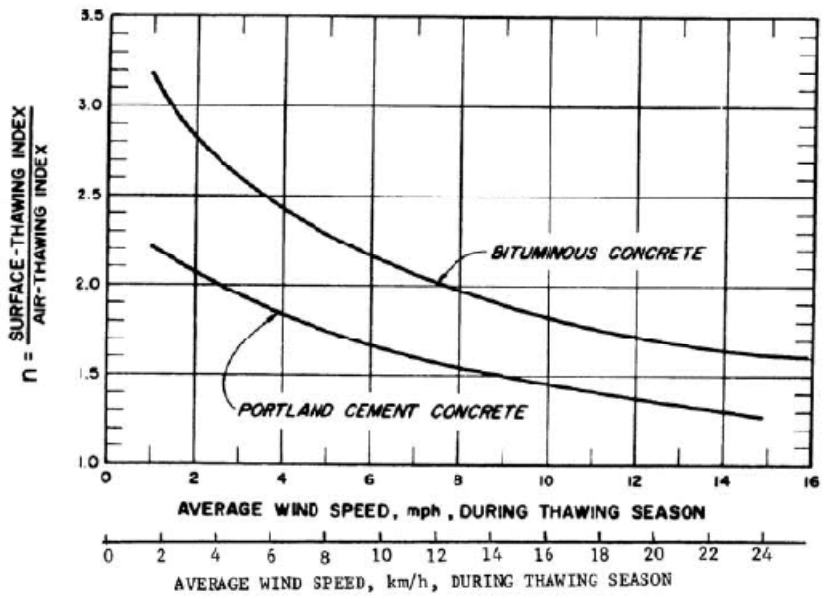

Figure 3-14 Relation between N-factor and wind speed.
(Source: department of the Army 1966)

According to the data from Environment Canada collected at the weather station of Winnipeg (Richardson AWOS), mean wind speed and thawing indices for different months can be calculated as shown in Table 3-1.

Table 3-1 Wind Speeds and Thawing Indices in Different Months

Month	Wind Speed(km/h)	N-factor	Thawing Index
March	23.4	1.62	TI_{N3}= 1.62 x TI_{a3}
April	18.6	1.75	TI_{N4}= 1.75 x TI_{a4}
May	21.2	1.73	TI_{N5}= 1.73 x TI_{a5}
June	17.0	1.80	TI_{N6}= 1.80 x TI_{a6}

The pavement surface thawing index by N-factor can be calculated in equation 3-9:

$$TI_N = \sum N_t \times TI_{aj} \quad (3\text{-}9)$$

Where

j= 3,4,5,6 refer to the moths of March, April, May, and June 2009.

The meanings of other variables are as defined previously.

3.4.3 MEASURED FROST AND THAWING DEPTHS ON SITES

The frost and thawing depth in pavement was measured by thermistors. Zero degree Celsius is assumed to be the divide line between frozen and thawed. If the reading of a specific thermistor is positive, which means the pavement at that elevation is thawed; if the reading is negative, which means the pavement is frozen. If a thermistor's reading is positive, while the thermistor below is negative, linear interpolation method was chosen to calculate thawing depth.

3.4.4 MEASURED AND PREDICTED VALUES ON BOTH SITES

(a) Measured and predicted frost and thawing depth by using Mn/DOT reference temperature (method 1)

Figure 3-15 shows the measured and predicted frost and thawing depth at PTH11. The prediction of frost depth consists of two segments as can be seen in equation 3-10:

$$\begin{cases} FD = -107.14 - 48.02 \times \sqrt{Fi_a} & (R^2=0.9956) \quad \text{Before March 1}^{st} \\ FD = 90.9 - 52.2 \times \sqrt{Fi_a} - 4.6 \times \sqrt{Ti_R} & (R^2=0.9095) \quad \text{After March 1}^{st} \\ TD = 2457.0 - 54.3 \times \sqrt{Fi_a} - 82.8 \times \sqrt{Ti_R} & (R^2=0.9767) \quad \text{After March 1}^{st} \end{cases} \tag{3-10}$$

Where

The meanings of variables are as defined previously.

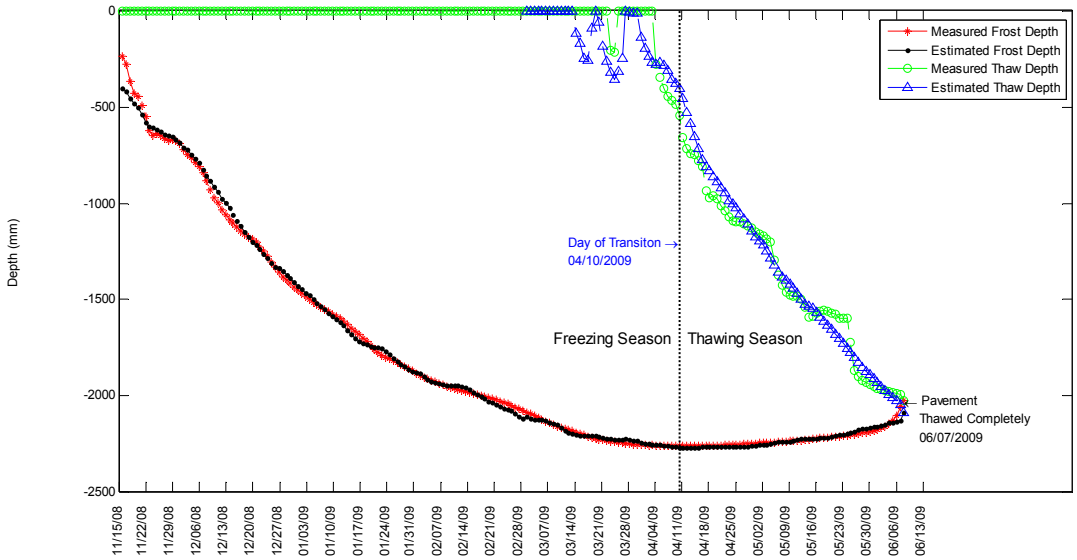

Figure 3-15 Freezing and thawing depth at PTH11 (method 1)

Figure 3-16 shows the measured and predicted frost and thaw depth at PR304. The predictions can be seen in equation 3-11:

$$\begin{cases} FD == -53.6 - 49.9 \times \sqrt{Fi_a} & (R^2=0.9817) \\ TD = 16381.8 - 365.7 \times \sqrt{Fi_a} - 106.8 \times \sqrt{Ti_R} & (R^2=0.8558) \end{cases} \quad (3\text{-}11)$$

After March 20th

Where

The meanings of variables are as defined previously.

The data from March 20, 2009 was chosen to predict the thawing depth in late March and early April. Measured thawing depths are not available after April 14, 2009 due to the malfunction of thermistors.

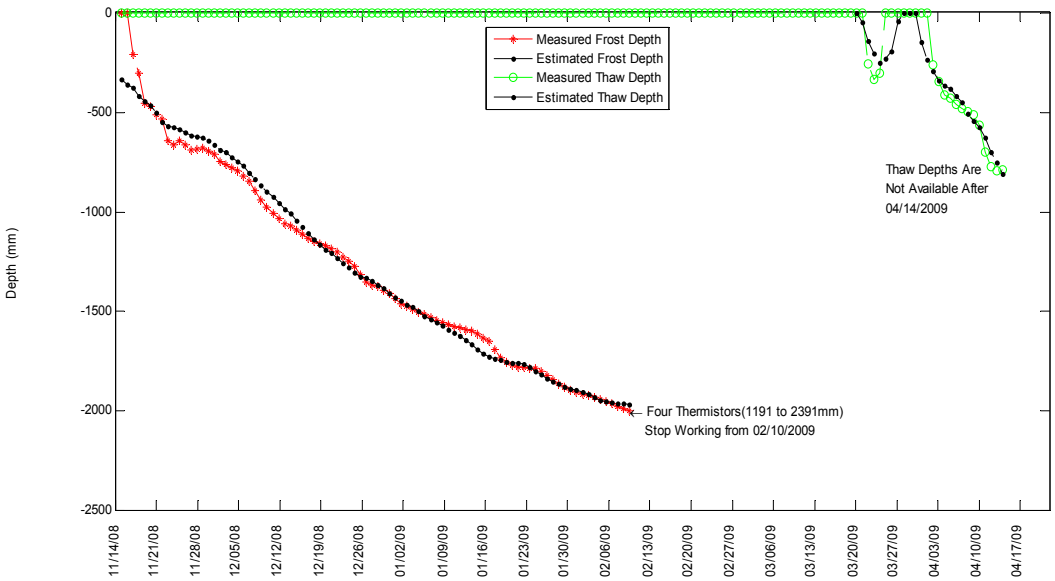

Figure 3-16 Freezing and thawing depth at PR304 (method 1)

(b) Measured and predicted frost and thawing depth by using MIT modified reference temperature (method 2)

Figure 3-17 shows the measured and predicted frost and thawing depth at PTH11. The prediction of frost depth consists of two segments as can be seen in equation 3-12:

$$\begin{cases} FD = -107.14 - 48.02 \times \sqrt{Fi_a} & (R^2=0.9956) \quad \text{Before March } 1^{st} \\ FD == -30.3 - 49.3\sqrt{Fi_a} - 4.5 \times \sqrt{Ti_{RM}} & (R^2=0.9208) \quad \text{After March } 1^{st} \\ TD = -95.0 + 5.0 \times \sqrt{Fi_a} - 79.3 \times \sqrt{Ti_{RM}} & (R^2=0.9679) \quad \text{After March } 1^{st} \end{cases} \tag{3-12}$$

Where

The meanings of variables are as defined previously.

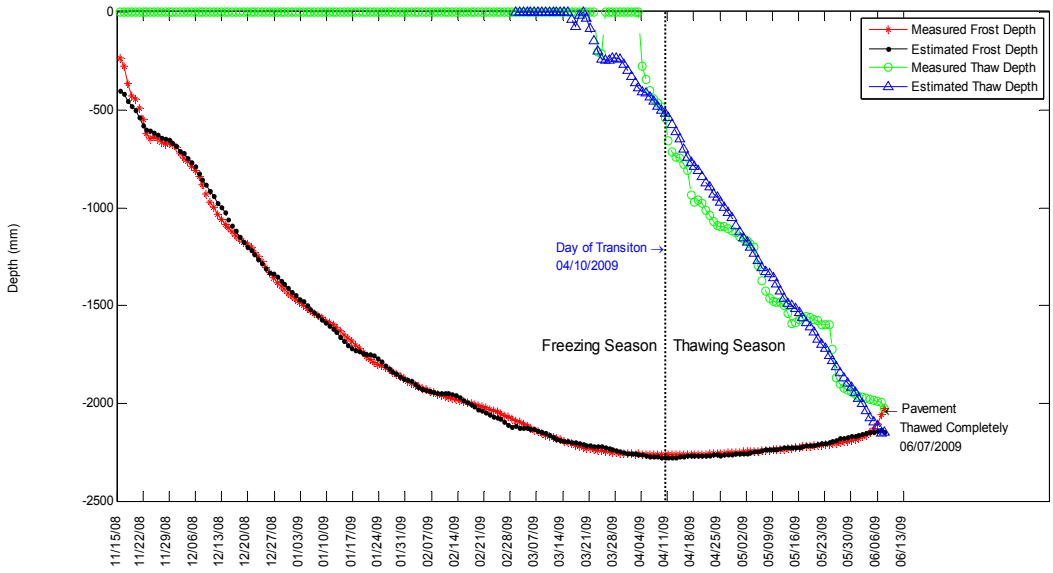

Figure 3-17 Freezing and thawing depth at PTH11 (method 2)

Figure 3-18 shows the measured and predicted frost and thawing depth at PR304. The predictions can be seen in equation 3-13:

$$\begin{cases} FD == -53.6 - 49.9 \times \sqrt{Fi_a} & (R^2=0.9817) \\ TD = -1826.3 + 55.4 \times \sqrt{Fi_a} - 157.2 \times \sqrt{Ti_{RM}} & (R^2=0.7798) \end{cases} \quad (3\text{-}13)$$

After March 20th

Where

The meanings of variables are as defined previously.

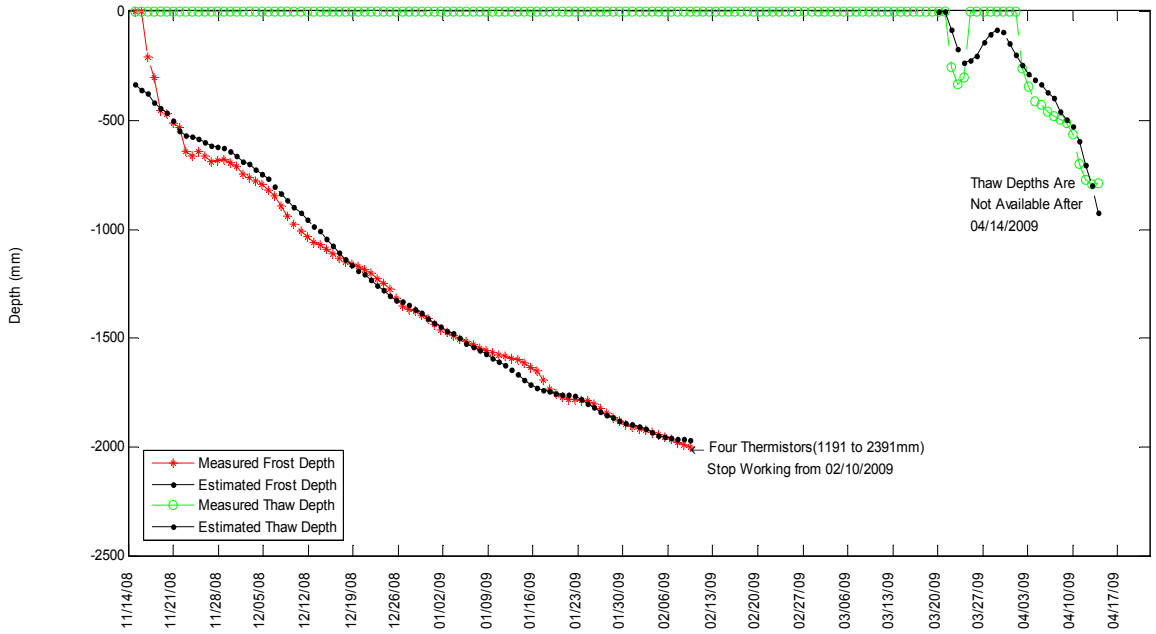

Figure 3-18 Freezing and thawing depth at PR304 (method 2)

(c) Measured and predicted frost and thawing depth using N-factor (method 3)

Figure 3-19 shows the measured and predicted frost and thawing depth at PTH11. The prediction of frost depth consists of two segments as can be seen in equation 3-14:

$$\begin{cases} FD = -107.14 - 48.02 \times \sqrt{Fi_a} & (R^2=0.9956)\ \text{Before March 1}^{st} \\ FD = 209.4 - 55.0 \times \sqrt{Fi_a} - 4.9 \times \sqrt{Ti_N} & (R^2=0.9010)\ \text{After March 1}^{st} \\ TD = 4699.5 - 108.4 \times \sqrt{Fi}\sqrt{Fi_a} - 88.6 \times \sqrt{Ti_N} & (R^2=0.9695)\ \text{After March 1}^{st} \end{cases} \quad (3\text{-}14)$$

Where

The meanings of variables are as defined previously.

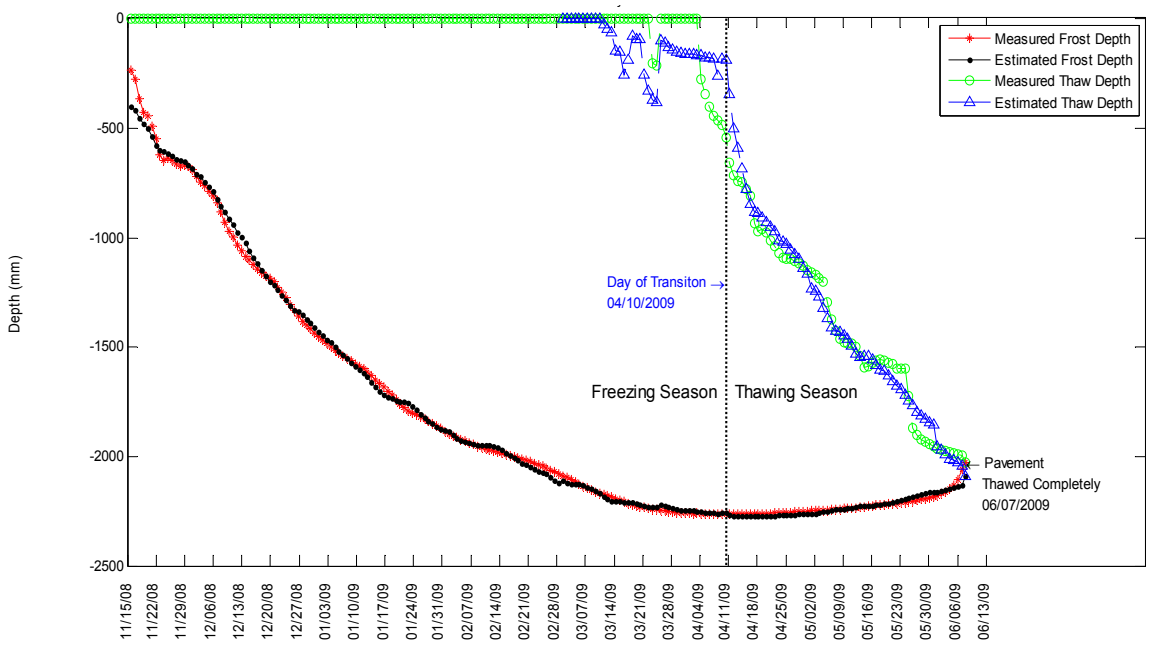

Figure 3-19 Freezing and thawing depth at PTH11 (method 3)

Figure 3-20 shows the measured and predicted frost and thawing depth at PR304. The predictions can be seen in equation 3-15:

$$\begin{cases} FD == -53.6 - 49.9 \times \sqrt{Fi_a} & (R^2=0.9817) \\ TD = 33620.0 - 758.0 \times \sqrt{Fi_a} - 111.4 \times \sqrt{Ti_N} & (R^2=0.7141) \end{cases} \qquad \text{(3-15)}$$

After March 20th

Where

The meanings of variables are as defined previously.

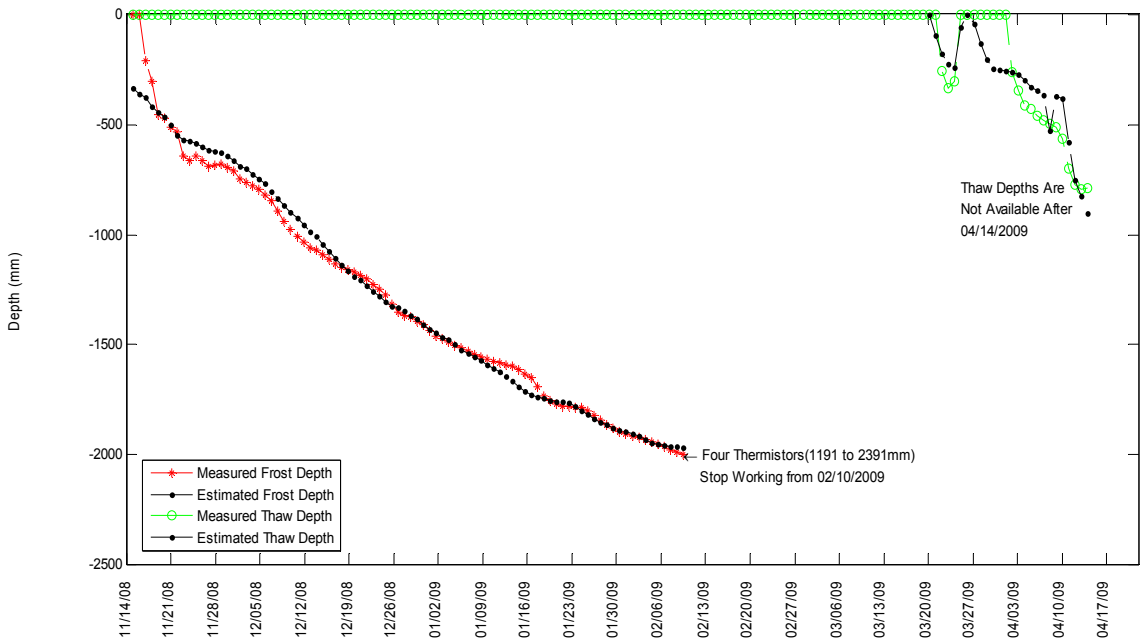

Figure 3-20 Freezing and thawing depth at PR304 (method 3)

3.4.5 USING MODIFIED BERGGREN EQUATION TO PREDICT FROST DEPTH AT PTH11

A rational formula for frost-depth penetration in mult-layered soil system is based on the modified Berggren equation developed by Aldrich and Paynter(1966). The modified Berggren equation in SI units is shown below in equation 3-16:

$$X = \lambda\sqrt{172800\frac{K.FI_{sf}}{L}} \qquad (3\text{-}16)$$

Where

X =frost depth,

k=soil thermal conductivity,

FI_{sf} =absolute value of surface freezing index,

L=latent heat of the soil.

As shown in Figure 3-21, the dimensionless coefficient λ is a function of other two dimensionless parameters, α and μ, which can be calculated in equation 3-17.

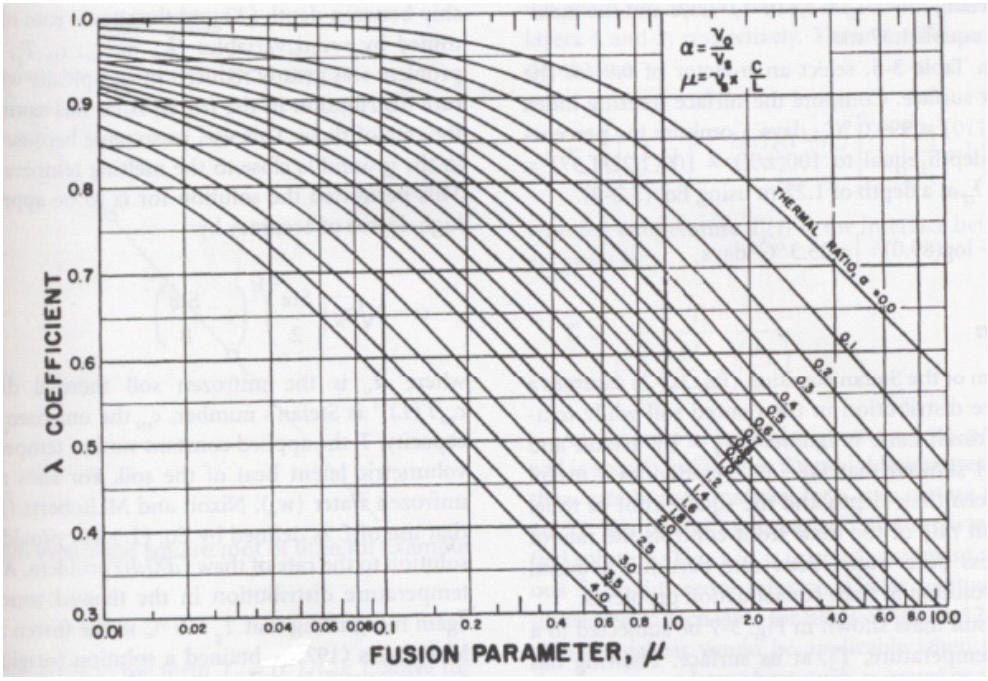

Figure 3-21 Coefficient in the modified Berggren equation.
(Source: Department of the Army 1966)

$$\alpha = \frac{v_0}{v_s} = \frac{v_0 t}{FI_{sf}} = \text{thermal ratio} \quad (3\text{-}17a)$$

$$\mu = \frac{c_v}{L} v_s = \frac{c_v \quad FI_{sf}}{L.t} = \text{fusion parameter} \quad (3\text{-}17b)$$

Where

c_v = soil volumetric heat capacity (kJ/m^3.K),

L = volumetric latent heat (kJ/m^3),

v_0 = mean annual surface temperature,

$v_s = \frac{FI_{sf}}{t}$, where FI_{sf} is the surface freezing index, t is the duration of the freezing period.

As shown in Figure 3-22. When applying the modified Berggren equation, it is assumed that the soil is a semi-infinite mass with uniform properties and existing

initially at a uniform temperature v_0 degree. It is also assumed that the surface temperature changes from its initial value of v_0 degrees positive to v_s degrees below freezing at the start of freezing period.

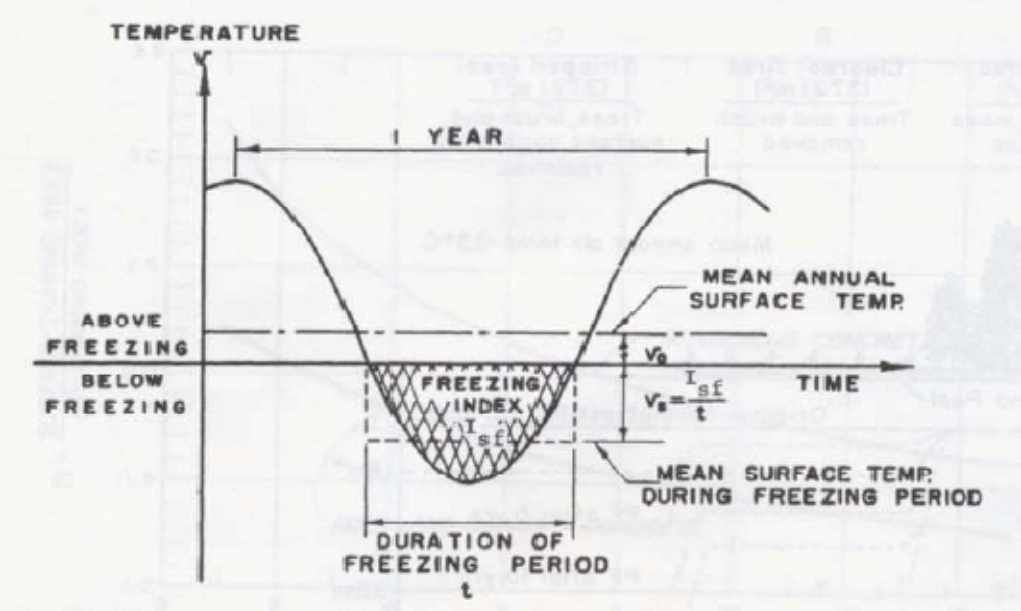

Figure 3-22 Assumed sinusoidal annual variation of surface temperature. (Source: Aldrich and Paynter)

The frost depth at PTH11 can be calculated by the following steps.

Step 1. Determine the pavement profile and thermal properties. For PTH11, the structure profile is shown in Table 3-2.

Table 3-2 Pavement Structure Profile of PTH11

Material	d(depth) (mm)	K_{avg} (W/m.°C)*	C_{avg} (MJ/m^3.°C)*	L (MJ/m^3)*
AC	125	1.38	1.88	0
Granular base	250	1.73	1.54	31.7
Subgrade		2.94	1.81	108

* Source: (Andersland and Ladanyi, 2004)

Step 2. Determine freezing N-factor and surface freezing index. Select freezing N-factor n_f=0.9 According to the readings of mini weather station on site, air freezing index FI_a=2013.1 °C-days. The surface freezing index FI_{sf}=0.9 x 2013.1=1811.79 °C-days

Step 3. Select a trial frost depth X=d_1+ d_2+ d_3=2.27 m and compute the effective L/k value.

$$\frac{L}{k}=\frac{2}{X^2}\left[\frac{d_1}{k_1}\left(\frac{L_1 d_1}{2}+L_2 d_2+L_3 d_3\right)+\frac{d_2}{k_2}\left(\frac{L_2 d_2}{2}+L_3 d_3\right)+\frac{d_3}{k_3}\left(\frac{L_3 d_3}{2}\right)\right]$$

$$=\frac{2}{2.27^2}\left[\frac{0.125}{1.38}(0+31.7\times 0.25+108\times 1.895)+\frac{0.25}{1.73}\left(\frac{31.7\times 0.25}{2}+108\times 1.895\right)+\frac{1.895}{2.94}\left(\frac{108\times 1.895}{2}\right)\right]\times 10^6$$

$$=45.62\times 10^6$$

Step 4. Compute weighted values of c_v and L within the estimated depth of frost penetration.

$$c_{wt}=(c_1 d_1+c_2 d_2+c_3 d_3)/\mathrm{X}$$

$$=(1.88\times 0.125+1.54\times 0.25+1.81\times 1.895)/2.27$$

$$=1.91$$

$$L_{wt}=(L_1 d_1+L_2 d_2+L_3 d_3)/\mathrm{X}$$

$$=(0\times 0.125+31.7\times 0.25+108\times 1.895)/2.27$$

$$=93.65$$

Step 5. Compute the effective values for the thermal ratio α and the fusion parameter μ using Eq. 3-17.

According to the data at the weather station of Winnipeg Richardson AWOS, Environment Canada, mean annul air temperature Tair=2.6 ℃ ; the annual pavement temperature at the depth of 191 mm at PR304 is T191=5.9 ℃ (data from 11/14/2008 to

11/14/2009). Choose the average value of these two temperatures as the surface annual mean temperature. (v_0= (2.6+5.9)/2=4.3℃).

$$\alpha = \frac{v_0 t}{FI_{sf}} = \frac{4.3 \times 141}{1811.79} = 0.335$$

$$\mu = \frac{c_{wt} FI_{sf}}{L_{wt} t} = \frac{1.91 \times 1811.79}{93.65 \times 141} = 0.262$$

Step 6. Determine from Figure 3-21 the correction coefficient λ. λ=0.88

Step 7. Using equation 3-3, compute the depth of frost penetration.

$$X = \lambda \left(172{,}800 \frac{K.FI_{sf}}{L}\right)^{1/2}$$

$$= 0.88 \left(172{,}800 \frac{2 \times 60 \times 60 \times 24 \times 1811.79}{45.62 \times 10^6}\right)^{1/2}$$

= 2.30 m

With the computed value of X (2.30 m) being close to the initial assumed X (2.27 m), steps 3 through 7 do not have to be repeated.

It can be concluded that the predicted frost depth by modified Berggren equation is close to the measured frost depth at PTH11 which is 2.26 m.

3.5 IMPLEMENT SPRING LOAD RESTRICTION ACCORDING TO PAVEMENT THAWING INDICES

According to measured air temperature on sites from March 1 to May 5, 2009, the relation between pavement surface thawing indices based on reference temperature and N-factor is shown in Figure 3-23 and Figure 3-25 for PR304 and PTH11, respectively.

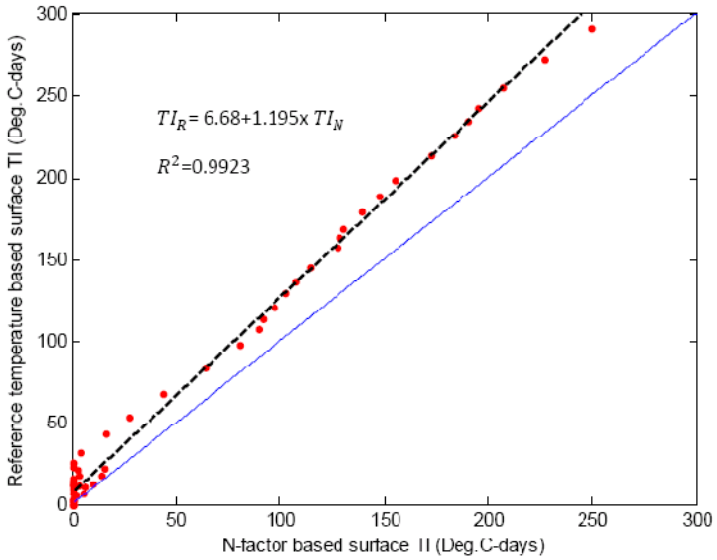

Figure 3-23 Relation between thawing indices by reference temperature and N-factor at PR304.

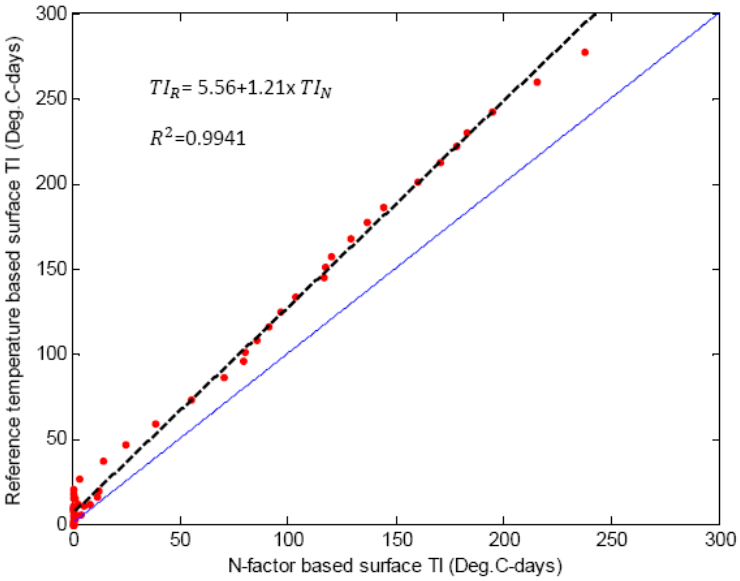

Figure 3-24 Relation between thawing indices by reference temperature and N-factor at PTH11.

The threshold of TI_R is 15 ^{o}C-days to implement SLR in Manitoba. By plugging in TI_R =15 to the linear regression functions in Figure 3-23 and Figure 3-24, we get TI_N =7 ^{o}C-days which will be used as threshold for TI_N at PR304 and PTH11. Figure 3-25 and Figure 3-

26 show TI_R, TI_N, and the dates of SLR should be in place at PR304 and PTH11, respectively. In practice, MIT implemented SLR on March 23, 2009 for climatic zone 1 in Manitoba. Figure 3-27 shows the two climatic zones in Manitoba.

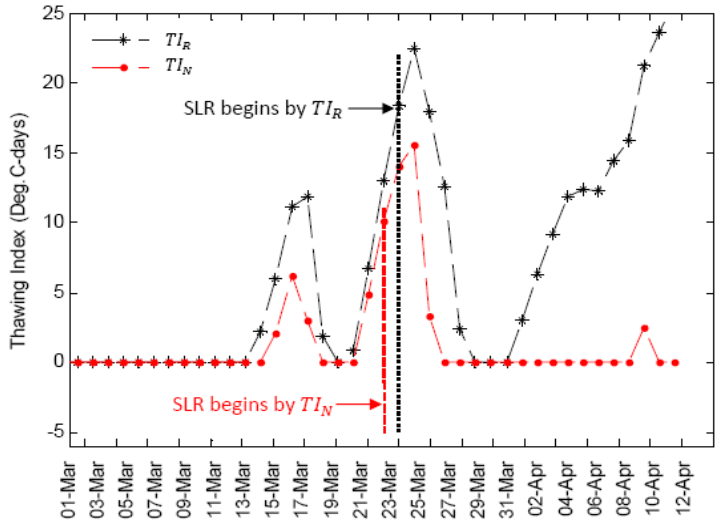

Figure 3-25 Implement SLR according to different thawing indices at PR304.

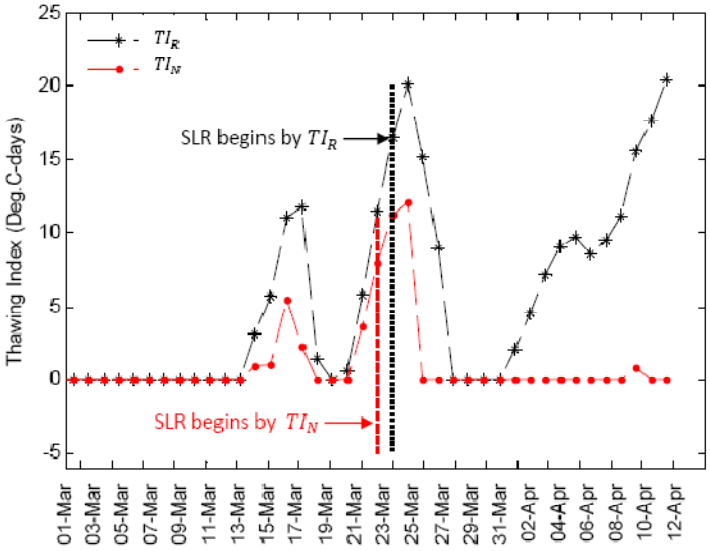

Figure 3-26 Implement SLR according to different thawing indices at PTH11.

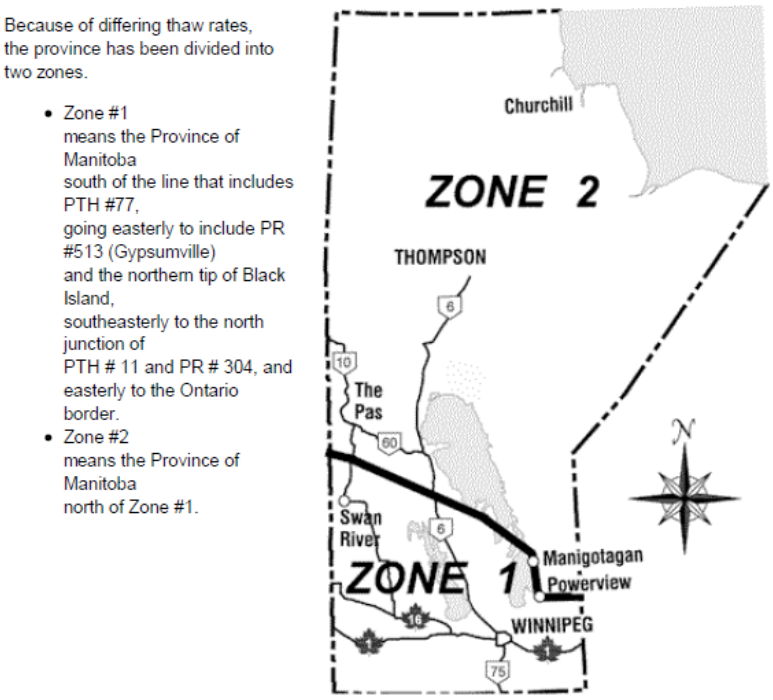

Figure 3-27 Two climatic zones in Manitoba (source: MIT)

If the modified pavement surface thawing index TI_{RM} in Manitoba was chosen to decide the SLR date, and the threshold is still 15 ^{o}C-days, it yields that the SLR should be implemented on March 22, 2009 instead of March 23, 2009 according to TI_R in 2009. In conclusion, the three pavement thawing indices give very similar results for implementing SLR in Manitoba in 2009. The result by using TI_R is one day later than the others.

3.6 SUMMARY

Based on the discussion in this chapter, the following conclusions can be drawn:

- The air freezing index at PTH11 was -2013.1 (^{o}C-days) in 2009. The corresponding value at PR304 was -2011.9 (^{o}C-days).

- The maximum frost depth at PTH11 was 2265mm in 2009.
- On June 7, 2009, the pavement thawed out at PTH11.
- In terms of the prediction of thawing depth, Ti_{R}, Ti_{N}, $\mathrm{Ti}_{\mathrm{RM}}$ are all good indicators. They can be used to predict the dates of SLR implementation.

CHAPTER 4 VOLUMETRIC MOISTURE CONTENT AT TEST SITES

4.1 INTRODUCTION

The moisture content variation within different layers of pavement is an important parameter that influences the overall strength of flexible pavement. For this project, the Campbell Scientific water content reflectometer probe (WCR) was selected to monitor moisture content of the various pavement layers.

4.2 SOIL SAMPLES AND CALIBRATION PARAMETERS

Soil samples were collected during the installation of WCR probe at test sites. The volumetric moisture content (VMC)of all the soil samples was tested in the lab. According to the *Soil survey report for PTH11 and PR304 (MIT)* and *the manual of WCR probe* from Campbell Scientific, different groups of calibration parameters were tested to calculate moisture readings at test sites. The best fitted parameters were selected.

4.2.1 PR304

Table 4-1 shows the test results of soil samples and calibration of VMC at PR304.

Table 4-1 Lab tested and calculated VMC at PR304

Depth (mm)	Porosity of soil sample (%)	VMC by soil sample (%)	VMC By linear calibration (%)	VMC By quadratic calibration (%)
130	29.43	16.98*	8.9	8.07
550	28.39	18.76	26.51	23.98
850	26.96	27.03	18.57	16.14
1150	35.03	41.72	37.01	37.78
1500	32.20	35.69	35.92	36.43

** For the granular base material, it is difficult to take bulk soil sample with original moisture content. The moisture content of the soil sample might be changed during collection of soil samples.*

As can be seen from Table 4-1, there is not much difference between linear and quadratic calibration of the WCR readings. By comparing to the VMC from the bulk soil samples taken on site during the installation of WCR, both calibration methods can provide VMC for the soils at different depths of pavement with reasonable accuracy.

4.2.2 PTH11

Table 4-2 shows the test results of soil samples and calibration of VMC at PTH11.

Table 4-2 Lab tested and calculated VMC at PTH11

Depth (mm)	Porosity of soil sample (%)	VMC by soil sample (%)	VMC By linear calibration (%)	VMC By quadratic calibration (%)
200	5.05	30.27	9.16	8.26
510	24.89	41.7	23.55	22.72
830	30.80	50.77	53.94	61.5
1170	36.40	50.56	58.04	68.06
1520	32.31	52.64	55.58	64.09

VMC-SM, volumetric moisture content of the bulk soil sample taken on October 16, 2008 during installation of WCRs. Porosity, the porosity of bulk soil samples.
VMC-linear, volumetric moisture content according to the installed WCR readings on October 17, 2008 with linear calibration.
VMC-quadratic, volumetric moisture content according to the installed WCR readings on October 17, 2008 with quadratic calibration.

According to the soil survey report about the test sites from MIT in September 2008 before the installation of WCRs, the WCR at the depth of 200 mm was installed within granular base where the WCR should work well. As to the soil at the depth of 510 mm, 17.1% pass the No. 200 sieve, by choosing calibration coefficients for sandy clay loam with bulk density 1.6 g/cm^3 and electrical conductivity at saturation 0.75 dS m^{-1} for linear and quadratic forms (Campbell Scientific, Inc., 2006); the VMC was 18.93 and 18.32 percent, respectively. These values match the test results of bulk soil sample

which gave the VMC at 18.76 percent (refer to Table 4-2). As a result, any other calibration was not applied to the readings of WCR at 510 mm.

For the WCRs at the depths of 830 mm, 1170 mm, and 1520 mm, they were all installed in clay some of which the clay content is as high as 79 % with certain amount of organic materials (Tomko, 2008). According to the manual of WCR from Campbell Scientific, the amount of organic matter and clay in a soil can alter the response of dielectric-dependent methods to change in water content. Organic metter and some clays are highly polar. These solid constituents can affect WCR response to water content change and require specific calibration. It would be convient if the calibration of water content to WCR output being adjusted according to some parameter of the soil which reflects the character of the signal attenuation.

As shown in Table 4-2, The VMC from the WCRs at the depths of 830 mm, 1170 mm, and 1520 mm are extremly high, which are even higher than the porosity of the corrsponding soil samples. The volumetric moisture content from the soi samples are quite different from the WCR readings. In order to represent the volumetric moisture content from these WCRs appropriety, the WCR readings were shifted to the corrsponding values of the VMC from soil smaples. For example, the WCR at the depth of 1170 mm gaves the value of VMC at 58.04% by linear calibration on October 16, 2008, while the VMC from soil sample is 41.72 %. So the curve of this WCR was shifted to match the value from soil sample . The reading of WCRs at the depths of 830 mm and

1500 mm were shifted too. For the WCRs at the depths of 200 mm and 510 mm, no adjustment were applied.

With only one value of VMC of bulk soil samples took on October 16, 2008 during the installation of WCRs, the authour understands the limitations of this kind of adjustment of VMC curves. After such adjustment all the readings from WCRs were showing a reasonably acurate trend. All the readings from WCRs at different depths were also showing pricipitation and frozen point clearly.

4.3 VOLUMETRIC MOISTURE CONTENT ON TEST SITES

Figure 4-1 and Figure 4-2 show the general trend of the moisture level at the test sites of PR304 and PTH11, respectively.

4.4 VOLUMETRIC MOISTURE CONTENT PROFILES ON TEST SITES

Figure 4-4 through Figure 4-6 show the VMC profiles at test site from the beginning of March 2009.

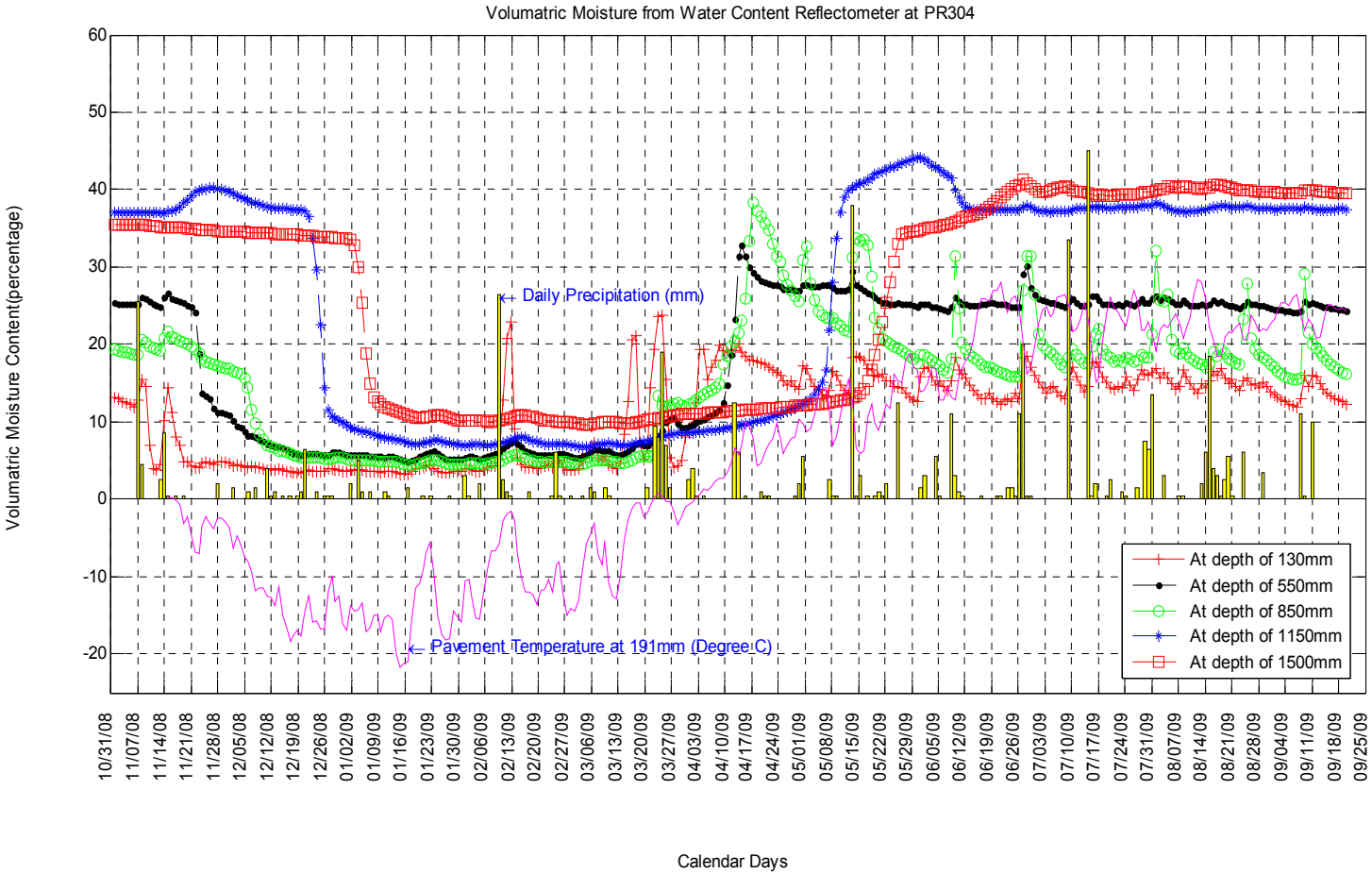

Figure 4-1 Volumetric moisture content at PR304.

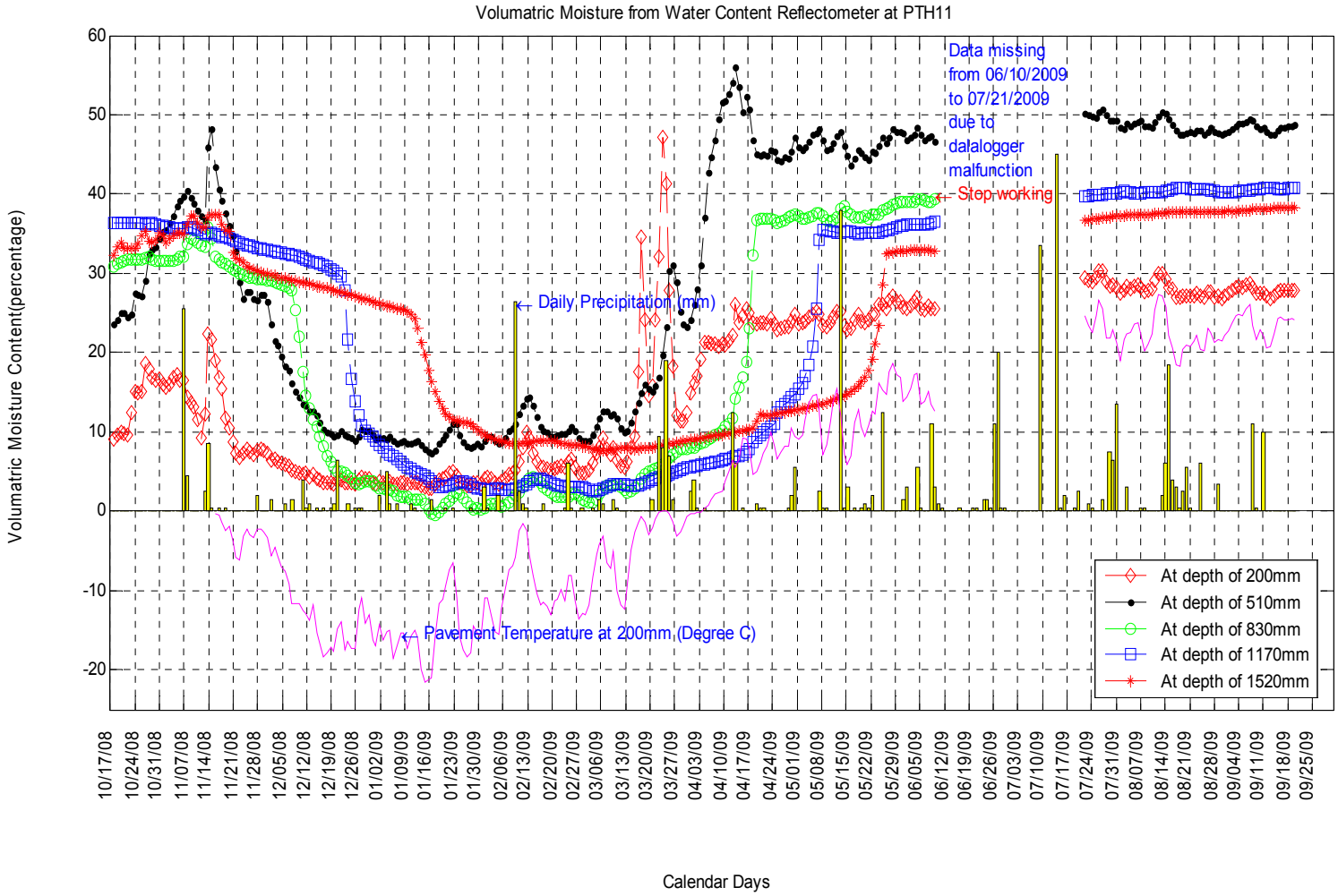

Figure 4-2 Volumetric moisture content at PTH11.

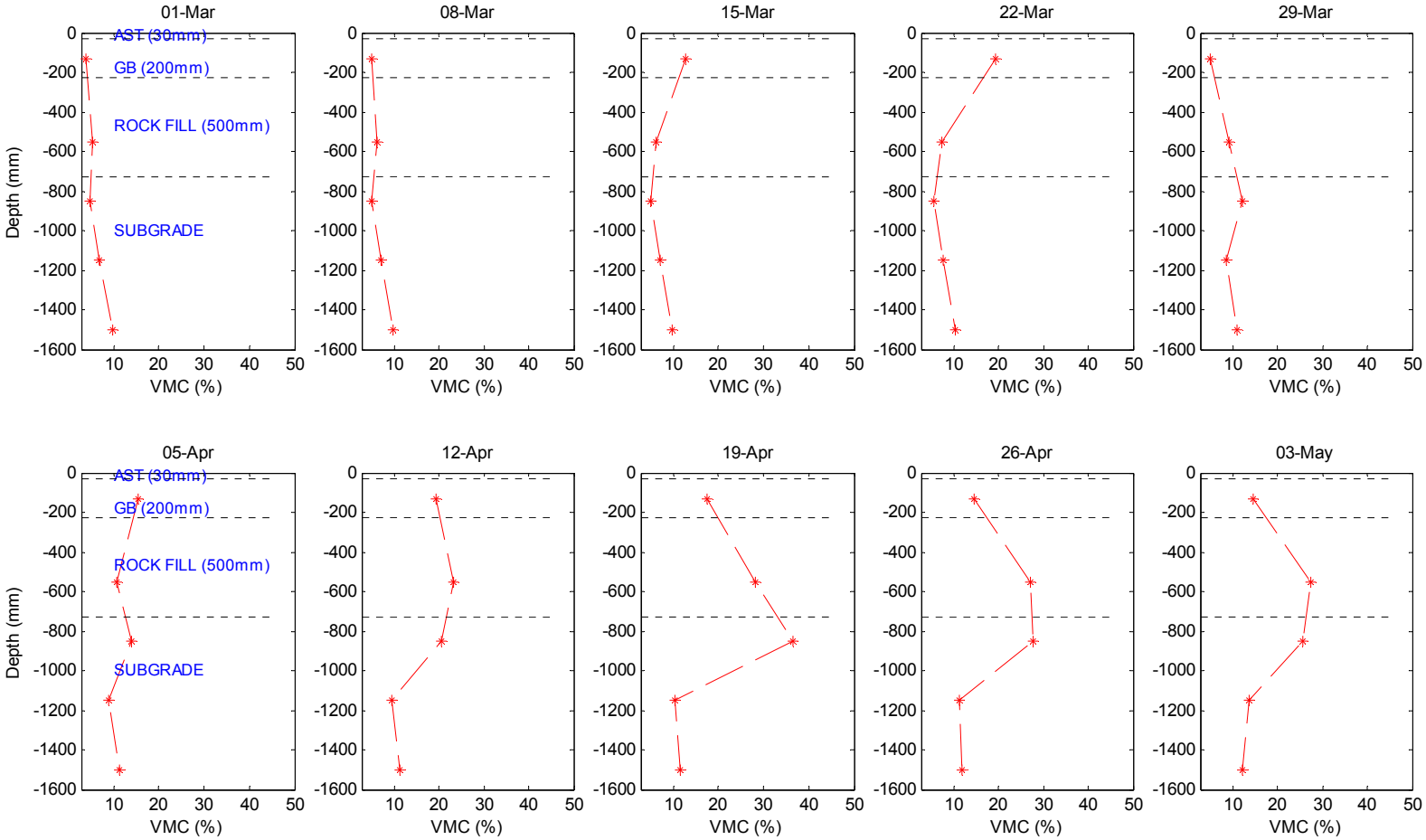

Figure 4-3 Volumetric moisture content profile at PR304

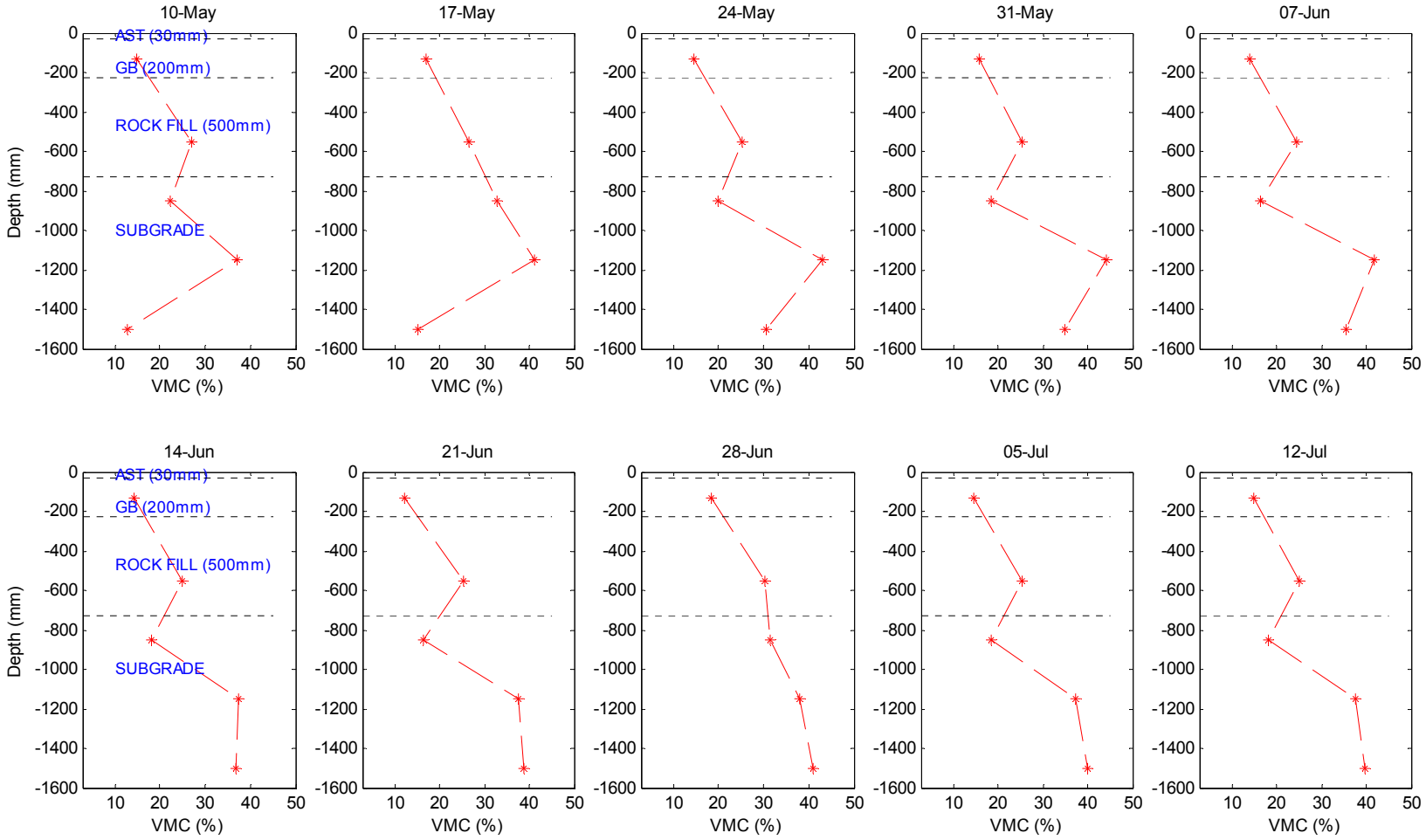

Figure 4-4 Volumetric moisture content profile at PR304 (cont'd)

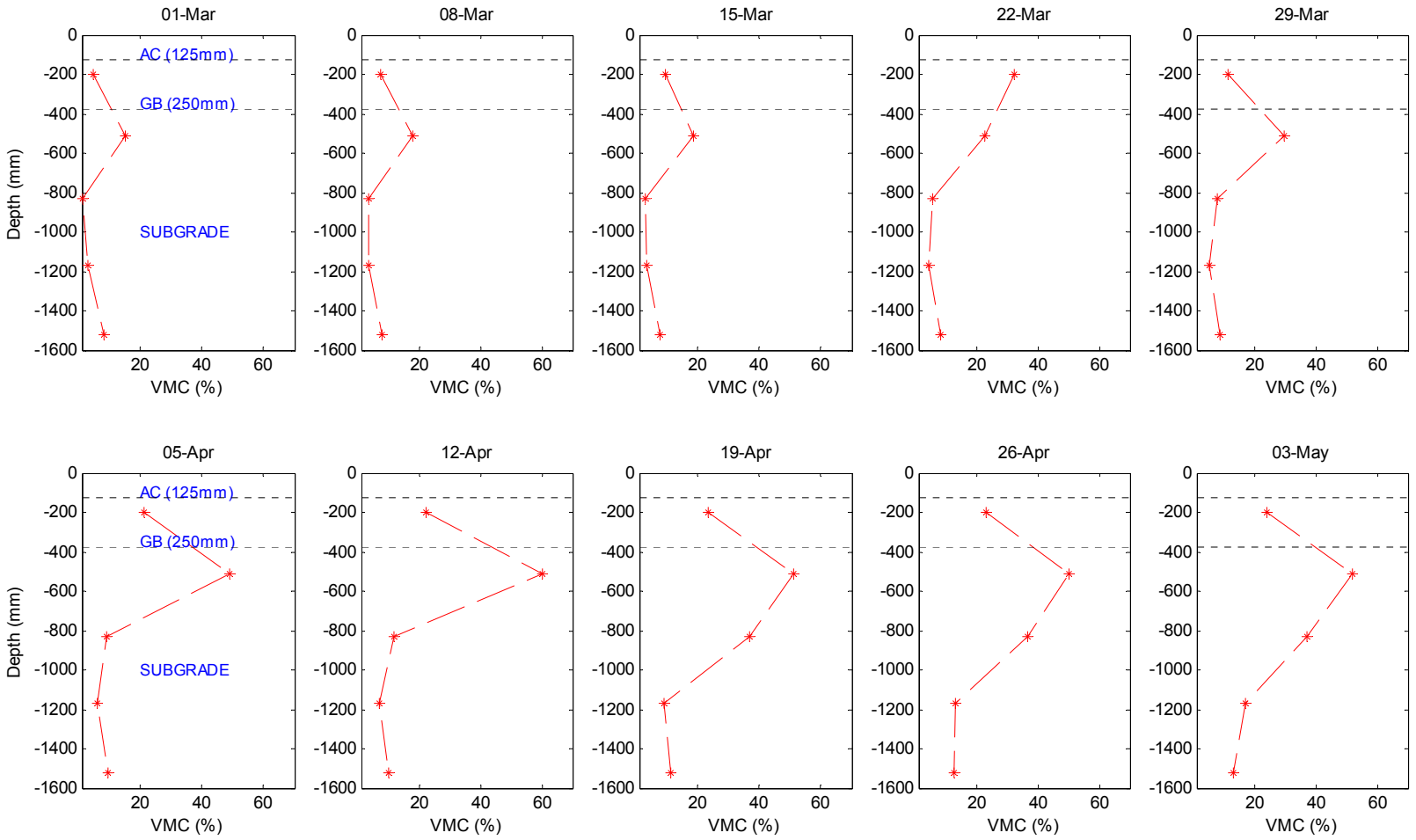

Figure 4-5 Volumetric moisture content profile at PTH11

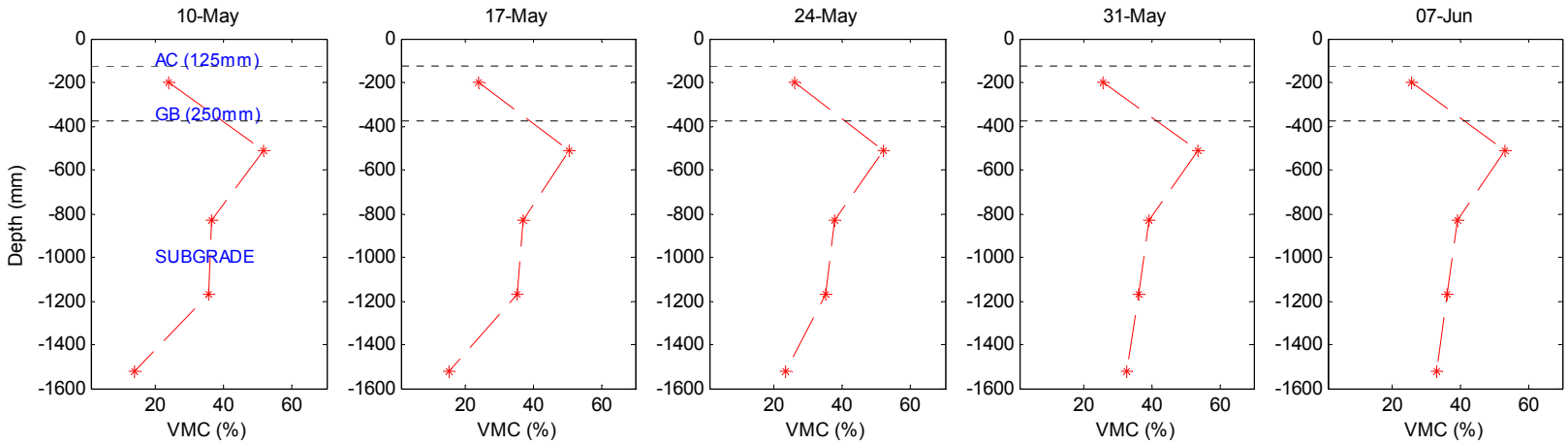

Figure 4-6 Volumetric moisture content profile at PTH11 (cont'd)

4.5 CHECK VMC WITH MEASURED THAWING DEPTH IN PAVEMENT

Figure 4-7 and Figure 4-8 show the VMC and thawing depth at both sites in March and early April, 2009. It can be seen from these two figures, when the pavements began to thaw, the volumetric moisture content at the depth of 130 mm at PR304 and 200 mm at PTH11 began to increase very fast, then the VMC in lower layer at 550 mm of PR304 and 510 mm of PTH11 began to increase gradually which indicated that the water at the up layer of pavement could not drain off efficiently because the lower layer of pavement was still frozen, which means the pavement was weak at that moment. It can be concluded that the implementation of SLR on March 23, 2009 is reasonable.

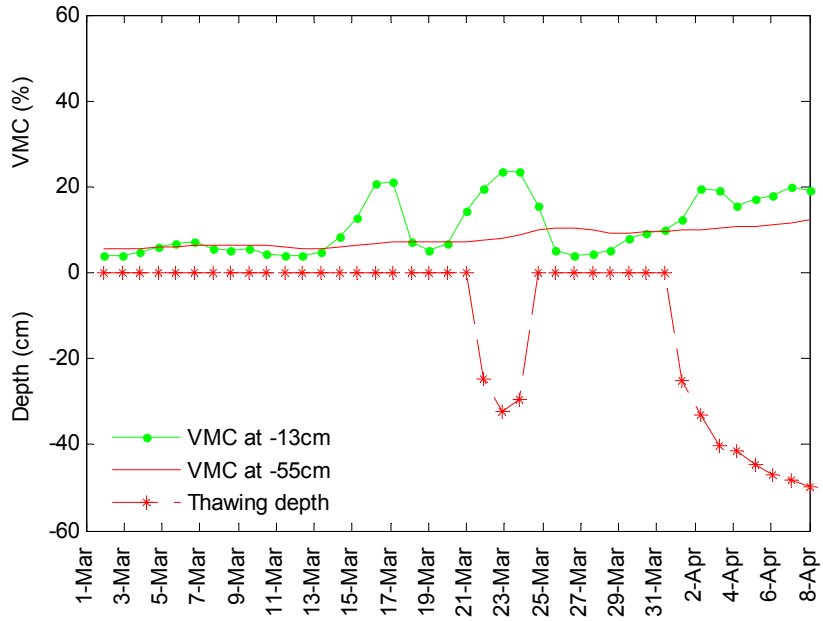

Figure 4-7 Measured volumetric moisture content and thawing depth at PR304.

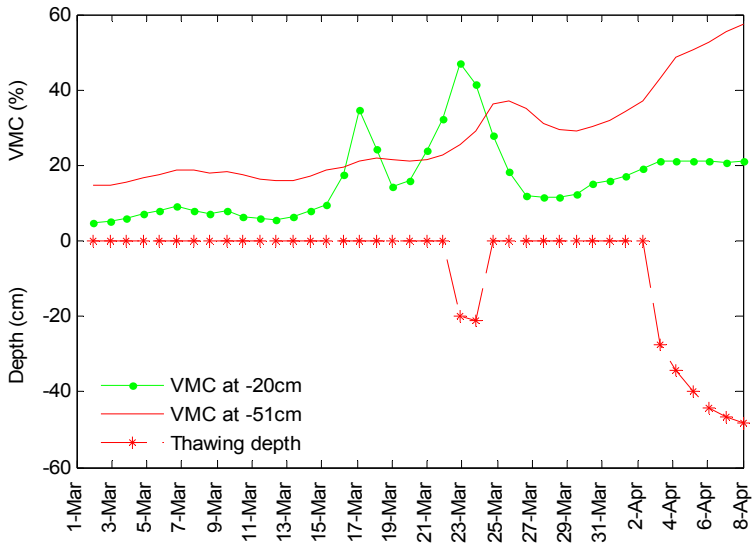

Figure 4-8 Measured volumetric moisture content and thawing depth at PTH11.

4.6 SUMMARY

Based on the VMCs at base and subgrade, the pavement can be divided into four periods:

- Form November 24, 2008 to March 14, 2009 the pavement of both PTH11 and PR304 were in the period of deep frost period.
- From March 15, 2009 to April 15, 2009 the pavements were in the period of rapid strength loss.
- From April 16, 2009 to May 8, 2009 the pavements were in the period of rapid strength recovery.
- Began on May 9, 2009 the pavements were in the period of slow strength recovery.

CHAPTER 5 TIRE PRESSURE CONTROL SYSTEM TESTS

Two series of TPCS tests were carried out at the instrumented sections at PTH11 and PR304 in spring and fall 2009, respectively.

As shown in Figure 5-1, the X direction is to the lateral side of the tire; The orthogonal coordinate system is defined as the X and Y axes are parallel to the pavement surface and the Z axis is pointed vertically from the road surface into the pavement structure.

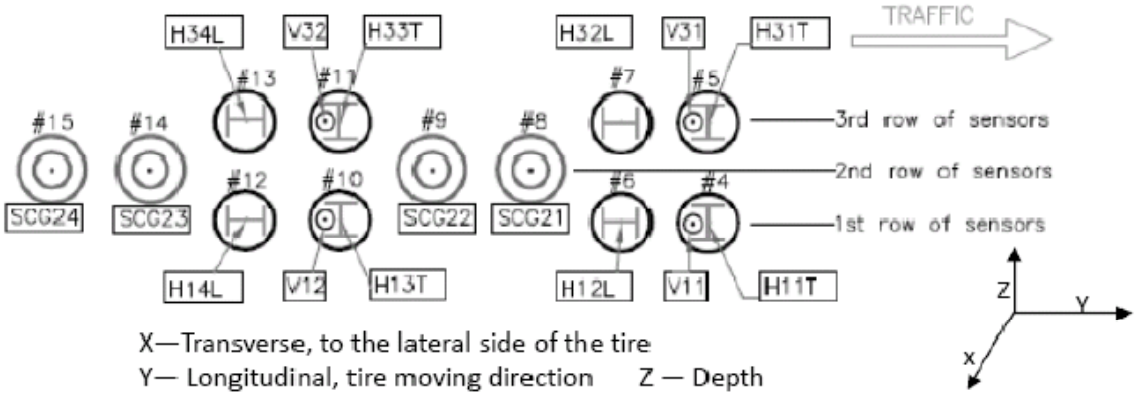

Figure 5-1 Coordinate system and strain gauges installed

5.1 TPCS TEST AND DATA ANALYSIS IN THE SPRING

5.1.1 FIELD TESTS

On May 21 and 22 TPCS tests were conducted on test site at PTH11, MB with a B-train equipped with tire pressure control system. The tests consist of three runs at each variable combination. Table 5-1 shows the test matrix which spans the practical range of main variables in this research: tire pressure from 345 kPa to 690 kPa, axle weight at A1 level 1 (A1L1) load, A1 normal (A1N) load, and Roads and Transportation Association of Canada (RTAC) normal load,

axle configuration from single axle single tire to tridem axle dual tire, and the truck speed at 20 km/h or 70 km/h. Table 5-2 shows SLR for 8-axle B-train in Manitoba.

Table 5-1 TPCSTest Matrix at PTH11

Order	Testing	Speed @20 km/h	Speed @70 km/h
1	B-train @345kPa (A1L1)	3 runs	3 runs
2	B-train @690kPa (A1L1)	3 runs	3 runs
3	B-train @345kPa(A1N)	3 runs	3 runs
4	B-train @690kPa (A1N)	3 runs	3 runs
5	B-train @345kPa (RTAC)	3 runs	3 runs
6	B-train @690kPa (RTAC)	3 runs	3 runs

Table 5-2 Spring Load Restrictions for 8-axle B-train in Manitoba

SLR rating	Tandem drive axle (kg)	Front trailer tridem axle (kg)	Rear trailer tandem axle (kg)	Gross vehicle weight(kg)
A1L1	14400	20700	14400	50850
A1N	16000	20700	16000	56500
RTAC	17000	23000	17000	62500

Notes:
Restriction Level1 is 90% of normal loads and restriction Level2 is 65% of normal loads.
Maximum steering axle mass is 5500 kg for all SLR ratings.

A video camera was set up to monitor the track of the test B-train. By reviewing the video footage of each run, the offset of each tire group can be retrieved. Table 5-3 shows wheel offsets of each tire group for tests at the load level of A1L1. Offset is defined as the distance of the centerline of outer tire to the centerline of installed sensor. Negative value means the tire tracked inside of sensor centerline. The width of tread face of test tire is 213.5 mm. It means the tire 'missed' the target sensor if the offset is greater than half the width of tread face. We focused mainly on drive axles during TPCS tests. It is considered as a good run if the offset of drive tire is less than half width of tread face.

As pointed out by Timm and Willis (2008), there are mainly four sources of variability: wheel wander, the precision of the gauge themselves, material variability, and the gauge alignment. It is impossible to eliminate completely all sources of variability when using instrumentation. Howard et al. reported at the ROADHOG project, the differences of measured strain are in the range of ±35%. (Howard et al, 2008)

Table 5-3 Wheel Offset of Each Tire Group of Test Truck at A1L1 Load

Runs	Tire pressure (kPa)	Speed (km/h)	Steering (mm)	Drive (mm)	Trailer1 (mm)	Trailer2 (mm)
1	345	20	-96.75	3.5	83.5	113.25
2	345	20	-106.75	3.5	103.5	123.25
3	345	20	-96.75	13.5	123.5	143.25
1	345	70	-86.75	23.5	113.5	133.25
2	345	70	-116.75	-26.5	83.5	103.25
3	345	70	-46.75	63.5	N/A*	N/A
1	690	20	-106.75	-16.5	103.5	123.25
2	690	20	-106.75	-16.5	103.5	123.25
3	690	20	-106.75	-16.5	73.5	93.25
1	690	70	-166.75	-76.5	33.5	73.25
2	690	70	-126.75	-26.5	73.5	103.25
3	690	70	-146.75	-36.5	63.5	83.25

*----Not available

As illustrated in Figure 5-2, tire contact pressure was captured by using Tirescan 3150 pressure mapping system. Tire and axle load were weighted right before test. Figure 5-3 shows two tire footprints for A1L1 load at tire inflation pressure of 345 kPa and 690 kPa. These footprints are the inputs of FE model.

(a) (b)

Figure 5-2 Measure tire contact pressure using Tirescan 3150 (a) and weigh tire load(b).

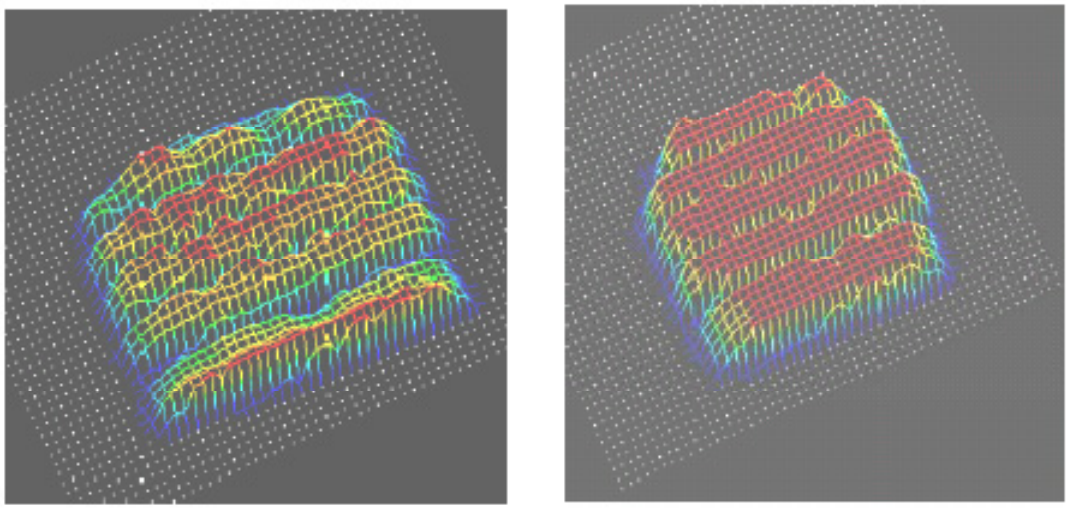

(a) (b)

Figure 5-3 Footprints for A1L1 load at tire inflation pressure of 345 kPa (a) and 690 kPa (b).

Strains for the 12 strain gauges were collected at 4,800 Hz simultaneously when the test truck passed the instrumented sections. The recorded data were then processed and converted from voltage readings to strains. An example of strain response and tire groups of the test B-train is shown in Figure 5-4. Third, the strains were divided into four groups according to tire configuration: Steering, Drive, Trailer1, and Trailer2. Finally the maximum strain for each tire

group was processed no matter which tire within each group produced the maximum strain. Although ϵ_{xx} , ϵ_{yy} , and ϵ_{zz}were all recorded during the test, focus is mainly on ϵ_{yy} in this thesis which is found the least variable during the test.

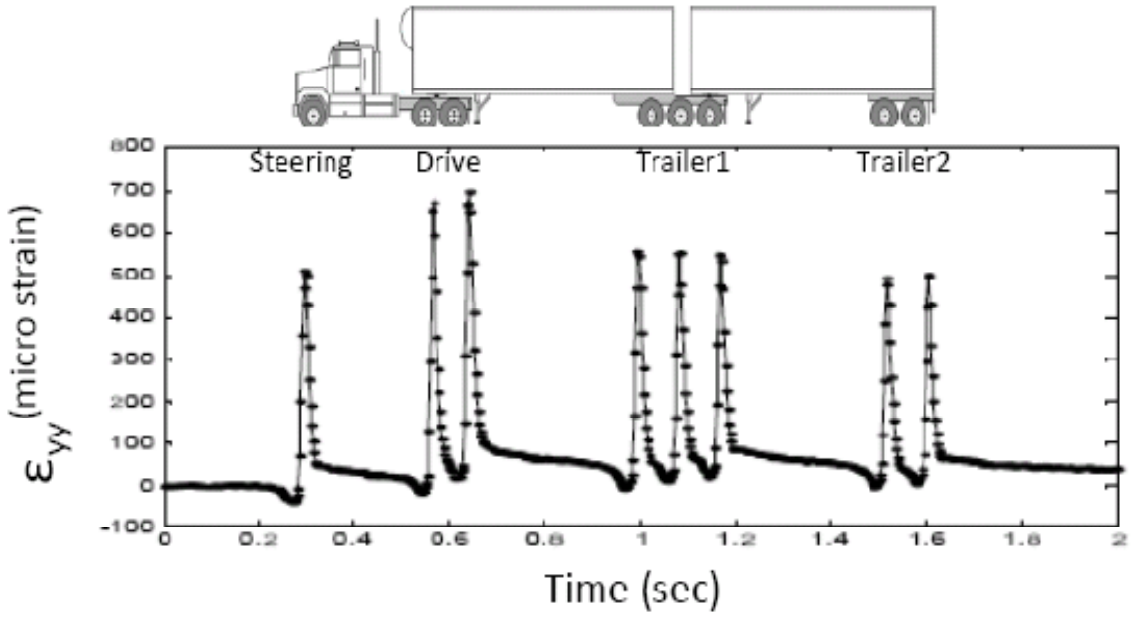

Figure 5-4 Strain response and tire groups.

5.1.2 DATA ANALYSIS FOR A1 LEVEL 1(A1L1) LOAD

Figure 5-5 shows longitudinal strain measured by H12L and H14L when a B-train passed the gauges at 20 km/h. The strains by all axles except steering axle decreased when tries' pressure deflated from 690 kPa to 345 kPa while the inflation pressure of steering tire keeps constant. For steering axle, the opposite trends were observed maybe because of load shifting (Detailed discussion is beyond this research).

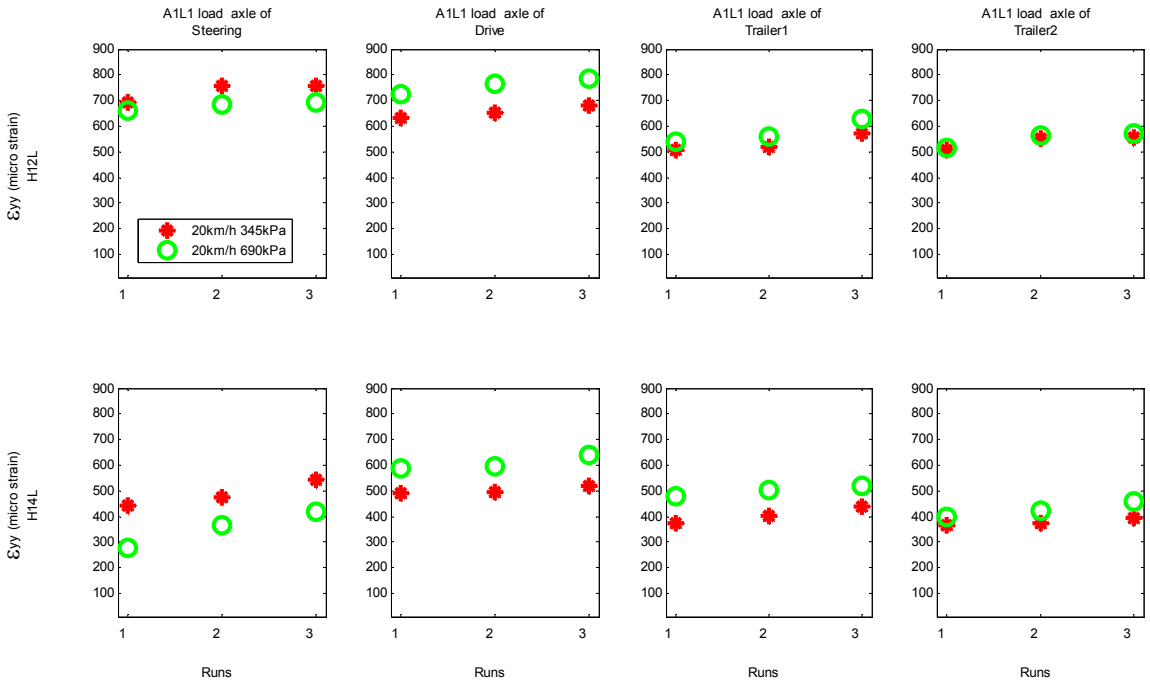

Figure 5-5 Longitudinal strain by a B-train A1L1 load 20 km/h and various tire pressures.

Table 5-4 summaries longitudinal strain difference in percentage for different group of axles when tires' pressure deflated from 690 kPa to 345 kPa with A1L1 Load at 20 km/h.

Table 5-4 Longitudinal Strain Differences (%) when Tires' Pressure Deflated from 690 kPa to 345 kPa with A1L1 Load at 20 km/h

Sensor	Runs	Steering	Drive	Trailer1	Trailer2
H12L	1	4.8	-13.0	-6.2	-1.4
	2	10.7	-14.8	-7.0	-2.3
	3	9.1	-13.3	-8.9	-3.0
	3-run average	8.2	-13.7	-7.4	-2.2
H14L	1	59.7	-16.2	-21.6	-7.6
	2	29.7	-16.9	-20.3	-10.8
	3	29.9	-19.0	-16.0	-13.4
	3-run average	39.8	-17.4	-19.3	-10.6

Note: Negative value means decrease; positive value means increase.

Figure 5-6 shows transverse strain measured by H11T and H13T when a B-train passed the gauges at 20 km/h. It indicates that the strains by all axles except steering axle decreased when

tries' inflation pressure deflated from 690 kPa to 345 kPa while the inflation pressure of steering tire keeps constant. For steering axle, the opposite trend was observed.

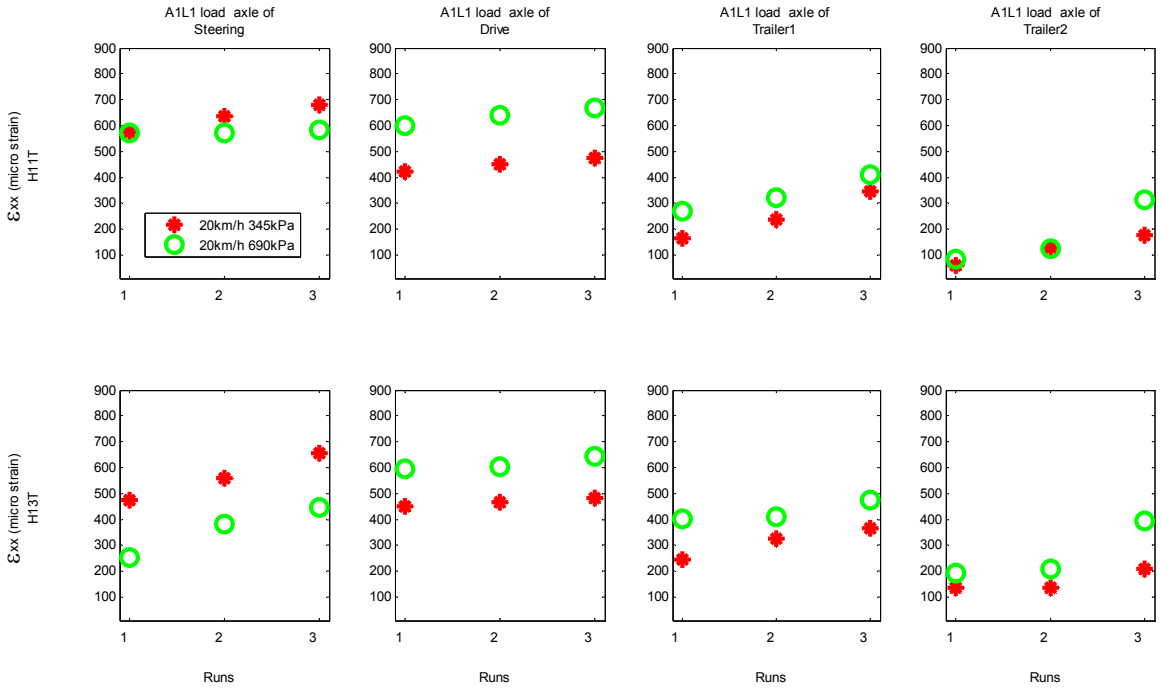

Figure 5- 6 Transverse strain by a B-train A1L1 load 20 km/h and various tire pressures.

Table 5-5 summaries the transverse strain difference in percentage for different group of axles when tires' pressure deflated from 690 kPa to 345 kPa with A1L1 Load at 20 km/h.

Table 5- 5 Transverse Strain Differences (%) when Tires' Pressure Deflated from 690 kPa to 345 kPa with A1L1 Load 20 km/h

Sensor	Runs	Steering	Drive	Trailer1	Trailer2
H11T	1	0.6	-29.6	-39.6	-28.2
	2	11.1	-29.5	-27.1	4.1
	3	16.8	-28.9	-15.7	-43.2
	3-run average	9.5	-29.3	-27.5	-22.4
H13T	1	87.2	-24.2	-38.4	-29.9
	2	45.4	-22.8	-20.9	-35.0
	3	47.3	-25.3	-22.8	-47.0
	3-run average	60.0	-24.1	-27.3	-37.3

Figure 5-7 shows ϵ_{yy} measured by H12L and H14L when a B-train passed the gauges at 70 km/h. It indicates that the strains by all axles except steering axle decreased when tries' inflation pressure deflated from 690 kPa to 345 kPa while the inflation pressure of steering tire keeps constant. For steering axle, the opposite trend was observed.

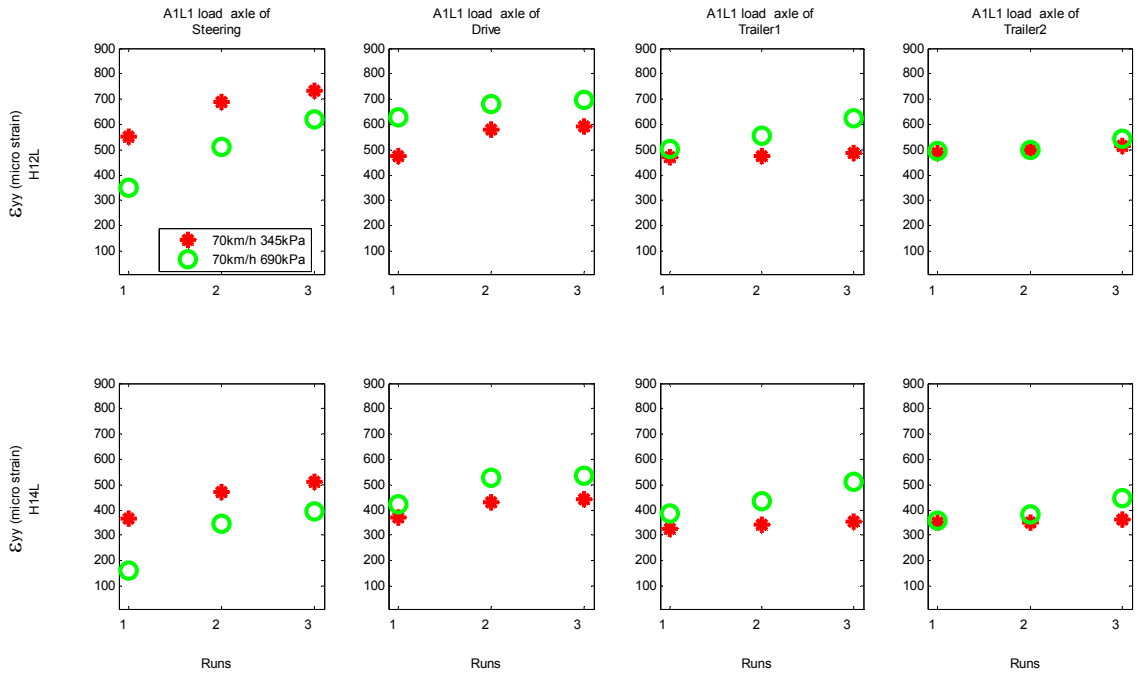

Figure 5-7 Longitudinal strain by a B-train A1L1 load 70 km/h and various tire pressures.

Table 5-6 shows the longitudinal strain difference in percentage for different group of axles when tires' pressure deflated from 690 kPa to 345 kPa with A1L1 Load at 70 km/h.

Table 5-6 Longitudinal Strain Differences (%) when Tires' Pressure Deflated from 690 kPa to 345 kPa with A1L1 Load at 70 km/h

Sensor	Runs	Steering	Drive	Trailer1	Trailer2
H12L	1	56.5	-24.5	-7.1	-2.1
	2	34.8	-14.8	-14.1	-0.5
	3	18.3	-15.3	-21.8	-5.3
	3-run average	36.5	-18.2	-14.3	-2.6
H14L	1	127.7	-12.4	-15.6	-1.9
	2	35.8	-18.2	-20.8	-7.9
	3	29.7	-17.0	-30.8	-18.9
	3-run average	64.4	-15.9	-22.4	-9.6

Figure 5-8 shows ϵ_{xx} measured by H11T and H13T when a B-train passed the gauges at 70 km/h. It indicates that the strains by all axles except steering axle decreased when tries' inflation pressure deflated from 690 kPa to 345 kPa while the inflation pressure of steering tire keeps constant. For steering axle, the opposite trend was observed.

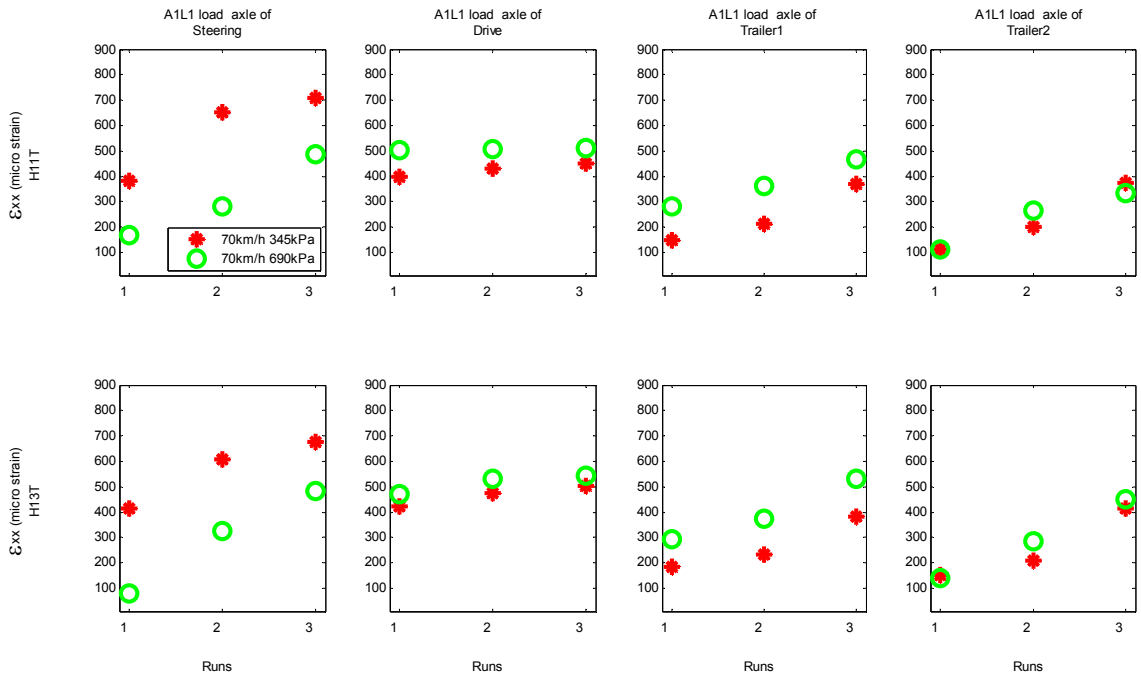

Figure 5-8 Transverse strain by a B-train A1L1 load 70 km/h and various tire pressures.

Table 5-7 summaries transverse strain difference in percentage for different group of axles when tires' pressure deflated from 690 kPa to 345 kPa with A1L1 Load at 70 km/h.

Table 5-7 Transverse Strain Differences (%) when Tires' Pressure Deflated from 690 kPa to 345 kPa with A1L1 Load 70 km/h

Sensor	Runs	Steering	Drive	Trailer1	Trailer2
H11T	1	129.1	-21.1	-47.0	-0.8
	2	131.3	-14.9	-40.5	-24.1
	3	45.0	-11.9	-21.2	11.6
	3-run average	101.8	-16.0	-36.2	-4.5
H13T	1	424.4	-10.0	-37.0	8.7
	2	85.9	-10.7	-37.7	-27.2
	3	40.1	-7.0	-28.3	-8.3
	3-run average	183.5	-9.2	-34.3	-8.9

Figure 5-9 compares the longitudinal strain by a B-train with A1L1 load at tire pressure of 345 kPa when the speeds increased from 20 km/h to 70 km/h. In all cases, the higher the truck speed, the lower the longitudinal strain was observed.

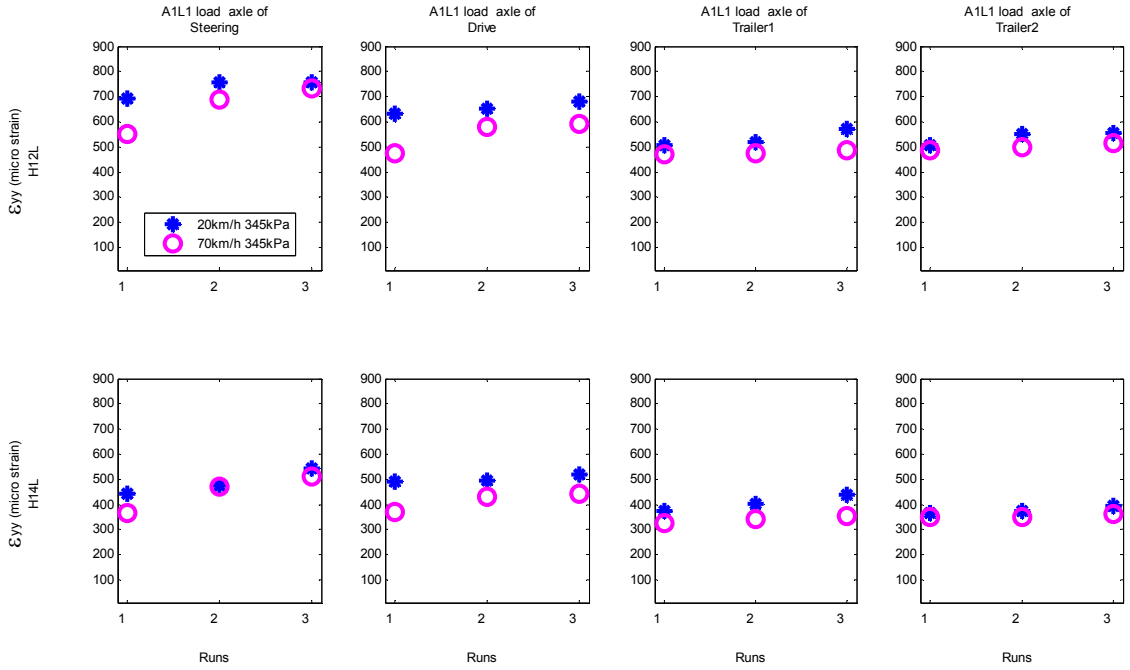

Figure 5-9 Longitudinal strain by a B-train A1L1 load 345 kPa and various speeds.

Table 5-8 shows longitudinal strain difference in percentage for different axles when truck's speed increased from 20 km/h to 70 km/h at tire pressure of 345 kPa with A1L1 Load.

Table 5-8 Longitudinal Strain Differences (%) from 20 km/h to 70 km/h

Sensor	Runs	Steering	Drive	Trailer1	Trailer2
H12L	1	-20.6	-24.8	-7.4	-4.3
	2	-8.9	-11.1	-8.5	-9.5
	3	-2.8	-13.2	-14.5	-7.4
	3-run average	-10.8	-16.3	-10.1	-7.1
H14L	1	-17.1	-24.2	-13.4	-4.5
	2	-1.0	-12.6	-14.7	-6.3
	3	-6.1	-14.3	-19.3	-8.3
	3-run average	-8.1	-17.0	-15.8	-6.4

Figure 5-10 compares the transverse strain by a B-train with A1L1 load at tire pressure of 345 kPa when the speeds increased from 20 km/h to 70 km/h.

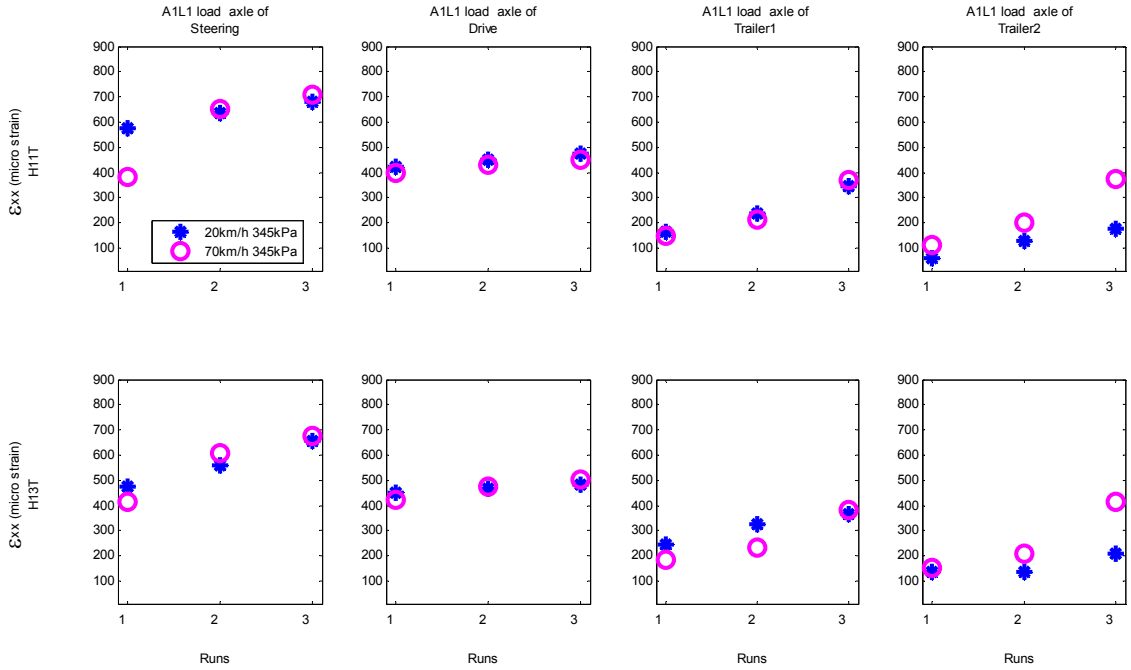

Figure 5-10 Transverse strain by a B-train A1L1 load 345 kPa and various speeds.

Table 5-9 shows the transverse strain difference in percentage for different group of axles when truck's speed increased from 20 km/h to 70 km/h at tire pressure of 345 kPa with A1L1 Load.

Table 5-9 Transverse Strain Differences (%) from 20 km/h to 70 km/h

Sensor	Runs	Steering	Drive	Trailer1	Trailer2
H11T	1	-33.5	-6.1	-8.3	83.2
	2	2.2	-4.3	-8.8	54.1
	3	4.3	-5.1	6.6	109.3
	3-run average	-9.0	-5.1	-3.5	82.2
H13T	1	-13.1	-6.5	-24.8	12.7
	2	9.1	1.9	-28.5	53.1
	3	2.8	4.4	3.8	97.8
	3-run average	-0.4	-0.1	-16.5	54.5

Figure 5-11 compares the longitudinal strain by a B-train with A1L1 load at tire pressure of 690 kPa when the speeds increased from 20 km/h to 70 km/h.

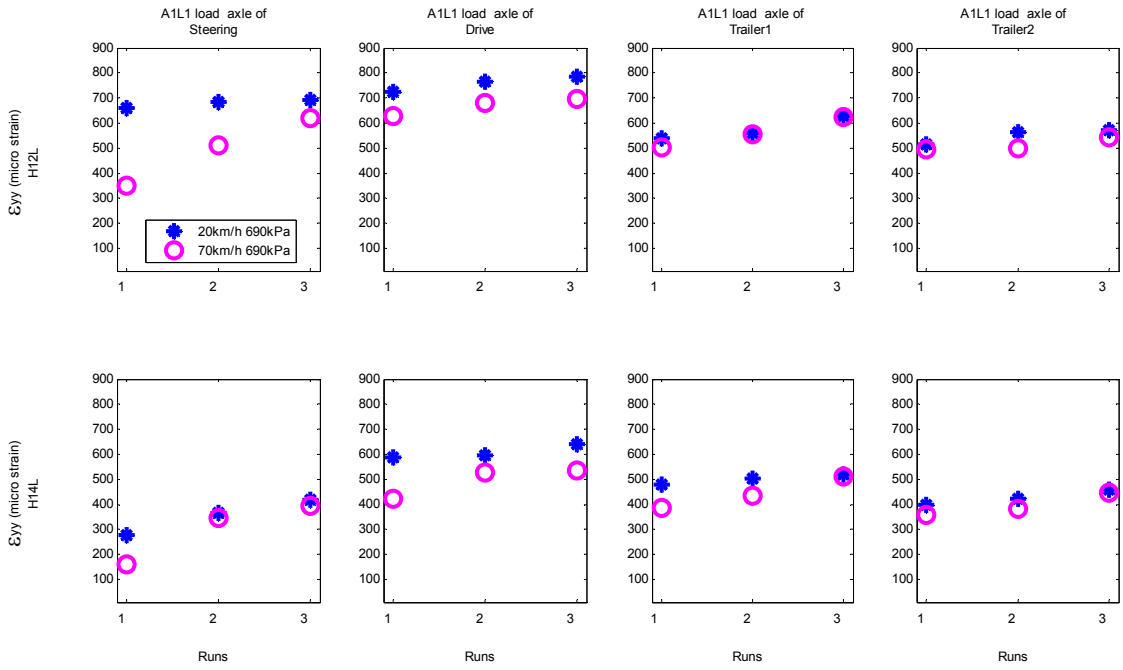

Figure 5-11 Longitudinal strain by a B-train A1L1 load 690 kPa and various speeds.

Table 5-10 summaries the longitudinal strain difference in percentage for different group of axles when truck's speed increased from 20 km/h to 70 km/h at tire pressure of 690 kPa with A1L1 Load. In all cases, the measured longitudinal strain decreased when the truck speed increased from 20 km/h to 70 km/h.

Table 5-10 Longitudinal Strain Differences (%) when Truck's Speed Increased from 20 km/h to 70 km/h at Tire Pressure of 690 kPa with A1L1 Load

Sensor	Runs	Steering	Drive	Trailer1	Trailer2
H12L	1	-46.8	-13.3	-6.6	-3.6
	2	-25.2	-11.0	-0.8	-11.2
	3	-10.3	-11.1	-0.4	-5.2
	3-run average	-27.4	-11.8	-2.6	-6.6
H14L	1	-41.8	-27.6	-19.7	-10.1
	2	-5.4	-11.1	-14.1	-9.2
	3	-6.0	-16.4	-2.0	-2.1
	3-run average	-17.8	-18.4	-11.9	-7.1

Figure 5-12 compares the transverse strain by a B-train with A1L1 load at tire pressure of 690 kPa when the speed increased from 20 km/h to 70 km/h.

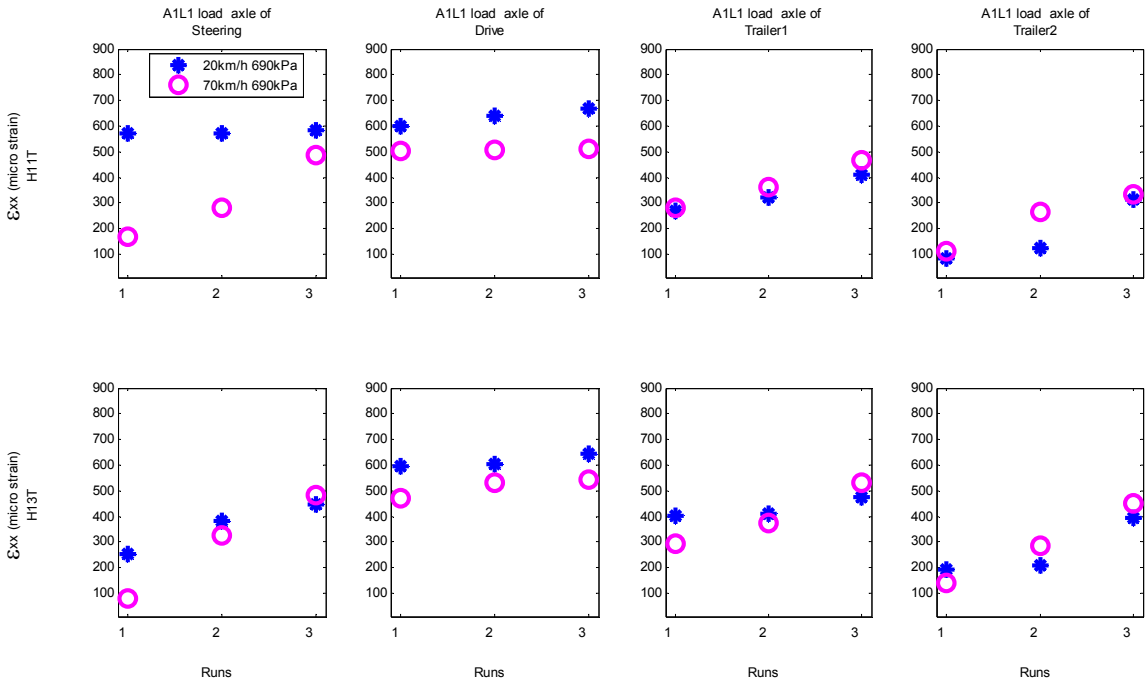

Figure 5-12 Transverse strain by a B-train A1L1 load 690 kPa and various speeds.

Table 5-11 summaries the transverse strain difference in percentage for different group of axles when truck's speed increased from 20 km/h to 70 km/h at tire pressure of 690 kPa with A1L1 Load. In 11 out of 12 cases for steering and drive axles, the measured transverse strain decreased when truck speed increased from 20 km/h to 70 km/h. For the trailer1 and trailer2 axles, the trend is different.

Table 5-11 Transverse Strain Differences (%) when Truck's Speed Increased from 20 km/h to 70 km/h at Tire Pressure of 690 kPa with A1L1 Load

Sensor	Runs	Steering	Drive	Trailer1	Trailer2
H11T	1	-70.8	-16.2	4.5	32.6
	2	-50.9	-20.7	11.7	111.4
	3	-16.0	-23.4	13.9	6.6
	3-run average	-45.9	-20.1	10.0	50.2
H13T	1	-69.0	-21.3	-26.5	-27.4
	2	-14.7	-11.9	-9.2	36.6
	3	8.1	-16.2	11.7	14.3
	3-run average	-25.2	-16.4	-8.0	7.8

5.1.3 EXAMPLES FOR A1 NORMAL (A1N) AND RTAC LOAD

By analyzing the data due to load levels of A1N and RTAC, similar trends were found. Figure 5-13 and Figure 5-14 are examples for measured longitudinal strains with the loads of A1N and RTAC, respectively. For RTAC load, the truck was unable to be speeded up to 70 km/h during test. So the maximum test speed of 65 km/h was used for RTAC load.

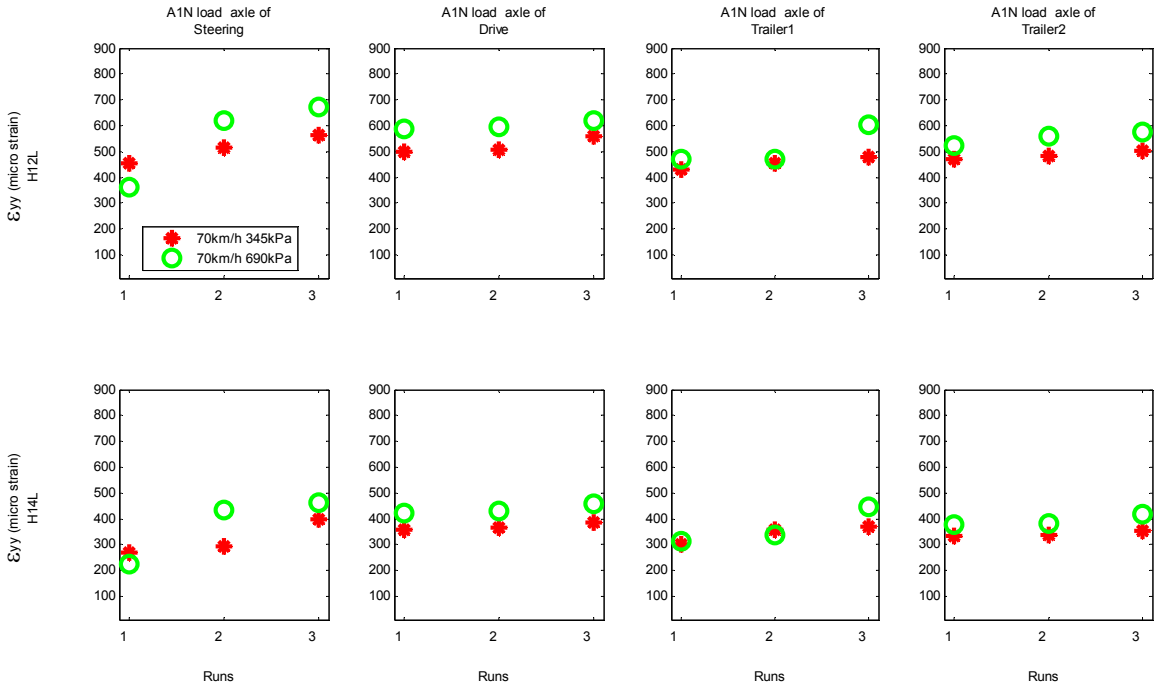

Figure 5-13 Longitudinal strain by a B-train A1N load 70 km/h and various tire pressures.

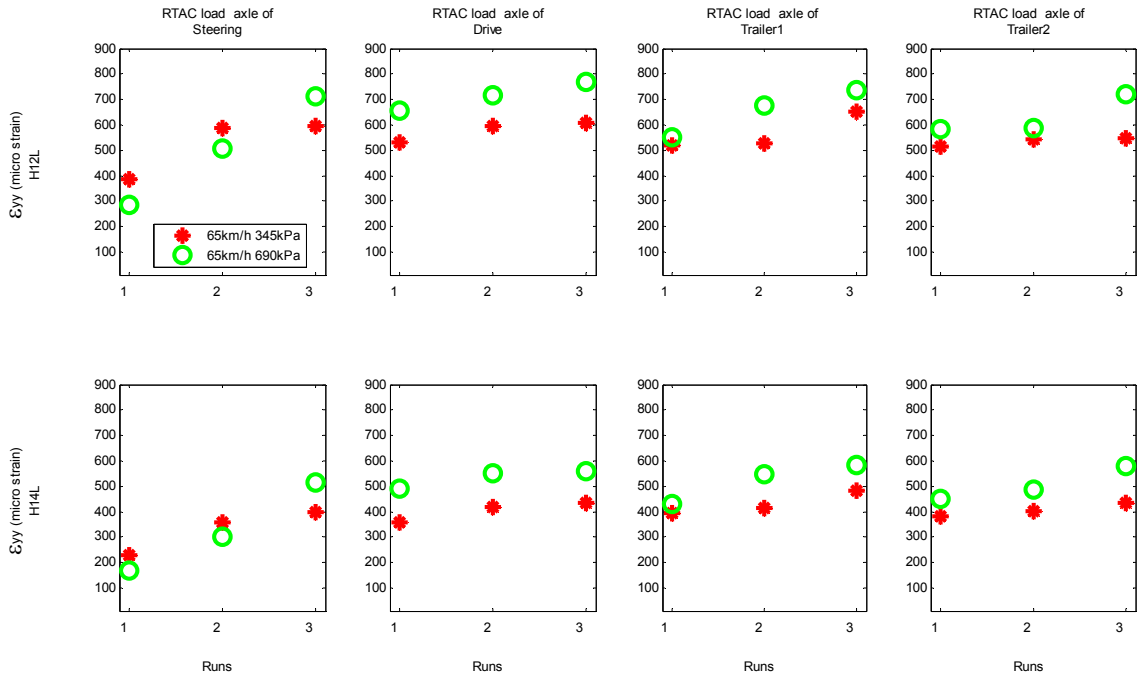

Figure 5-14 Longitudinal strain by a B-train RTAC load 65 km/h and various tire pressures.

5.1.4 COMPARING THE STRAINS FOR THREE LOAD LEVELS

Figure 5-15 through Figure 5-18 compare the measured longitudinal strains at different configurations of load levels, truck speeds, and tire pressures. As can be seen from these figures, the maximum strains are produced by either the steering axles or the drive axles which depends on the offsets of the wheel. In all cases, RATC load generated the maximum recorded longitudinal strains. But, the measured strains under A1N load were, in most cases, less than those under A1L1 load, which is contradictory to theoretical analysis since A1N load is heavier than A1L1 load. By referring to the pavement temperature, it is clear that the pavement temperature was higher when the tests with A1L1 load were carrying out than with A1N load, meaning that the pavement was weaker when the tests with A1N load was carrying out.

Table 5-12 shows the average air temperature and pavement temperature at the depth of 200 mm which is the shallowest possible pavement temperature during test period for different load levels. Figure 5-19 shows pavement temperature at the depth of 200 mm and air temperature every two hours from mid night of May 21, 2009 to the mid night of May 22, 2009. The relation of the pavement strength with pavement temperature is not discussed in this thesis.

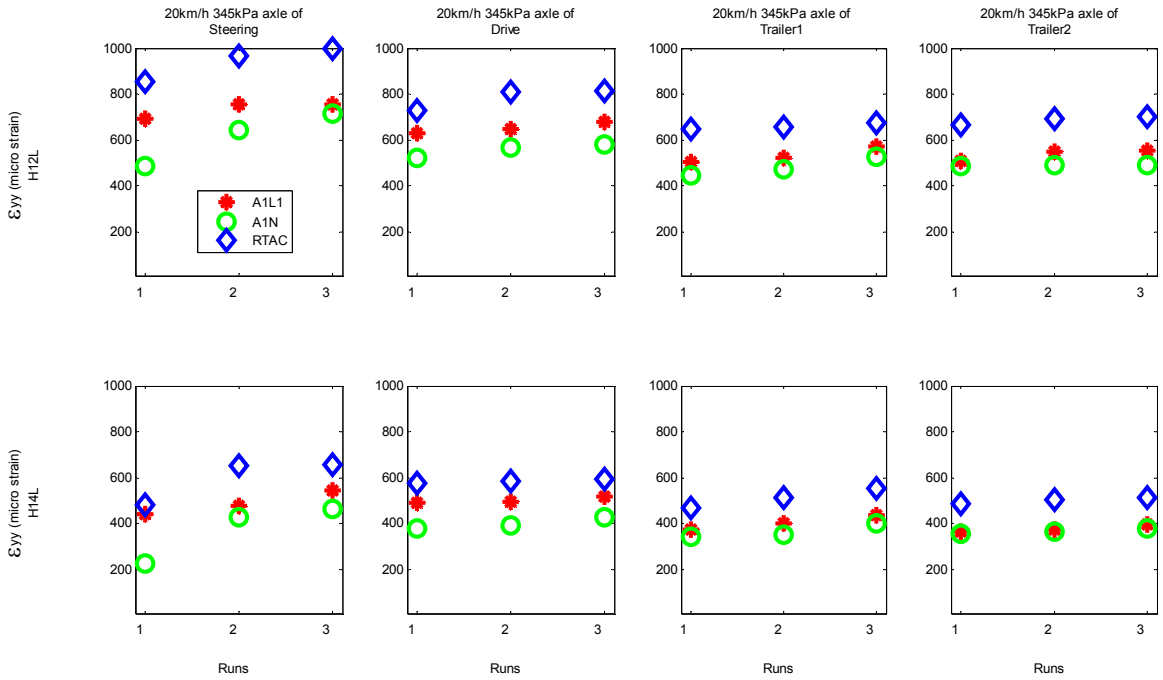

Figure 5-15 Comparing measured longitudinal strain for various loads at 20 km/h 345 kPa.

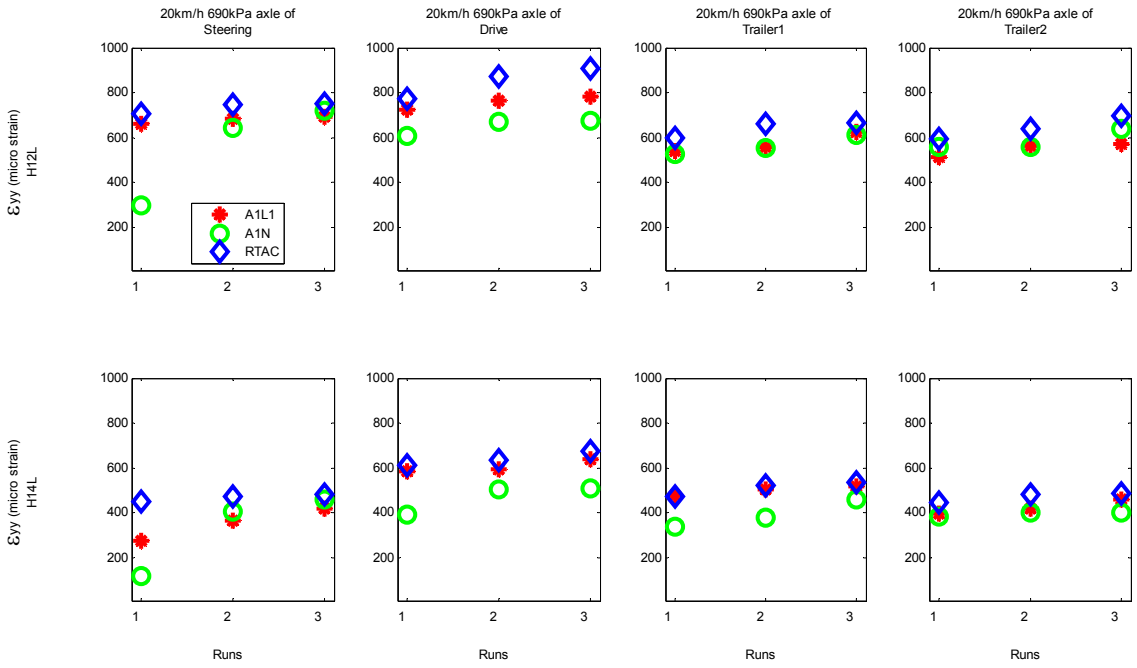

Figure 5-16 Comparing measured longitudinal strain for various loads at 20 km/h 690 kPa.

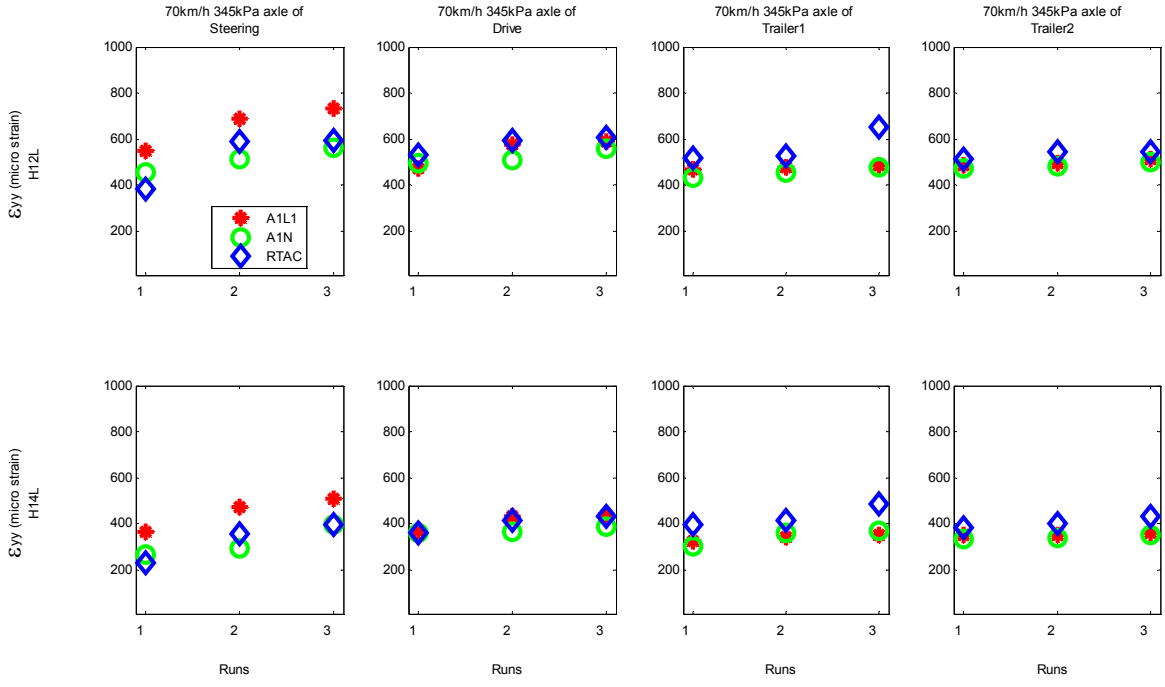

Figure 5-17 Comparing measured longitudinal strain for various loads at 70 km/h 345 kPa.

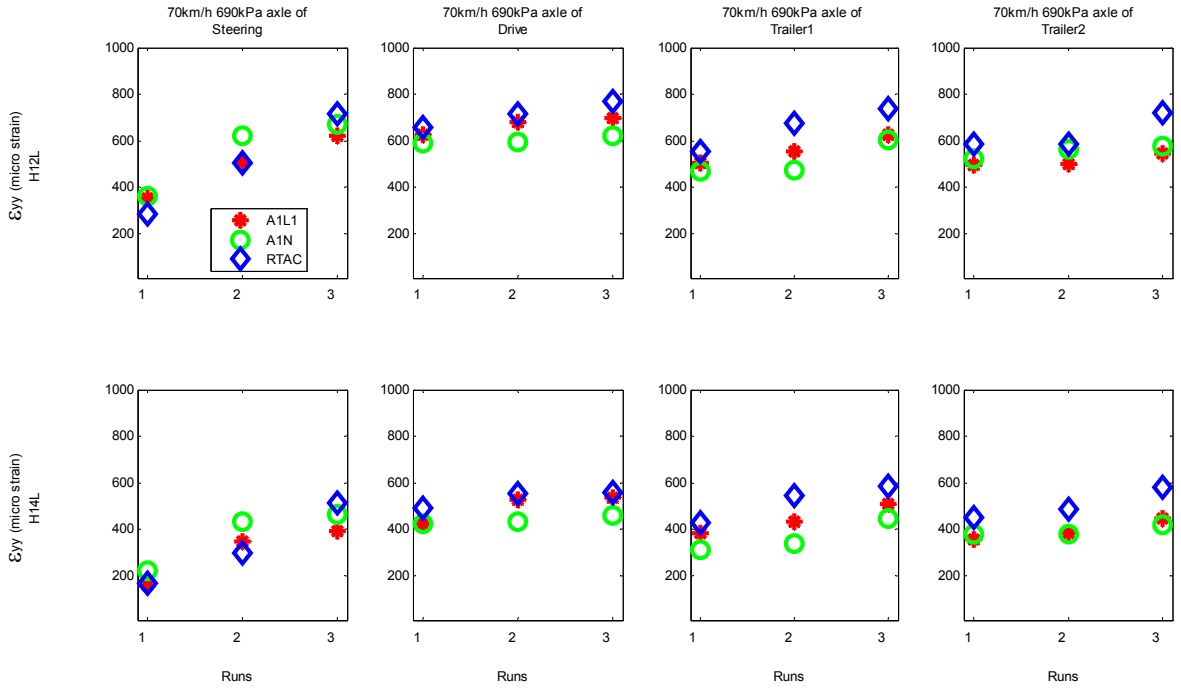

Figure 5-18 Comparing measured longitudinal strain for various loads at 70 km/h 690 kPa.

Table 5-12 Average Pavement and Air Temperature during Test Period

Load level	Test date	Test time	Pavement Temperature (°C) at depth of 200 mm	Air Temperature (°C)
A1N	5/21/09	11:17 am--1:11 pm	8.97	13.2
RTAC	5/21/09	3:54 pm--6:48 pm	15.12	7.27
A1L1	5/22/09	8:40 am--10:27 am	10.62	11.15

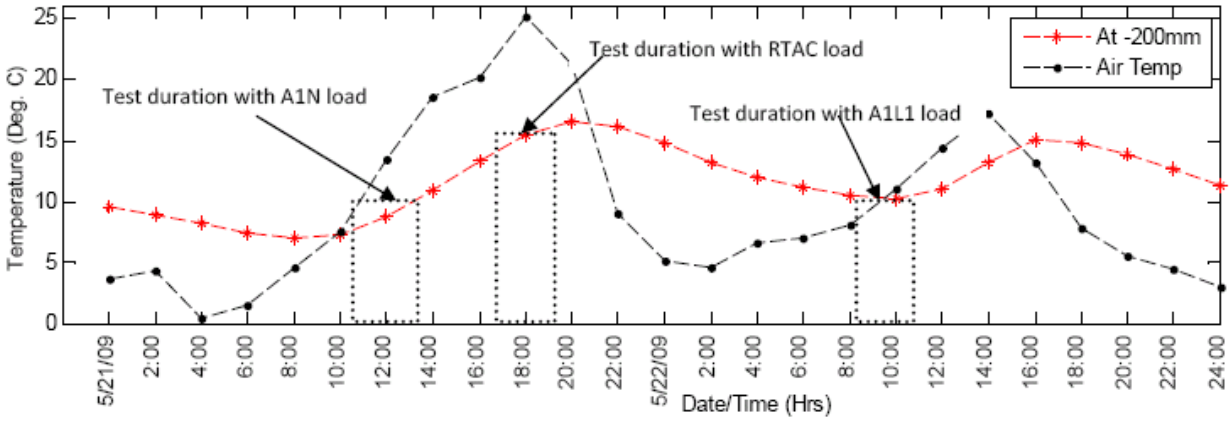

Figure 5-19 Pavement and air temperatures during test period.

5.2 TPCS TEST AND DATA ANALYSIS IN THE FALL

5.2.1 FIELD TESTS

In September, 2009 CTI tests were conducted on test site of PTH11, MB with a B-train equipped with tire pressure control system. The tests consist of six runs at each variable combination; tire pressure at 345 kPa, 518 kPa, and 690 kPa, axle weight at A1 level1 (A1L1), A1 Normal (A1N), and Roads and Transportation Association of Canada (RTAC) normal load, axle configuration from single axle single tire to tridem axle dual tire, and the truck speed at 20 km/h. The main goal of the TPCS in the fall is to find the difference of the pavement reaction between normal conditions in fall and weaken conditions during spring thaw period. The data will also be used to validate the finite element model of the pavement. Figure 5-20 shows the measured longitudinal strains by two strain gauges, H12L and H14L under a B-train with A1L1 load at speed of 20 km/h with various tire pressures. The tire pressure of steering axle was never change during the tests. For steering axle, as can be seen from Figure 5-20, no constant difference was recorded by the two strain gauges when other tire pressure was reduced from 690 kPa to 518 kPa then to 345 kPa. For the drive axle, a very clear trend was recorded when tire pressure was changed for all runs except the first run at pressure of 690 kPa. By checking video footage, the wheel offset of first run is the biggest at 166.0 mm. (The other offsets are: 76.0, 146.0, 146.0, 136.0, and 146.0 mm)

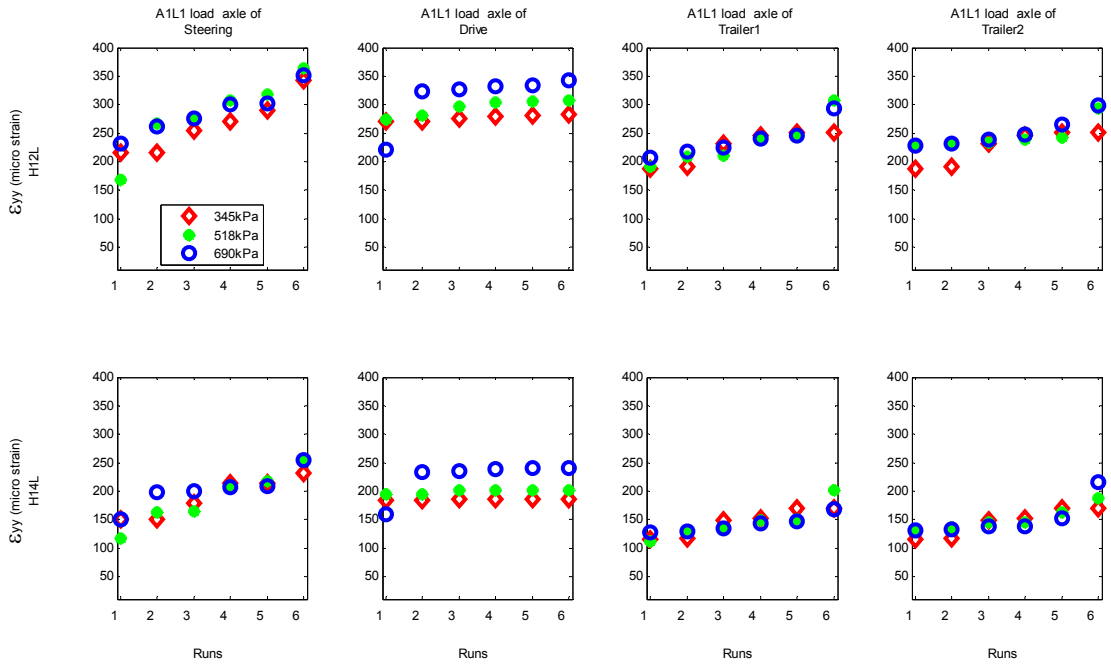

Figure 5-20 Longitudinal strain by B-train A1L1 load 20 km/h and various tire pressures.

Table 5-13 summaries the difference in percentage for longitudinal strain measured by strain gauges of H12L and H14L for different group of axles when tires' pressure deflated from 518 kPa to 345 kPa with A1L1 Load at 20 km/h.

Table 5-13 Longitudinal Strain Differences (%) when Tires' Pressure Deflated from 518 kPa to 345 kPa A1L1 Load 20 km/h

Sensor	Runs	Steering	Drive	Trailer1	Trailer2
H12L	1	28.5	-1.3	-1.8	-18.8
	2	-19.1	-3.7	-8.7	-17.2
	3	-7.2	-7.2	9.3	-1.5
	4	-12.2	-8.0	2.8	2.8
	5	-9.3	-8.2	2.4	3.9
	6	-5.6	-7.8	-18.0	-14.2
	6-run average	-4.2	-6.0	-2.3	-7.5
H14L	1	29.1	-5.0	2.5	-14.1
	2	-8.1	-5.6	-9.1	-13.5
	3	7.9	-8.1	10.1	2.7
	4	2.0	-7.8	2.8	4.9
	5	-1.9	-7.8	13.7	4.3
	6	-9.6	-7.9	-15.1	-8.7
	6-run average	3.2	-7.0	0.8	-4.1

Table 5-14 summaries the difference in percentage for longitudinal strain measured by strain gauges of H12L and H14L for different group of axles when tires' pressure deflated from 690 kPa to 518 kPa with A1L1 Load at 20 km/h.

Table 5-14 Longitudinal Strain Differences (%) when Tires' Pressure Deflated from 690 kPa to 518 kPa A1L1 Load 20 km/h

Sensor	Runs	Steering	Drive	Trailer1	Trailer2
H12L	1	-27.6	N/A	-7.8	0.7
	2	2.2	-12.9	-4.0	-0.6
	3	-0.6	-8.8	-5.8	-2.0
	4	2.4	-8.4	0.0	-3.3
	5	5.6	-8.4	0.1	-8.8
	6	3.4	-10.5	4.3	-1.8
	6-run average	-2.4	-9.8	-2.2	-2.6
H14L	1	-22.4	N/A	-12.3	1.0
	2	-17.1	-16.3	0.4	1.5
	3	-17.4	-14.7	0.9	5.1
	4	1.0	-15.5	3.2	5.3
	5	4.6	-16.2	2.3	7.8
	6	1.1	-16.0	19.8	-13.5
	6-run average	-8.4	-15.7	2.4	1.2

Table 5-15 summaries the difference in percentage for measured longitudinal strain for various axles when tires' pressure deflated from 690 kPa to 345 kPa with A1L1 Load at 20 km/h.

Table 5-15 Longitudinal Strain Differences (%) when Tires' Pressure Deflated from 690 kPa to 345 kPa A1L1 Load 20 km/h

Sensor	Runs	Steering	Drive	Trailer1	Trailer2
H12L	1	-7.0	N/A	-9.4	-18.2
	2	-17.3	-16.1	-12.3	-17.7
	3	-7.8	-15.4	3.0	-3.4
	4	-10.1	-15.7	2.7	-0.5
	5	-4.1	-15.9	2.6	-5.2
	6	-2.4	-17.4	-14.5	-15.8
	6-run average	-8.1	-16.1	-4.7	-10.2
H14L	1	0.1	N/A	-10.1	-13.2
	2	-23.8	-21.0	-8.7	-12.2
	3	-10.9	-21.6	11.1	7.9
	4	3.0	-22.1	6.0	10.4
	5	2.6	-22.8	16.4	12.5
	6	-8.6	-22.7	1.6	-21.0
	6-run average	-6.3	-22.0	2.7	-2.6

Figure 5-21 shows the measured longitudinal strains by two strain gauges, H12L and H14L, under a B-train with A1N load at speed of 20 km/h with various tire pressures. Table 5-16, Table 5-17, and Table 5-18 summarize the differences in percentage for longitudinal strain measured by strain gauges of H12L and H14L for different group of axles when tires' pressure deflated from 518 kPa to 345 kPa, 690 kPa to 518 kPa , and 690 kPa to 345 kPa with A1N Load at 20 km/h. The focus of the test is the drive axles for all the runs. For drive axle, when tire pressure deflated from 690 kPa to 345 kPa, roughly a linear trend of longitudinal strain was recorded.

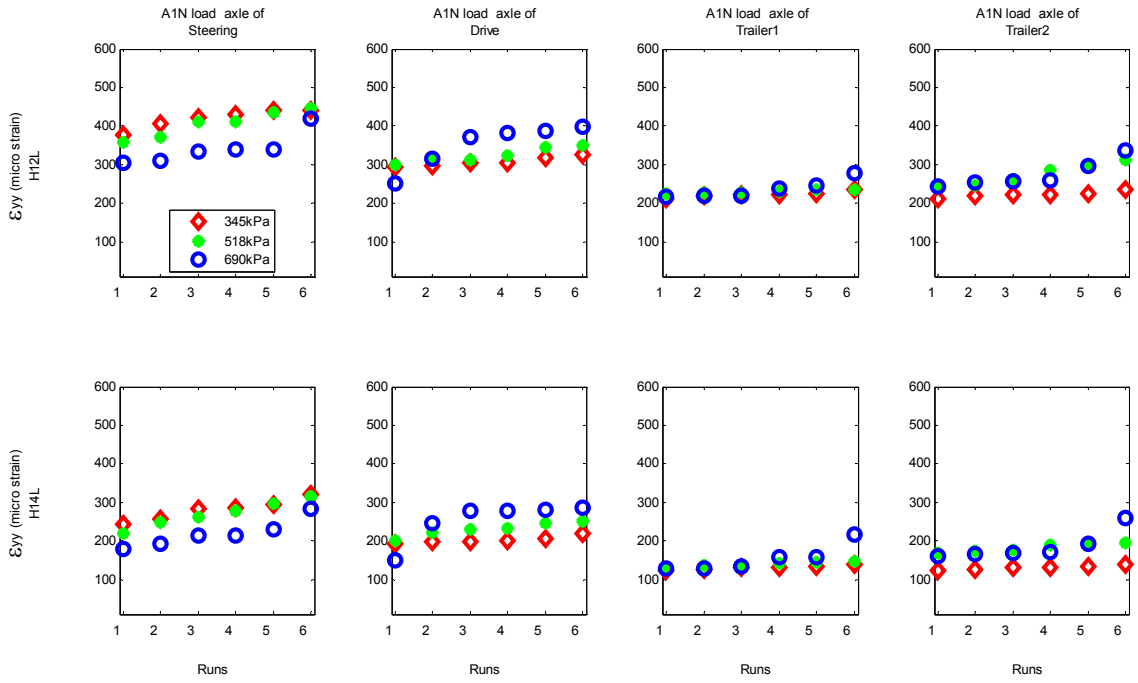

Figure 5-21 Longitudinal strain by B-train A1N load 20 km/h and various tire pressures.

Table 5-16 Longitudinal Strain Differences (%) when Tires' Pressure Deflated from 518 kPa to 345 kPa with A1N Load 20 km/h

Sensor	Runs	Steering	Drive	Trailer1	Trailer2
H12L	1	4.9	-2.1	-6.0	-12.8
	2	9.4	-5.4	-3.4	-11.0
	3	3.1	-3.3	-3.0	-15.2
	4	4.0	-6.0	-2.5	-22.1
	5	1.3	-7.2	-4.7	-25.1
	6	-1.3	-7.1	0.0	-24.4
	6-run average	3.6	-5.2	-3.3	-18.4
H14L	1	9.8	-4.2	-5.0	-26.8
	2	3.4	-11.5	-7.8	-28.0
	3	8.0	-13.3	-5.1	-25.8
	4	2.4	-14.1	-7.2	-30.2
	5	-0.9	-15.5	-8.6	-30.2
	6	1.3	-12.7	-5.6	-28.5
	6-run average	4.0	-11.9	-6.6	-28.3

Table 5-17 Longitudinal Strain Differences (%) when Tires' Pressure Deflated from 690 kPa to 518 kPa with A1N Load 20 km/h

Sensor	Runs	Steering	Drive	Trailer1	Trailer2
H12L	1	17.3	N/A	4.2	0.3
	2	19.6	-0.5	3.6	-3.1
	3	22.5	-15.4	4.1	2.1
	4	21.2	-15.5	-3.4	10.9
	5	27.6	-11.0	-4.3	0.8
	6	6.5	-11.7	-15.6	-7.4
	6-run average	19.1	-10.8	-1.9	0.6
H14L	1	23.7	N/A	0.8	4.1
	2	29.0	-9.2	4.8	5.3
	3	22.5	-17.3	2.9	5.0
	4	29.5	-16.0	-9.3	11.1
	5	29.4	-12.3	-8.6	-1.6
	6	11.6	-11.6	-32.1	-25.2
	6-run average	24.3	-13.3	-6.9	-0.2

Table 5-18 Longitudinal Strain Differences (%) when Tires' Pressure Deflated from 690 kPa to 345 kPa with A1N Load 20 km/h

Sensor	Runs	Steering	Drive	Trailer1	Trailer2
H12L	1	23.0	N/A	-2.1	-12.5
	2	30.9	-5.9	0.0	-13.8
	3	26.3	-18.3	1.0	-13.5
	4	26.2	-20.5	-5.8	-13.6
	5	29.3	-17.4	-8.8	-24.5
	6	5.1	-18.0	-15.6	-30.0
	6-run average	23.5	-16.0	-5.2	-18.0
H14L	1	35.9	N/A	-4.2	-23.8
	2	33.3	-19.7	-3.4	-24.2
	3	32.2	-28.3	-2.4	-22.1
	4	32.6	-27.8	-15.9	-22.5
	5	28.2	-25.8	-16.5	-31.3
	6	13.0	-22.8	-35.9	-46.5
	6-run average	29.2	-24.9	-13.0	-28.4

Figure 5-22 shows the measured longitudinal strains by two strain gauges, H12L and H14L, under a B-train with RTAC load at speed of 20 km/h with various tire pressures. Table 5-19, Table 5-20, and Table 5-21 show the difference in percentage for longitudinal strain measured by strain gauges of H12L and H14L for different group of axles when tires' pressure deflated from 690 kPa to 518 kPa , 518 kPa to 345 kPa, and 690 kPa to 345 kPa with RTAC Load at 20 km/h. For drive axle, when tire pressure deflated from 690 kPa to 518kPa, then to 345 kPa, almost a linear trend of longitudinal strain was recorded.

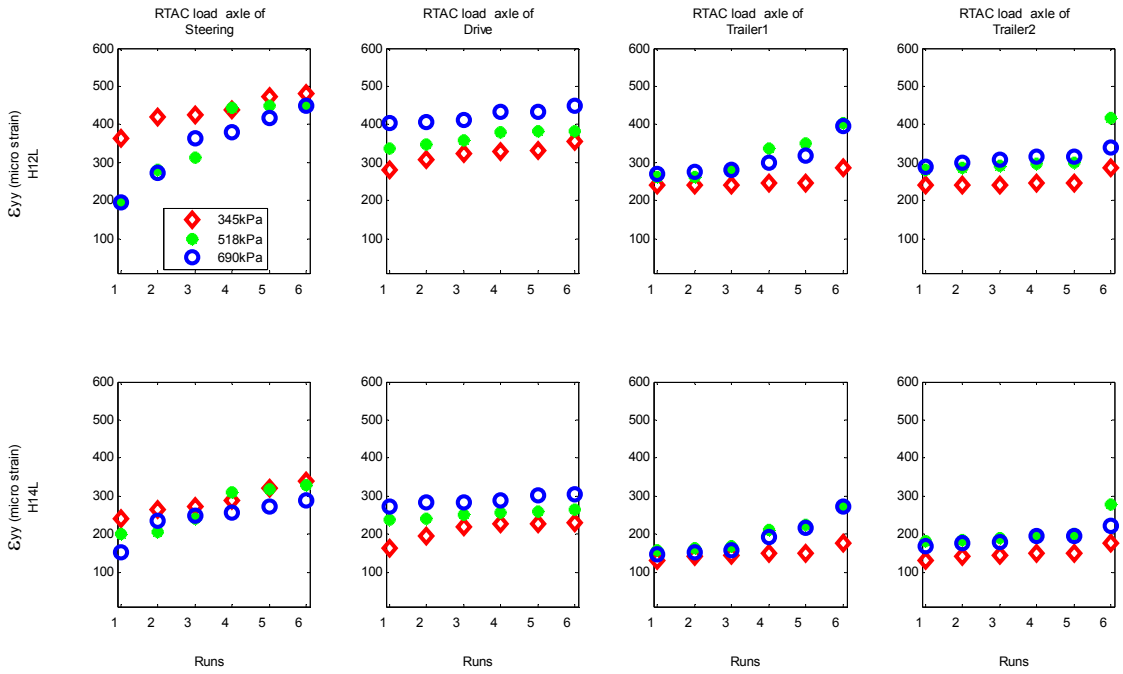

Figure 5-22 Longitudinal strain by B-train RTAC load 20 km/h and various tire pressures.

Table 5-19 Longitudinal Strain Differences (%) when Tires' Pressure Deflated from 690 kPa to 518 kPa RTAC Load 20 km/h

Sensor	Runs	Steering	Drive	Trailer1	Trailer2
H12L	1	-0.3	-16.7	-3.1	-2.9
	2	2.8	-14.6	-5.0	-4.1
	3	-14.5	-13.0	0.9	-4.9
	4	16.4	-11.9	12.3	-5.6
	5	7.5	-12.0	10.3	-5.5
	6	0.9	-15.3	1.9	23.1
	6-run average	2.2	-13.9	2.9	0.0
H14L	1	30.7	-12.9	7.4	8.4
	2	-13.0	-14.7	6.1	4.1
	3	-3.0	-11.0	7.7	5.1
	4	20.9	-11.1	10.4	-0.4
	5	16.2	-14.3	3.8	1.5
	6	13.3	-12.9	0.8	24.7
	6-run average	10.9	-12.8	6.0	7.2

Table 5- 20 Longitudinal Strain Differences (%) when Tires' Pressure Deflated from 518 kPa to 345 kPa RTAC Load 20 km/h

Sensor	Runs	Steering	Drive	Trailer1	Trailer2
H12L	1	87.2	-16.1	-8.2	-14.4
	2	49.1	-11.3	-8.4	-16.4
	3	36.2	-9.6	-14.2	-17.2
	4	-0.9	-13.6	-27.1	-17.3
	5	5.5	-13.4	-29.6	-17.3
	6	6.4	-6.7	-29.1	-31.6
	6-run average	30.6	-11.8	-19.4	-19.0
H14L	1	20.6	-31.0	-17.0	-28.1
	2	28.7	-18.5	-13.0	-22.9
	3	12.7	-12.7	-14.3	-23.3
	4	-6.4	-11.9	-29.3	-23.0
	5	0.7	-12.7	-33.2	-24.8
	6	3.8	-12.7	-35.4	-36.3
	6-run average	10.0	-16.6	-23.7	-26.4

Table 5-21 Longitudinal Strain Differences (%) when Tires' Pressure Deflated from 690 kPa to 345 kPa RTAC Load 20 km/h

Sensor	Runs	Steering	Drive	Trailer1	Trailer2
H12L	1	86.7	-30.1	-11.1	-16.8
	2	53.2	-24.3	-13.0	-19.8
	3	16.5	-21.4	-13.5	-21.3
	4	15.4	-23.9	-18.1	-22.0
	5	13.5	-23.8	-22.4	-21.9
	6	7.4	-21.0	-27.8	-15.7
	6-run average	32.1	-24.1	-17.6	-19.6
H14L	1	57.7	-39.9	-10.8	-22.0
	2	12.0	-30.5	-7.7	-19.7
	3	9.3	-22.3	-7.7	-19.4
	4	13.2	-21.7	-22.0	-23.2
	5	17.0	-25.1	-30.7	-23.7
	6	17.6	-24.0	-34.9	-20.6
	6-run average	21.1	-27.3	-19.0	-21.4

5.2.2 COMPARING MEASURED STRAINS IN THE FALL FOR THREE LOAD LEVELS

Figure 5-23 through Figure 5-25 compare the measured longitudinal strains at different configurations of load levels, truck speeds, and tire pressures. As can be seen from these figures, the maximum strains were produced by steering axle, drive axle, or sometimes tridem (trailer1) axle which depends on the offsets of the wheel. In all cases, RATC load generated the maximum recorded longitudinal strains.

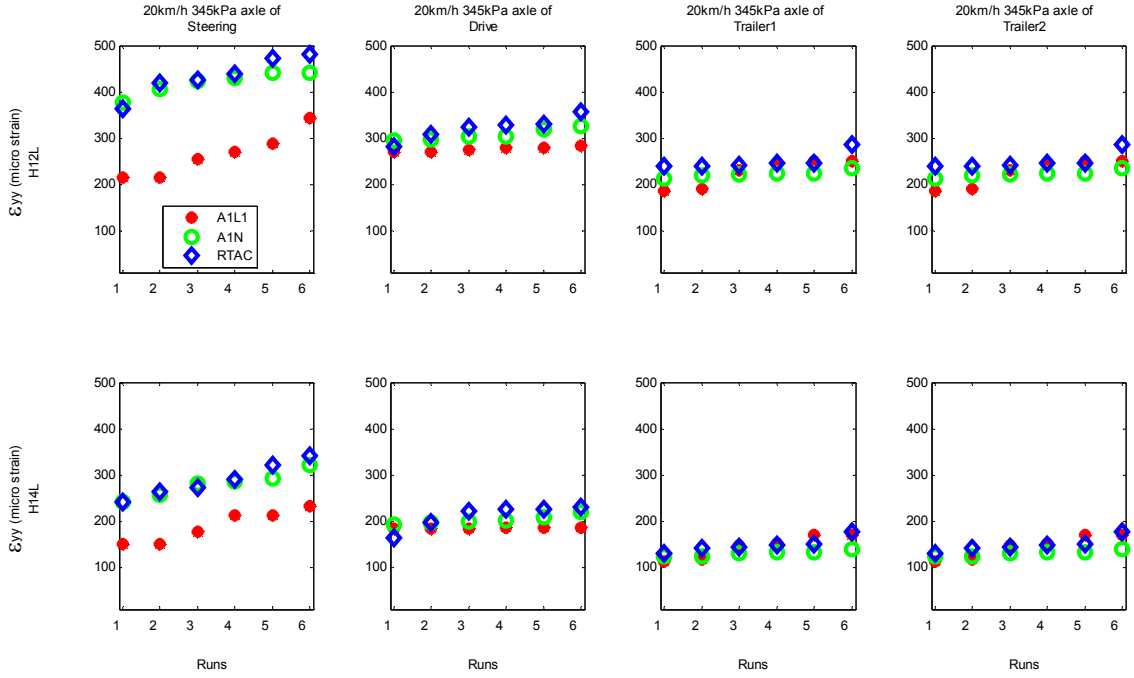

Figure 5-23 Measured longitudinal strain in September for various loads at 20 km/h 345 kPa.

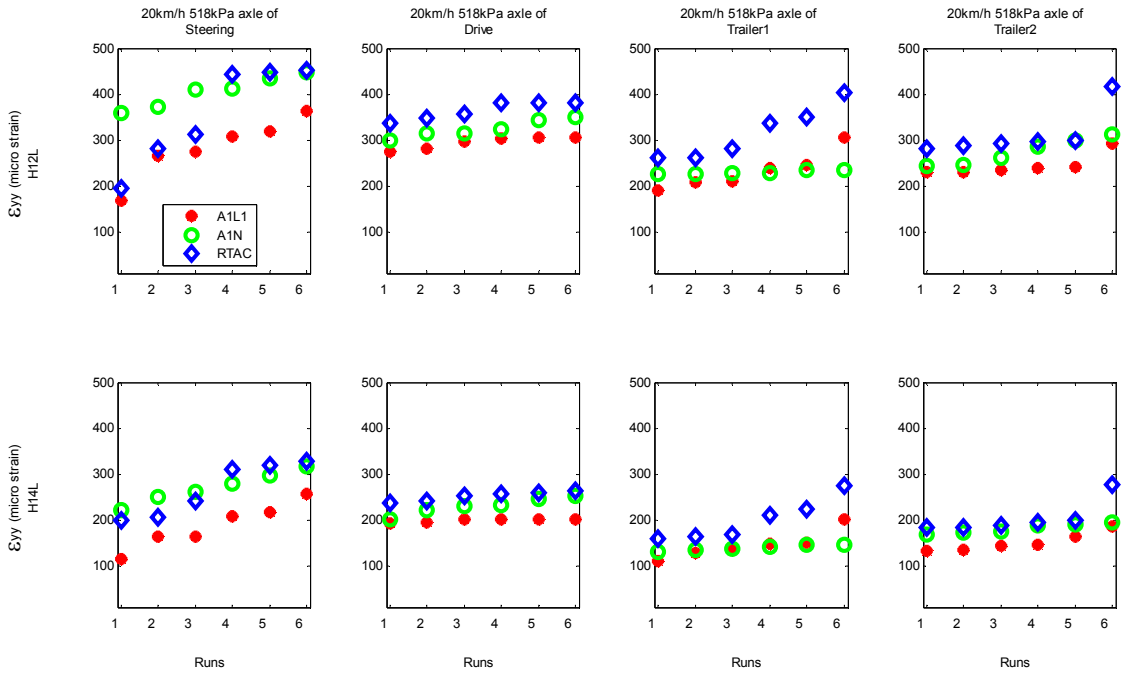

Figure 5-24 Measured longitudinal strain in September for various loads at 20 km/h 518 kPa.

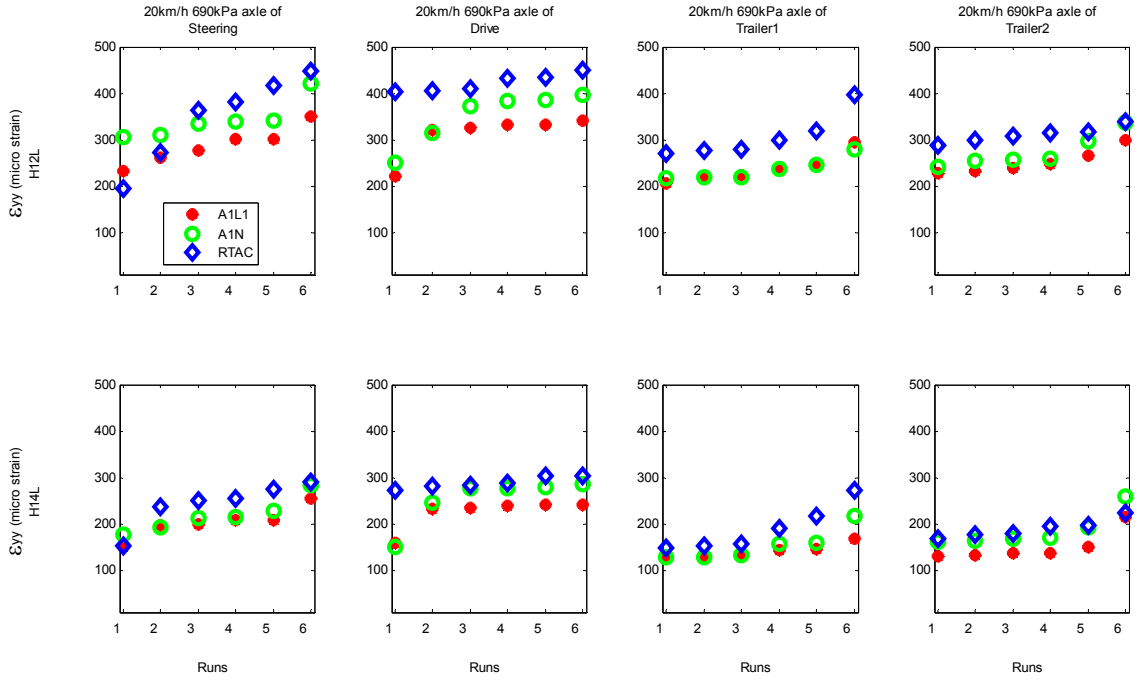

Figure 5-25 Measured longitudinal strain in September for various loads at 20 km/h 690 kPa.

Table 5-22 shows the average air temperature and pavement temperature at the depth of 200 mm during test period for different load levels. Figure 5-26 shows pavement temperature at the depth of 200 mm and air temperature every two hours from mid night of September 22, 2009 to the mid night of September 23, 2009.

Table 5-22 Average Pavement and Air Temperature during Test Period in September

Load level	Test date	Test time	Pavement Temperature (°C) at depth of 200 mm	Air Temperature (°C)
A1L1	9/22/09	9:20 am--10:40 am	17.92	13.32
A1N	9/22/09	1:10 pm--2:30 pm	19.62	18.32
RTAC	9/23/09	9:40 am—11:40 am	16.88	16.04

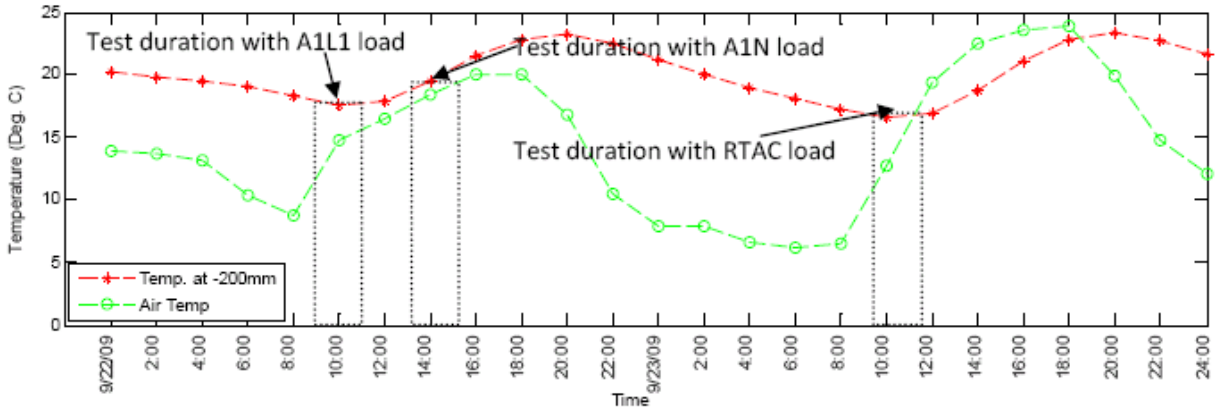

Figure 5-26 Pavement and air temperatures during test period in September.

5.2.3 COMPARING MEASURED STRAIN IN THE SPRING WITH IN THE FALL

Figure 5-27 through Figure 5-32 compare longitudinal strain in May to the strain in September 2009 for three load levels at tire pressure of 345 kPa and 690 kPa when the test B-train passed the strain gauges of H12L and H14L at the speed of 20 km/h. It is clear that the measured longitudinal strain in September is much lower than corresponding values in May for all axles

for all different configuration of load and tire pressure, which indicates that the pavement in September is much stronger than in May during spring thaw period. Table 5-23 and Table 5-24 summarize the percentage decreased of measured longitudinal stain in September than in May by strain gauges of H12L and H14L, respectively. It can be seen from these two Tables, the measured longitudinal strain decreased from 40% to 70% in most cases for different configurations of tire pressure, load levels, and axle groups.

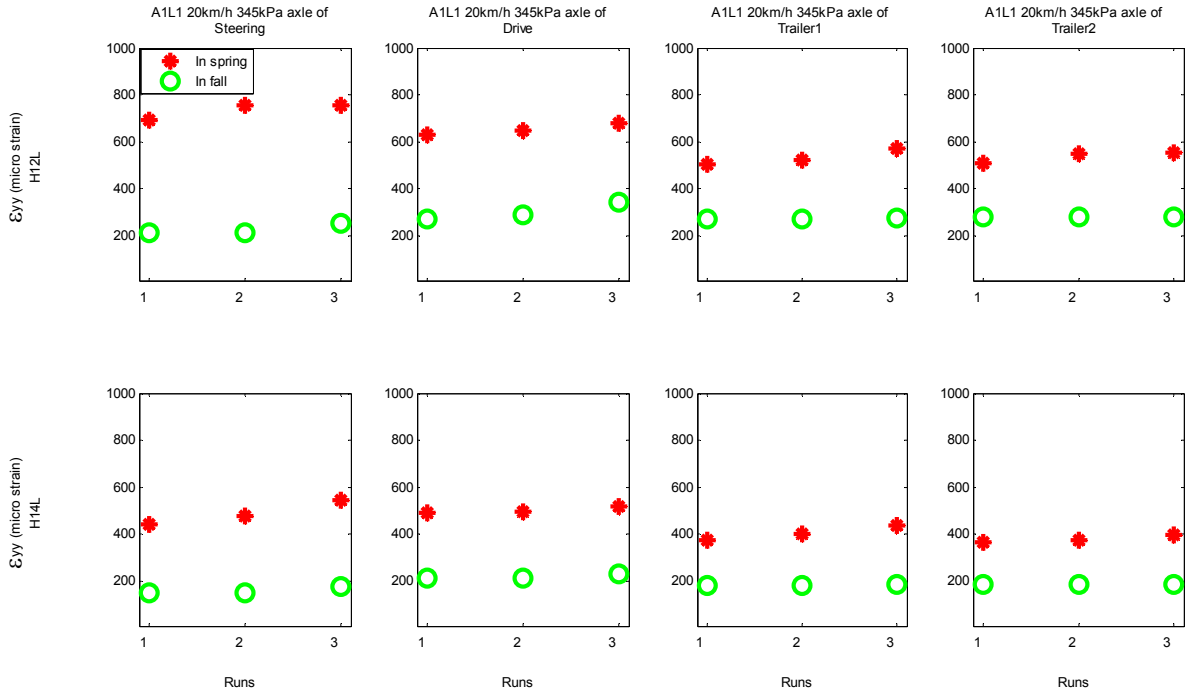

Figure 5-27 Comparing strain in May and September A1L1 load 20 km/h 345 kPa.

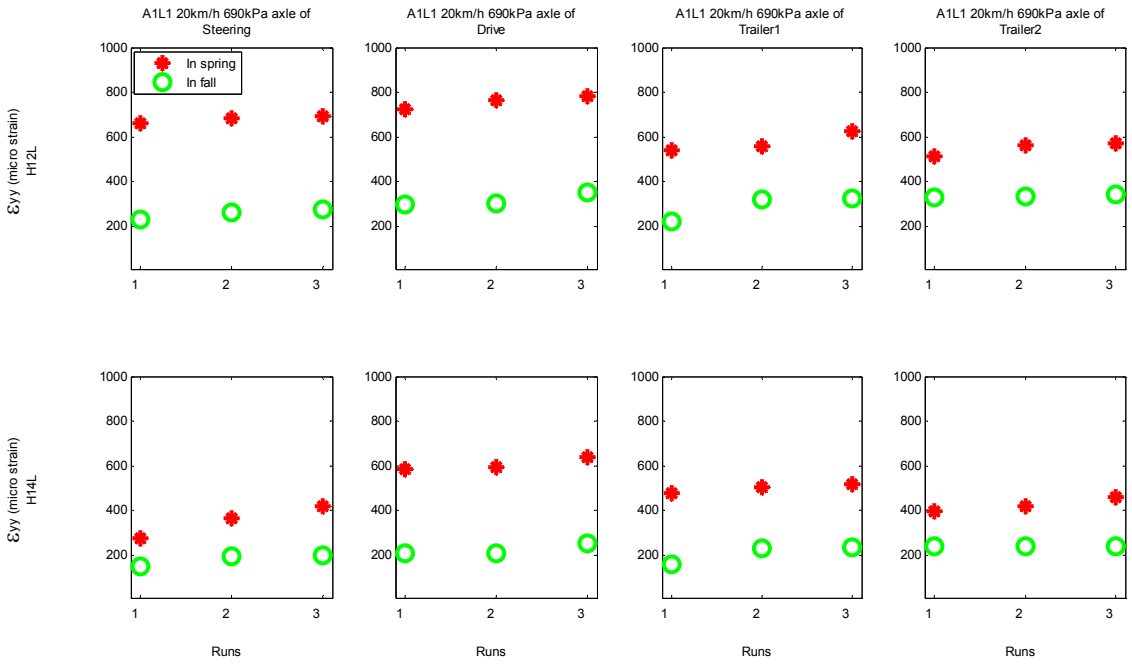

Figure 5-28 Comparing strain in May and September A1L1 load 20 km/h 690 kPa.

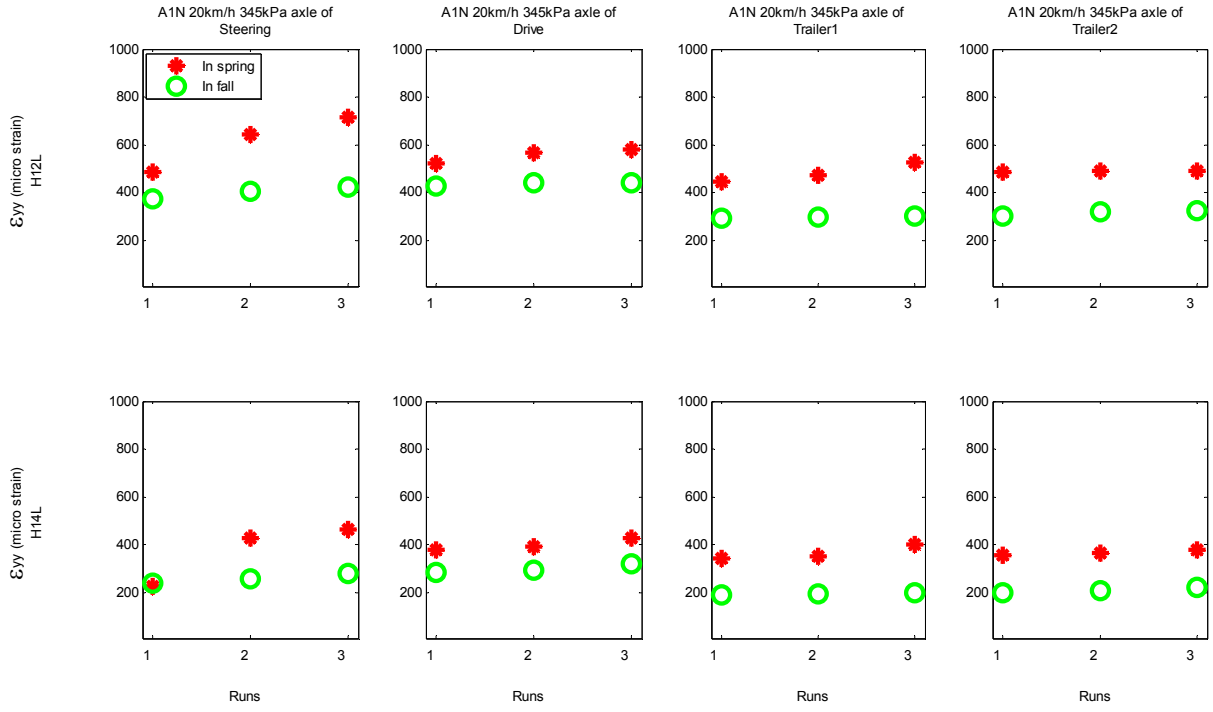

Figure 5-29 Comparing strain in May and September A1N load 20 km/h 345 kPa.

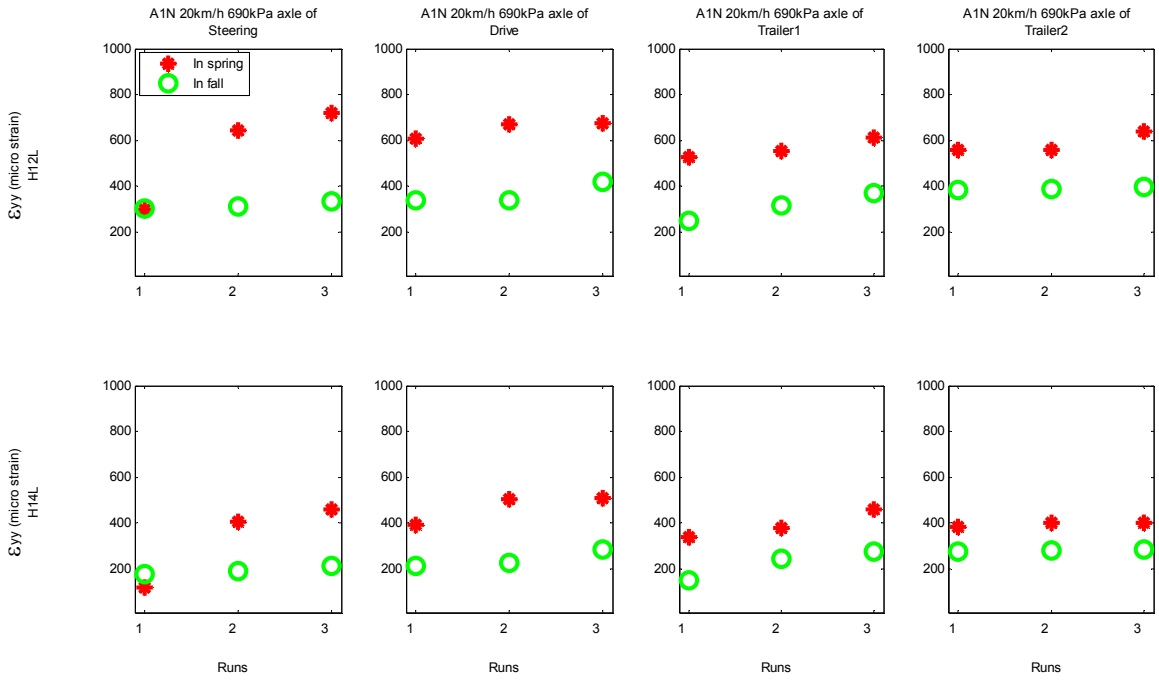

Figure 5-30 Comparing strain in May and September A1N load 20 km/h 690 kPa.

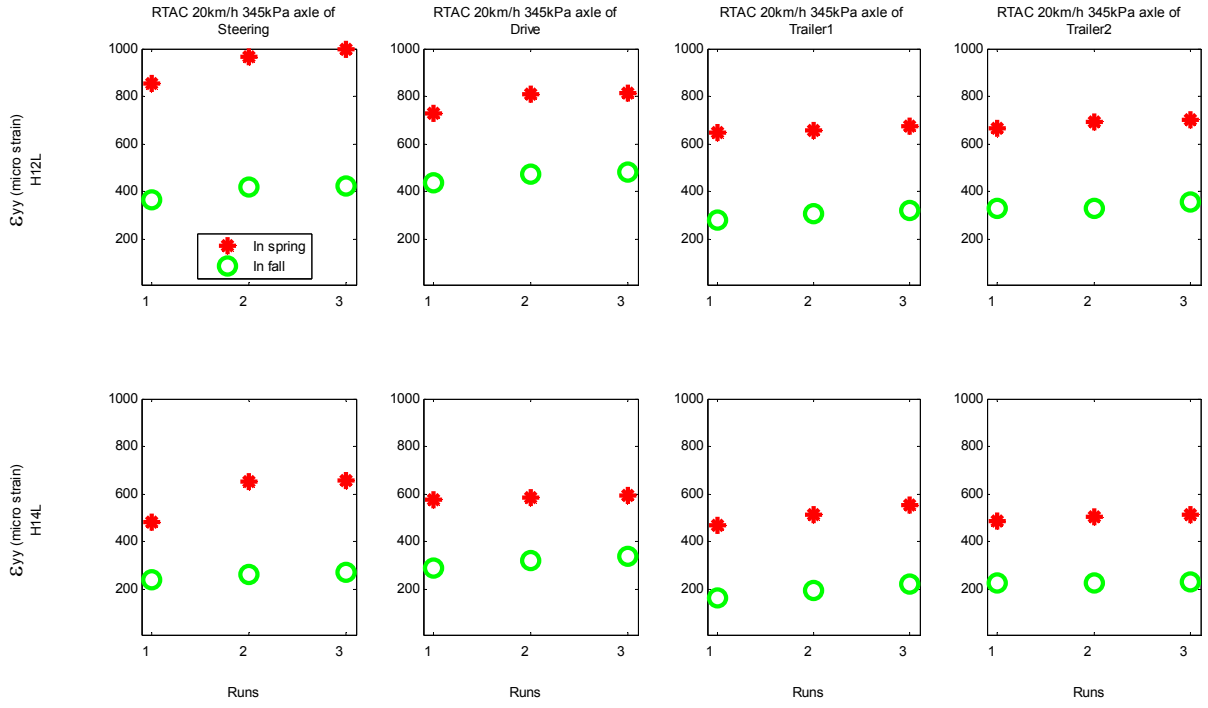

Figure 5-31 Comparing strain in May and September RTAC load 20 km/h 345 kPa.

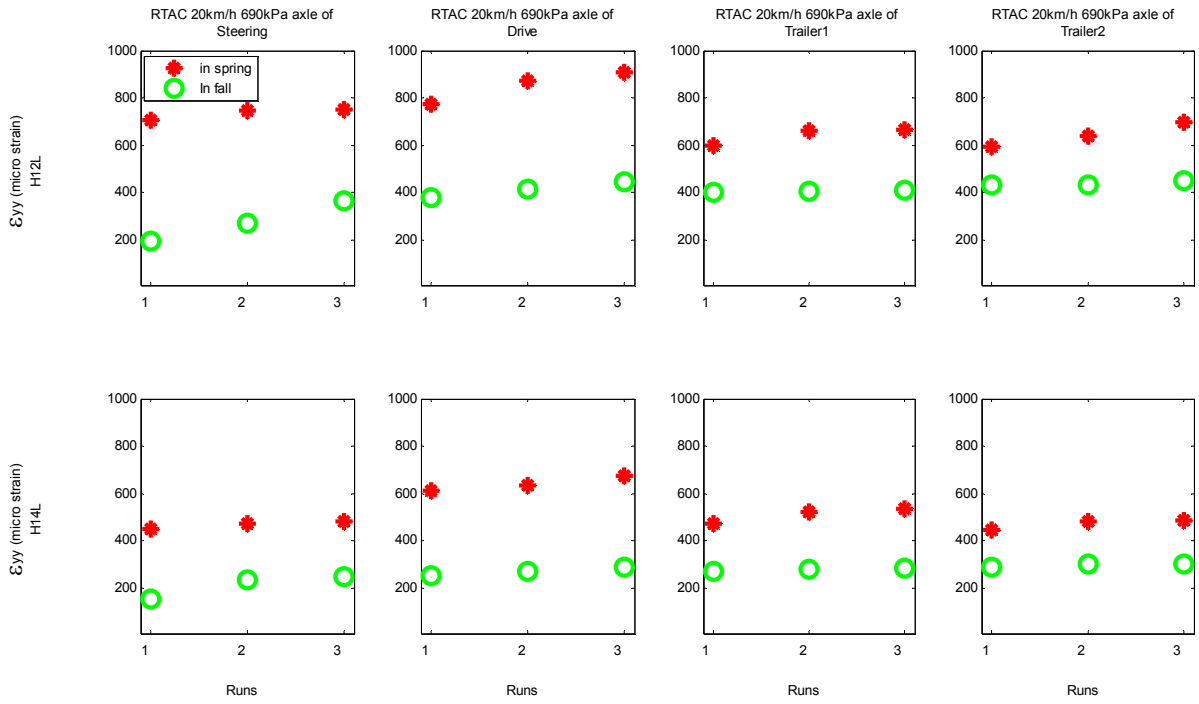

Figure 5-32 Comparing strain in May and September RTAC load 20 km/h 690 kPa.

Table 5-23 Percentage (%) Decreased of Measured Strain by H12L in Sep. than in May

Load	Tire pressure (kPa)	Runs	Steering	Drive	Trailer1	Trailer2
A1L1	345	1	-68.9	-51.9	-46.2	-46.4
		2	-71.4	-50.2	-43.7	-47.5
		3	-66.3	-53.5	-45.1	-43.1
		3-run average	-68.9	-51.9	-45.0	-45.7
	690	1	-64.9	-76.1	-50.6	-43.4
		2	-61.7	-64.5	-50.2	-48.4
		3	-60.1	-66.2	-58.3	-48.3
		3-run average	-62.2	-68.9	-53.0	-46.7
A1N	345	1	-23.0	-46.7	-47.7	-56.4
		2	-36.7	-41.9	-39.6	-42.0
		3	-41.0	-38.9	-42.3	-37.5
		3-run average	-33.6	-42.5	-43.2	-45.3
	690	1	deleted	-119.5	-104.8	-105.9
		2	-51.8	-55.3	-51.9	-47.5
		3	-53.5	-41.9	-54.6	-53.1
		3-run average	-52.7	-72.3	-70.4	-68.8
RTAC	345	1	-57.4	-52.3	-47.4	-49.5
		2	-56.7	-52.0	-43.2	-46.9
		3	-57.5	-49.2	-43.3	-46.2
		3-run average	-57.2	-51.2	-44.6	-47.5
	690	1	-72.3	-52.8	-46.5	-43.0
		2	-63.5	-62.0	-51.2	-45.2
		3	-51.5	-66.2	-51.3	-52.2
		3-run average	-62.4	-60.3	-49.7	-46.8

Table 5-24 Percentage (%) Decreased of Measured Strain by H14L in Sep. than in May

Load	Tire pressure (kPa)	Runs	Steering	Drive	Trailer1	Trailer2
A1L1	345	1	-66.1	-69.4	-59.1	-57.3
		2	-68.5	-65.3	-59.9	-54.3
		3	-67.2	-61.5	-53.1	-45.6
		3-run average	-67.2	-65.4	-57.4	-52.4
	690	1	-45.9	-154.3	-127.2	-96.2
		2	-46.3	-98.7	-102.6	-78.5
		3	-52.2	-96.8	-92.5	-76.5
		3-run average	-48.1	-116.6	-107.4	-83.7
A1N	345	1	deleted	-82.8	-96.6	-104.1
		2	-39.8	-46.1	-52.7	-56.1
		3	-39.4	-49.0	-58.3	-53.0
		3-run average	-39.6	-59.3	-69.2	-71.1
	690	1	deleted	-204.9	-176.5	-187.9
		2	-52.6	-63.6	-61.0	-57.6
		3	-53.4	-50.9	-70.8	-51.1
		3-run average	-53.0	-106.5	-102.7	-98.9
RTAC	345	1	-49.9	-85.5	-70.2	-73.6
		2	-59.6	-59.2	-56.8	-55.7
		3	-58.4	-57.1	-62.7	-55.9
		3-run average	-56.0	-67.2	-63.2	-61.7
	690	1	-66.2	-74.4	-71.8	-61.4
		2	-50.1	-74.3	-77.7	-65.1
		3	-48.2	-80.8	-78.8	-63.8
		3-run average	-54.8	-76.5	-76.1	-63.4

5.3 SUMMARY

Based on the results and discussion in this chapter, the following conclusions can be drawn:

- TPCS is effective to reduce the strain at the bottom of asphalt pavement. The measured strain decreased significantly for all the configurations of load levels and truck speeds when tires were deflated from 690 kPa to 345 kPa.

- When other tires' pressure decreased from 690 kPa to 345 kPa, the measured strain in the spring of steering axle increased although the pressure of steering tires never changed, which indicates that the effect of steering tires upon the pavement is quite different from other tires for a truck equipped with TPCS.
- Longitudinal gauges recorded the least variable strains for all the TPCS tests in the spring and the fall.
- Measured longitudinal strain at the bottom of AC layer in the fall is 40% to 70% less than in the spring.
- For different truck speeds, the strain variation is different when the tire pressure was reduced from 690 kPa to 345 kPa. The higher the truck speed, the more significant strain differences have been observed.
- Maximum strain is usually generated by either drive or trailer1 axle, sometimes by steering axle.

CHAPTER 6 FINITE ELEMENT SIMULATION OF PAVEMENT RESPONSES

6.1 INTRODUCTION

Is it safe to haul fully loaded during the last several weeks of the SLR period with no measureable increase in pavement rutting or cracking? To answer this question, one method is to measure the pavement responses directly as mentioned in the previous chapter; alternatively, theoretical analysis, finite element modeling, for instance, can also be used to simulate pavement responses due to tire loading.

Fatigue cracking and rutting are the two major flexible pavements distresses, which could be related to immediate pavement responses and explained in a mechanistic way. Horizontal tensile strains at the bottom of AC layer can explain fatigue cracks that initiate at the bottom and progress to the pavement surface, while vertical compressive strains at the top of the subgrade are considered related to pavement rutting due to compaction and consolidation of the subgrade soil (Hung, 1993).

Traditionally, in flexible pavement design, it is assumed that each tire has a circular contact area with the pavement, the uniform contact pressure is generally assumed equal to tire pressure. However, studies have demonstrated that the tire-pavement contact stress is far from uniformly distributed and the distribution of contact stress primarily depends on tire pressure, tire load, and tire type (Wang and Machemehl,

2006). By comparing pavement responses computed using measured non-uniform contact stress with results predicted using the traditional tire-pavement contact model, Wang and Machemehl found that the traditional model tends to overestimate tensile strains at the bottom of AC layer but underestimate vertical strains on top of the subgrade (Wang and Machemehl, 2006)

As mentioned in Chapter 5, measured non-uniform tire-pavement contact stress data for different tire load and inflation pressure conditions and for three configurations of tires (single tire single (steering) axle, dual-tire tandem (drive) axles, and dual-tire tridem (trailer) axles) were inputted to the finite element model with ABQUS to compute immediate pavement responses for two types of asphalt pavement structure. Moduli of different layers were back calculated by Elmod 5 according to FWD test results.

Pavement stress and strain were computed from finite element model for a factorial experiment design of different tire loads, tire pressures, pavement structures, and tire configurations. Typical finite element results using the measured footprint were compared with the strain gauge readings.

6.2 FACTORIAL EXPERIMENT DESIGN AND FOOTPRINT

Three load levels were tested for each test section. The corresponding footprints for different tire were captured. Table 6-1 shows the configurations of tire load and tire pressures.

Table 6-1 Factorial Design for Tire Load and Tire Pressure

load level	Tire load (kg)	Axle	Tire model	Tire configuration	Test tire pressure (KPa)
B1L2	2505	steer	ST230	single tire single axle	690
	1092.5	drive	DR675	dual tire tandem axle	345,448,690
B1N	1702.5	drive	ST234	dual tire tandem axle	345,448,690
	1600	trailer 1	TR101	dual tire tridem axle	345,517,690
	2165	trailer2	HN595	dual tire tandem axle	345,517,690
A1N	1872.5	drive	ST234	dual tire tandem axle	345,448,690
	1847.5	trailer 1	TR101	dual tire tridem axle	345,517,690
	2050	trailer2	HN595	dual tire tandem axle	345,517,690
RTAC	2167.5	drive	ST234	dual tire tandem axle	345,448,690
	1902.5	trailer 1	ST230	dual tire tridem axle	345,517,690
	2167.5	trailer2	HN595	dual tire tandem axle	345,517,690

As shown in Figures 6-2 and 6-3, the footprint (tire-pavement contact stress) was captured by using Tirescan 3150 pressure mapping system. The lateral and longitudinal spacing between the pad sensing cells is 8.382 mm, making the effective rectangular element of each sensing cell area 70.2579 mm^2.

A measured numerical non-uniform tire-pavement contact stress data is displayed in Figure 6-1, with a total of 1120 elements (equal to the number of sensing cells of the pressure mapping system) for various configuration of load and tire pressure. The number in each small rectangle represents the contact stress in kPa, uniformly distributed over that element. The longitudinal direction is the truck moving direction; the transverse direction is the lateral side of the tire.

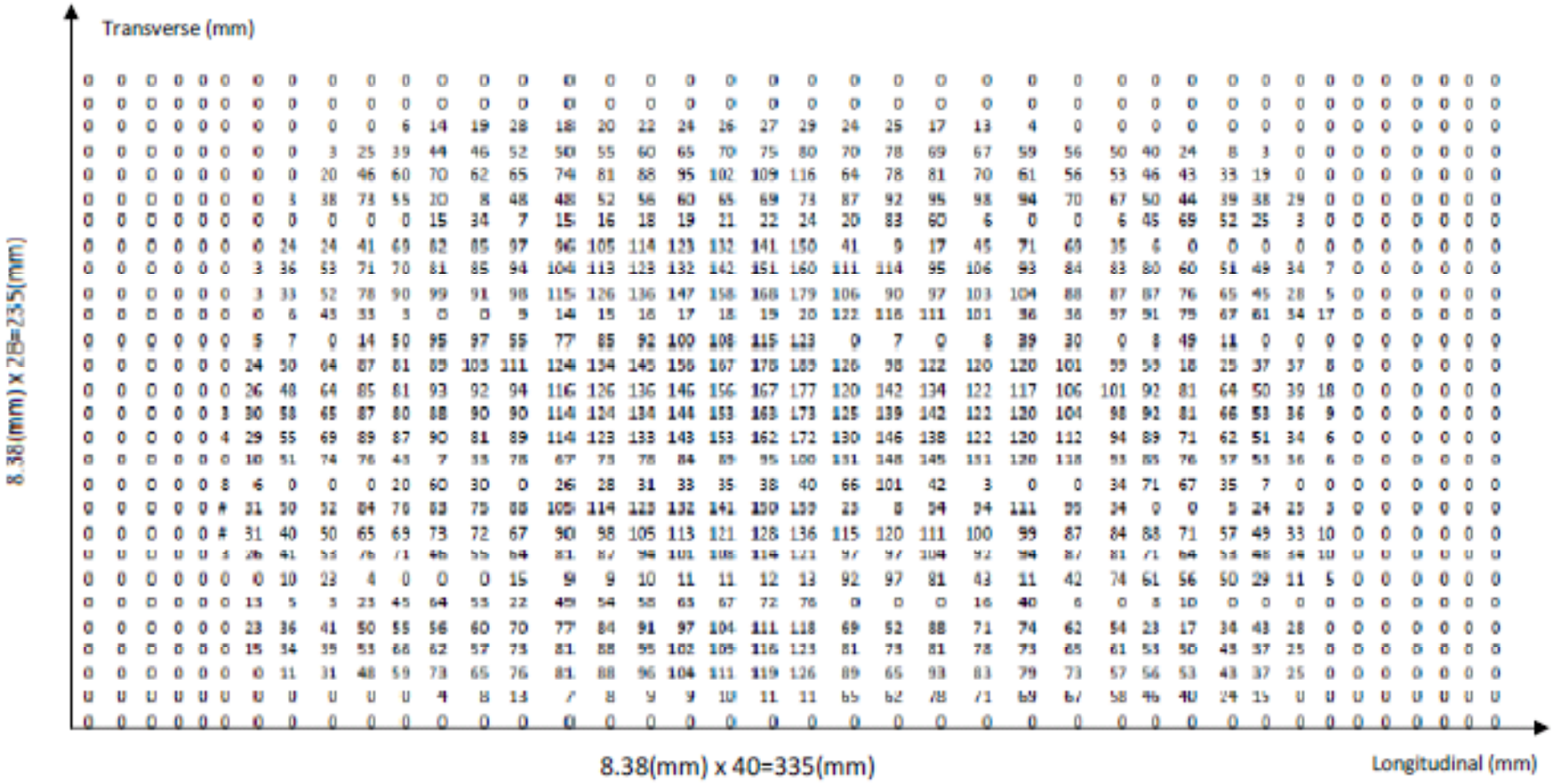

Figure 6-1 Numerical footprint in kPa (tire pressure = 690 kPa, tire load=1873 kg)

The measured footprints can be imported into Matlab environment. Figure 6-2 shows graphically two typical footprints under A1N load at the tire pressure of 690 kPa and 345 kPa, respectively.

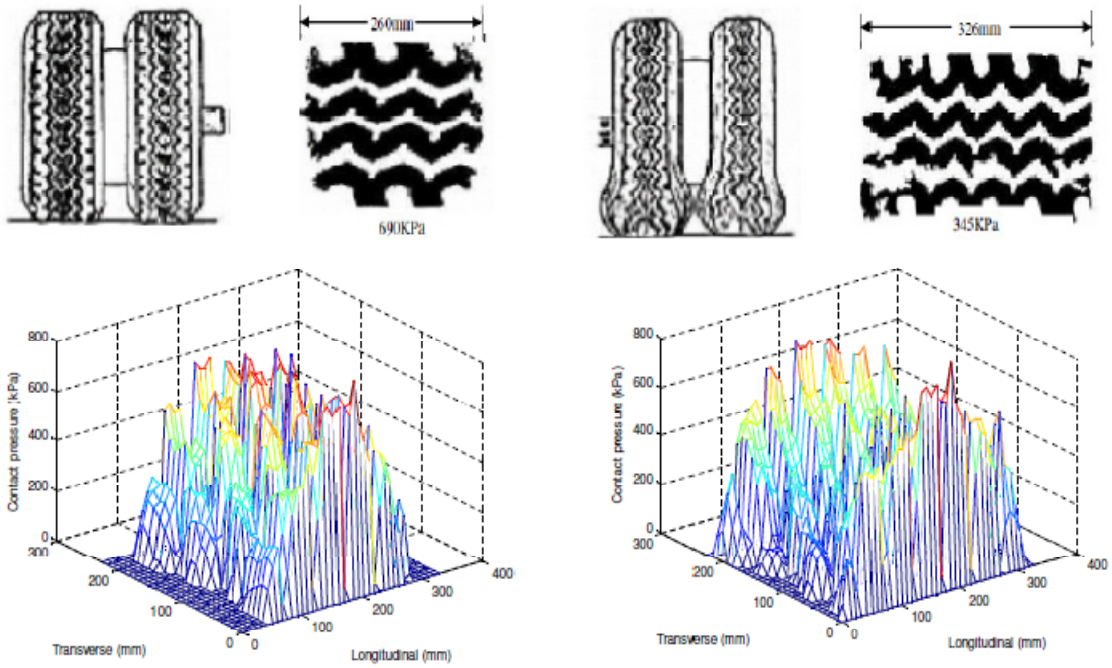

Figure 6-2 Measured tire prints at 690 kPa (a) and 345 kPa (b) under tire load of 1873 kg

As shown in Table 6-2, resilient moduli of pavement layers were back calculated from FWD deflections.

Table 6-2 Material properties of pavement layers at test sites

Highway	Material /layer	Thickness (mm)	FE model thickness (mm)	Moduli in May (MPa)	Moduli in Sep (MPa)	Poisson's ratio*
PTH11	AC	130	130	4374	6204	0.3
	GB	250	250	291	401	0.35
	Subgrade	infinite	5620	48	69	0.4
PR304	AST	30	30	1169	1100	0.3
	GB/rock fill	500	500	285	385	0.35
	*Sub*grade	infinite	5470	52	70	0.4

*Estimated value

6.3 GENERATION OF FE MESH

Using ABAQUS version 6.7-5, 3D FE model were developed to simulate pavement response of PTH11 and PR304. The eight-node, linear brick elements (C3D8) were used for the finite elements analysis.

Duncan (1968) reported that reasonable pavement responses were obtained when the analysis boundary moved to 50-times the radius of circular loading area (R) in the vertical direction and 12-times R in the horizontal direction. Kim and Tutumluer (2007) found that the domain size of 140-times R in the vertical direction and 20-times R in the horizontal direction gives more accurate results using the 8-node isoparametric quadrilateral elements.

Al-Qadi et al (2008) found that the horizontal location of the infinite boundary from the load center needs to be greater than 900 mm in order to have the closest solution to the full-size reference FE model. The location of the bottom infinite boundary element was recommended at a depth of 1100 mm, where the maximum compressive stress in the subgrade became insignificant at 1% or less of the maximum tire-pavement contact stress. ARA (2004) suggested the infinite boundaries at 760 to 2000 mm.

Park found that a finite element mesh with lateral and longitudinal dimensions of 3810 mm x 3810 mm was appropriate with infinite elements in depth (Park, 2008). In their

study, Wang and Machemehl (2006) found a pavement structure solid having X, Y, and Z of 4000 mm X 4000 mm x 6000 mm is accurate enough to validate roller boundary conditions.

As shown in Figure 6-3, a pavement block with X, Y, and Z of 2200 mm X 4400 mm x 6000 mm was used to compute the pavement responses for dual tire tandem axle and dual tire tridem axle, for single tire single axle the corresponding dimensions are 4400 mm X 4400 mm x 6000 mm which can be seen in Figure 6-4. Good interface bonding was assumed for different layers.

A finer FE mesh was placed under the loaded area where the change in strain is greatest and increasingly coarser mesh was employed away from the load where the change in strain is slower. The element dimension of the finer mesh was chosen equal to the size of footprint sensing area which is 8.38 mm for both longitudinal and transverse directions.

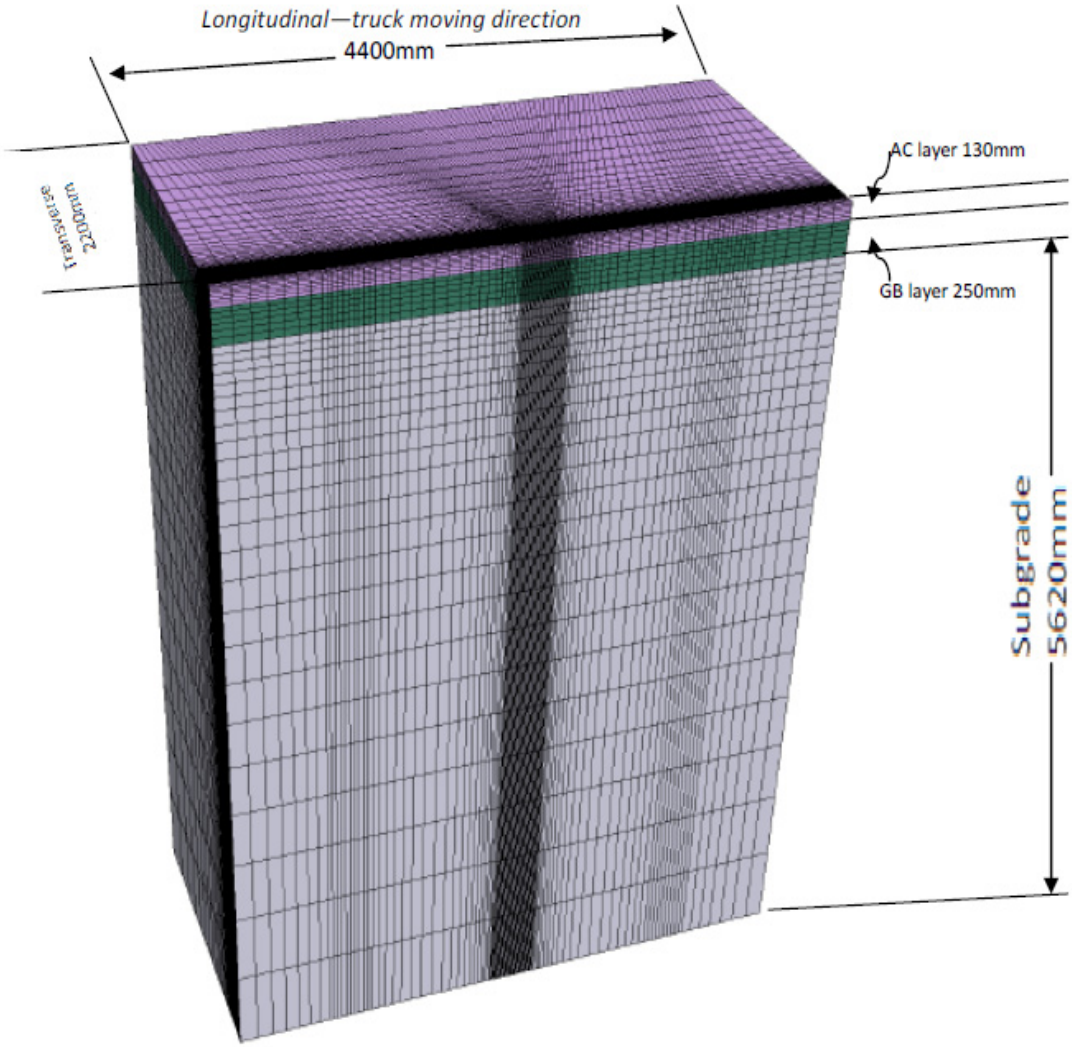

Figure 6-3 Mesh and materials for dual tire tandem and tridem axle model at PTH11

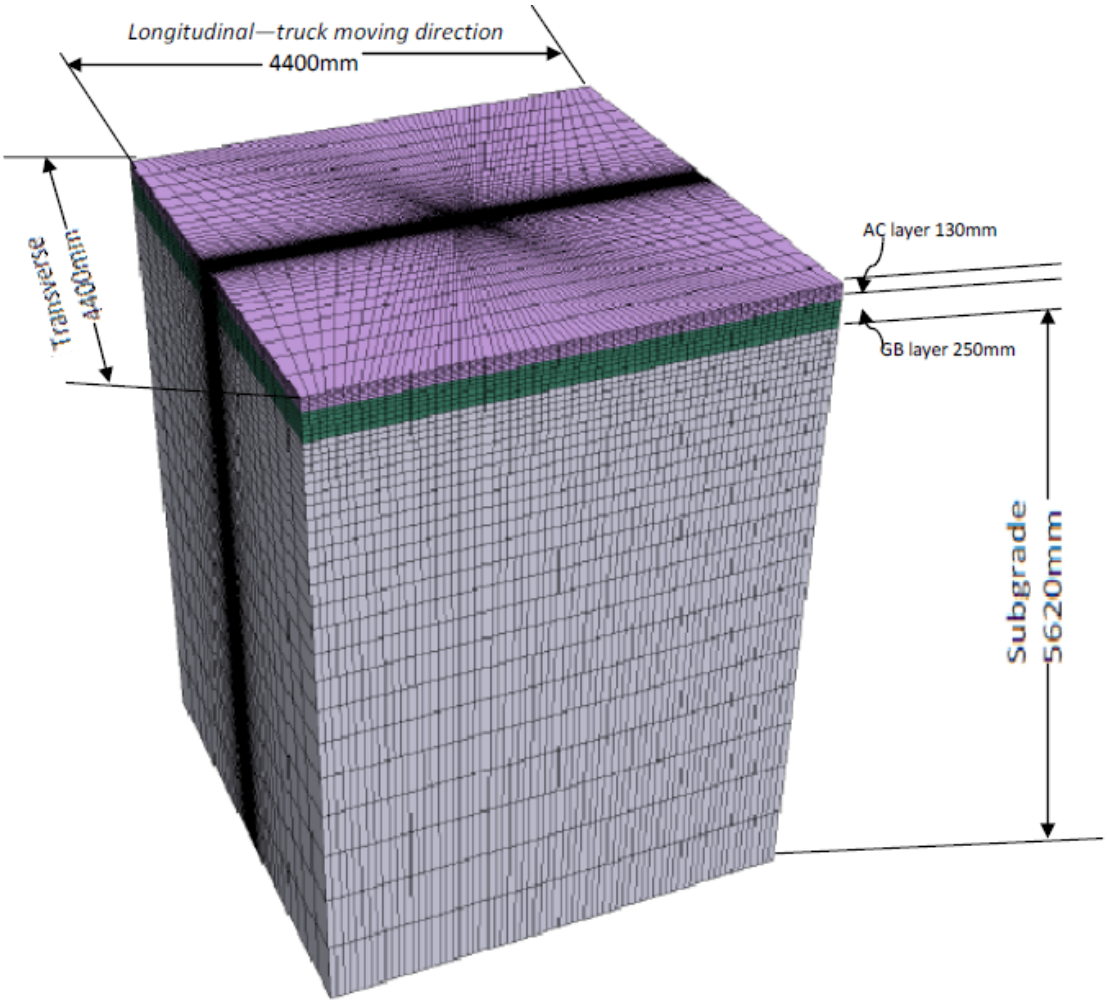

Figure 6-4 Mesh and materials for single tire single axle model at PTH11

6.4 VISUALIZATION OF FE MODELING RESULTS

For this research, as shown in Figure 6-4, a B-train was chosen as the testing vehicle. According to the readings of strain gauges, the critical strains for all different configurations were always produced by either tandem drive axle or tridem trailer axle. As the result, FE modeling focuses on the simulation of tandem and tridem dual tire axle. The steering axle-- single tire single axle was also modeled. These configurations are the most popular loading conditions.

As can be seen in Figure 6-1, for the FE modeling, the coordinate system is defined as follows: The orthogonal coordinate system X and Y axes are parallel to the pavement surface with X to the transverse direction, Y is to the longitudinal or truck moving direction; Z axis is pointed vertically out of the road surface from the pavement structure.

As shown in Figure 6-5, Figure 6-6 and Figure 6-8, for dual tire configuration including tandem and tridem axle, only one tire was analyzed for each axle by using symmetric boundary condition for the surface of YZ under the centre of dual tire. For all other surfaces including the bottom of the block, roller condition was employed. For single tire single axle, only roller is used for boundary condition as shown in Figure 6-10.

6.4.1 DUAL TIRE TRIDEM AXLE

Figure 6-5 shows the plan view of FE modeling area for dual tire tridem or tandem axle analysis. For the tandem axle, axle 3 will not exist.

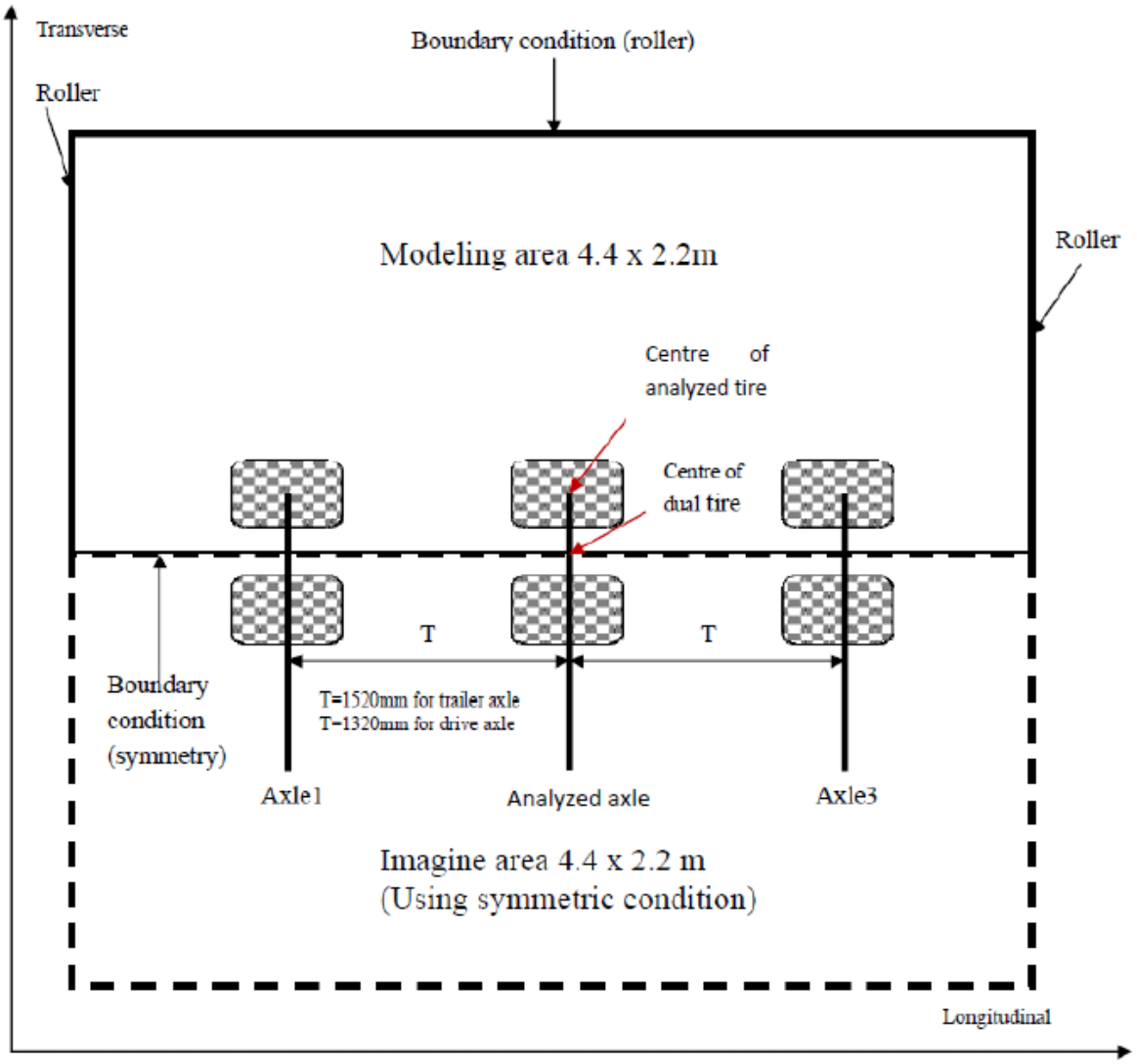

Figure 6-5 Plan view of FE modeling area for dual tire tridem or tandem axle

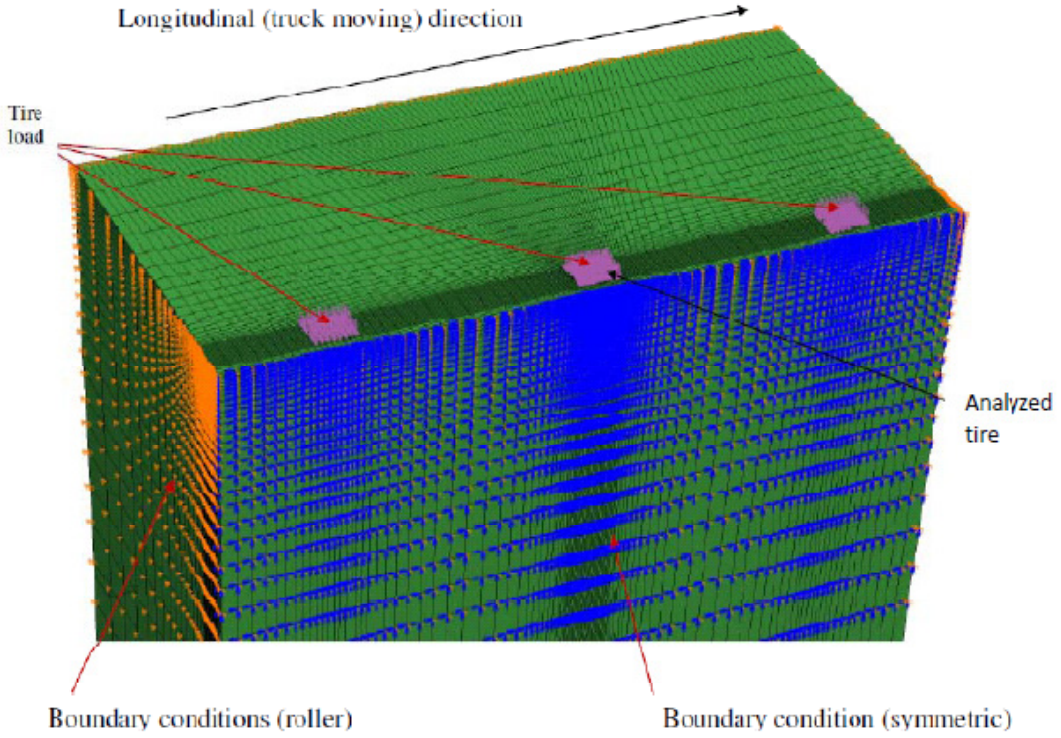

Figure 6-6 Loads and boundary conditions—dual tire tridem (trailer) axle

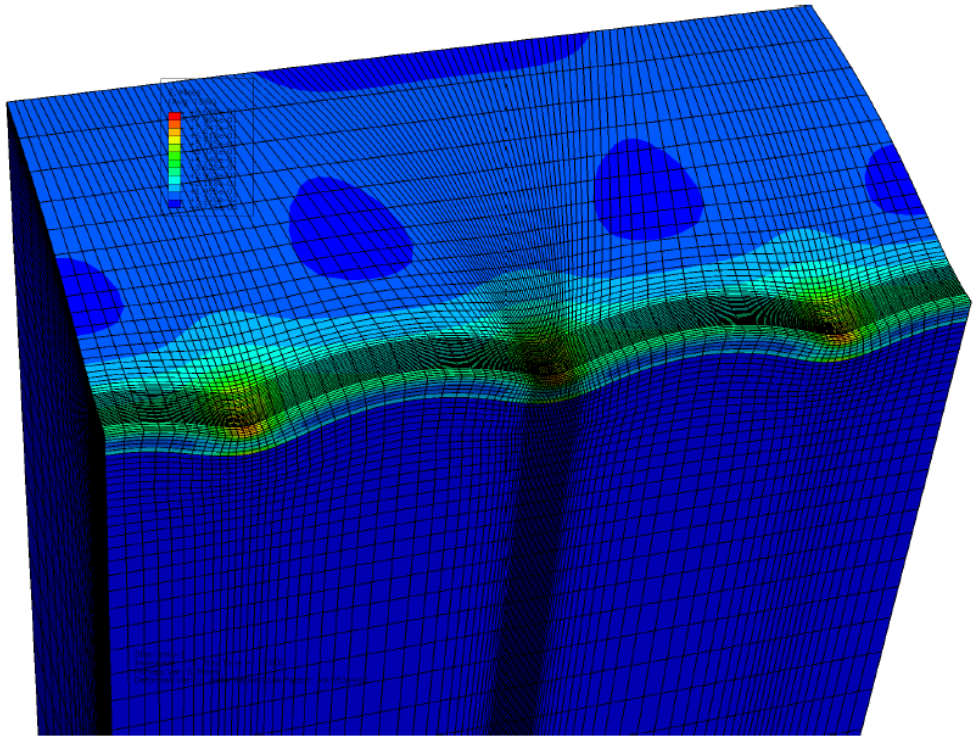

Figure 6-7 FE modeling results—Stress on top of the pavement (dual tire tridem axle)

6.4.2 DUAL TIRE TANDEM AXLE

Figure 6-8 shows the numerical load and boundary of the mesh for a highway block.

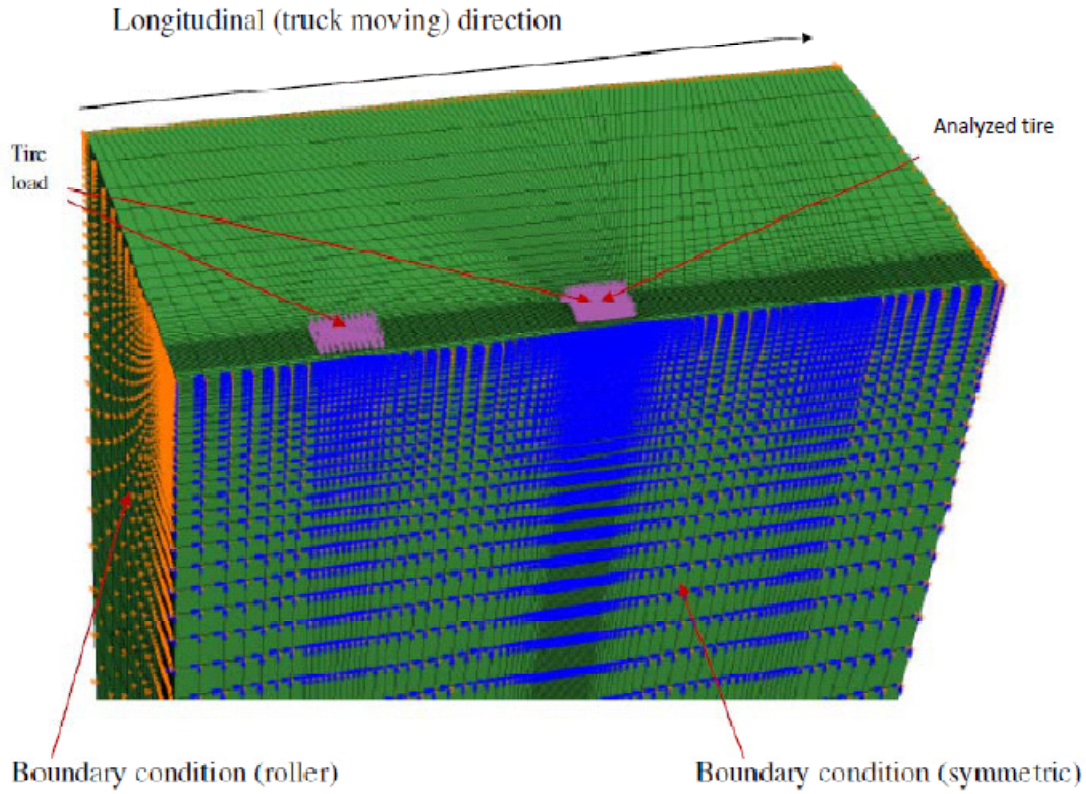

Figure 6-8 Load and boundary conditions—dual tire tandem (drive) axle

Figure 6-9 shows the simulated stress distribution on top of the pavement for dual tire tandem axle. Figure 6-10 shows the plan view of FE modeling area for single tire single (steering) axle. Figure 6-11 shows the numerical load and boundary of the mesh for a highway block for single tire single (steering) axle, while Figure 6-12 is the stress distribution correspondingly.

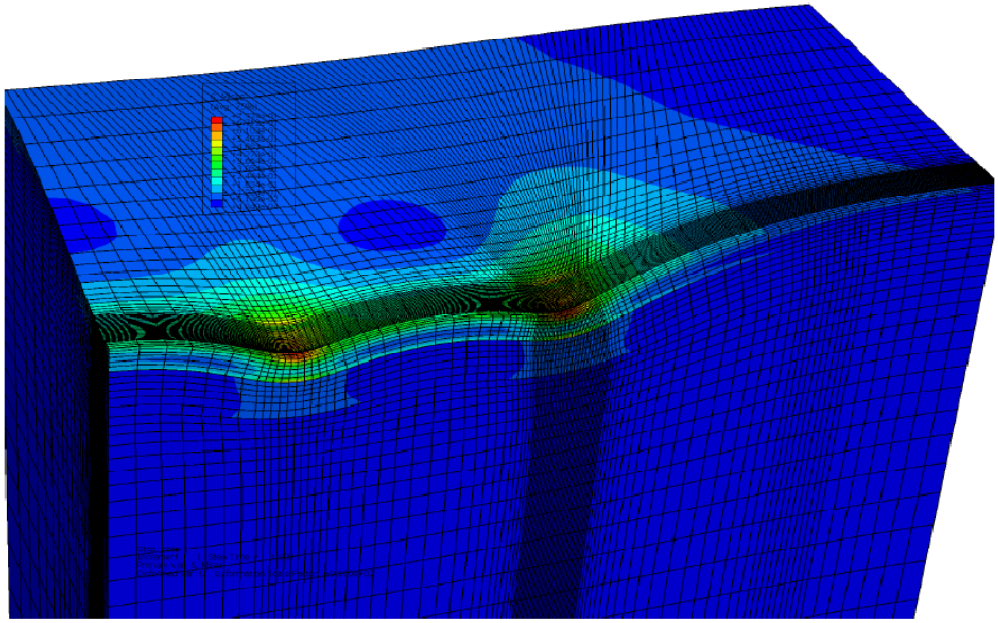

Figure 6-9 FE modeling results—Stress on top of the pavement (dual tire tandem axle)

6.4.3 SINGLE TIRE SINGLE AXLE

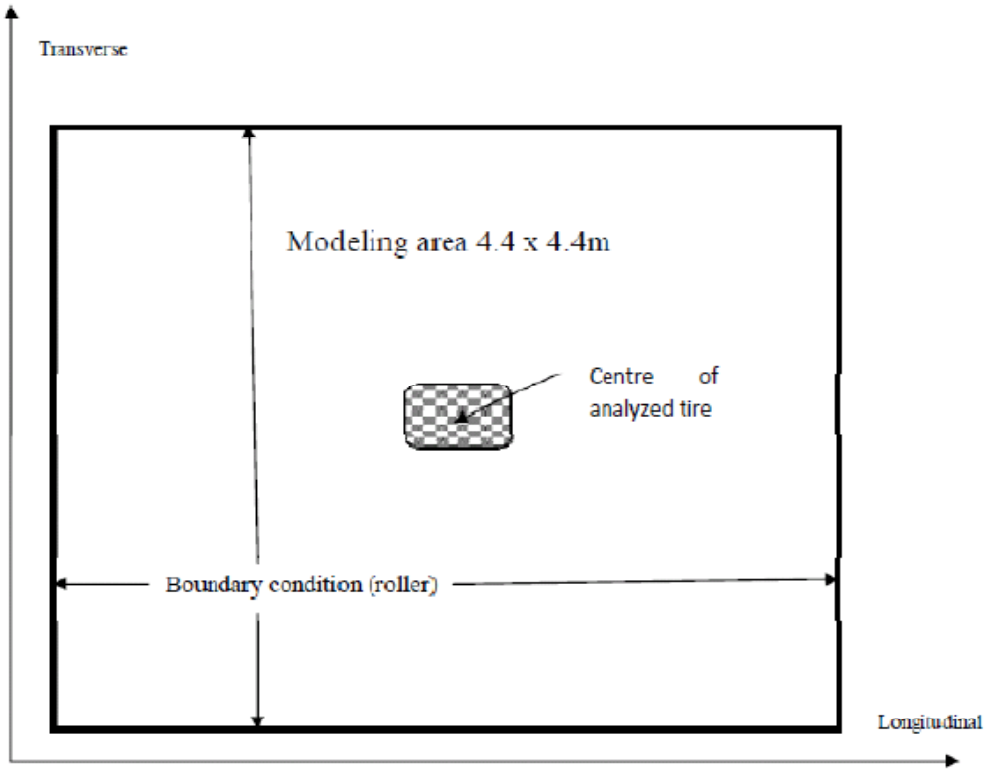

Figure 6-10 Plan view of FE modeling area for single tire single (steer) axle

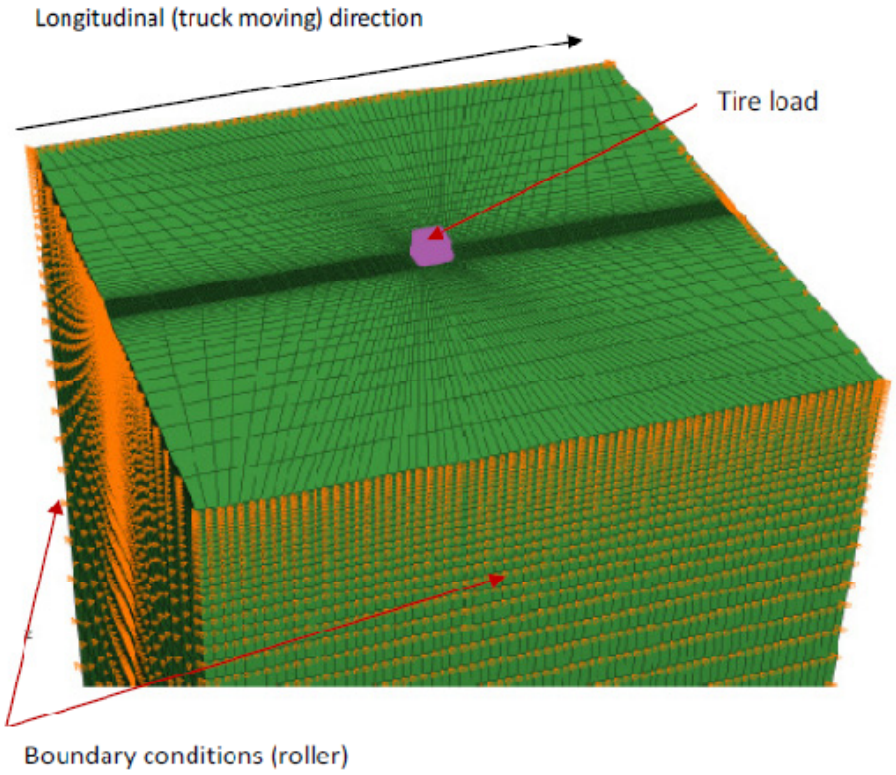

Figure 6-11 Load and boundary conditions—single tire single (steering) axle

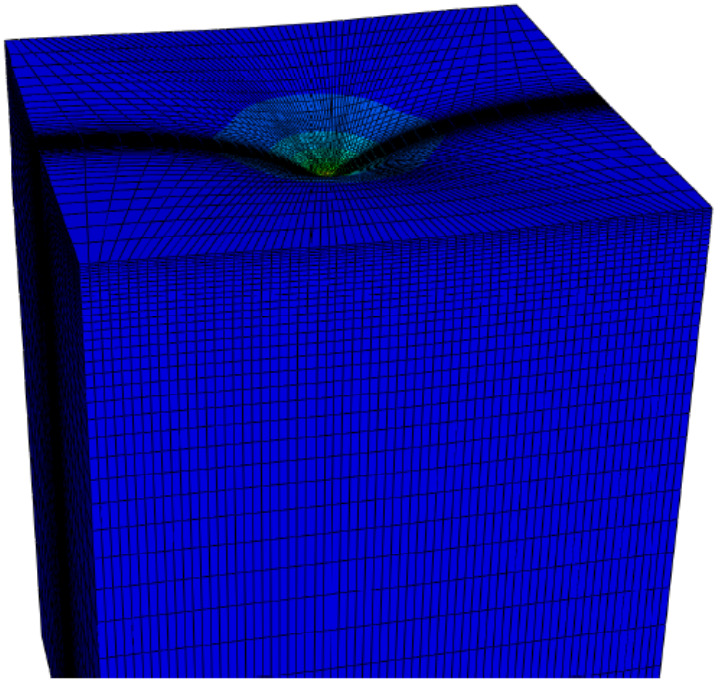

Figure 6-12 FE modeling results—Stress on top of the pavement (single tire single axle)

6.5 COMPUTED PAVEMENT RESPONSES

The strains of the two test highways were computed for different configurations of tire load, tire pressure, and type of axle in May and in September. The distribution of horizontal strains at the bottom of AC layer and vertical strain on the top of subgrade were plotted at ***6.5.1***; the critical responses of the pavement were tabulated at ***6.5.2.***

6.5.1 DISTRIBUTION OF COMPUTED STRAINS AT PTH11

Figure 6-13 through Figure 6-18 show the distributions of computed pavement responses by dual tire tandem (drive) axle under A1N load in May for PTH11. Figure 6-19 through Figur e6-24 show the distributions of computed pavement responses by single tire single axle (steering tire) for PTH11. The tire pressure of steering tire is always the same at 690 kPa during test period.

As can be seen from Figure 6-13, the maximum transverse strain at the bottom of AC layer is always under the centre of analyzed tire. The maximum strain decreased by 13.9% from 79 to 68 micro strains under the centre of the analyzed tire when tire pressure deflated from 690 kPa to 345 kPa.

From the centre of the analyzed tire to the centre of the dual tire(the distance is 165.9 mm), the transverse strain decreased from 79 to 24 micro strains (tire pressure 690

kPa), which gives the reason why the measured transverse strain by strain gauges is so sensitive to wheel offset of test truck.

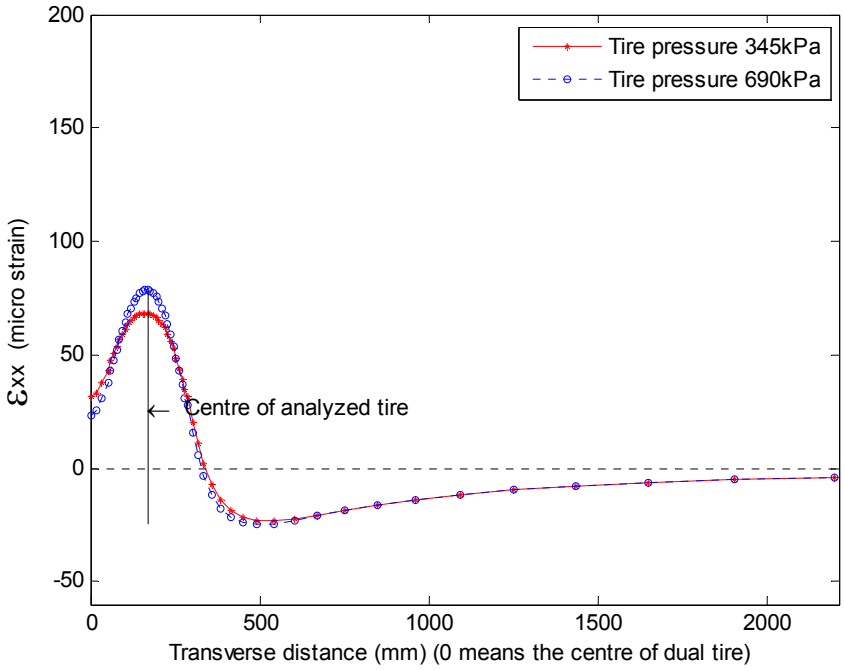

Figure 6-13 Transverse strain at bottom of AC layer along transverse direction under the centre of analyzed tire

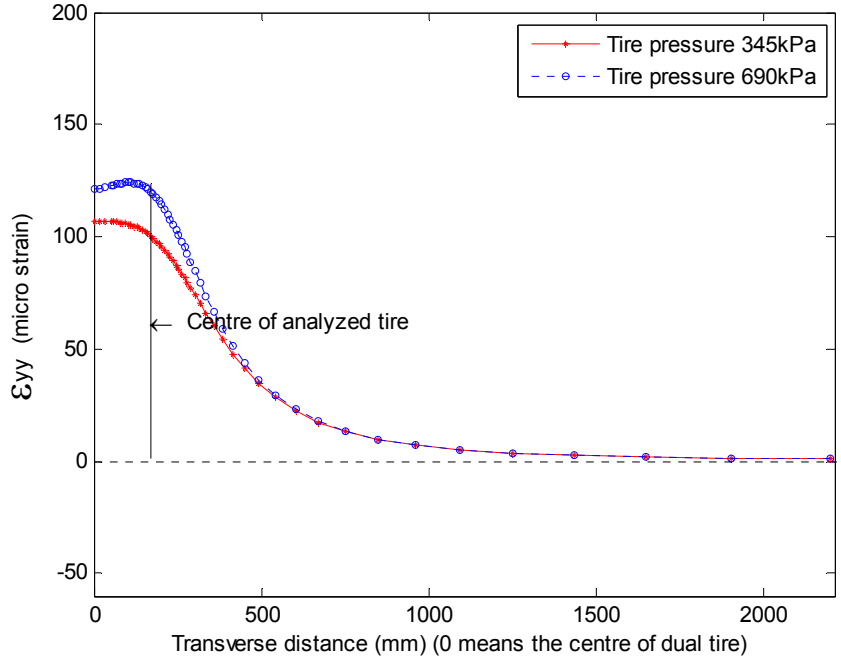

Figure 6-14 Longitudinal strain at bottom of AC layer along transverse direction under the centre of analyzed tire

As can be seen from Figure 6-14, the longitudinal strain at the bottom of AC layer does not change much from the centre of analyzed tire to the center of the dual tires. The strain is 120 micro strains under the centre of analyzed tire; the corresponding value is 121 micro strains under the centre of dual tire at tire pressure of 690 kPa. This gives the reason why, during the field test as mentioned in chapter 6, longitudinal strain gauges always captured much better readings than transverse strain gauges.

The maximum longitudinal strain is not produced under centre of the analyzed tire. The maximum strain is produced somewhere between the centre of dual tire and the centre of analyzed tire depending on tire pressure. For example, the maximum longitudinal strain (124 micro strains) is 67 mm away from the centre of analyzed tire toward the centre of dual tire at tire pressure of 690 kPa; the corresponding value is 117 mm when tire pressure is 345 kPa.

The maximum longitudinal strain decreased by 13.7% from 124 to 107 micro strains when tire pressure deflated from 690 kPa to 345 kPa.

As can be seen from Figure 6-15, the maximum transverse strain is almost under the centre of analyzed tire with a small distance of shifting towards each other of the two axles of the tandem (drive) axles due to the effect of strain overlap. The computed distance of shifting depends on the size of the element. For example, the shifting of

axle1 is much bigger than the analyzed tire because coarser mesh was used at the area under the centre of axle1 (tire1) comparing to the area under the analyzed tire.

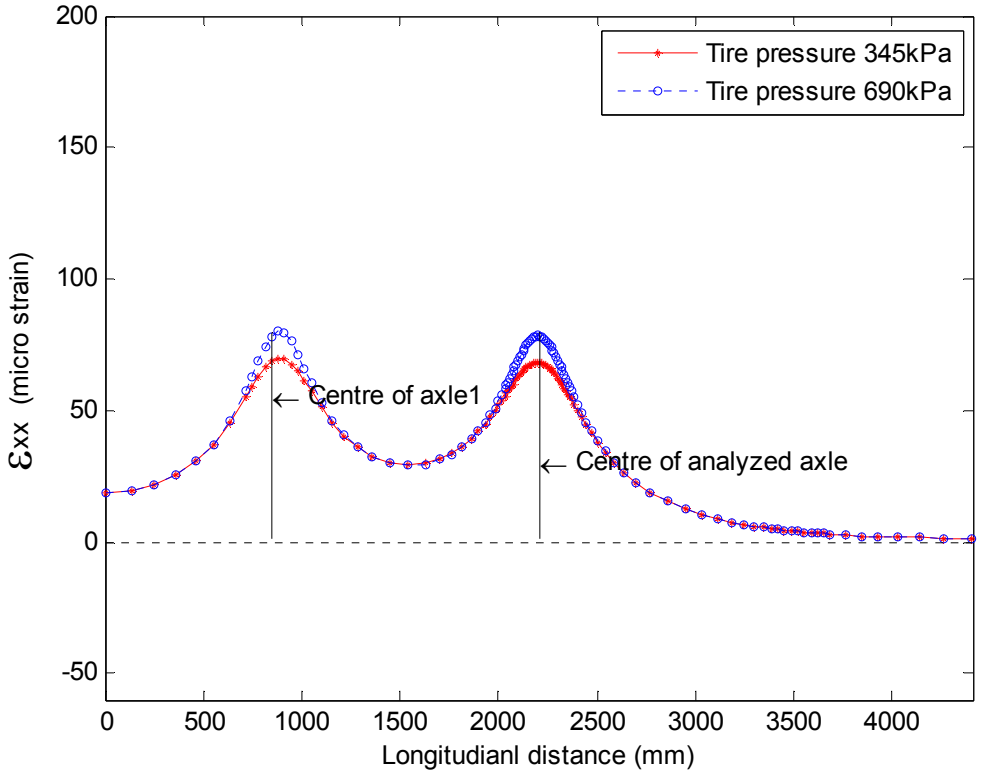

Figure 6-15 Transverse strain at bottom of AC along longitudinal direction under the centre of analyzed tire

Figure 6-16 shows the distribution of longitudinal strain at bottom of AC layer along longitudinal direction. Comparing to transverse strain at the bottom of AC layer as shown in Figure 6-15, longitudinal strain is very sensitive to longitudinal position of the test tire. For example, when tire pressure is 690 kPa, the longitudinal strain is 124 micro strains under the centre of analyzed tire; the corresponding strain is -30 micro strains under the centre of the tandem axles.

The longitudinal strain is very sensitive to the longitudinal position of the test tire, but not sensitive to the transverse position of the test tire; in contrast, the transverse strain is sensitive to transverse position of the test tire, but not sensitive to longitudinal position of the test tire. This gives the reason why longitudinal strain gauges recorded much better strain bulbs than transverse strain gauges during the field tests.

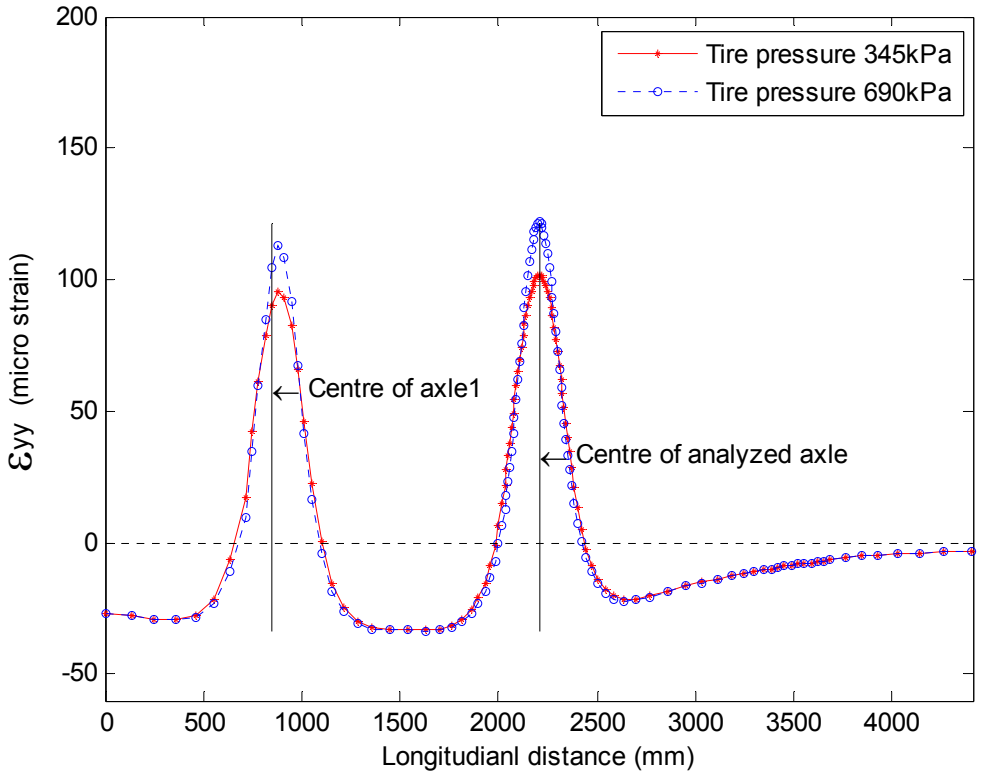

Figure 6-16 Longitudinal strain at bottom of AC along longitudinal direction under the centre of analyzed tire

Figure 6-17 shows the distribution of vertical strains on top of subgrade along transverse direction. Figure 6-18 shows the distribution of vertical strain on top of subgrade along longitudinal direction under the centre of dual tire.

The maximum vertical strain on top of subgrade is always under the centre of the dual tire because of the effect of strain overlap of the two tires of each axle. The vertical strain on top of the subgrade decreased only 1.8% when tire pressure deflated from 690 kPa to 345 kPa. This may indicate that CTI technique is effective to prevent bottom up failure of AC layer, but might not be as effective to prevent the rutting of the pavement.

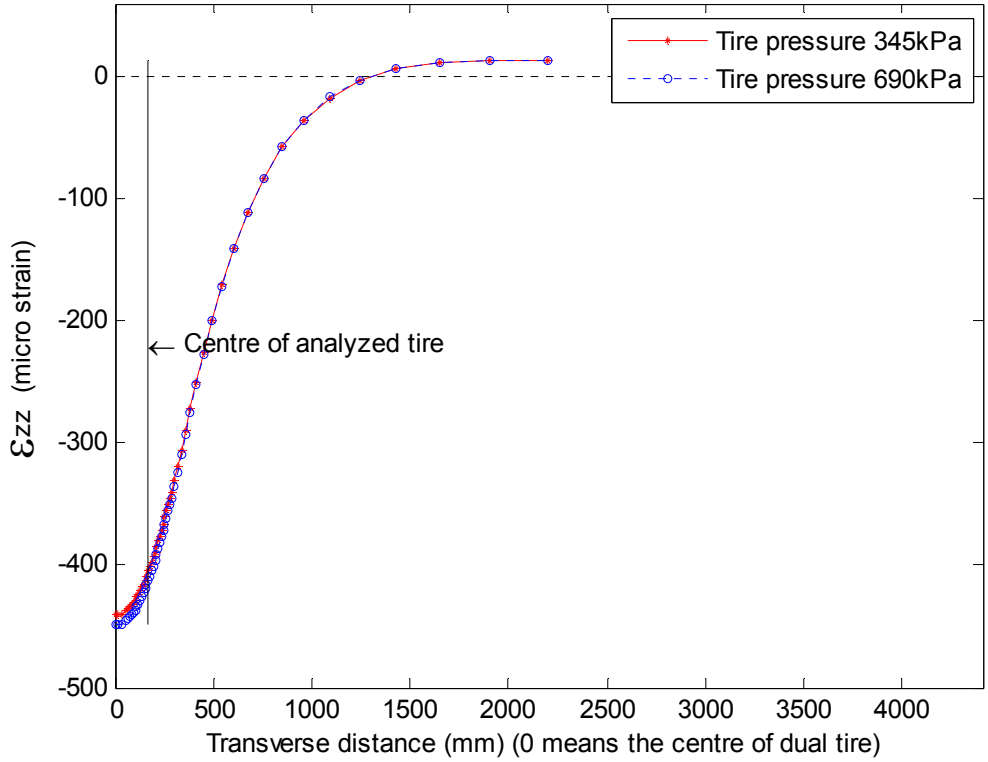

Figure 6-17 Vertical strain on top of subgrade along transverse direction under the centre of analyzed tire

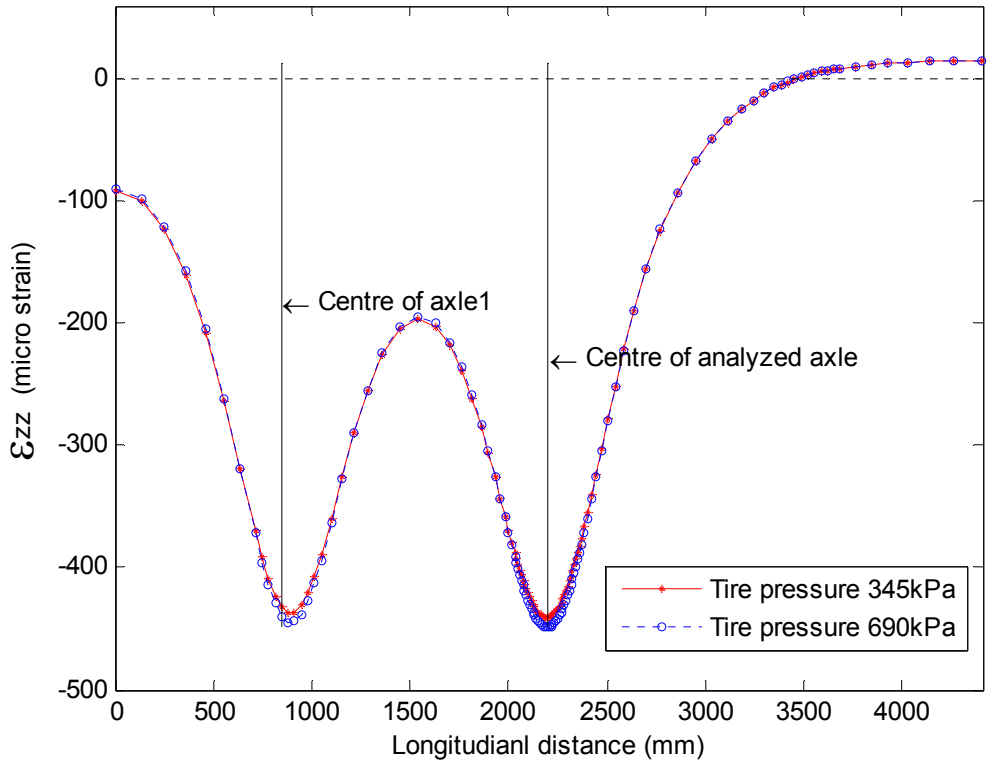

Figure 6-18 Vertical strain on top of subgrade along longitudinal direction under the centre of dual tire

Figure 6-19 shows the distribution of transverse strains at the bottom of AC layer along transverse direction under the centre of steering tire. It is clear that the transverse strain is very sensitive to transverse distance.

By comparing the pavement responses in May and in September, the distribution of transverse train is similar but the pavement is stronger is September than in May. The maximum transverse strain decreased 29.0% from 131 micro strains in May to 93 micro strains in September.

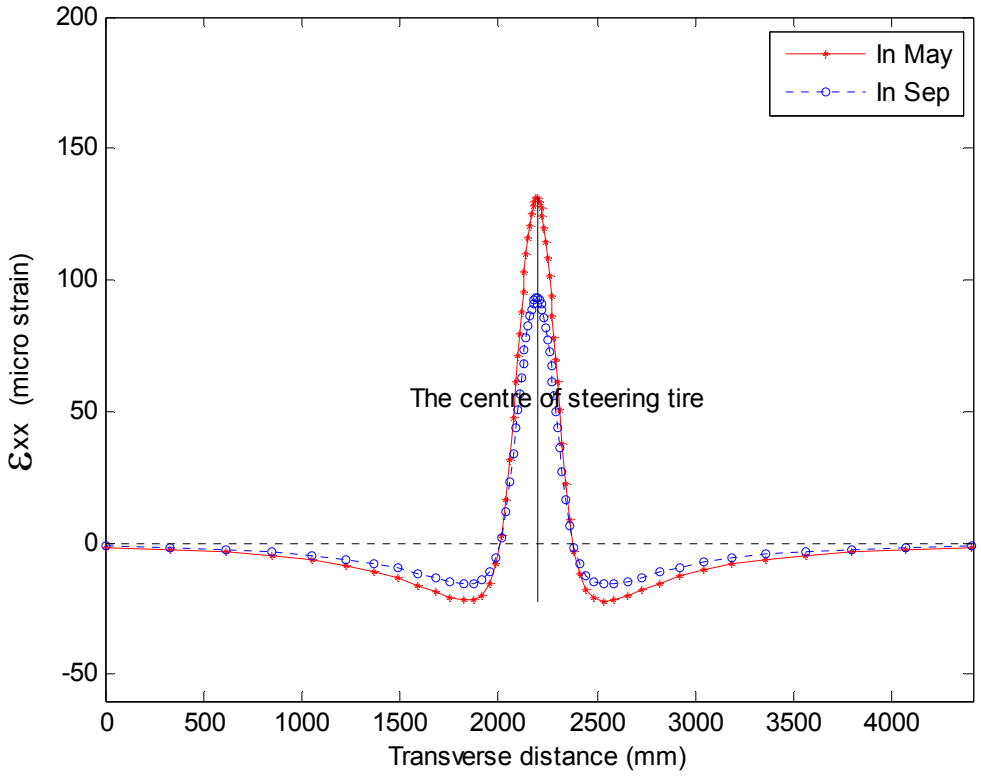

Figure 6-19 Transverse strains at bottom of AC layer along transverse direction under the centre of steering tire

Figure 6-20 shows the distribution of longitudinal strains at the bottom of AC layer along transverse direction under the centre of steering tire. It is clear that the transverse strain is not as sensitive as transverse strain to the transverse distance.

By comparing the pavement responses in May and in September, the distribution of longitudinal train is similar. The maximum longitudinal strain decreased 28.9% from 135 micro strains in May to 96 micro strains in September.

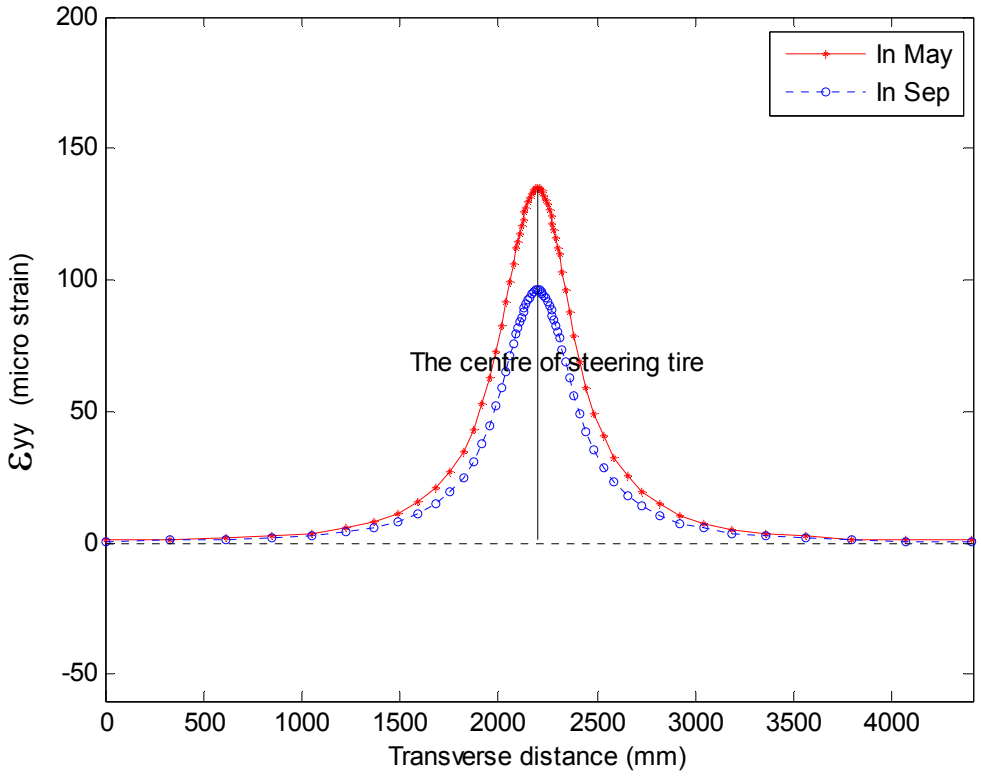

Figure 6-20 Longitudinal strains at bottom of AC layer along transverse direction under the centre of steering tire

Figure 6-21 shows the distribution of vertical strains on top of subgrade along transverse direction under the centre of steering tire.

By comparing the pavement responses in May and in September the distribution of vertical train is similar. The maximum vertical strain decreased 29.4% from 354 micro strains in May to 250 micro strains in September.

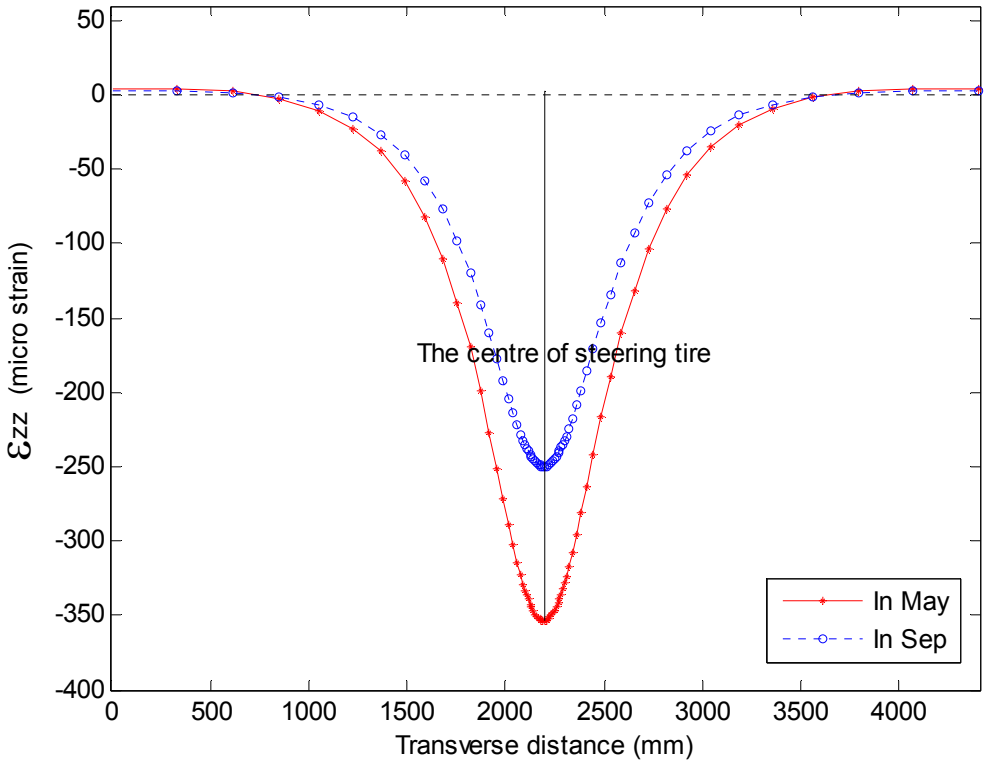

Figure 6-21 Vertical strains on top of subgrade along transverse direction under the centre of steering tire

Figure 6-22 through Figure 6-24 show the distributions of transverse strains, longitudinal strains, and vertical strains along longitudinal direction under the centre of the steering tire.

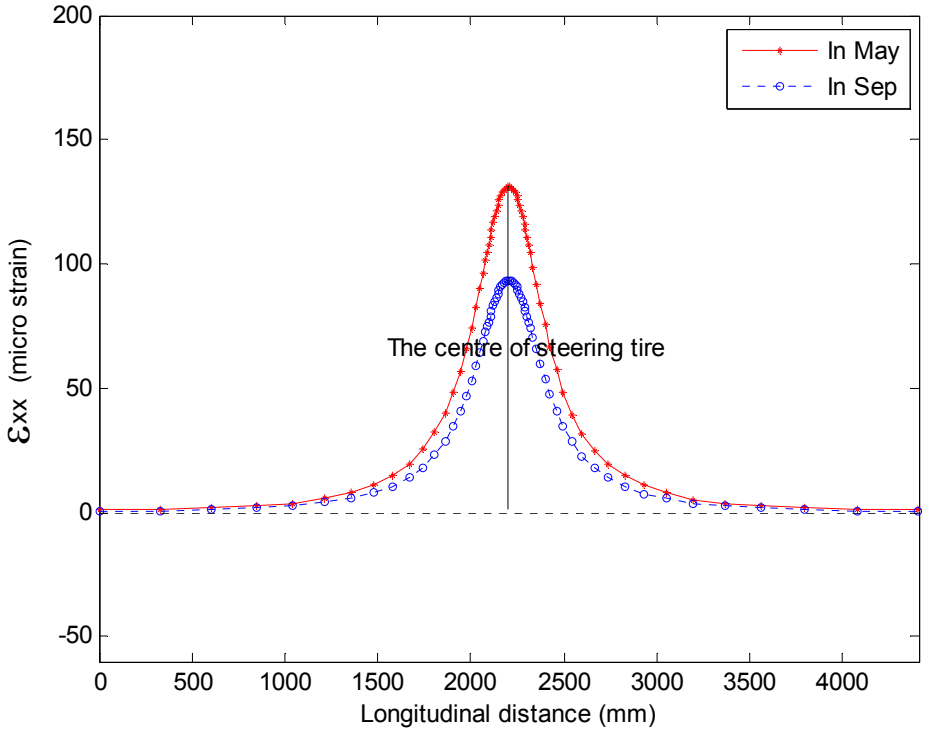

Figure 6-22 Transverse strains at bottom of AC layer along longitudinal direction under the centre of steering tire

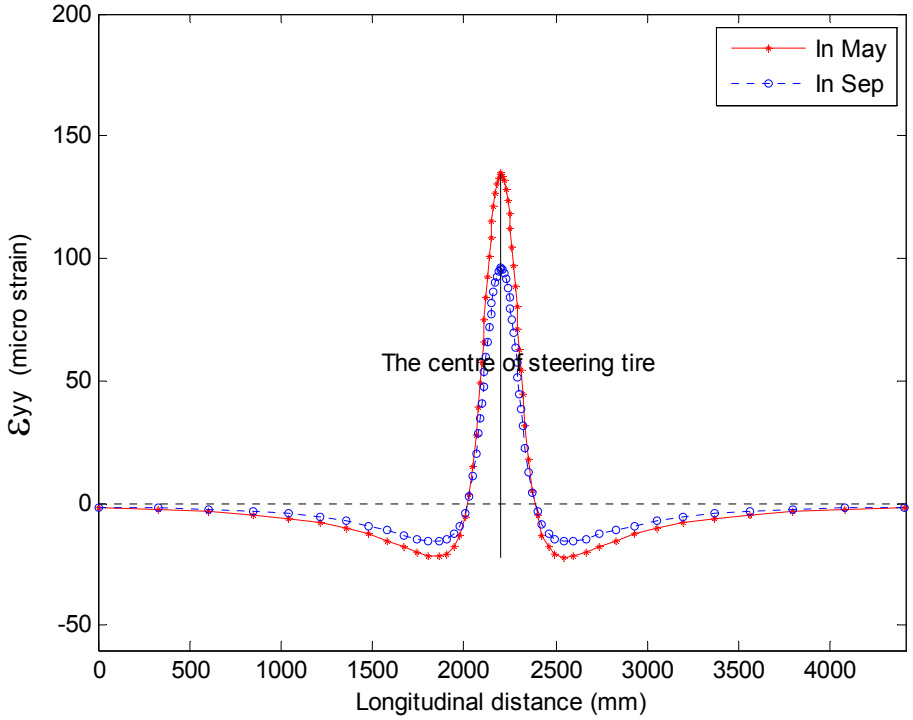

Figure 6-23 Longitudinal strains at bottom of AC layer along longitudinal direction under the centre of steering tire

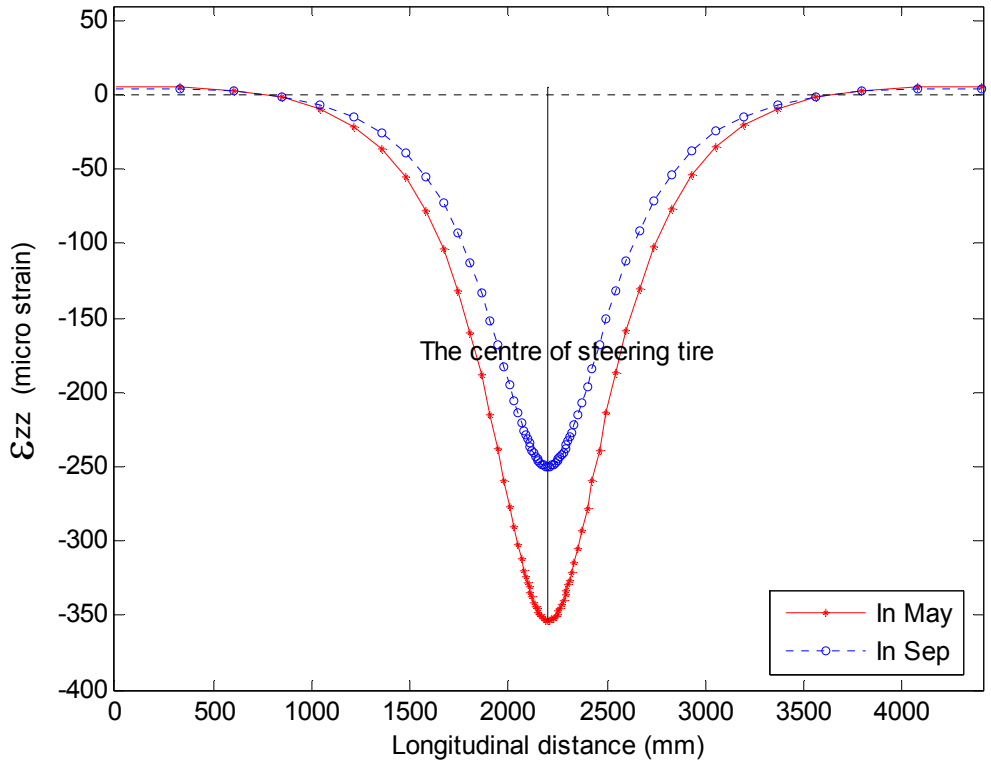

Figure 6-24 Vertical strains on top of subgrade along longitudinal direction under the centre of steering tire

6.5.2 SUMMARY OF COMPUTED STRAINS

(a)Computed strains at PTH11

Table 6-3 summarized the computed critical pavement responses at the bottom of AC layer under different load levels at PTH11 in May. For drive axle at A1L1 load, computed longitudinal strain decreased by 15.7% when tire pressure deflated from 690 kPa to 345 kPa, which is compatible to measured values. As can be seen in Table 6-4, the measured longitudinal strain decreased by 15.6% (gauges H12L and H14L in average)

when tire pressure decreased from 690 kPa to 345 kPa. For trailer1, the computed value is 10.1%, while the measured value is 13.4%.

Table 6-4 summarized the computed critical pavement responses at the bottom of AC layer under different load levels at PTH11 in September. For drive axle at A1L1 load, computed longitudinal strain decreased by 15.1% when tire pressure deflated from 690 kPa to 345 kPa, which is compatible to measured values. As can be seen in Table 6-15, the measured longitudinal strain decreased by 19.1% (gauges H12L and H14L in average) when tire pressure decreased from 690 kPa to 345 kPa. For trailer1, the computed value is 10.3%, while the measured value is 10.8%.

Table 6-3 Computed Critical Pavement Responses at Bottom of AC Layer of PTH11 in May

Axle	Tire load (kg) (level)	Tire pressure at 690 KPa (100 psi)			Tire pressure at 448/518 KPa (65/75 psi)			Tire pressure at 345 KPa (50 psi)			Strain difference (%) between 690 KPa and 345 KPa		
		$\varepsilon 1_{xx}$ (10^{-6})	$\varepsilon 1_{yy}$ (10^{-6})	$\varepsilon 1_{zz}$ (10^{-6})	$\varepsilon 2_{xx}$ (10^{-6})	$\varepsilon 2_{yy}$ (10^{-6})	$\varepsilon 2_{zz}$ (10^{-6})	$\varepsilon 3_{xx}$ (10^{-6})	$\varepsilon 3_{yy}$ (10^{-6})	$\varepsilon 3_{zz}$ (10^{-6})	$\frac{(\varepsilon 3_{zz} - \varepsilon 1_{zz}) * 100}{\varepsilon 1_{zz}}$	$\frac{(\varepsilon 3_{yy} - \varepsilon 1_{yy}) * 100}{\varepsilon 1_{yy}}$	$\frac{(\varepsilon 3_{zz} - \varepsilon 1_{zz}) * 100}{\varepsilon 1_{zz}}$
Dual tire Tandem (Drive) axle	1702.5 (A1L1)	76	121	-115	70	110	-105	66	102	-97	-13.2	-15.7	-15.7
	1872.5 (A1N)	79	124	-118	71	112	-105	68	107	-100	-13.9	-13.7	-15.3
	2167.5 (RTAC)	92	145	-137	83	131	-123	79	122	-115	-14.1	-15.9	-16.1
Dual tire Tridem (Trailer1) axle	1600 (A1L1)	79	109	-110	74	104	-104	70	98	-98	-11.4	-10.1	-10.9
	1847.5 (A1N)	89	122	-123	86	118	-119	80	111	-111	-10.1	-9.0	-9.8
	1902.5 (RTAC)	93	128	-129	89	122	-123	83	111	-113	-10.8	-13.3	-12.4

Table 6-4 Computed Critical Pavement Responses at Bottom of AC Layer of PTH11 in Sep.

Axle	Tire load (kg) (level)	Tire pressure at 690 KPa (100 psi)			Tire pressure at 448/518 KPa (65/75 psi)			Tire pressure at 345 KPa (50 psi)			Strain difference (%) between 690 KPa and 345 KPa		
		$\mathcal{E}1_{xx}$ (10^{-6})	$\mathcal{E}1_{yy}$ (10^{-6})	$\mathcal{E}1_{zz}$ (10^{-6})	$\mathcal{E}2_{xx}$ (10^{-6})	$\mathcal{E}2_{yy}$ (10^{-6})	$\mathcal{E}2_{zz}$ (10^{-6})	$\mathcal{E}3_{xx}$ (10^{-6})	$\mathcal{E}3_{yy}$ (10^{-6})	$\mathcal{E}3_{zz}$ (10^{-6})	$\frac{(\mathcal{E}3_{zz}-\mathcal{E}1_{zz})*100}{\mathcal{E}1_{zz}}$	$\frac{(\mathcal{E}3_{yy}-\mathcal{E}1_{yy})*100}{\mathcal{E}1_{yy}}$	$\frac{(\mathcal{E}3_{zz}-\mathcal{E}1_{zz})*100}{\mathcal{E}1_{zz}}$
Dual tire Tandem (Drive) axle	1702.5 (A1L1)	54	86	-82	50	78	-74	47	73	-69	-13.0	-15.1	-15.9
	1872.5 (A1N)	56	89	-84	51	80	-75	49	76	-71	-12.5	-14.6	-15.5
	2167.5 (RTAC)	65	103	-98	59	94	-88	56	87	-82	-13.8	-15.5	-16.3
Dual tire Tridem (Trailer1) axle	1600 (A1L1)	55	78	-78	53	74	-74	50	70	-70	-9.1	-10.3	-10.3
	1847.5 (A1N)	63	87	-87	61	84	-84	57	79	-79	-9.5	-9.2	-9.2
	1902.5 (RTAC)	67	91	-92	63	87	-87	59	79	-80	-11.9	-13.2	-13.0

Table 6-5 shows the measured strains at the bottom of AC layer by strain gauges of H12L, H14L, and H33T at PTH11 under static load in September.

Table 6-5 Measured Pavement Responses at Bottom of AC at PTH11 under Static load in Sep.

Test load	Axle	Tire pressure (kPa)	Strain gauge readings (micro strain)			
			H12L	H14L	(H12L+H14L)/2	H33T
A1L1	Drive	345	315	124	219.5	N/A*
		690	312	137	224.5	N/A
	Trailer1	345	256	166	211	N/A
		690	168	189	178.5	N/A
	Steering	690	184	182	183	206
A1N	Drive	345	238	216	227	N/A
		690	343	270	306.5	188
	Trailer1	345	304	192	248	N/A
		690	317	201	259	N/A
	Steering	690	227	230	228.5	238
RTAC	Drive	345	286	247	266.5	N/A
		690	267	N/A	267	N/A
	Trailer1	345	291	197	244	198
		690	304	N/A	304	338
	Steering	690	438	339	388.5	295

*Not available

Table 6-6 is comparing the measured and computed pavement responses at the bottom of AC layer at PTH11 in September. F_y is defined as measured longitudinal strain divided by computed longitudinal strains. F_x is the corresponding transverse values. F_y=2.96 in averaged (steering axle is not included); F_x=3.92 in averaged (steering axle is not included). F_y is more reliable than F_x because of the following reasons: first, twelve F_y values are available, while only three F_x values are available in Table 6-6. Second, as discussed in 6.5.1, measured longitudinal strain demonstrated much more stable than transverse strain, which has been verified by the distribution of computed strains. As a result, a factor of 2.96 will be applied to the FE molding results.

Table 6-6 Measured and Computed Pavement Responses at Bottom of AC at PTH11 in Sep.

Test load	Axle	Tire pressure (kPa)	Measured ε_{yy} (10^{-6})	Computed ε_{yy} (10^{-6})	$\frac{Measured\ \varepsilon_{yy}}{Computed\ \varepsilon_{yy}}=F_y$	Measured ε_{xx} (10^{-6})	Computed ε_{xx} (10^{-6})	$\frac{Measured\ \varepsilon_{xx}}{Computed\ \varepsilon_{xx}}=F_x$
A1L1	Drive	345	219.5	73	3.01	N/A	47	N/A
		690	224.5	86	2.61	N/A	54	N/A
	Trailer1	345	211	70	3.01	N/A	50	N/A
		690	178.5	78	2.29	N/A	55	N/A
	Steering	690	183	96	1.91	206	93	2.22
A1N	Drive	345	227	76	2.99	N/A	49	N/A
		690	306.5	89	3.44	188	56	3.36
	Trailer1	345	248	79	3.14	N/A	57	N/A
		690	259	87	2.98	N/A	63	N/A
	Steering	690	228.5	N/A*	N/A	238	N/A	N/A
RTAC	Drive	345	266.5	87	3.06	N/A	56	N/A
		690	267	103	2.59	N/A	65	N/A
	Trailer1	345	244	79	3.09	198	59	3.36
		690	304	91	3.34	338	67	5.04
	Steering	690	388.5	N/A	N/A	295	N/A	N/A

N/A—Not available

Table 6-7 and Table 6-8 summarized the computed critical pavement responses on top of subgrade at PTH11 in May and September, respectively. When tire pressure deflated from 690 kPa to 345 kPa, the vertical strain decreased only from 1.1% to 3.2%; while the horizontal strain decreased from 9.0% to 15.7%. This result may indicate that CTI is effective to prevent the bottom up failure of AC layer; but may not be effective to prevent the rutting of the pavement. Table 6-9 shows the computed critical pavement responses by steering axle at PTH11. The foot print of steering axle was measured only for A1L1 load. The computed strains at the bottom of AC layer and on top of subgrade are about 29% less in September than in May, which is compatible to the results by drive and trailer1 axles.

(b)Computed strains at PR304

Table 6-10 shows the computed critical pavement responses at the depth of 132 mm at PR304 in May. Table 6-10 shows the computed critical pavement responses at the depth of 132 mm at PR304 in September. Due to the malfunction of the installed strain gauges, it was unable to carry out field test at PR304 in September. As a result, the factor of FE molding result is not available for PR304.

Table 6-12 and Table 6-13 summarized the computed critical pavement responses on top of subgrade at PR304 in May and in September. Comparing to the results at PTH11, a quite similar pattern was observed at PR304 when tire pressure deflated from 690 kPa to 3345 kPa.

Table 6-14 shows the computed critical pavement responses by steering axle at PR304. The foot print of steering axle was measured only for B1N load. The computed strains in GB layer at the depth of 132 mm and on top of subgrade are about 24.5% less in September than in May, which is compatible to the results by drive and trailer1 axles.

Table 6-7 Computed Critical Pavement Responses on Top of Subgrade at PTH11 in May

Axle	Tire load (kg) (level)	Tire pressure at 690 KPa (100 psi)			Tire pressure at 448/518 KPa (65/75 psi)			Tire pressure at 345 KPa (50 psi)			Strain difference (%) between 690 KPa and 345 KPa		
		$\varepsilon 1_{xx}$ (10^{-6})	$\varepsilon 1_{yy}$ (10^{-6})	$\varepsilon 1_{zz}$ (10^{-6})	$\varepsilon 2_{xx}$ (10^{-6})	$\varepsilon 2_{yy}$ (10^{-6})	$\varepsilon 2_{zz}$ (10^{-6})	$\varepsilon 3_{xx}$ (10^{-6})	$\varepsilon 3_{yy}$ (10^{-6})	$\varepsilon 3_{zz}$ (10^{-6})	$\frac{(\varepsilon 3_{zz} - \varepsilon 1_{zz}) * 100}{\varepsilon 1_{zz}}$	$\frac{(\varepsilon 3_{yy} - \varepsilon 1_{yy}) * 100}{\varepsilon 1_{yy}}$	$\frac{(\varepsilon 3_{zz} - \varepsilon 1_{zz}) * 100}{\varepsilon 1_{zz}}$
Dual tire Tandem (Drive) axle	1702.5 (A1L1)	161	145	-412	160	143	-408	159	140	-404	-1.2	-3.4	-1.9
	1872.5 (A1N)	176	157	-449	175	154	-444	174	152	-441	-1.1	-3.2	-1.8
	2167.5 (RATC)	205	183	-522	203	179	-515	202	175	-510	-1.5	-4.4	-2.3
Dual tire Tridem (Trailer1) axle	1600 (A1L1)	159	110	-377	158	109	-374	157	108	-372	-1.3	-1.8	-1.3
	1847.5 (A1N)	185	127	-436	185	126	-434	183	124	-431	-1.1	-2.4	-1.1
	1902.5 (RATC)	190	131	-449	189	130	-447	183	126	-435	-3.7	-3.8	-3.1

Table 6-8 Computed Critical Pavement Responses on Top of Subgrade at PTH11 in Sep.

Axle	Tire load (kg) (level)	Tire pressure at 690 KPa (100 psi)			Tire pressure at 448/518 KPa (65/75 psi)			Tire pressure at 345 KPa (50 psi)			Strain difference (%) between 690 KPa and 345 KPa		
		$\varepsilon 1_{xx}$ (10^{-6})	$\varepsilon 1_{yy}$ (10^{-6})	$\varepsilon 1_{zz}$ (10^{-6})	$\varepsilon 2_{xx}$ (10^{-6})	$\varepsilon 2_{yy}$ (10^{-6})	$\varepsilon 2_{zz}$ (10^{-6})	$\varepsilon 3_{xx}$ (10^{-6})	$\varepsilon 3_{yy}$ (10^{-6})	$\varepsilon 3_{zz}$ (10^{-6})	$\frac{(\varepsilon 3_{zz} - \varepsilon 1_{zz}) * 100}{\varepsilon 1_{zz}}$	$\frac{(\varepsilon 3_{yy} - \varepsilon 1_{yy}) * 100}{\varepsilon 1_{yy}}$	$\frac{(\varepsilon 3_{zz} - \varepsilon 1_{zz}) * 100}{\varepsilon 1_{zz}}$
Dual tire Tandem (Drive) axle	1702.5 (A1L1)	114	103	-291	113	78	-288	112	99	-285	-1.8	-3.9	-2.1
	1872.5 (A1N)	124	111	-317	123	109	-313	123	107	-311	-0.8	-3.6	-1.9
	2167.5 (RATC)	144	129	-368	143	126	-363	143	124	-360	-0.7	-3.9	-2.2
Dual tire Tridem (Trailer1) axle	1600 (A1L1)	112	78	-266	111	77	-264	110	76	-262	-1.8	-2.6	-1.5
	1847.5 (A1N)	130	90	-308	130	89	-306	129	88	-304	-0.8	-2.2	-1.3
	1902.5 (RATC)	134	93	-317	133	92	-315	129	89	-307	-3.7	-4.3	-3.2

Table 6-9 Computed Critical Pavement Responses by Steering Axle at PTH11

Axle	Tire load (kg)	Tire pressure (kPa)	Time	Bottom of AC layer			Top of Subgrade		
				ε_{xx} (10^{-6})	ε_{yy} (10^{-6})	ε_{zz} (10^{-6})	ε_{xx} (10^{-6})	ε_{yy} (10^{-6})	ε_{zz} (10^{-6})
Single tire single (steering) axle	2505 (A1L1)	690	May	131	135	-155	142	142	-354
			Sep	93	96	-110	100	101	-250
			(Sep-May)/May (%)	-29.0	-28.9	-29.0	-29.6	-28.9	-29.4

Table 6-10 Computed Critical Pavement Responses at Depth of 132 mm at PR304 in May

Axle	Tire load (kg) (level)	Tire pressure at 690 KPa (100 psi)			Tire pressure at 448/518 KPa (65/75 psi)			Tire pressure at 345 KPa (50 psi)			Strain difference (%) between 690 KPa and 345 KPa		
		$\varepsilon 1_{xx}$ (10^{-6})	$\varepsilon 1_{yy}$ (10^{-6})	$\varepsilon 1_{zz}$ (10^{-6})	$\varepsilon 2_{xx}$ (10^{-6})	$\varepsilon 2_{yy}$ (10^{-6})	$\varepsilon 2_{zz}$ (10^{-6})	$\varepsilon 3_{xx}$ (10^{-6})	$\varepsilon 3_{yy}$ (10^{-6})	$\varepsilon 3_{zz}$ (10^{-6})	$\frac{(\varepsilon 3_{zz} - \varepsilon 1_{zz}) * 100}{\varepsilon 1_{zz}}$	$\frac{(\varepsilon 3_{yy} - \varepsilon 1_{yy}) * 100}{\varepsilon 1_{yy}}$	$\frac{(\varepsilon 3_{zz} - \varepsilon 1_{zz}) * 100}{\varepsilon 1_{zz}}$
Dual tire Tandem (Drive) axle	1092.5 (B1L2)	148	222	-600	127	197	-542	118	186	-517	-20.3	-16.2	-13.8
	1702.5 (B1N)	184	294	-809	149	242	-695	126	205	-617	-31.5	-30.3	-23.7
	1872.5 (A1N)	175	281	-797	136	221	-663	120	195	-605	-31.4	-30.6	-24.1
Dual tire Tridem (Trailer1) axle	1600 (B1N)	200	288	-805	177	260	-740	154	233	-674	-23.0	-19.1	-16.3
	1847.5 (A1N)	216	306	-877	199	287	-830	170	251	-745	-21.3	-18.0	-15.1

Table 6-11 Computed Critical Pavement Responses at Depth of 132 mm at PR304 in Sep.

Axle	Tire load (kg) (level)	Tire pressure at 690 KPa (100 psi)			Tire pressure at 448/518 KPa (65/75 psi)			Tire pressure at 345 KPa (50 psi)			Strain difference (%) between 690 KPa and 345 KPa		
		$\varepsilon 1_{xx}$ (10^{-6})	$\varepsilon 1_{yy}$ (10^{-6})	$\varepsilon 1_{zz}$ (10^{-6})	$\varepsilon 2_{xx}$ (10^{-6})	$\varepsilon 2_{yy}$ (10^{-6})	$\varepsilon 2_{zz}$ (10^{-6})	$\varepsilon 3_{xx}$ (10^{-6})	$\varepsilon 3_{yy}$ (10^{-6})	$\varepsilon 3_{zz}$ (10^{-6})	$\frac{(\varepsilon 3_{zz} - \varepsilon 1_{zz}) * 100}{\varepsilon 1_{zz}}$	$\frac{(\varepsilon 3_{yy} - \varepsilon 1_{yy}) * 100}{\varepsilon 1_{yy}}$	$\frac{(\varepsilon 3_{zz} - \varepsilon 1_{zz}) * 100}{\varepsilon 1_{zz}}$
Dual tire Tandem (Drive) axle	1092.5 (B1L2)	110	167	-456	98	147	-409	87	138	-390	-20.9	-17.4	-14.5
	1702.5 (B1N)	135	219	-611	108	178	-522	90	150	-461	-33.3	-31.5	-24.5
	1872.5 (A1N)	128	207	-599	136	221	-663	85	141	-450	-33.6	-31.9	-24.9
Dual tire Tridem (Trailer1) axle	1600 (B1N)	148	215	-610	130	194	-558	112	172	-507	-24.3	-20.0	-16.9
	1847.5 (A1N)	160	228	-662	146	213	-625	124	185	-560	-22.5	-18.9	-15.4

Table 6-12 Computed Critical Pavement Responses on Top of Subgrade at PR304 in May

Axle	Tire load (kg) (level)	Tire pressure at 690 KPa (100 psi)			Tire pressure at 448/518 KPa (65/75 psi)			Tire pressure at 345 KPa (50 psi)			Strain difference (%) between 690 KPa and 345 KPa		
		$\mathcal{E}1_{xx}$ (10^{-6})	$\mathcal{E}1_{yy}$ (10^{-6})	$\mathcal{E}1_{zz}$ (10^{-6})	$\mathcal{E}2_{xx}$ (10^{-6})	$\mathcal{E}2_{yy}$ (10^{-6})	$\mathcal{E}2_{zz}$ (10^{-6})	$\mathcal{E}3_{xx}$ (10^{-6})	$\mathcal{E}3_{yy}$ (10^{-6})	$\mathcal{E}3_{zz}$ (10^{-6})	$\frac{(\mathcal{E}3_{zz}-\mathcal{E}1_{zz})*100}{\mathcal{E}1_{zz}}$	$\frac{(\mathcal{E}3_{yy}-\mathcal{E}1_{yy})*100}{\mathcal{E}1_{yy}}$	$\frac{(\mathcal{E}3_{zz}-\mathcal{E}1_{zz})*100}{\mathcal{E}1_{zz}}$
Dual tire Tandem (Drive) axle	1092.5 (B1L2)	95	88	-243	94	87	-241	94	87	-240	-1.1	-1.1	-1.2
	1702.5 (B1N)	145	135	-373	144	132	-369	142	130	-365	-2.1	-3.7	-2.1
	1872.5 (A1N)	158	146	-406	157	143	-401	156	141	-398	-1.3	-3.4	-2.0
Dual tire Tridem (Trailer1) axle	1600 (B1N)	147	105	-344	142	104	-341	141	102	-339	-4.1	-2.9	-1.5
	1847.5 (A1N)	166	120	-398	166	119	-396	165	117	-393	-0.6	-2.5	-1.3

Table 6-13 Computed Critical Pavement Responses on Top of Subgrade at PR304 in Sep.

Axle	Tire load (kg) (level)	Tire pressure at 690 KPa (100 psi)			Tire pressure at 448/518 KPa (65/75 psi)			Tire pressure at 345 KPa (50 psi)			Strain difference (%) between 690 KPa and 345 KPa		
		$\varepsilon 1_{xx}$ (10^{-6})	$\varepsilon 1_{yy}$ (10^{-6})	$\varepsilon 1_{zz}$ (10^{-6})	$\varepsilon 2_{xx}$ (10^{-6})	$\varepsilon 2_{yy}$ (10^{-6})	$\varepsilon 2_{zz}$ (10^{-6})	$\varepsilon 3_{xx}$ (10^{-6})	$\varepsilon 3_{yy}$ (10^{-6})	$\varepsilon 3_{zz}$ (10^{-6})	$\frac{(\varepsilon 3_{zz} - \varepsilon 1_{zz}) * 100}{\varepsilon 1_{zz}}$	$\frac{(\varepsilon 3_{yy} - \varepsilon 1_{yy}) * 100}{\varepsilon 1_{yy}}$	$\frac{(\varepsilon 3_{zz} - \varepsilon 1_{zz}) * 100}{\varepsilon 1_{zz}}$
Dual tire Tandem (Drive) axle	1092.5 (B1L2)	71	67	-184	71	66	-183	71	66	-182	0.0	-1.5	-1.1
	1702.5 (B1N)	109	102	-282	108	100	-279	107	99	-276	-1.8	-2.9	-2.1
	1872.5 (A1N)	119	111	-307	157	143	-401	117	107	-302	-1.7	-3.6	-1.6
Dual tire Tridem (Trailer1) axle	1600 (B1N)	107	80	-260	106	79	-258	106	78	-256	-0.9	-2.5	-1.5
	1847.5 (A1N)	125	92	-301	124	91	-300	124	89	-297	-0.8	-3.3	-1.3

Table 6-14 Computed Critical Pavement Responses by Steering Axle at PR304

Axle	Tire load (kg)	Tire pressure (kPa)	Time	GB layer at 132 mm			Top of Subgrade		
				ε_{xx} (10^{-6})	ε_{yy} (10^{-6})	ε_{zz} (10^{-6})	ε_{xx} (10^{-6})	ε_{yy} (10^{-6})	ε_{zz} (10^{-6})
Single tire single (steering) axle	2505 (B1N)	690	May	366	382	-1191	129	129	-318
			Sep	272	285	-900	97	98	-242
			(Sep-May)/May (%)	-25.7	-25.4	-24.4	-24.8	-24.0	-23.9

6.6 SUMMARY

The results and discussion in this chapter can be summarized as follows:

- Transverse strain is very sensitive to the transverse distance to the centre of analyzing tire; longitudinal strain is sensitive to the longitudinal distance to the centre of analyzing tire. This observation gives the reason why longitudinal strain gauges always have less variable readings than transverse stain gauges during field TPCS tests.
- A factor of 2.96 can be applied to FE molding results under static load for thin AC pavement.
- TPCS is effective to prevent bottom up failure of AC layer, but not effective to prevent pavement rutting.
- TPCS is effective for both thin AC and AST pavement.
- The pavements of PTH11 and PR304 are about 30% stronger in September than in May.

Future works of this research and recommendations are as follows:

- A FE model with dynamic loading is necessary to simulate further the pavement responses with truck load.
- The moduli of different layers of pavement are the most import inputs for the FE model. In this research, the moduli are back calculated according to FWD tests which are subject to certain error.
- To find the relation among moduli of different layers, pavement temperature and moisture level will be helpful to predict pavement responses by FE simulation.

CHAPTER 7 CONCLUSIONS AND RECOMMENDATIONS

7.1 CONCLUSIONS

7.1.1 PAVEMENT AND AIR TEMPERATURES

Temperature data has been collected from mid November, 2008 to present. Based on this research, the following conclusions can be drawn:

- The air freezing index at test sites was -2013.1 (^{o}C-days) in 2009. The maximum frost depth at PTH11 was 2265 mm in 2009.
- Pavement at PTH11 was thawed completely on June 7, 2009.
- In terms of the prediction of thawing depth, $\mathrm{Ti_R}$, $\mathrm{Ti_N}$, $\mathrm{Ti_{RM}}$ are all good indicators. They can be used to predict the dates of SLR implementation.

7.1.2 PAVEMENT VOLUMETRIC MOISTURE CONTENT

- Pavement volumetric moisture content was monitored by water content reflectometer probe (WCR) which works well on both sites. The moisture profiles agree with pavement temperature profiles. Based on the moisture profile, the pavement can be divided into four periods as follows:
- Form November 24, 2008 to March 14, 2009 the pavement of both PTH11 and PR304 were in the period of deep frost.
- From March 15, 2009 to April 15, 2009 the pavements were in the period of rapid strength loss.

- From April 16, 2009 to May 8, 2009 the pavements were in the period of rapid strength recovery.
- Began from May 9, 2009 the pavements were in the period of slow strength recovery.

7.1.3 TIRE PRESSURE CONTROL SYSTEM TESTS

- TPCS is effective to reduce the strain at the bottom of asphalt pavement. The measured strain decreased significantly for all the configurations of load levels and truck speeds when tires were deflated by 50% from 690 kPa to 345 kPa.
- When other tires' pressure decreased from 690 kPa to 345 kPa, the strain produced by steering axle increased although the pressure of steering tires never changed, which indicates that the effect of steering tires upon the pavement is quite different from other tires for a truck equipped with TPCS.
- Longitudinal gauges recorded the least variable strains for all the TPCS tests. This observation was verified by FE model.
- Measured longitudinal strain at the bottom of AC layer in September is 40% to 70% less than in May.
- For different truck speeds, the strain variation is different when the tire pressure was changed the same amount. The higher the truck speed, the more significant strain differences have been observed.
- Maximum strain is usually generated by either drive or trailer1 axle, which depends on wheel offset of test truck.

- In all cases, the measured longitudinal strain decreased when the truck speed increased. For example, when the test truck speed increased from 20 km/h to 70 km/h at A1L1 load, the measured longitudinal strain decreased from 11.8% to 18.4% for different runs.

7.1.4 FINITE ELEMENT SIMULATION

A 3D FE model with ABAQUS version 6.7-5 was developed to simulate a block of pavement for PTH11 and PR304. The eight-node, linear brick elements (C3D8) were used for the analysis. The inputs of the model are back calculated resilient moduli of different layers based on FWD test, measured footprint, simulation time of the pavement (the spring or the fall), axle group (steering, drive or trailer), and the dimensions of pavement block. In order to do factorial study, a code was developed by using Matlab. Based on the simulation results, the following conclusions can be drawn:

- Transverse strain is very sensitive to the transverse distance to the centre of analyzed tire; longitudinal strain is sensitive to the longitudinal distance to the centre of analyzed tire. This supports the observation that longitudinal strain gauges always have less variable readings than transverse stain gauges during field tests.
- A factor of 2.96 can be applied to FE molding results under static load for thin AC pavement in September.
- Tire pressure reduction is effective to prevent bottom up failure of AC layer, but not effective to prevent pavement rutting.

- Tire pressure reduction is effective for both thin AC and AST pavement.
- The pavements of PTH11 and PR304 are about 30% stronger in the fall than in the spring thaw period.

7.2 RECOMMENDATIONS FOR FUTURE WORK

7.2.1 INSTRUMENTATION

The quality of instrument installation is extremely important for field data. Great attention was paid to the installation of all sensors in this project. External contractors were hired to complete the following tasks: coring into the road surface, drilling into the road base and subgrade, and excavation of trenches in the road shoulder and ditches. Also CTL was retained to install the MDDs. Six months after the installation, all sensors worked well, and another four months later 50% of the strain gauges and one sensors of MDD stopped working. The survival rate of this project is compatible with other reported projects.

For this research, trouble shooting of the malfunction sensors will be continuing; single depth deflectometer was installed in September, 2009 to check with MDD readings.

At least 50% back up of sensors is necessary for instrumentation; using some different kind of sensor for similar purpose is a good idea.

7.2.2 TIRE PRESSURE CONTROL SYSTEM TESTS AND FE MODELING

In addition to field TPCS tests, a full scale, indoor loading test in pavement testing indoor facility is very helpful. With indoor loading test, it is easy to control and measure the wheel offset. Also it is not difficult to find the moduli of different layers of pavement with better quality than back calculated values based on FWD test in this project.

A FE model with dynamic loading is necessary to simulate further the pavement responses with truck load.

REFERENCES

#21, C-SHRP Technical Brief. (2000). Seasonal Load Restrictions in Canada and Around the World. TRB 2004 annual Meeting CD_ROM.

Acum, W. and Fox, L. (1951). Computation of Load Stresses in a Three-Layer Elastic System. *Geotechnique, Vol. 2* , 293-300.

Aircti. (2009). *Homepage*. Retrieved 09 13, 2009, from Web Site of AIR CTI: http://www.aircti.com/

Aldrich, H. and Paynter, H. (1966). *Depth of Frost Penetration in Non-uniform Soil.* U.S. Army cold Regions Research and Engineering Laboratory special Report.

Al-Qadi, I., Wang, H., and Yoo, P. (2008). Dynamic Analysis and In-Situ Validation of Perpetual Pavement Response to Vehicular Loading. *TRB 2008 Annual Meeting CD-ROM.*

Andersland, O. and Ladanyi, B. (2004). *Frozen Ground Engineering. 2nd ed.* Hoboken: John Wiley & Sons, Inc.

Andersland, Q. and Ladanyi, B. (2004). *Frozen Ground Engineering.* Hoboken: John Wiley & Sons, Inc.

Barksdale, R. (1967). Predicting Performance of Bituminous Surfaced Pavements. *Proceedings, Second International conference on the Structural Design of Asphalt Pavement* (pp. 321-340). University of Michigan.

Benson, A., Williamson, D., and other memebers. (2001). *2000 Spring Load Restrictions Task Force Legislative Report*. Retrieved July 14, 2009, from Mn/DOT: http://www.mrr.dot.state.mn.us/research/pdf/2001MRRDOC001.pdf

Bradley, A. (2006). Hauling with Full axle Weights and Reduced Tire Pressure on Weight-Restricted Roads in British Columbia. *Transportation Research Record: Journal of the Transportation Research Board (No. 1967)* , 20-26. Washington D.C.: Transportation Research Board of the National Academies.

Brown, C. and Sessions, J. (1999). *Variable Tire Pressures for Tropical Forest? "Synthesis of Concepts and Applications"*. Retrieved 09 14, 2009, from Food and Agriculture Organization of the United Nations (FAO) CORPORATE DOCUMENT REPOSITORY: http://www.fao.org/docrep/w2809E/w2809e03.htm#P8_0

Brown, E. (1963). Relation between mean annual air and ground temperature in the Permafrost Region of Canada. *Conference on permafrost*, (pp. 241-247). Washington D.C.

Burmister, D. (1943). The Theory of Stress and Displacement in Layered Systems and Application to the Design of Airport Runway. *Proceedings, Highway Research Board.*

Campbell Scientific Inc. (2006). CS616 and CS625 Water Content Reflectometers--Instruction Manual.

Della-Morette, L. and Hodges, H. (1986). Off-highway tire/road damage and healing mechanisms. *1986 Summer Meeting of American Society of Agricultural Engineers*, (p. 10). San Luis Obispo, CA.

Diefenderfer, B., Al-Qadi, I., and Loulizi, A. (2001). Continuous Monitoring of Pavement Moisture Using Time Domain Reflectometry Probes. *TRB 80th Annual Meeting.* Washington, D.C.: Transportation Research Board.

Duncan, J., Monismith, C., and Wilson, E. (1968). Finite Element Analyses of Pavements. *Highway Research Record No. 228, Highway Research Board* , 18-33.

Edlefsen, N. and Anderson, A. (1943). Thermodynamics of Soil Moisture. *Journal of Agriculture Science* , 31-298.

Feng, M. , Fredlund, D., and Shuai, F. (2002). A Laboratory Study of the Hysteresis of A thermal conductivity Soil Suction Sensor. *Geotechnical Testing Journal* , 303-314.

Feng, M. and Fredlund, D. (2003). Calibration of Thermal Conductivity Sensors with Consideration of Hysteresis. *Canadian Geotechnical Journal* , 1048-1055.

Fredlund, D., and Xing, A. (1994). Equations for the soil-water characteristic curve. *Canadian Geotechnical Journal* , 521-532.

Fredlund, D., Shuai, F., and Feng, M. (2002). Use of grain-size distribution for estimation of the soil water characteristics curve. *Canadian Geotechnical Journal* , 1103-1117.

Grau, R. (1993). *Effects of Variable Tire Pressure On Road Surfacings. Volume I: Design, Construction, Behavior under Traffic, and Test Ressults.* Vicksburg, Miss: US Armay Corps Of Engineers, Waterways Exxperiment Station. Technical Report GL-93-20. Prepared for the U.S. Department of Agriculture Forest Service.

Gupta, S., and Wang, D. (2006, March 27). Water Retention in soil. *Encyclopedia of Soil Science* .

Howard, I., Warren, K., Eamon, C., and Lord, C. (2008). Variability Analysis of Low Volume Instrumented Thin Flexible Pavement. *Presented at 87th Annual Meeting of the Transportation Research Board* . Washington, D.C.

Huang, B., Mohammad, L., and Rasoulian, M. (2001). Three-Dimensional Numerical Simulation of Asphalt Pavement at Louisiana Accelerated Loading Facility. *Transportation Research Record No. 1764* , 44-58.

Huang, Y. (1967). Stresses and displacements in Viscoelastic Layered System under Circular Loaded Areas. *Proceedings, Second International Conference on the Structure Design of Asphalt Pavement* (pp. 225-244). University of Michigan.

Hung, Y. (1993). *Pavement analysis and design.* Englewood Cliffs, New Jersey: Prentice-Hall, Inc.

Janoo, V. and Berg, R. (1990). predicting the behavior of asphalt concrete pavements in seasonal frost areas using nondestructive techniques. *CRREL Report* .

Khan, A. and Shalaby, A. (2002). Performance of a road base constructed with shredded rubber tires. *Annual conference of the Canadian Society for Civil Engineering.* Montreal, QC.

Kim, M. and Tutumluer, E. (2007). Nonlinear Pavement Foundation Modeling for Three-Dimensional Finite Element Analysis of Flexible Pavements. *TRB2007 Annual Meeting CD-ROM.*

Kubo, Y.and Sugaware, M. (1982). The influence of frost action on the bearing capacity of flexible pavements. *Proceedings of International Symposium on bearing capacity of roads and airfields*, (p. 344). Trondheim.

Levinson, D., Li, N., Zou, X., Smalkoski, B., and Hashamil, M. (2004). A Framework for Analyzing the Effects of Spring Load Restriction. *Transportation Research Record: Journal of the Transportation Research Board* , 181-188. Washington, D.C.: No. 1874,Transportation Research Board of the National Academies.

Lunardini, V. (1978). Theory of n-factor and correlation of data. *Third Int. Conf. on permafrost.* Edmonton,AB.

Lungal, M. and Si, B. (2008). Coiled Time Domain Reflectometry matric Potential Sensor. *Soil Science Society of America* .

MIT. (2002). Thawing Index Calculation for Manitoba. TRANSPORTATION AND GOVERNMENT SERVICES MATERIALS ENGINEERING BRANCH.

Mn/DOT. (2009). *Thaw Definitions and Load Restriction Criteria*. Retrieved July 23, 2009, from Mn/DOT Materials and Road Research: http://www.mrr.dot.state.mn.us/research/seasonal_load_limits/thawindex/thawdefs.asp

Munro, R. and MacCulloch, F. (2008). *Tyre Pressure Control on Timer Haulage Vehicles--Some observations on a trial in Highland, Scotlan.* ROADEXIII NORTHERN PERIPHERY.

Park, D. (2008). Prediction f Pavement Fatigue and Rutting Life Using Different Tire Types. *KSCE Journal of Civil Engineering* , 297-303.

Refsdal, G., Senstad, P., and Soerlie, A. (2004). The Lifting of All Seasonal Load Restrictions in Norway in 1995-Background and Effects. TRB 2004 Annual Meeting CD-ROM.

Scrivner, F., and Peoh, R. (1969). *Detecting seasonal changes in load-carrying capabilities of flexible pavements.* National cooperative highway research program report 76.

Shuai, F., Clements, C., Ryland,L., and Fredlund, D. (2002). Some factors that influence soil suction measurement using a thermal conductivity sensor. *Third International Conference on Unsaturated Soils.* Recife, Brazil.

Siddharthan, R., Krishnamenon, N.,and El-Mously, M. (2002). Investigation of tire contact stress distribution on pavement response. *Journal of Transportation Engineering* , 136-144.

The University of Toledo (Mechanics of Unsaturated Soils). (2009). Retrieved March 15, 2009, from http://www.eng.utoledo.edu

Tielking, J. and Robert, F. (1987). tire contact pressure and its effect on pavement strain. *Journal of Transportation Engineering* , 56-71.

Timm, D. and Willis J. (2008). Repeatability of Asphalt Strain measurement Under Full-Scale Dynamic Loading. *Transportation Research Record: Journal of the Transportation Research Board (No. 2087)* , 40-48. Washington D.C.: Transportation Research Board of the National Academies.

Tomko, P. (2008). *Soil Survey Report.* Winnipeg.

Wang, F. and Machemehl, R. (2006). Mechanistic-Empirical Study of Effects of Truck Tire Pressure on Pavement: Measured Tire-Pavement Contact Stress Data. *Transportation Research Record: Journal of the Transportation Research Board* , 136-145.

Wang, F. and Machemehl, R. (2006). *Predicting Truck Tire Pressure Effects upon Pavement Performance.* Texas: Center for Transportation Research, University of Texas at Austin.

White, T. (1998). Application of Finite Element Analysis to Pavement Problems. *Finite Element for Pavement Analysis and Design, Proceeding of the First National Symposium on 3D Finite Element Modeling for Pavement Analysis & Design.* Charleston, W. Virginia.

Witczak, M., Schwartz, C., Feng, Y., Uzan, J., and Mirza, W. (2004). Finite element Procedures for Flexible Pavement Analysis. *NCHRP Finial Document, Appendix RR* . Washington D.C.: Transportation Research Board.

Yoo, P., Al-Qadi, M., and Elseifi, M. (2006). Effect of Moving Wheel Load Amplitude and Interface Condition on Flexible Pavement Responses. *Transportation Research Board 85th Annual Meeting.* Washington, D.C.

Zaghloul, S. (1993). Non-Linear Dynamic Analysis of Flexible and Rigid Pavement. *Ph.D. Dissertation* . Purdue University.

Zollinger, D., Lee, S., Puccinelli, J., and Jackson, N. (2008). *Long Term Pavement Performance Computed Parameter: Moisture Content.* Mclean, VA.

APPENDIX: INSTRUMENTATION

A.1 INTRODUCTION

This chapter outlines the types and locations of instrumentation sensors and data acquisition methods at each of the sites. It also covers calibration, installation and testing of the various components that were installed at the two instrumented section on two-way provincial trunk highway 11 (PTH11) and two-way provincial road 304 (PR304) near Pines Falls, MB.

A.2 SITE SELECTION

A.2.1 LOCATIONS OF TEST SITES

Figure A-1 shows the locations of the test sections at PTH11 and PR304.

(a)PTH11

The general condition of the test section can be seen in Figure A-2. Figure A-3 shows the arrangement of the instrumentation and the cabinet for the data acquisition system (DAS).

- The test section is located 2.70 km South-East of the intersection of PR304 and PTH11.
- The test lane is the westbound lane.

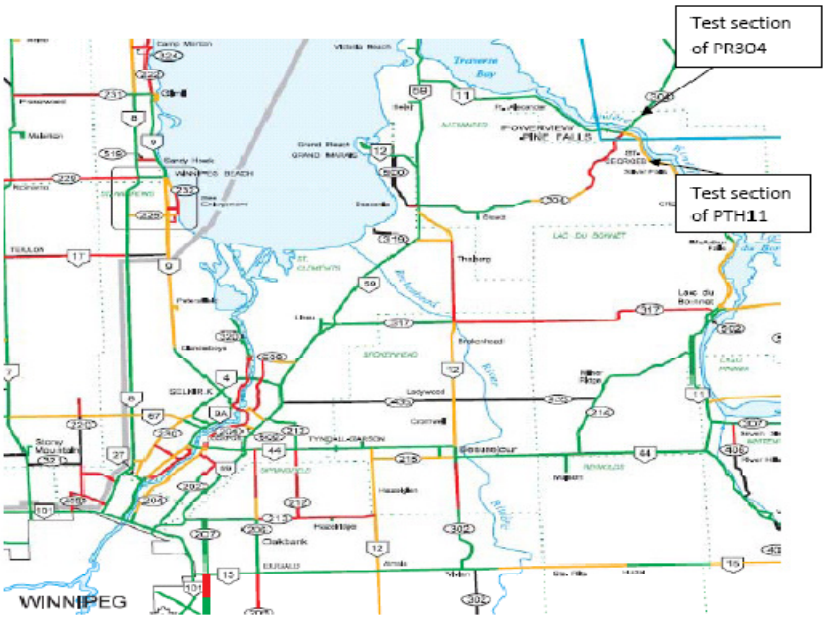

Figure A-1 Locations of test sites at PTH11 and PR304.

Figure A-2 Test section of PTH11.

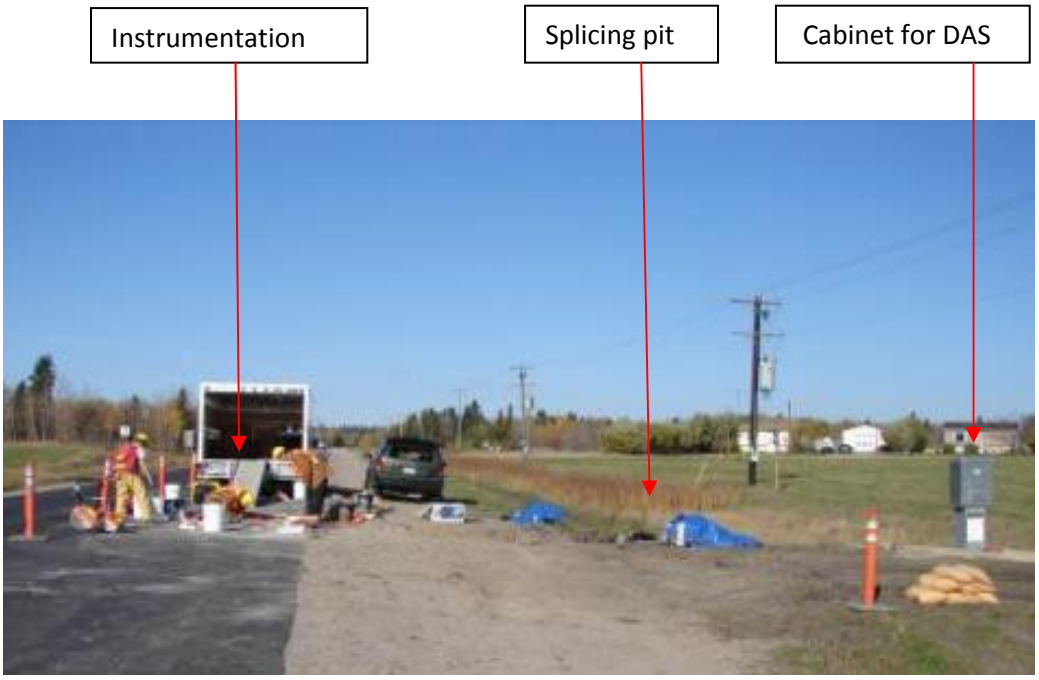

Figure A-3 Instrumentation and data acquisition system at PTH11

(b) PR304

The general condition of the test section can be seen in Figure A-4. Figure A-5 shows the arrangement of the instrumentation and the cabinet for DAS.

- The test section is located 2.40 km North-East of the intersection of PR304 and PTH11.
- The test lane is the southbound lane.

Figure A-4 Test section at PR304.

Figure A-5 General layout of instrumentation for PR304.

A.2.2 ROAD STRUCTURE AT TEST SITES

PTH11 is comprised of an asphalt concrete (AC) pavement structure. PR304 has an asphalt surface treatment (AST) over an aggregate base. These two types of structures are representative of the majority of provincial pavements subject to SLR. The road structure information provided by MIT at the project outset did not indicate a rock fill layer in PR304, however, a 500 mm-thick rock fill layer was discovered during a subsurface investigation conducted in September 2008. This rock fill layer is an unusual characteristic and is not found with typical AST roads in Manitoba. Information about the two road structures is presented in Table A-1. Figure A-6 shows the rock fill at PR304

Table A-1 Road structures and traffic information at test sites (source: MIT)

Highway	Structure	Classification	BBRE (mm)	SLR	Vehicles per day	Percent Trucks	Comments
PR304	30AST, 200GB, 500 rock fill, Sandy clay subgrade	B1 Secondary Arterial	1.494	Level1	265	5.5	Moderately strong AST
PTH11	130 AC, 250 GB, High plastic clay subgrade	RTAC Secondary Arterial	2.020	Level1	1210	3.2	Weak AC

Figure A-6 500 mm rock fill visible in an excavation in the shoulder of PR304.

The paved layers at the PR304 and PTH11 test sites can be seen in Figures A-7 and A-8**.**

Figure A-7 30 mm-thickness AST layer of PR304.

Figure A-8 AC cores extracted at the test site of PTH11.

A.3 PAVEMENT INSTRUMENTATION

The pavement instrumentation was divided into two groups: (1) weather and environmental sensors, (2) strain and deflection sensors. A total of forty-eight (48) and thirty-nine (39) sensors were installed within the pavement test sections at PTH11 and PR304, respectively.

A.3.1 WEATHER AND ENVIRONMENTAL MONITORING SENSORS

Four types of weather and environmental sensors were installed at each site.

(a) Water Content Reflectometer (WCR)probe

The moisture content variation within different layers of pavement is an important parameter that influences the overall behavior of flexible pavement. For this project,

the Campbell Scientific water content reflectometer probe was selected to monitor moisture content of the various pavement layers.

As seen in Figure A-9, the WCR probe consists of two parallel conducting rods that are 300 mm in length. The oscillation frequency of the multivibrator is dependent upon the dielectric constant of the material surrounding the conducting rods. The period of the square wave from the multivibrator ranged between 0.7 to 1.6 milliseconds. The relationship between the volumetric moisture content and the dielectric constant is determined by using a regression equation programmed into the data acquisition system (Campbell Scientific, Inc.).

Figure A-9 Water Content Reflectometer (CS616).

Five WCRs were installed at each site. Tables A-2 and A-3 show the locations of the WCR probes at PR304 and PTH11, respectively.

Table A-2 Water Content Reflectometer installed at PR304

Sensor	Label	Installation date	Depth from surface (mm)	Lateral position (mm)*
CS616-48294-100FT-06	M6	14/10/08	130	100
CS616-35744-25FT-01	M7	14/10/08	550	105
CS616-35744-25FT-02	M8	14/10/08	850	105
CS616-35744-25FT-03	M9	14/10/08	1150	150
CS616-35744-25FT-04	M10	14/10/08	1500	150

** Refers to the distance from centre of the CS616 probes to the edge of pavement*

Different calibration coefficients should be used for different matrials. For mineral soil with bulk electrical conductivity less than 0.05 Siemens (which is the SI derived unit of electric conductance and electric admittance. One siements is equal to the reciprocal of one ohm) per metre (ds/m), bulk density less than 1.55 g/cm^3, and clay content less

than 30%, using standard calibration coefficients should provide accurate volumetric water content. For sandy clay loam, the calibration coefficients depend on the bulk electrical conductivity and bulk density. Organic matter and some clay are highly polarized. These solid constituents can affect WCR response to water content change and require specific calibration.

Table A-3 Water Content Reflectometer installed at PTH11

Sensor	Label	Installation date	Depth from surface (mm)	Lateral position (mm)*
CS616-48294-100FT-01	M1	16/10/08	200	50
CS616-48294-100FT-02	M2	16/10/08	510	50
CS616-48294-100FT-03	M3	16/10/08	830	50
CS616-48294-100FT-04	M4	16/10/08	1170	50
CS616-48294-100FT-05	M5	16/10/08	1520	50

** Refers to the distance from centre of the WCR probes to the edge of pavement*

It is important to make sure that the WCR rods have good contact with the surrounding soil; also, keeping the rods parallel is critical to get an accurate moisture reading of the soil. As can be seen in Figure A-10, a pilot tool was used to install WCR probes correctly. Figure A-11 illustrates the five WCR probes installed at PTH11.

Figure A-10 Using a pilot tool to install WCR probe at PTH11.

Figure A-11 Five WCR probes were installed at PTH11.

All of the WCR probes were installed from an open pit on road side. They were inserted horizontally into the undisturbed roadbed of the trench wall to ensure the probes had good contact with the soil.
Bulk soil samples were collected from the same layer in which WCR were installed to verify the accuracy of sensor readings against lab-determined soil moisture content.

(b) Fredlund Thermal Conductivity (FTC) Sensor

The Fredlund thermal conductivity sensor (FTC-100) was chosen to measure the potential matric suction gradient developed within the pavement, especially during freezing and thawing. Figure A-13 shows an FTC.

Figure A-12 Fredlund Thermal Conductivity sensor (FTC-100).

The FTC was developed by Geotechnical Consulting and Testing Systems (GCTS) for laboratory and field applications such as the monitoring of matric suction of soils. The FTC sensor measures the soil temperature to get the matric suction of the soil mass based on the thermal conductivity of a ceramic block. The ceramic block is buried at the location where the suction is to be measured. The sensor is allowed to equilibrate to the same matric suction as the surrounding soil. The centre of the ceramic block contains a

small heating element and digital temperature sensor. When the heating element is heated with a standard quantity of heat, the temperature in the block reaches a peak value depending on the thermal conductivity of the block at the time of testing. The thermal conductivity is dependent on the water content of the block, which in turn depends on the matric suction of the surrounding soil (GCTS, 2004-2005). This chain of relationships is illustrated in Figure A-13.

Figure A-13 Matric suction in sensor controls temperature rise (source: FTC-100 manual).

At PR304 and PTH11 test sites nine and twelve FTC sensors, respectively, were installed together with WCRs. Two arrays of FTC sensors were installed at each site. One array of FTC-100 sensors was installed near the edge of the pavement; the other was located between the inner and outer wheel paths. Tables A-4 and A-5 show the locations of each FTC-100 sensor for PR304 and PTH11, respectively.

According to the September 2008 subsurface investigation, the water table at PR304 is 1.8 m from the surface. The test plan was to install ten FTC sensors, in two arrays, down to a depth of 1.5 m; however, the presence of the rock fill precluded the installation of sensor T19 at the depth of 500 mm from surface.

Table A-4 FTC Sensors installed at PR304

Serial Number	Label	Installation date	Depth from surface (mm)	Transverse position (mm)*
31-19	T13	14/10/08	130	200
31-20	T14	14/10/08	600	370
31-21	T15	14/10/08	850	200
31-22	T16	14/10/08	1150	200
32-04	T17	14/10/08	1500	200
32-06	T18	14/10/08	130	700
32-10	T20	14/10/08	850	710
32-12	T21	14/10/08	1150	1180
32-13	T22	14/10/08	1500	1180

** Refer to the distance from centre of FTC-100 sensor to the edge of pavement*

Table A-5 FTC Sensors installed at PTH11

Serial Number	Label	Installation date	Depth from surface (mm)	Transverse position (mm)*
31-02	T1	16/10/08	200	300
31-04	T2	16/10/08	510	410
31-06	T3	16/10/08	830	300
31-08	T4	16/10/08	1170	340
31-10	T5	16/10/08	1520	350
31-12	T6	16/10/08	1809	345
31-13	T7	16/10/08	200	400
31-14	T8	16/10/08	510	600
31-15	T9	16/10/08	830	850
31-16	T10	16/10/08	1170	850
31-17	T11	16/10/08	1520	750
31-18	T12	16/10/08	1921	573

** Refer to the distance from centre of FTC sensor to the edge of pavement*

The FTC sensors should be installed such that the ceramic tips are in good contact with the surrounding soil; otherwise equilibration to the correct suction matric value cannot be assured. Also sensors should be installed horizontally to give the best estimate of soil water profile. Each sensor was inserted in a horizontally drilled hole. Figures A-14 through A-17 show the tools and procedures used to install FTC sensors.

Figure A-14 Tools for installing FTC.

Figure A-15 Drilling a hole for installing an FTC with 28 mm diameter auger at PTH11.

Figure A-16 Inserting a FTC into a drilled hole with sensor insertion tool at PTH11.

Figure A-17 Backfilling the hole using tamping dowel after inserting a FTC.

(c) Thermistor

The thermistor probes (Figure A-18) were selected to make the thermistor string. The thermistors were supplied by Campbell Scientific.

Figure A-18 Thermistor.

As shown in Figure A-19, seven thermistor probes were assembled in a custom-made thermistor string for each test site. A 50 mm-diameter plastic pipe was chosen to protect thermistors from any damage during and after installation. The thermistor strings were used to determine the temperature profile and depth of frost/thaw in each pavement structure under the outer wheel path to the depth of 2400 mm at both sites.

Figure A-19 Thermistor string with seven thermistor probes.

As presented in Figure A-20, a 38 mm-diameter hole was made for each thermistor. Each thermistor was mounted such that the sensitive tip was exposed to soil mass.

Expansive foam was applied above and below the location of each thermistor within the pipe as thermal barrier.

Figure A-20 38 mm-diameter hole for each thermistor.

The reported precision of the thermistor is ±0.4 °C over the range of -24 °C to 48 °C and ±0.9 °C over the range of -38 °C to 53 °C (Campbell Scientific, Inc.). The thermistor string was installed in a vertical borehole, which was subsequently backfilled with sand and compacted. Tables A-6 and A-7 show the locations of each thermistor installed at PR304 and PTH11, respectively.

Table A-6 Thermistors Installed at PR304

Sensor	Serial Number	Label	Depth from surface (mm)	Lateral position (mm)
107B-100FT-C7126	C7126	C8	191	Outer wheel path, 800 mm from the edge of pavement
107B-100FT-C7127	C7127	C9	491	
107B-100FT-C7128	C7128	C10	791	
107B-25FT-C6931	C6931	C11	1191	
107B-25FT-C6936	C6936	C12	1591	
107B-25FT-C6937	C6937	C13	1991	
107B-25FT-C6938	C6938	C14	2391	

Table A-7 Thermistors Installed at PTH11

Sensor	Serial Number	Label	Depth from surface (mm)	Lateral position (mm)
107B-100FT-C7119	C7119	C1	200	Outer wheel path, 800 mm from the edge of pavement
107B-100FT-C7120	C7120	C2	500	
107B-100FT-C7121	C7121	C3	800	
107B-100FT-C7122	C7122	C4	1200	
107B-100FT-C7123	C7123	C5	1600	
107B-100FT-C7124	C7124	C6	2000	
107B-100FT-C7125	C7125	C7	2400	

(d) Air temperature and relative humidity probe

Air temperature and relative humidity are important indices to predict the temperatures of highway structures. Highway structure temperature is useful in determining the timing of SLR. Figure A-21 illustrates the air temperature and relative humidity probe that was installed beside the DAS cabinet at each site.

Figure A-21 Humidity and temperature probe beside a DAS

The air temperature and relative humidity probe was made by Rotronic Instrument Corporation, and measures air temperature with a Pt100 RTD and relative humidity based on HygroClip technology (Campbell Scientific, Inc. , 2007).

A.3.2 STRAIN AND DEFLECTION GAUGES

(a) General layouts

Sensors were installed within the outer wheel path as defined by existing traffic conditions (rutting, for instance) and as is the practice for Long Term Pavement Performance Tests. The layout of strain and deflection gauges was based on the conventional spacing of a tridem axle with dual tires. The groups of strain gauges were installed 1850 mm longitudinally away from one another. The strain gauges were installed just under the centre of the dual tires.

Because the strain gauges were installed at about 150 mm below the road surface, stress overlap is not expected. The soil compression gauges at both sites and multi-depth deflectometer at the PTH11 were installed at depths from 250 mm to 2000 mm where stress overlap is expected. They were installed under the centre of outer wheel path.

(b)Asphalt Strain (horizontal) Gauge

Asphalt strain gauge (ASG) from Construction Technology Laboratories, Inc. (CTL) was selected for measuring horizontal roadbed strains. The full-bridge configuration of the selected strain gauge eliminates the need for expensive data-acquisition and signal-conditioning systems to provide bridge completion. Braided shielding protects the lead wire from electrical noise, while an abrasion-resistant, Teflon polymer coating withstands temperatures up to 205 ^{o}C (400 °F). This all contributes to longer sensor life. The full scale is 1500 micro-strain; operating temperature is -34 ^{o}C (-30 °F) to 204 ^{o}C (400 °F) (CTL Group). Figure A-22 shows an ASG.

Figure A-22 Asphalt strain gauge.

Eight ASGs were installed in 300 mm-diameter coring holes at each site. The gauges at PTH11 were installed horizontally at the bottom of AC layer with four oriented in longitudinal road direction and four oriented transversely. The gauges at the PR304 site were installed horizontally in GB layer at a depth of about 150 mm below road surface with four oriented longitudinally and four oriented transversely. All the strain gauges were installed within the outer wheel path. Tables A-8 and A-9 show the locations of each ASG at PR304 and PTH11, respectively.

Table A-8 Horizontal Asphalt Strain Gauges Installed at PR304

Serial Number	Installation date	Depth from surface (mm)	Orientation
S-11	15/10/08	140	Transverse
S-12	15/10/08	140	Transverse
S-13	15/10/08	140	Longitudinal
S-14	15/10/08	140	Longitudinal
S-15	15/10/08	125	Transverse
S-16	15/10/08	147	Transverse
S-22	15/10/08	140	Longitudinal
S-23	15/10/08	135	Longitudinal

Table A-9 Horizontal Asphalt Strain Gauges Installed at PTH11

Serial Number	Installation date	Depth from surface (mm)	Orientation
S-3	17/10/08	134	Transverse
S-4	17/10/08	140	Transverse
S-5	17/10/08	142	Longitudinal
S-6	17/10/08	137	Longitudinal
S-7	17/10/08	134	Transverse
S-8	17/10/08	130	Transverse
S-9	17/10/08	135	Longitudinal
S-10	17/10/08	137	Longitudinal

The manufacturer recommended installation procedure was followed carefully. After preparing a 300 mm diameter core hole, the following steps were performed:

- Determined the depth for gauge installation.
- Applied a thin layer of asphalt primer to the leveled base surface at each gauge location. The primer covered an area of 150 mm x 250 mm square.
- Prepared a mastic mix consisting of Type CSS1 Bitumen and aggregate passing the No. 10 sieve in an approximate 1:2 ratio. The mixture had a consistency of thick paste but was pourable.
- After the primer cured, applied a 3 mm thick layer of the mastic mix to each gauge location.
- Placed the gauge into the mastic mix by gently pressing down on the gauge and anchors until they both came into full contact with the mix. The gauges were placed so they were flat at the position. The wire of each sensor was place loosely into the core hole to avoid damaging from compaction of back fill materials and traffic.
- Read and recorded the output of each gauge using a strain indicator readout unit.
- Prepared cold mix, hand removed large aggregate particles, and placed approximately 50 mm of the mix over and around each gauge. This protection layer was compacted by applying a static pressure with a 90 cm^2 steel plate.
- Lead wires were routed from each gauge in a 50 mm deep groove leading to the shoulder edge, where they were later routed to the DAS cabinet.

(c)Vertical Asphalt Strain Gauge

Similarly, vertical asphalt strain gauge from CTL was chosen to measure vertical strains. Their full scale is 1500 micro-strain and operating temperature is -34 ^oC to 204 ^oC Figure A-23 shows a vertical asphalt strain gauge.

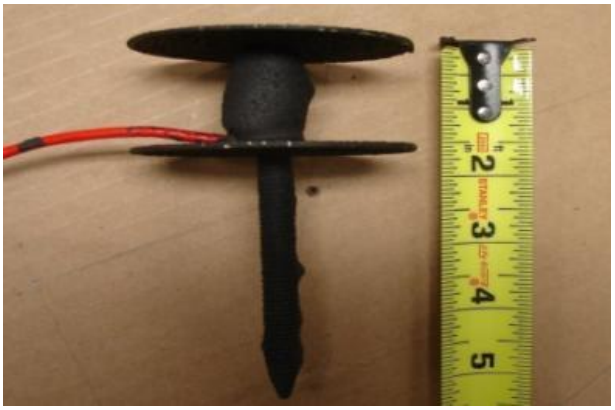

Figure A-23 Vertical Asphalt Strain Gauge.

Four vertical asphalt strain gauges were installed at each site in 300 mm-diameter cored holes. At PTH11 the gauges were installed at the bottom of AC layer; while on PR304 the gauges were installed in GB layer to the depth about 150 mm from the top of AST. All the strain gauges were installed within the outer wheel path. Tables A-10 and A-11 show the locations of each vertical asphalt strain gauge at PR304 and PTH11, respectively.

Table A-10 Vertical Asphalt Strain Gauge Installed at PR304

Serial Number	Installation date	Depth from surface (mm)*
S-20	15/10/08	132
S-21	15/10/08	132
S-24	15/10/08	121
S-25	15/10/08	128

*refers to the distance from the surface of pavement to the centre of the gauge

Table A-11 Vertical Asphalt Strain Gauge Installed at PTH11

Serial Number	Installation date	Depth from surface (mm)*
S-1	17/10/08	124
S-2	17/10/08	123
S-17	17/10/08	118
S-18	17/10/08	115

*refers to the distance from the surface of pavement to the centre of the gauge

After preparing 300 mm diameter core hole, the strain gauges were installed as follows:

- Using hand driven stake to make a 9 mm diameter hole, 100 mm deep in the base course material.
- Applied a thin layer of asphalt primer to the leveled base surface at each location. The primer completely covered an area 150 mm x 150 mm square and filled the hole.
- Placed the gauge into the drilled hole and mastic mix by gently pressing the gauge down into the hole until the bottom disc plate came into full contact with

the mix. The wire of each sensor was place loosely into the core hole to avoid damaging from compaction of back fill materials and traffic. Removed the top screw and top disc plate from the gauge, and read and recorded the output of each gauge using a strain indicator readout unit. Replaced the screw (not the plate) and attached several strands of survey marking material under the screw before tightening.

- Hand removed large aggregate particles from the cold mix and then placed mix around each gauge. This protection layer was compacted by applying a static pressure with a 90 cm^2 steel plate around the gauge area, leaving the coloured marking material standing up.
- Removed the screw and coloured strands, hand compacted (with a tamping plate) the area immediately around the gauge, and then replaced the top disc plate and screw.
- Lead wires were routed from each gauge in a 50 mm-deep groove leading to the shoulder edge, and later routed to the DAS cabinet.

Figures A-24 to A-32 illustrate the installation of strain gauges at PTH11 and PR304.

Figure A-24 Core hole arrangement for strain gauges at PR304.

Figure A-25 Core holes with saw cut grooves for wire leads at PTH11.

Figure A-26 Installing horizontal ASG at PR304.

Figure A-27 Installing horizontal ASG at PTH11.

Figure A-28 Strain gauges installation at PTH11.

Vertical ASG top plate was removed to compact surrounding material

Horizontal strain gauge

Figure A-29 Horizontal and vertical ASGs were installed together in base layer of PR304.

Figure A-29 Installing vertical ASG into granular base layer of PR304.

Figure A-30 Installing vertical ASG at PTH11.

Figure A-31 Strain gauge holes backfilled with compacted cold mix at PTH11.

(d) Soil compression gauge

The soil compression gauge (SCG) was also made by CTL. The movement range of these gauges is 25 mm; total gauge length is 160 mm. Figure A-33 shows a soil compression gauge.

Figure A-32 Soil compression gauge.

Four SCGs were installed at each site. At PTH11, all the SCGs were located in subgrade; while at PR304 two SCGs were installed in subgrade and the other two were installed in the GB layer. Tables A-12 and A-13 show the locations of each SCG at PR304 and PTH11, respectively.

Table A-12 Soil Compression Gauges Installed at PR304

Serial Number	Installation date	Depth from surface (mm)*
F-5	15/10/08	156
F-6	15/10/08	156
F-7	13/11/08	837.5
F-8	13/11/08	778

*refers to the distance from the surface of pavement to the centre of the gauge

Table A-13 Soil Compression Gauge Installed at PTH11

Serial Number	Installation date	Depth from surface (mm)*
F-1	12/11/08	845
F-2	12/11/08	635
F-3	12/11/08	650
F-4	12/11/08	860

*refers to the distance from the surface of pavement to the centre of the gauge

Figures A-34 through A-37 illustrate the installation of SCGs at PR304 and PTH11.

Figure A-33 A SCG installed into granular base layer of PR304.

Figure A-34 Separate cylindrical mass of soil into two halves.

Figure A-35 Pack the two halves of soil mass around SCG.

Figure A-36 Insert the mass of soil and SCG into hole at PR304.

(e)Multi-Depth Deflectometer

The Multi-Depth Deflectometer (MDD) was fabricated by CTL. This instrument is used to measure the average vertical deflection under load of multiple layers of the pavement and subgrade. The vertical deformations are measured from a reference head near the top surface to predetermined depths. Overall vertical deflection is referenced to a fixed anchor in the subgrade material.

The MDD can be configured to measure deformations in up to seven layers within the 2.2 m length of the MDD. The depth of the fixed anchor must be relatively deep so that it experiences minimal deformation under load. Sensors used for measuring displacement are 25 mm (full scale) linear potentiometers. Their resolution is better than 0.03 mm. Spacing of vertical measurements (layers) must be 50 mm or greater to obtain quality data. The top reference head is located approximately 90 mm below the pavement surface and measurement layers start from there. The reference head assembly is housed within a road box that is grouted into the pavement and becomes integral with the pavement. Figure A-38 shows the dimensions of the reference head positioned in the road box. When the pavement deflects under load, the reference head moves downward, compressing the potentiometer plungers various amounts (CTL Group).

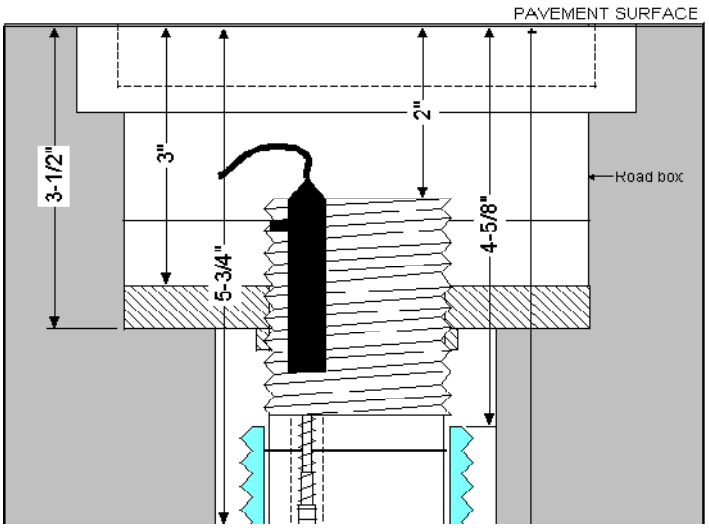

Figure A-37 Reference head assembly positioned in road box.

Figures A-39 and A-40 show the MDD assembly installed at PTH11. CTL was contracted to install the MDDs in order to obtain a top quality installation.

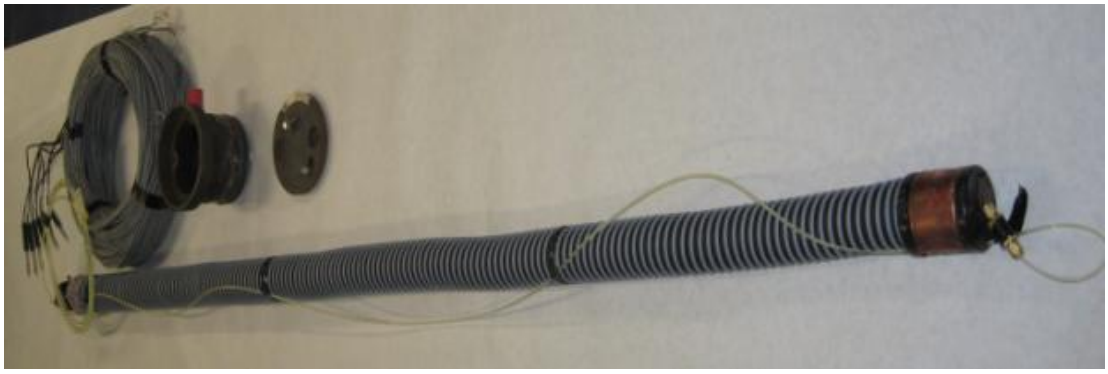

Figure A-39 Multi-Depth Deflectometer.

Figure A-380 Reference head, road box, and transducers of MDD.

Table A-14 shows the elevation of each measurement location of MDD at PTH11.

Table A-14 MDD Installed at PTH11

Serial Number	Depth from surface(mm)	Transverse position (mm)
ML-1	350	within outer wheel path, 800 mm from the edge of the pavement
ML-2	500	
ML-3	650	
ML-4	950	
ML-5	1250	
ML-6	2000	

The following figures illustrate the installation of the MDD at PTH11. Figure A-41 shows how a plastic setting tube was attached to the top of MDD after the MDD was inserted into the borehole. The elevation of the MDD was set by pinning the tube (and MDD) with a cross piece inserted through a hole near the top of the setting tube.

Figure A-39 Precisely setting the MDD elevation with a pinned setting tube.

As shown in Figure A-42, a hand pump was connected to hydraulic fitting. A dial guage was used to monitor the applied pressure. At the beginning, as the copper bladder of the hydraulic anchor was expanded, the pressure readings rose from 0 to 345 kPa. When the hydraulic anchor was expanded to meet the surrounding soil, the reading increased due to soil resistance. The MDD was well anchored when the pressure read about 690 kPa.

Figure A-40 Expansion of the MDD hydraulic anchor.

Figure A-43 shows a 6 mm-diameter copper water tube was attached to a pump sprayer Water was pumped into the hole starting from bottom. The copper tube was drawn out of the hole as the annular space was backfilled with water-expanded bentonite provided by CTL.

Figure A-41 Backfilling the annular space around the MDD.

Figure A-44 shows the inserting of MDD road box into AC layer after backfilling the hole.

Figure A-42 Inserting MDD road box into AC layer.

As can been seen from Figure A-45, six transducers were inserted into the reference head of MDD after the installation of road box.

Figure A-43 Six transducers inserted in the reference head within MDD road box.

Figure A-46 shows the top of the fully installed MDD at PTH11.

Figure A-44 MDD assembly fully installed at PTH11.

A.3.3 WIRING SYSTEM

As can be seen in Figure A-47, a small groove (5 mm-wide by 50 mm-deep) was cut using an asphalt saw from each sensor hole in AC layer to a common location at road edge. All AC cuttings were carefully cleaned out of the grooves. The sensor wires, or groups of wires, were then carefully laid along to the bottom of the grooves. Finally, the grooves were sealed with 3M™ Detector Loop Sealant 5000.

Figure A-45 Cutting a groove in AC layer for a sensor wire (PTH11).

Figure A-48 shows that the grooves were cut diagonally to the edge of pavement. By cutting the grooves diagonally to the edge of pavement instead of perpendicularly, a smoother ride will be produced because the individual tires of a dual assembly will pass over each groove at a different time.

Figure A-46 Grooves for sensor wires were cut diagonally to the edge of pavement (PTH11).

As shown in Figure A-49, the grooves were cleaned carefully after cutting.

Figure A-49 Cleaning wire grooves (PR304).

Figure A-50 shows a groove containing a group of sensor wires being sealed. Sealant encapsulates, insulates and protects the wires of a detector loop from the effects of roadway environment.

Figure A-47 Sealing groove after wires were inserted (PR304).

When all of the sensor wires were installed to the pavement shoulder, as can be seen in Figure A-51, a 300 mm deep trench was excavated from the pavement edge to a splicing pit on the outside edge of the ditch. All of the wires were laid along the trench to the splicing pit and buried with fine sand. The wires were laid out in the trench with some slack to prevent potential damage in the event of freeze-thaw expansion of the roadbed. The wires were fed through four 50 mm-diameter conduits previously installed by MIT from the splicing pit to the data acquisition system cabinet (previously installed on a concrete base by MIT).

Figure A-51Trench to splicing pit.

The Figures A-52 and A-53 shows respectively the splicing pit and the whole wiring system.

Figure A-48 Splicing pit.

Figure A-49 Wiring was routed from roadbed via trench and splicing pit to DAS cabinet.

A.3.4 DATA ACQUISITION SYSTEM

Four dataloggers were required for the sensors. Table A-15 shows dataloggers used in this research.

Table A-15 Dataloggers for the research

Datalogger	Manufacturer	Sensors monitored	Sample rate
CR1000	Campbell Scientific	water content reflectometer thermistor	every two hours
TCCON-016	GCTS	Fredlund thermal conductivity sensor	every four hours
DI-718	DATAQ Instrument	ssphalt strain gauge	400 Hz per channel
DI-715	DATAQ Instrument	multi-depth deflectometer soil compression gauge	400 Hz per channel

Figure A-54 shows the data acquisition system arranged within its cabinet at the PTH11 test site.

Figure A-54 Cabinet and data acquisition system at PTH11.

A.4 SUMMARY

This chapter covers the selection and installation of instrumentation for the two test sections on PTH11 and PR304. Temperature, moisture, humidity, strain and deflection sensors were calibrated and tested in the laboratory during the period of May to October 2008, and installed during the period of October 14 to November 14, 2008.

All the sensors were tested and calibrated before installation. Software programs were developed and installed in each logger to collect data. All eighty-seven (87) sensors for both sites were tested and calibrated successfully and verified using external devices. Operating instructions for each datalogger and all types of sensors were developed.

A detailed instrumentation plan including sensor layout, instrumentation manuals, parameter manuals, field recording journal, and some potential problems and their corresponding solutions, was developed before installing the sensors.

MIT delivered power supply lines to each of the sites on 13 November 2008, and installed a data acquisition system cabinet, wiring splicing pit, and wiring conduits between them at each site.

The installation was completed by the Pavement Research Group and FPInnovations. External contractors were hired to complete the following tasks: coring into the road surface, drilling into the road base and subgrade, and excavation of trenches on road shoulder and ditches. Also CTL was retained to install the MDDs. All sensors were installed successfully and tested at the end of the installation confirmed their operation.

REFERENCES

Geotechnical Consulting & Testing Systems (GCTS). 2004-2005. Fredlund thermal conductivity sensor, FTC-100, operating instruction, version 1.02.

GCTS. SuctionData. 1.13. User's Guide and Reference.

Campbell Scientific, Inc. CR1000 Measurement and Control System. Revision: 7/08

Campbell Scientific, Inc. CS616 and CS625 Water Content Reflectometers. Revision: 8/06

Campbell Scientific, Inc. Model 107 Temperature Probe. Revision: 2/07

Campbell Scientific, Inc. 2007. HC-S3 & HC-S3-XT Temperature and relative humidity probe

Construction Technology Laboratories, Inc. Vertical asphalt strain gauge (ASG-VS). Installation Procedure

Construction Technology Laboratories (CTL), Inc. Asphalt strain gauge (ASG). Installation Procedure

Construction Technology Laboratories (CTL), Inc. Soil compression gauge (SCG). Installation Procedure

Construction Technology Laboratories (CTL), Inc. Preparation for and installation of mult-depth deflectometer

Dami Adedapo. 2008. In situ moisture and temperature monitoring system of clay subgrade and aggregate base courses along PTH 59 south and PR201 near ILE-DES CHENES instrumentation installation report (draft). KGS group. Project number 07-300-03

DATAQ Instruments, Inc. DI-718Bx Series. 16 Channel Data Logger with Signal-Conditioned Inputs. User's Manual. Manual Revision J

Robert A. Trunk. 'How to Calibrate Strain Gauge-Based Transducers Using DI-5B38 Strain Amplifiers'. DATAQ Instruments

DATAQ Instruments, Inc. DI-715B Series USB or Ethernet Data Logger with Signal-Conditioned Inputs. User's Manual. Manual Revision Q.

DATAQ Instruments, Inc. WINDAQ Acquisition. Waveform Recording Software. WINDAQ Waveform Browser. Playback and Analysis Software.